Colloidal Metastability

Helen Sedgwick

Thesis submitted for the degree of Doctor of Philosophy

School of Physics

University of Edinburgh

2003

Abstract

Aggregation and gelation have been studied in two different colloidal systems. Firstly, a model colloid-polymer mixture has been used to investigate the non-ergodicity transition at low colloid volume fractions. Secondly the interaction between kinetic arrest and phase separation has been studied in a globular protein solution.

A model colloid-polymer mixture with a short ranged attraction was suspended in a solvent of approximately the same density as the particles. Confocal microscopy revealed an ergodic single phase fluid at low polymer concentration c_p, and on increasing c_p the colloids were observed to aggregate across a sharp boundary. The *onset* of aggregation is associated with the non-ergodicity transition predicted by mode coupling theory (MCT). Starting from this 'standard model' the effects of charge and gravity on the aggregation and non-ergodicity of colloidal systems have been explored.

When the colloids in this aggregating system were charged, the electrostatic repulsion was found to stabilise the clusters against further growth. This results in a stable and equilibrium long-lived cluster phase. The *onset* of aggregation was again associated with the MCT non-ergodicity transition. At sufficiently high inter-particle attractions the aggregates grew large enough to become non-ergodic. The experimentally observed non-ergodicity boundary is shifted to higher inter-particle attractions due to the charge on the particles.

When gravity is introduced to the system sedimentation may prevent the sample from becoming non-ergodic. The onset of aggregation above a sharp boundary is again associated with the MCT non-ergodicity transition. However, if aggregates undergo significant sedimentation before they meet then the sample does not become non-ergodic. Therefore the samples became non-ergodic at higher inter-particle attractions due to the presence of gravity.

The phase behaviour of protein solutions has been studied. The addition of salt to a protein solution causes an effective attractive interaction between the proteins, and non-equilibrium behaviour is observed at sufficiently high attractions. Optical microscopy revealed four regimes: gas-liquid phase separation, non-coalescing 'beads', large aggregates and transient gelation. The interaction between the gas-liquid binodal and the ergodic to non-ergodic transition line is found to be essential in understanding the non-equilibrium phase behaviour. Gas-liquid phase separation can be interrupted by the formation of a gel in the high concentration liquid phase. If the liquid phase is percolating the sample will form a transient gel.

Declaration

This thesis has been composed by myself and has not been submitted in any previous application for a degree. The work reported within was performed by me unless otherwise stated.

Helen Sedgwick

Acknowledgements

There are a number of people I would like to thank for their inspiration and support. I have no doubt that, without their help, this work would have been impossible.

Firstly I wish to thank my supervisors, Wilson Poon for his encouragement, excitement and criticism, and Stefan Egelhaaf for his endless patience and optimism.

Many thanks to Klaus Kroy for his ideas and discussions, and to Andy Schofield for providing the colloids. I am also grateful to Malcolm Robertson for his extensive help with NMR, and to David Dryden and Lindsay Sawyer for their valuable protein support. For useful discussions I would like to thank Mike Cates, Peter Pusey and Mark Haw. And thank you to all the 'squidgy' group for making this a productive and enjoyable three years, especially Paul Smith, Miriam Clincy, Colin Holmes and Otti Crooze for both their help and their humour. For valuable reading of the manuscript I thank James Lawrence, Iris Coe and Anniina Salonen.

Special thanks to all my friends, both here and elsewhere, and to Dan for keeping me sane and smiling while writing my thesis. And my heartfelt thanks to Iris and Lorna, my partners in crime, for making it all good again.

Finally I would like to thank my family, Mum, Dad, Steve and Ally for being exactly who they are. Thank you.

For my Dad

Contents

1 Introduction 1

1.1 Colloidal Suspensions - *A Historical Perspective* 2

1.2 Colloid Physics Today 3

1.3 Thesis Summary 3

2 Hard-Sphere Colloids 5

2.1 Introduction 6

2.2 Hard-Sphere Phase Behaviour 6

2.3 Polydispersity 7

2.4 Colloidal Stability 8

2.4.1 Van der Waals Forces 8

2.4.2 Charge Stabilisation 9

2.4.3 Steric Stabilisation 10

3 Colloid-Polymer Mixtures 13

3.1 Introduction 14

3.2 The Depletion Potential 14

3.3 Equilibrium Phase Behaviour 18

3.3.1 Representation 18

3.3.2 Topology 19

3.4 Free Energy Landscapes 21

3.4.1 Fluid-Crystal Phase Separation 21

3.4.2 Gas-Liquid Phase Separation 22

3.5 Mechanisms of Gas-Liquid Phase Separation 23
3.6 Non-Equilibrium Phase Behaviour 25
3.6.1 Transient Gelation 26
3.6.2 Diffusion Limited Cluster Aggregation 27
3.6.3 Percolation 30
3.6.4 Mode Coupling Theory 31
3.6.5 Sedimentation and the Influence of Gravity 34
3.7 Summary: Colloid-Polymer Mixtures 35

4 Charged Colloidal Suspensions **37**
4.1 Introduction 38
4.2 The Nature of Charged Colloids 38
4.3 Phase Behaviour of Charged Colloidal Suspensions 39
4.4 DLVO potential 40
4.4.1 Van der Waals Component 42
4.4.2 Screened Coulomb Potential 43
4.4.3 Applicability of the DLVO Potential 45
4.5 Phase Behaviour of Charged Colloid-Polymer Mixtures 47
4.6 Beyond the DLVO Potential 50
4.7 Gelation in Charged Colloid-Polymer Mixtures 52
4.8 Chapter Summary 54

5 Protein Solutions **57**
5.1 Introduction 58
5.2 Protein Structure 58
5.3 Controlling the Charge 59
5.3.1 Importance of pH 59
5.3.2 Acids and Bases 60
5.3.3 Amino Acids and Proteins 62
5.3.4 Buffer Action 63
5.4 Phase Behaviour of Proteins 65

5.5 DLVO Potential 66
5.6 Salting-In 68
5.7 The Hofmeister Series 69
5.8 The Lysozyme-NaCl System 70
5.9 Summary 71

6 Experimental Techniques **73**
6.1 Introduction 74
6.2 Microscopy 74
6.2.1 Basic Principles 74
6.2.2 The Confocal Microscope 80
6.3 Nuclear Magnetic Resonance 85
6.3.1 Nuclear Magnetic Effects 86
6.3.2 Principles of relaxation 88
6.3.3 NMR experiments 90
6.4 Summary 92

7 Experimental System 1: *Colloid-Polymer Mixtures* **93**
7.1 Introduction 94
7.2 Colloid-Polymer Mixtures in *Cis*-Decalin 94
7.2.1 Colloids 94
7.2.2 Polymer 95
7.2.3 Sample Preparation 98
7.3 Colloid-Polymer Mixtures in Density Matched Solvents 99
7.3.1 Colloids 99
7.3.2 Polymer 102
7.3.3 Screening the Charge 103
7.3.4 DLVO Potential 103
7.3.5 Sample Preparation 104
7.4 Combining the Solvents: Charge and Gravity 106
7.4.1 Sample Preparation 106
7.5 Summary of Experimental Systems 106
7.6 Colloid-Polymer Sample Composition 107
7.6.1 Errors 109

8 Results 1:
Colloid-Polymer Mixtures **113**

8.1 Introduction 114

8.2 System 1 115

8.2.1 Phase Diagram 115

8.2.2 Detailed Observations 117

8.2.3 Interpretation 119

8.3 System 2 128

8.3.1 Phase Diagrams 128

8.3.2 Detailed Observations 129

8.3.3 Interpretation 131

8.4 System 3 141

8.4.1 Phase Diagram 141

8.4.2 Detailed Observations 141

8.4.3 Interpretation 146

8.5 System 4 148

8.5.1 Phase Diagram 148

8.5.2 Detailed Observations 148

8.5.3 Interpretation 149

8.6 Summary 149

9 Experimental System 2:
Protein Solutions **153**

9.1 Introduction 154

9.2 Controlling the Charge 154

9.3 Effect of NaCl 155

9.4 Protein Stock Preparation 156

9.5 NaCl Stock Preparation 157

9.6 Sample Composition 157

9.6.1 Errors 158

10 Results 2:
Protein Solutions **161**

10.1 Introduction 162
10.2 Phase Behaviour 162
10.3 Interpretation 166
10.4 NMR Measurements of Mobility 174
10.4.1 Lysozyme Spectra 174
10.4.2 Relaxation Time Measurements 176
10.5 Temperature Dependence 178
10.6 Discussion 183
10.6.1 Literature Review 183
10.6.2 Gas-Liquid Phase Separation in the Colloid-Polymer System 188
10.6.3 Literature Review 191
10.6.4 A Return to Gravity 193
10.7 Summary 195

11 Future Work **197**

11.1 Introduction 198
11.2 Gelation and Aggregation 198
11.3 Charged Colloids 200

12 Conclusion **201**

Appendicies **204**

List of Tables **217**

List of Figures **218**

Index **229**

Bibliography **232**

Chapter 1

Introduction

1.1 Colloidal Suspensions - *A Historical Perspective*

Colloidal suspensions are a complex state of matter, consisting of small particles (the dispersed phase) suspended within a continuous phase (the dispersion medium). The length scale of colloidal particles lies the mesoscopic regime, intermediate between the microscopic length scale of atoms and molecules and the macroscopic one of objects resolvable by the naked eye. Although colloidal suspensions have existed in geology and in mankind's food and technology for thousands of years, the particulate nature of their composition and the importance of the dispersed particle size was only discovered within the past two hundred years.

The first description of matter as being particulate dates back to 360 BC when Plato put forward his philosophy that each type of matter, earth, air, fire and water, is made up of particles or 'primary bodies'. Each particle is a regular geometric solid, itself composed of triangles [69]. Although the details of the theory are incorrect, the insight into the molecular and atomic nature of matter (Plato's 'particles' and 'triangles' respectively) is remarkable.

Throughout the following two millennia virtually no scientific advances were made to either contradict or support Plato's ideas. While mankind constantly made use of states of matter incorporating small particles, in the preparation of bread and butter to the making of bricks and ink, their crafts were dependent on the empirical characterisation of materials passed down through generations, with no real scientific understanding. The mysticism surrounding the nature of matter perhaps reached its height in the study of Alchemy and the search for the supposed Elixir of Life, itself in fact a form of colloidal gold.

The first systematic study of a colloidal suspension was made by Faraday in 1856, who demonstrated some of the most important properties of colloidal dispersions including sedimentation, light scattering and coagulation by salts. The phrase 'colloid' was introduced by Graham a few years later in 1861 to describe a group of substances which would not pass through a parchment membrane on account of the particle size. Graham postulated the size of these particles to be in the range from one nanometer to one micrometer, a range which is still given today to define colloidal particles. The word comes from the Greek $\kappa o \lambda \lambda \alpha$ meaning glue-like, and reflects the property of such particles to easily stick together. Indeed the propensity of colloidal particles to aggregate is still subject to intensive study today and forms much of the content of this thesis.

In the beginning of the twentieth century, colloidal science established a connection between chemistry and physics when Einstein discovered the connection between Brownian motion and the diffusion coefficient. Ever since, colloidal science and the study of 'soft matter' systems has linked different disciplines of science from chemistry and materials sciences to physics.

1.2 Colloid Physics Today

But what of the study of the colloidal state today? Even in relatively simple model colloidal suspensions, features such as the inter-particle interactions, metastable states and glassy behaviour still present enormous potential to advance our understanding. The study of 'soft matter' has moved beyond suspensions of solid colloidal spheres, to include polymers, liquid-crystals, surfactants, biological macromolecules, and mixtures of these.

In this thesis an experimental study of metastable phase behaviour in colloid-polymer mixtures and protein solutions is presented. In colloid-polymer mixtures the strength and range of the inter-particle attraction can be finely tuned and controlled, by altering the concentration and size of the polymer. Furthermore, the interaction potential of a mixture of charged colloids with polymer can be varied if the charge is screened by the addition of salt to the suspension. Thus, colloidal suspensions on the addition of polymer and salt provide a model system with which phase behavior can be studied for inter-particle potentials of different strengths, and where the range of both the attraction (polymer induced) and repulsion (charge induced) can be controlled.

There are an increasing number of physical scientists studying the phase behaviour of globular proteins. The addition of salt to a protein solution screens the charge on the proteins, inducing an effective inter-particle attraction, the strength of which is dependent on the salt concentration. Therefore globular protein solutions provide another system in which phase behaviour can be studied as the inter-particle interaction is varied.

The understanding gained from the study of colloidal suspensions can be applied to a range of other systems, varying from atomic systems to the biological environment within cells of living organisms. Food and cosmetic industries apply our understanding of soft matter systems to products such as salad dressing and shampoo, and the nature of soft condensed matter systems from crystals to gels, liquids to glasses, can enhance our understanding of the nature of the world around us.

1.3 Thesis Summary

This thesis presents two distinct experimental studies of the metastable aggregation, gelation and phase separation of particles with a short-ranged attraction. Firstly, it is a study of a single, well characterised colloid-polymer mixture from which the effects of charge and gravity on the

gelation transition have been discerned. Secondly, it is a study of the globular protein lysozyme, through which the interaction between phase separation and kinetic arrest has provided insights into the nature of transient gelation.

In chapter 2 the concept of the ideal hard sphere system is introduced, and the ideal hard-sphere phase behaviour presented. The key issues relating to the use of colloidal particles as a model for hard-spheres are discussed. Chapter 3 describes the current understanding of the interaction potential and phase behaviour of colloid-polymer mixtures. Chapter 4 extends this discussion to charged colloidal systems, and chapter 5 introduces globular proteins and the extent to which their interaction potential and phase behaviour is currently understood. The experimental techniques used in this work, principally those of optical and confocal microscopy and nuclear magnetic resonance spectroscopy, are presented in chapter 6.

Chapter 7 provides details about the colloidal systems studied including characterisation of the particles and preparation of the samples. Results from the study of colloid-polymer mixtures in systems with and without the complicating effects of charge and gravity are presented in chapter 8, and interpreted using a range of theoretical frameworks.

Chapter 9 provides details about the proteins studied including characterisation of the particles and preparation of the samples. In chapter 10 results from the study of the non-equilibrium phase behaviour of globular proteins on the addition of salt are presented. The results are interpreted and compared to other protein and colloidal systems in the literature.

Chapter 11 suggests ideas for future work, and chapter 12 concludes the thesis.

Chapter 2

Hard-Sphere Colloids

2.1 Introduction

Colloidal suspensions are a complex state of matter, consisting of small particles suspended within a continuous phase. The size of the colloids must lie in the range of nanometers to micrometers, placing the colloidal length-scale in the mesoscopic regime between microscopic atoms and molecules and the macroscopic objects that can be seen by the naked eye. This ensures that the particles are small enough for Brownian motion to keep them dispersed, yet large enough that they have a definable shape and size, and that the molecules of the medium can be treated as a continuum.

2.2 Hard-Sphere Phase Behaviour

Ideal hard spheres are perfectly rigid, spherical particles which exert no force on one another until they come into contact. Once they touch, their rigidity means that an arbitrarily large force will prevent any overlap or deformation. When determining the phase behaviour only entropic effects need to be considered, so the system can be characterised by the number density of the particles alone. This is commonly expressed as the colloid volume fraction ϕ and for a collection of N spheres of radius a in volume V is given by:

$$\phi = \frac{4}{3}\pi a^3 \frac{N}{V} \tag{2.1}$$

The simplest theoretical model that can be considered is a suspension of monodisperse identical hard spheres. The phase behaviour has been predicted by computer simulation [115, 39] and is shown in figure 2.1. Below a freezing volume fraction of $\phi = 0.494$ a colloidal fluid is the stable phase. Each particle is able to explore the whole sample volume through diffusion, and the arrangement of particles will show only short ranged order.

Above the melting volume fraction, $\phi_M = 0.545$ the system is fully crystalline. Between the freezing and melting volume fractions the system phase separates into a coexisting fluid phase at $\phi_F = 0.494$ and crystal phase at $\phi_M = 0.545$. Small iridescent crystallites nucleate which then sediment to form a polycrystalline phase at the bottom of the sample.

Further increasing the volume fraction will produce a more compact crystalline arrangement up to a maximum close packed volume fraction of $\phi_{cp} \simeq 0.74$. However, at $\phi_G \simeq 0.58$ crystallisation is suppressed by the formation of an amorphous solid known as a colloidal glass.

Above the glass transition volume fraction ϕ_G long-time diffusion is suppressed. If the particles adopt a random close packed arrangement then the maximum volume fraction obtainable will be $\phi_{rcp} \simeq 0.64$ [80].

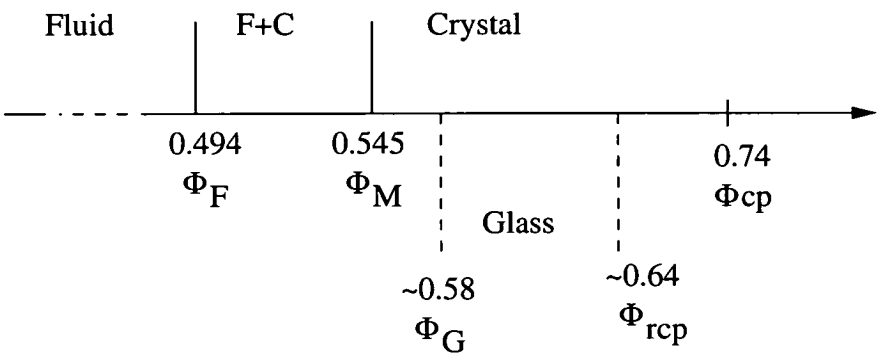

Figure 2.1: The hard sphere phase diagram. Below a freezing volume fraction ϕ_F the stable phase is a fluid, and above a melting volume fraction ϕ_M the system is fully crystalline. At intermediate volume fractions the system phase separates into coexisting fluid and crystal phases.

A system driven solely by entropy can form an ordered arrangement of particles because of the competition between configuration and free volume entropy. This is shown schematically in figure 2.2 for the two dimensional case of hard disks. When the disks are packed in a random arrangement, figure 2.2 (a), they have a high configurational entropy, but because each disk is restricted in its movement they have a low free volume entropy. However, when they are arranged in an ordered state, figure 2.2 (b), although they have a low configurational entropy they have a high free volume entropy because each disk is now free to move about its average position. Crystallisation of a suspension of hard-spheres occurs when the entropy gained by creating more free volume for each particle exceeds that lost by having an ordered arrangement. The increase in the free volume around each particle in an ordered crystalline state is emphasised by the higher volume fraction of the crystalline close packed arrangement of particles at $\phi_{cp} = 0.74$ with respect to the disordered random close packed volume fraction $\phi_{rcp} \simeq 0.64$. The crystalline close packed arrangement of particles is the more efficient packing state.

2.3 Polydispersity

Thus far single-sized, or monodisperse, colloidal particles have been discussed. However, a suspension of identical particles is difficult to achieve in practise. In any colloidal system, with the exception of some biological molecules such as proteins, there is a distribution in the size

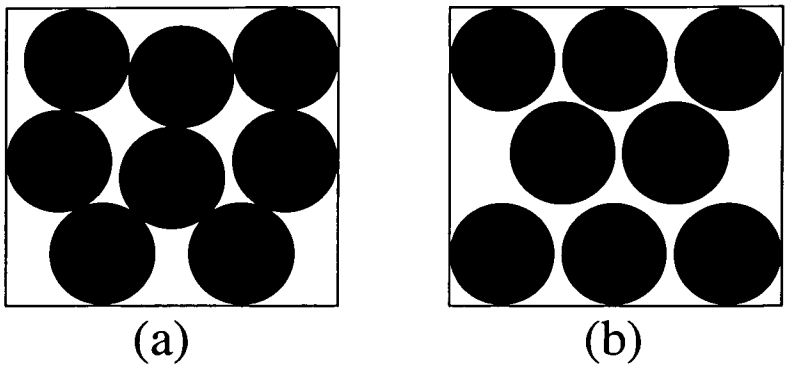

Figure 2.2: Competition between configurational and free volume entropy

of the particles. The suspension is then said to be polydisperse. The size polydispersity σ is defined as the standard deviation in the size distribution divided by the mean value:

$$\sigma = \frac{\sqrt{\left(\overline{R^2} - \overline{R}^2\right)}}{\overline{R}}. \tag{2.2}$$

Polydispersity can have an effect on the physical properties of a system [26]. For example, it is believed that crystallisation is suppressed for polydispersities greater than a critical value $\sigma > \sigma_C$. For a nearly hard-sphere suspension, Fairhurst [26] reported that no crystallisation took place in suspensions where the colloids had a polydispersity of $\sigma \simeq 0.18$. Only slow crystallisation was reported for polydispersity $\sigma \simeq 0.095$ at volume fractions $0.53 < \phi < 0.56$, and above $\phi = 0.56$ no fully crystalline behaviour was observed. Polydispersity is generally hard to take into account in theoretical studies, so it is important to make colloids with a low polydispersity, so that they may be approximated to monodisperse systems. A typical polydispersity for the polymethylmethacrylate (PMMA) colloids used in the work reported here is ~ 0.06.

2.4 Colloidal Stability

2.4.1 Van der Waals Forces

Van der Waals forces are the result of interactions between the fluctuating electron clouds of atoms or molecules and therefore affect any two bodies of matter. They exist even if the atoms or molecules are electrically neutral. These universal forces (known as dispersion forces

or London forces) are due to the polarisation of one molecule by fluctuations in the charge distribution of a second molecule.

For two identical atoms separated by a distance r the attraction goes as r^{-6}. For spherical particles in a solvent, the dispersion interaction pair potential $U(r)$ [45] is given by integrating over all pairs of atom-atom interactions, and is given by equation 2.3:

$$U_A(r) = -\frac{A}{12}\left(\frac{4R^2}{r^2-4R^2} + \frac{4R^2}{r^2} + 2ln[1-\frac{4R^2}{r^2}]\right), \tag{2.3}$$

where r is the centre to centre separation, R is the radius of the particles and A is the Hamaker constant. The value of the Hamaker constant depends on the material properties of the particles and solvent considered, in particular on their frequency-dependent polarisabilities. If the particles and the suspension medium have equal polarisabilities then $A = 0$. Thus one could attempt to minimise van der Waals interactions by matching the refractive indices of the particle and liquid at a particular frequency, although difference in polarisabilities at other frequencies might still exist.

For large inter-particle separations $r \to \infty$, the r^{-6} behaviour is recovered, as expected,

$$\lim_{r\to\infty} U_A(r) = -\frac{16}{9}A\left(\frac{R}{r}\right)^6. \tag{2.4}$$

However, for particles close to touching $r \to 2R$, the potential goes inversely as the inter-surface separation $(r - 2R)$:

$$\lim_{r\to 2R} U_A(r) = -\frac{A}{12}\frac{R}{r-2R}. \tag{2.5}$$

This deep minimum in the potential near $r = 2R$ can be many times greater than the thermal energy k_BT and causes irreversible aggregation in suspensions of unprotected particles. To counteract this effect and avoid aggregation the particles need some stabilisation. The two most common approaches are charge and steric stabilisation [57, 101].

2.4.2 Charge Stabilisation

Certain colloidal particles have ionisable groups on their surfaces which mostly dissociate if the particles are dispersed in a polar solvent. This provides an electrostatic charge on each

particle. The counter-ions liberated from each particle are partially dispersed by Brownian motion but remain in the particle's electric field. Effectively the particle now consists of a macro-ion surrounded by an ion cloud, the electrical double layer, which is composed of the counter-ions and the ions of any electrolyte present in the suspension, figure 2.3(a). When two macro-ions approach each other the overlap of their electrical double layers causes a repulsive force which can stabilise the particles against aggregation. This is called charge stabilisation.

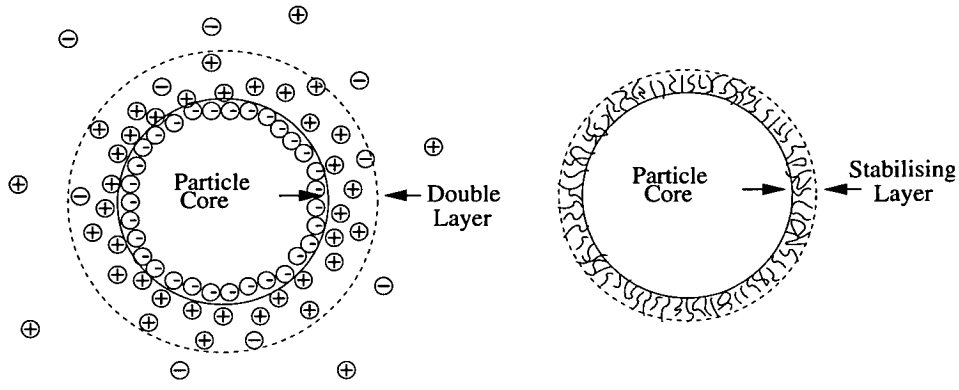

a) Charge Stabilisation b) Steric Stabilisation

Figure 2.3: Schematic illustration of charge and sterically stabilised colloids

2.4.3 Steric Stabilisation

Steric stabilisation is achieved by coating the colloids with a layer of polymers. When two polymer-coated surfaces approach each other they experience a force once the outer segments begin to overlap. This interaction usually leads to a repulsive osmotic force due to the unfavourable entropy associated with compressing the chains between the surfaces. The forces involved depend on the quantity or coverage of the polymer on each surface, on whether the polymer is physically adsorbed from solution (reversible process) or chemically grafted onto the surface (irreversible process), and on the quality of the solvent used (poor, theta or good solvent for the coating polymer). Figure 2.3(b) shows a schematic of one particle with a layer of polymer around it providing steric stabilisation against aggregation with other particles.

Silica particles are often sterically stabilised, since a variety of polymers can be chemically grafted onto their surfaces. Another example is spherical colloidal aggregates of polymethyllethacrylate (PMMA) molecules with poly-12-hydroxystearic acid (PHSA) chemically grafted onto the particle surface.

A schematic illustration of the repulsive part of the interaction potential $U(r)$ for the hard sphere case, the sterically stabilised case, and the charged stabilised case is shown in figure 2.4.

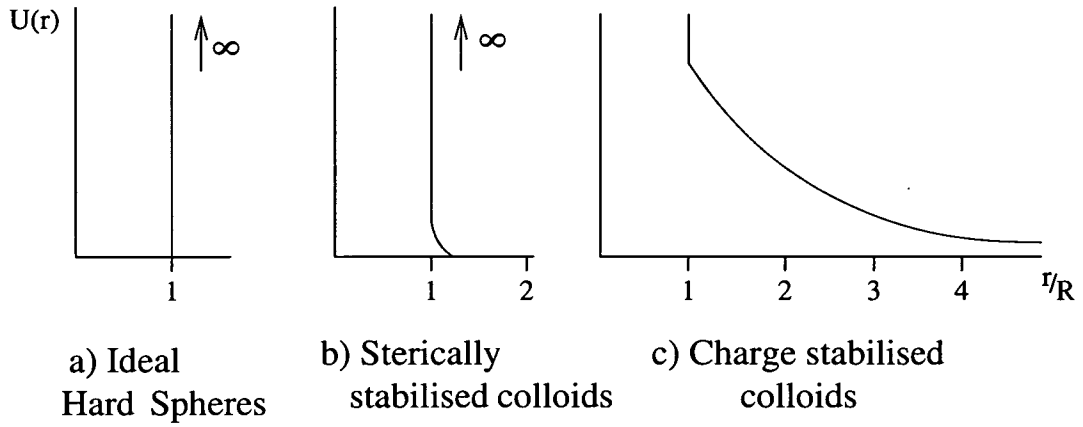

Figure 2.4: Schematic illustration of the repulsive interaction potential for ideal hard spheres, sterically stabilised 'nearly hard sphere' colloids and charge stabilised 'soft sphere' colloids [97].

For both charged and sterically stabilised particles there is a deviation from ideal hard sphere behaviour, and there are limitations to the adequacy of these systems as ideal monodisperse systems. The two main limiting factors are the softness of the potential (figure 2.4) and the inevitable presence of size polydispersity.

Chapter 3

Colloid-Polymer Mixtures

3.1 Introduction

In this chapter the phase behaviour and interaction potential of a suspension of uncharged and sterically-stabilised colloids on the addition of non-adsorbing polymer are discussed. The effect of mixing non-adsorbing polymer into a colloidal suspension is to induce an effective attraction between the colloids. Colloid-polymer mixtures exhibit a wide range of phase behaviour of fundamental scientific interest.

3.2 The Depletion Potential

The first theoretical interpretation of phase separation induced by the addition of non-adsorbing polymer to an otherwise stable colloidal suspension was given by Asakura and Oosawa [4] and independently by Vrij [110], in terms of a 'depletion' effect. The simplest model is shown schematically in figure 3.1. The polymer coils are assumed to be spheres of radius equal to the radius of gyration of the polymer R_g. The colloidal particles are hard spheres of radius a. Polymer coils and colloidal particles are mutually impenetrable and so the polymer centres are excluded from a region around each colloid of the order of the polymer radius of gyration R_g, called the depletion zone.

The depletion potential can be described in terms of the free volume available to the polymer coils. The centres of the polymer coils are restricted to the free volume V_{free}, which is the region not occupied by colloidal particles and their depletion zones. The overlap of the depletion layers of nearby colloids creates more free volume for the polymer coils, and thus lowers the free energy by maximising the entropy. In this way an effective attraction between the particles is induced, the depletion potential.

For an alternative description of the depletion potential consider the isotropic osmotic pressure Π_p that each isolated particle experiences, exerted by the surrounding polymer solution. When two particles approach each other so that their depletion regions start to overlap, the polymer coils can no longer fit in the gap between the particles and get squeezed out. This results in a drop in the osmotic pressure exerted on the adjacent surfaces of the particles. The imbalance in osmotic pressure thus pushes the particles together.

The attraction between the particles can be expressed in the form of an attractive pair potential, the depletion potential $U_{dep}(r)$, given by:

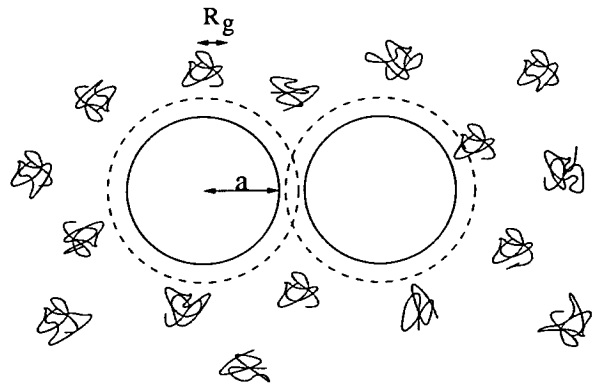

Figure 3.1: Schematic illustration of the overlapping depletion zones (dotted lines) around two colloidal particles in a colloid-polymer mixture.

$$U_{dep}(r) = \begin{cases} +\infty & : \quad r \leq \sigma \\ -\Pi_p V_{overlap} & : \quad \sigma < r \leq \sigma + 2R_g. \\ 0 & : \quad r > \sigma + 2R_g \end{cases} \tag{3.1}$$

The particle diameter is $\sigma = 2a$, R_g is the radius of gyration of the polymer and ξ is the size ratio given by R_g/a. The volume of the overlapping depletion regions between two particles at distance r, $V_{overlap}$, is given by the expression

$$V_{overlap} = \left(1 - \frac{3r}{2\sigma(1+\xi)} + \frac{1}{2}\left[\frac{r}{\sigma(1+\xi}\right]^3\right) \frac{\pi}{6}\sigma^3(1+\xi)^3. \tag{3.2}$$

An expression for the osmotic pressure of the polymer solution Π_p can be derived. We can assume that the polymer solution behaves as an ideal gas (a gas of molecules of negligible size and exerting no intermolecular forces) if the polymer solution is kept dilute (i.e. $c_p << c_p^*$, the concentration at which the polymer coils start to overlap). In this case Π_p is given by Van't Hoff's law, equation 3.3:

$$\Pi_p = n_p{}^{(R)} k_B T. \tag{3.3}$$

The number density of the polymers in the free volume, $n_p{}^{(R)}$, is given by the expression

$$n_p{}^{(R)} = \frac{N_p}{V_{free}}, \tag{3.4}$$

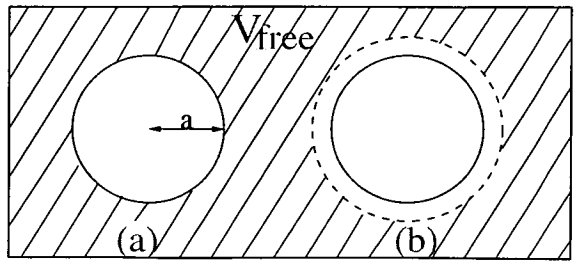

Figure 3.2: Approximations to the free volume fraction α. First approximation (a) is the total volume less the volume occupied by colloids alone, and the second approximation (b) is the total volume less the volume occupied by the colloids and their depletion zones $\phi(1+\xi)^3$. The free volume V_{free} is represented by the shaded area.

where N_p is the total number of polymer coils and V_{free} is the free volume. In other words, the volume not occupied by colloidal particles and their depletion zones given by $V_{free} = V - (V_{particle} + V_{dep} - V_{overlap})$. $n_p^{(R)}$ can also be expressed in terms of the polymer concentration c_p in mass per unit volume:

$$n_p{}^{(R)} = \frac{N_a}{M_w} c_p{}^{free}, \tag{3.5}$$

where N_a is Avogadro's number and M_w is the molecular weight. The free volume polymer concentration c_p^{free} can be related to the total polymer concentration by the free volume fraction α:

$$c_p{}^{free} = \frac{c_p}{\alpha}. \tag{3.6}$$

At very low colloid volume fractions we can assume there is no overlapping of the depletion regions, so the volume inaccessible to the polymer is simply the volume of the particles multiplied by $(1+\xi)^3$, as illustrated in figure 3.2. The free volume fraction can then be approximated as:

$$\alpha = 1 - \phi(1+\xi)^3. \tag{3.7}$$

At present there is no exact expression, or simulation results, for α at finite volume fractions. Scaled particle theory [55] gives the following approximate expression for α, for the case of *one* small particle (for example polymer) in a colloidal suspension:

$$\alpha = (1-\Phi)exp(-A\gamma - B\gamma^2 - C\gamma^3), \tag{3.8}$$

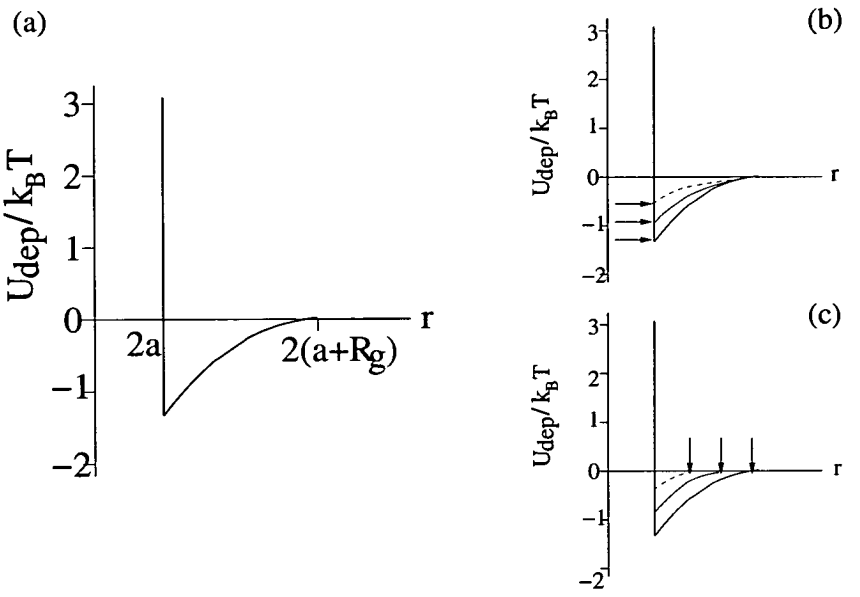

Figure 3.3: Generic form of the depletion potential $U_{dep}(r)$ induced by the addition of non-adsorbing polymer to hard sphere colloids. In (b), the different curves illustrate the effect of increasing the number density of polymer molecules in the sample n_p, at fixed colloidal volume fraction ϕ. The depth of the potential increases as the amount of polymer increases. Graph (c) illustrates the effect of the polymer-colloid size ratio ξ on U_{dep}. The different curves correspond to different values of ξ, at fixed n_p and ϕ. As the size ratio ξ is increased both the range and the well depth of the depletion potential increase.

where $A = 3\xi + 3\xi^2 + \xi^3$, $B = \frac{9\xi^2}{2} + 3\xi^3$, $C = 3\xi^3$, and $\gamma = \phi/(1-\phi)$.

In a real colloid-polymer mixture there are many polymers, so this approximate expression from scaled particle theory does not describe the true physical situation.

Depletion potentials $U_{dep}(r)$ are plotted in figure 3.3. The generic form of U_{dep} as a function of the particle inter-centre separation r is shown in (a). The depth of the potential well is of the order of k_BT. It depends on the number density of polymer molecules in the sample. Therefore, at a fixed colloid volume fraction, the strength of the attractive interactions between particles can be tuned by adjusting the polymer concentration of the system, (b). The range of the interaction is equal to $2(a+R_g)$, which can also be tuned by varying the polymer to colloid size ratio $\xi = R_g/a$, figure 3.3(c).

An expression for the depletion potential at the point of contact in terms of the free volume fraction of polymer can be derived, where we take the volume occupied by a polymer coil to be $\frac{4}{3}\pi R_g^3$. The free volume polymer concentration ${c_p}^{free}$ can be transformed into the free volume fraction of polymer $\eta_p^{(R)}$ using equation 3.9:

$$\eta_p^{(R)} = \frac{V N_a c_p^{free}}{M_w} = \frac{4\pi R_g^3 N_a c_p^{free}}{3M_w}. \tag{3.9}$$

Substituting this into the original expression (equation 3.1) for the depletion potential U_{dep} at contact, i.e. with $r = \sigma$, gives:

$$\frac{U_{dep}^{contact}}{k_B T} = \frac{3\eta_p^{(R)}}{4\pi R_g^3}\left(1 - \frac{3}{2(1+\xi)} + \frac{1}{2}\left[\frac{1}{1+\xi}^3\right]\right)\frac{\pi}{6}\sigma^3(1+\xi)^3. \tag{3.10}$$

Since $\sigma^3/{R_g}^3 = 8\xi^3$, we can write an expression for the depletion potential at the point of contact:

$$\frac{U_{dep}^{contact}}{k_B T} = \eta_p^{(R)}(1 + \frac{3}{2\xi}). \tag{3.11}$$

The pair potential for uncharged hard sphere colloids mixed with non-adsorbing polymer can be written as $U(r) = U_0(r) + U_{dep}(r)$, where U_0 is the inter-particle potential for the pure suspension (i.e.with no polymer) and $U_{dep}(r)$ is the depletion potential.

3.3 Equilibrium Phase Behaviour

3.3.1 Representation

The phase behaviour of a simple atomic substance such as argon is typically represented in a temperature-density phase diagram like that illustrated in figure 3.4(a). At high temperatures phases of fluid (F) and crystal (C) exist, and at temperatures below the critical point (CP) two separate fluid phases of gas and liquid are stable. On the triple line (dashed line) the three phases of gas, liquid and crystal coexist. Below the triple line gas and crystal coexist.

In colloid-polymer mixtures the experimental variable is the polymer concentration (at a constant temperature), so it is useful to plot the phase diagrams in terms of the effective volume fraction of polymer coils in the free volume of the sample $\eta_p^{(R)}$, given by the expression

$$\eta_p^{(R)} = \frac{4}{3}\pi R_g^3 n_p^{(R)}, \tag{3.12}$$

where ${n_p}^{(R)} = \frac{N_p}{V_{free}}$ is the number density of polymer in the free volume of the sample. Equivalently, ${n_p}^{(R)}$ is the number density of polymer coils in a reservoir of pure polymer

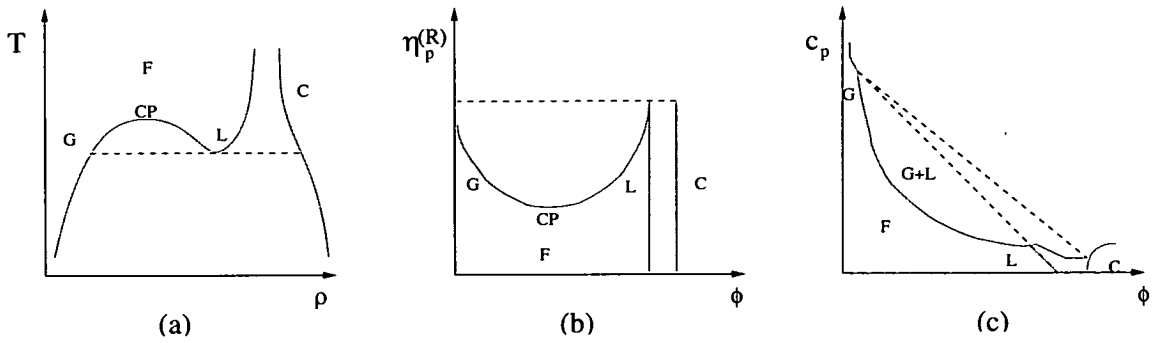

Figure 3.4: Schematic illustration of phase diagrams in (a) the temperature-density (T, ρ) representation, (b) the polymer effective volume fraction - colloid volume fraction representation $(\eta_p^{(R)}, \phi)$ and (c) the polymer concentration-colloid volume fraction (c_p, ϕ) representation, for size ratios ξ larger than ~ 0.25.

solution in osmotic equilibrium with the sample [42]. The polymer number density in the free volume ${n_p}^{(R)}$, and hence the effective volume fraction of polymer $\eta_p^{(R)}$, can be related to the polymer chemical potential μ_p by the expression

$$\mu_p = k_B T ln(n_p^{(R)} \lambda_p^3), \tag{3.13}$$

where λ_p is the de Broglie thermal wavelength for the polymer. In figure 3.4(b) the tie lines (lines connecting existing phases) in the two phase regions are horizontal, essentially expressing the constancy of chemical potentials in coexisting phases, and give no direct indication of the occurrence of polymer partitioning upon phase separation. The three phase coexistence appears as a triple line (dashed line); the colloid volume fractions in the three coexisting phases are different, but the polymer chemical potential remains the same.

The experimental variable used is the polymer concentration within the *sample* volume, c_p (in mass/volume). It is useful to plot the phase diagrams in terms of this experimental variable, figure 3.4(c). This representation leads to oblique tie lines in all two-phase regions, predicting polymer partitioning between coexisting phases. The three phase coexistence now appears as a triple region rather than as a triple line: the volume fractions of the colloid *and* the polymer are different in the three coexisting phases [42].

3.3.2 Topology

The topology of the phase diagram of a colloid-polymer mixture is dependent on the colloid to polymer size ratio ξ as shown schematically in figure 3.5. Experimentally determined phase diagrams for the size ratios of 0.08, 0.24 and 0.57 are shown in figure 3.6 [42].

At small size ratios ($\xi = 0.08$ is shown in figure 3.5(a)) the addition of polymer to a colloidal suspension has the effect of widening the fluid-crystal coexistence region of the phase diagram compared to the hard sphere (no polymer) case. Phase separation into regions of gas and liquid is not observed. As the size ratio increases the gas-liquid critical point becomes stable. The value of ξ where the critical point first appears in the phase diagram is known as the cross over size ratio and its theoretically predicted value is $\xi_{co} \simeq 0.3$ [29]. Only for systems where ξ is above this cross over value do we expect to see a liquid phase. In this case, a colloidal fluid phase separates into coexisting gas and liquid phases above a gas-liquid binodal, figure 3.5(c). Experimental results confirm this picture, figure 3.6, and the cross over size ratio is experimentally determined to be $\xi_{co} \simeq 0.24$ [42].

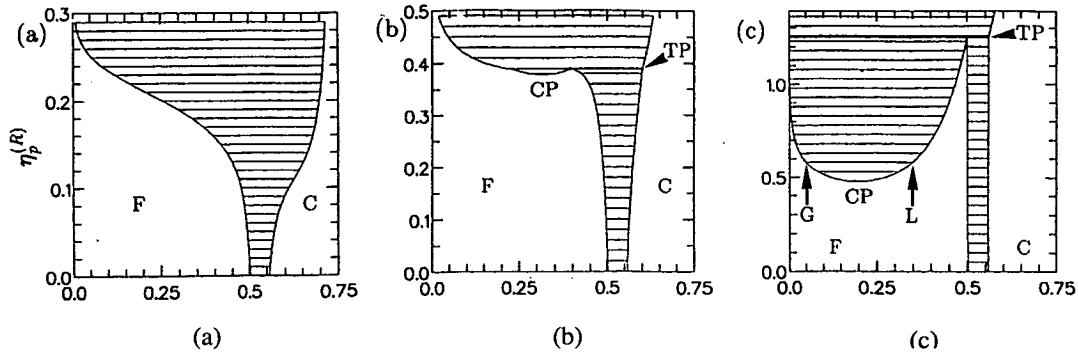

Figure 3.5: Schematic phase diagrams, Illet *et.al.*, [42], for size ratios of (a)$\xi = 0.08$, (b) $\xi = 0.25$ and (c) $\xi = 0.57$, the vertical axis plots the effective volume fraction of the polymer coils in the free volume of the sample $\eta_p^{(R)}$.

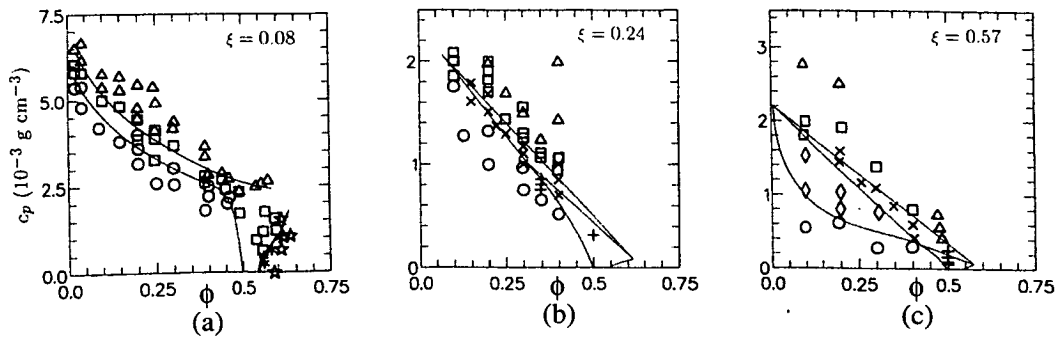

Figure 3.6: Experimental phase diagrams, Illet *et.al.* [42], for size ratios $\xi = 0.08$, 0.25 and 0.57. The vertical axis plots the polymer concentration in g/cm^4. Lines are drawn as guides to the eye. The symbols denote the following: ∘, fluid; ◇, gas plus liquid; ×, gas plus liquid plus crystal; +, liquid plus crystal; □, gas plus crystals; △, gel ($\xi = 0.08$) or no visible crystallites ($\xi = 0.24$ and 0.57); ∗, glass.

3.4 Free Energy Landscapes

3.4.1 Fluid-Crystal Phase Separation

The equilibrium phase behaviour of an N-particle system with potential energy $U(r_N)$ at temperature T confined to a volume V can be calculated by minimising the Helmholtz free energy:

$$F = -k_B T ln \int e^{-U(r_N)/k_B T} dr_N$$

The idea of minimising the free energy can be plotted in terms of a free energy landscape, which is a plot of the free energy density $f = F/V$ as a function of the density or volume fraction ϕ. Different phases give rise to different branches in the free energy landscape. Consider a colloid-polymer mixture of a low size ratio, with a phase diagram like that illustrated in figure 3.7. The free energy landscape of this system has a fluid branch and a solid (crystal) branch.

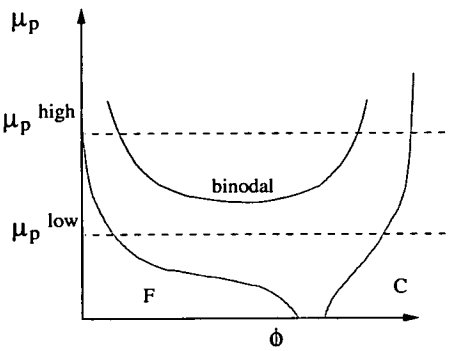

Figure 3.7: Schematic phase diagram for a colloid polymer mixture of size ratio less than 0.25. The variables are the colloid volume fraction ϕ and the polymer chemical potential μ_p. The gas-liquid binodal is hidden within the fluid-crystal coexistence region.

Figure 3.8 shows the simplest case where, at low polymer chemical potential μ_p^{low}, only phases of fluid and crystal are observed. The phase behaviour can be predicted using the common tangent construction [75, 74]. Construct the lowest *common tangent* and obtain points of common tangency at densities ϕ_F and ϕ_C. To minimise F (or f, since the volume is constant) the systems remains a single phase fluid at densities $\phi \leq \phi_F$, a single dense ordered phase (solid) for $\phi \geq \phi_C$, and at intermediate densities phase separates into coexisting fluid and solid phases at densities ϕ_F and ϕ_C respectively.

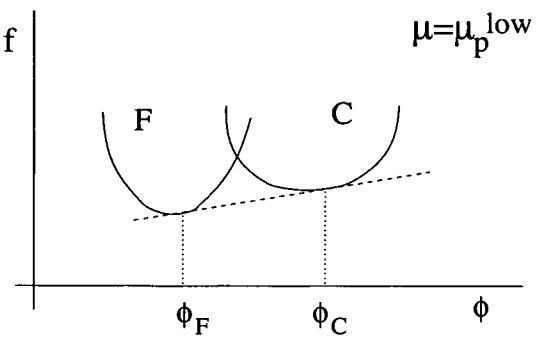

Figure 3.8: Free energy landscape showing fluid and crystal branches

3.4.2 Gas-Liquid Phase Separation

In colloid-polymer mixtures a situation might arise where the fluid branch of the free energy density curve exhibits two minima. Figure 3.9 shows schematic fluid free energy density curves for a colloid-polymer mixture at increasing polymer concentrations [57], where higher curves correspond to increasing polymer chemical potential μ_p.

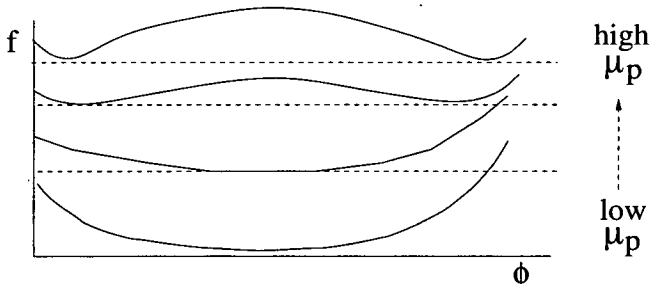

Figure 3.9: Schematic illustration of the free energy landscapes of the fluid branch for a colloid-polymer mixture on increasing polymer concentration [57].

At low μ_p the curve shows a single minimum indicating the phase is locally stable at all ϕ. On increasing μ_p (by increasing the concentration of polymer) the curve shows a flat minimum region around which the system can fluctuate with very little free energy cost. This is around the critical point of the system. As μ_p is increased further the curve develops a double minimum, indicating two distinct phases. By analogy with atomic systems, the low density phase is called a colloidal gas, and the high density is called a colloidal liquid. The composition of each phase can be determined via the common tangent construction (dashed lines).

Now consider again the system shown in figure 3.7, this time at the higher chemical potential μ_p^{high}. The fluid branch of the free energy landscape now has a double minimum structure corresponding to gas and liquid phases. A free energy landscape including all possible phases

can now be drawn, figure 3.10. The points on the equilibrium phase boundary are still obtainable by constructing a common tangent between the fluid and crystal branches, but it is now possible to draw a common tangent between the two minima of the fluid branch as well.

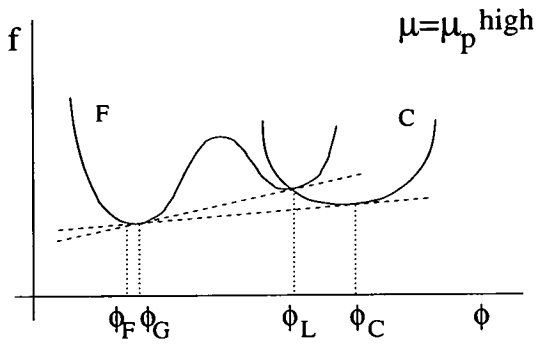

Figure 3.10: Free energy landscape for a colloid polymer mixture at high chemical potential.

The *lowest* common tangent, in this case that between the fluid and crystal minima, tells us the final equilibrium phase behaviour of the system, which will be fluid-crystal coexistence. However it provides no information about the process of how the phase separation takes place [75, 74].

3.5 Mechanisms of Gas-Liquid Phase Separation

Gas-liquid phase separation can occur via two mechanisms; nucleation and spinodal decomposition. Figure 3.11 shows a simplified phase diagram, where the basic process of interest is one when we start at a high temperature with a uniformly mixed solution of concentration ϕ_0, and then quench to a lower temperature T_1. At temperature T_1 the solution is thermodynamically metastable or unstable against separating into coexisting regions of the stable concentrations ϕ_α and ϕ_β.

The boundary between metastability and instability is called the spinodal. If ϕ_0 were chosen to be only slightly larger than ϕ_α, so that the system were quenched into a metastable state, then the process could be visualised as one in which droplets of concentration ϕ_β nucleate slowly out of the slightly super-saturated α phase. On the other hand, if ϕ_0 is roughly equidistant from ϕ_α and ϕ_β then the system undergoes a relatively fast 'spinodal decomposition' in which α-like and β-like regions appear in approximately equal proportions.

Spinodal decomposition is the mechanism by which phase separation occurs in a mixture that is quenched into a thermodynamically *unstable* state. A homogeneous suspension is quenched

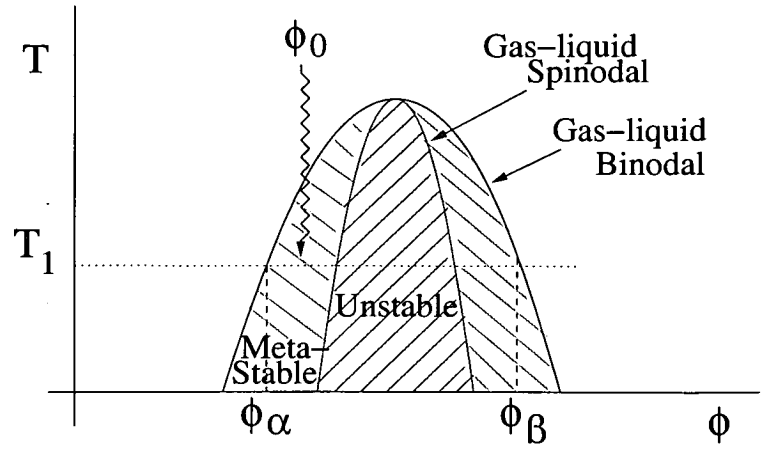

Figure 3.11: Schematic illustration of a phase diagram showing the binodal and associated spinodal.

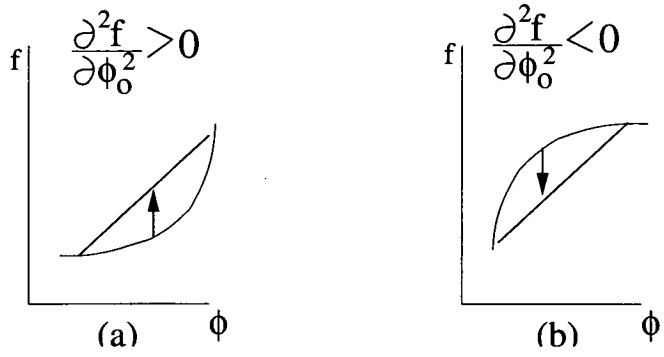

Figure 3.12: Schematic illustration of the free energy curves which lead to (a) stable and (b) unstable behaviour.

to a temperature T_1 inside the two-phase region. The system decomposes into two phases with concentrations ϕ_α and ϕ_β respectively [54, 15, 16, 34]. Consider fluctuations in the initial *local* concentration of a sample ϕ_0. If the initial state has a concentration ϕ_0 such that $\partial^2 f/\partial\phi_0^2 > 0$ then the amplitude of any fluctuation decreases in time, because any local movement around the free energy curve near this concentration results in an increase in the free energy, as shown in figure 3.12(a). In this case the system is metastable (or stable).

However, if $\partial^2 f/\partial\phi_0^2 < 0$ then the amplitude of the fluctuations will increase with time because any local change in the density along the free energy curve will result in a decrease in the free energy, as illustrated in figure 3.12(b). In this case gas-liquid phase separation will proceed by spinodal decomposition. The spinodal line, defined in the (ϕ, T) plane by the condition $\partial^2 f/\partial\phi^2 = 0$, separates the region of metastable states from the region of unstable states. Figure 3.13 shows a schematic illustration of a free energy landscape leading to binodal

and spinodal phase boundaries in the phase diagram.

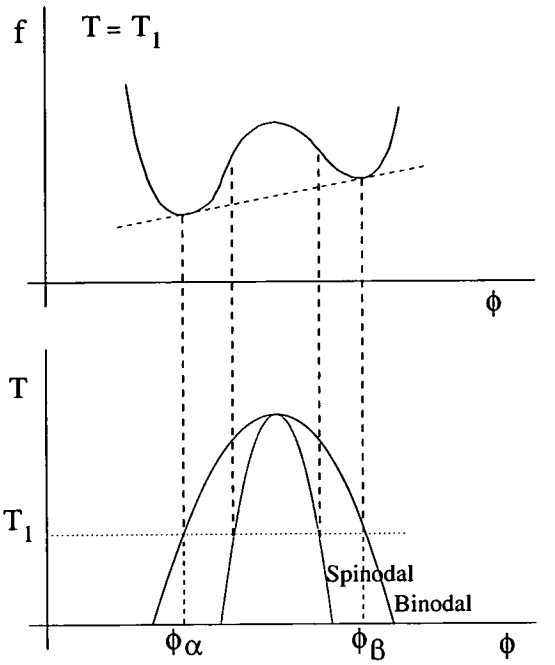

Figure 3.13: Schematic illustration of a free energy landscape leading to binodal and spinodal phase boundaries.

However, the spinodal is not a physically well-defined construct, it only gives a rough idea of where a smooth transition takes place between thermally activated processes e.g. nucleation, and spinodal processes for which there is no energy barrier. To understand this smoothness consider that on the metastable side of the spinodal line the activation barriers may be much smaller than k_BT, thus cannot be thought of as barriers at all. Conversely, on the unstable side of the line, activated processes with barriers of order k_BT or less may be more effective at initiating phase separation than the slow density fluctuations that become unstable. It follows that the spinodal line is not well defined, but represents a gradual transition between nucleation and spinodal decomposition.

3.6 Non-Equilibrium Phase Behaviour

Non-equilibrium behaviour is rife in colloidal systems. Transient non-equilibrium states, such as metastable gas-liquid phase separation, can precede or inhibit equilibrium fluid-crystal co-existence [73]. Furthermore, crystallisation can be suppressed altogether by dynamical arrest, such as the formation of a glass [68]. At lower volume fractions, the formation of system-

spanning aggregates known as colloidal gels has been extensively reported in a range of colloidal systems [102, 76, 78, 109, 51]. In this section I concentrate on some experimental results and theoretical descriptions of these transient colloidal gels.

3.6.1 Transient Gelation

The experimental phase diagram of a model colloid-polymer mixture at size ratio of $\xi = 0.1$ is reproduced in figure 3.14 [73]. At sufficiently high attractions three main types of non-equilibrium behaviour were observed, all within the equilibrium fluid-crystal coexistence region of the phase diagram. Immediately above a non-equilibrium boundary behaviour resembling gas-liquid phase separation was observed and labelled as nucleation-like and spinodal-like behaviour. The fact that the initial stages of this non-equilibrium behaviour resembled gas-liquid phase separation led to the suggestion that the non-equilibrium boundary can be associated with the metastable gas-liquid binodal buried within the fluid-crystal coexistence region [73]. At sufficiently high attractions transient gelation was observed.

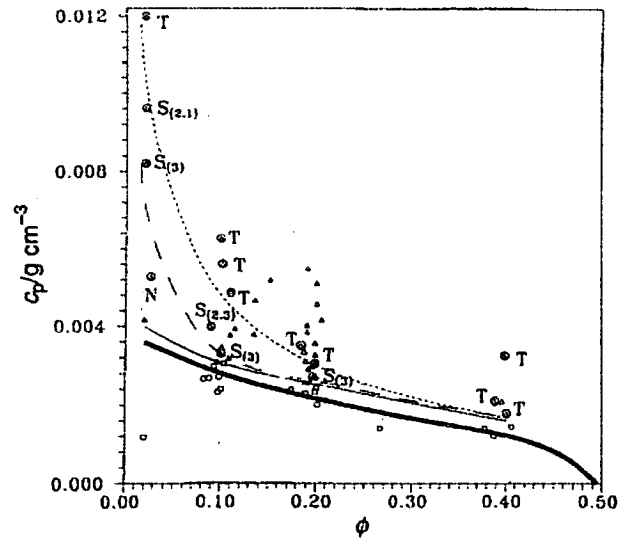

Figure 3.14: Experimental phase diagram of PMMA colloids on the addition of polystyrene at a size ratio $\xi = 0.1$. Regions of fluid ∘, fluid-crystal coexistence □ and non-equilibrium behaviour △ were observed. Lines are drawn to a guide to the eye, and show regions of Nucleation-like behaviour labelled N, spinodal-like behaviour S and transient gelation T [73].

Direct observation of the transient gels which are observed at high polymer concentration shows that they display delayed sedimentation [102, 76]. The defining characteristic of this behaviour is the existence of a delay time, during which very little settling of the suspension is

observed, followed by a rapid onset of sedimentation. Delayed sedimentation occurs in three stages, as illustrated in figure 3.15. A period of slow settling is first observed (A). This is followed, after the delay time τ, by a fast collapse during which time an amorphous sediment settles at the bottom of the sample. The final stage is a slow compaction of this sediment.

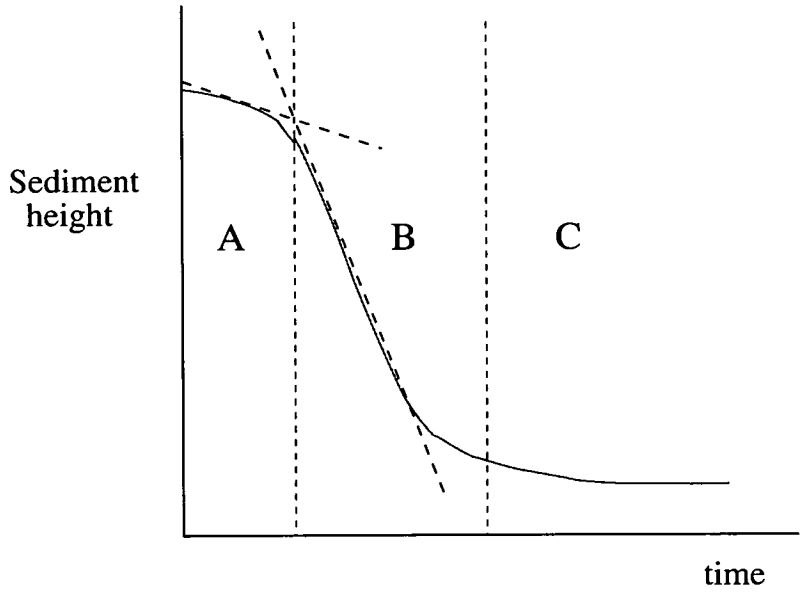

Figure 3.15: Schematic illustration of delayed sedimentation

The cause of transience in colloid-polymer gels is the subject of much debate [102, 76, 108, 91]. Effects such as the restructuring of the gel, thermal fluctuations and gravity have all been thought important when discussing the ageing and behaviour of transient gels [59, 102, 76, 101, 72, 2], as well as practical considerations such as the sample size and geometry [59, 101]. I consider three theoretical descriptions of aggregation and gelation and non-ergodicity in colloidal systems; Diffusion Limited Cluster Aggregation, Percolation, and Mode Coupling Theory.

3.6.2 Diffusion Limited Cluster Aggregation

Diffusion Limited Cluster Aggregation (DLCA) is often used to describe gelation in aggregating colloidal systems. In this model, the particles explore space by diffusion but form permanent inter-particle bonds when they touch. Clusters of particles are formed which continue to diffuse, and when two clusters meet they form a larger cluster.

Clusters formed by DLCA have a fractal structure as illustrated in figure 3.16, so the number

of particles in the cluster scales with the cluster radius to some power d_f, known as the fractal dimension. In three dimensions DLCA produces a fractal dimension of $d_f \sim 1.8$. Gelation occurs when the average volume fraction of each cluster is the same as the sample volume fraction, i.e. when all the clusters touch and span the sample.

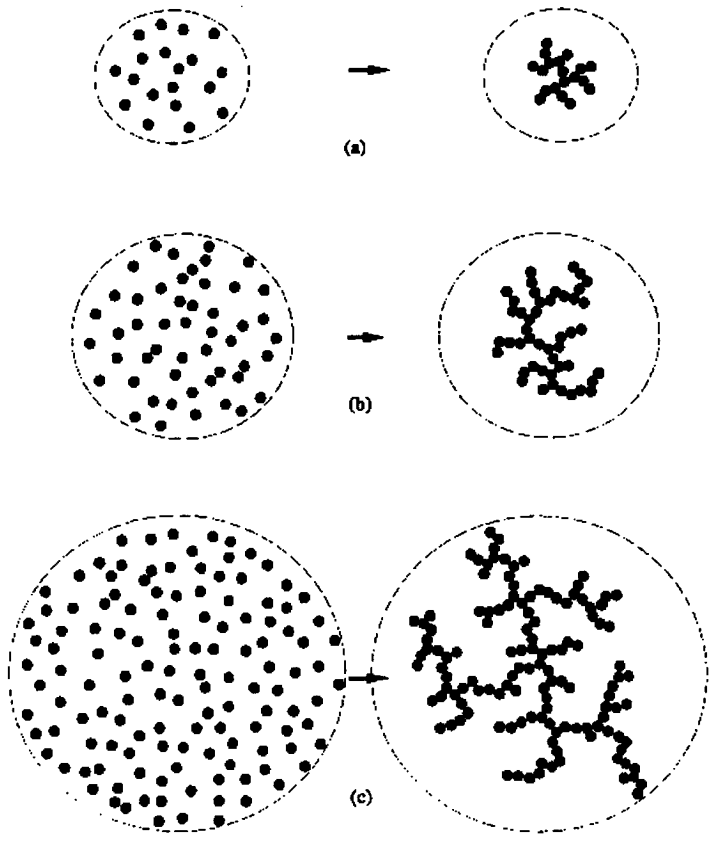

Figure 3.16: Schematic diagram showing the growth of a fractal cluster. As the cluster grows its average density decreases, and its structure becomes more tenuous [72].

The DLCA model describes systems with very strong attractions. However, in weakly aggregating systems the inter-particle bonds can be broken by the thermal energy of the particle, $\sim k_B T$. In this case particle aggregation and thermal fluctuations compete. This situation can be described by DLCA with finite bond energies, known as reversible DLCA [35]. In reversible DLCA the particles still bond upon touching but now there exists a finite probability that the bond can be broken. The probability of bond breaking follows a Boltzmann distribution $\sim exp(-U/k_B T)$.

Figure 3.17 shows three snapshots of particle aggregation produced from a 2D reversible DLCA simulation [36]. In each image black spots indicate the position of colloidal parti-

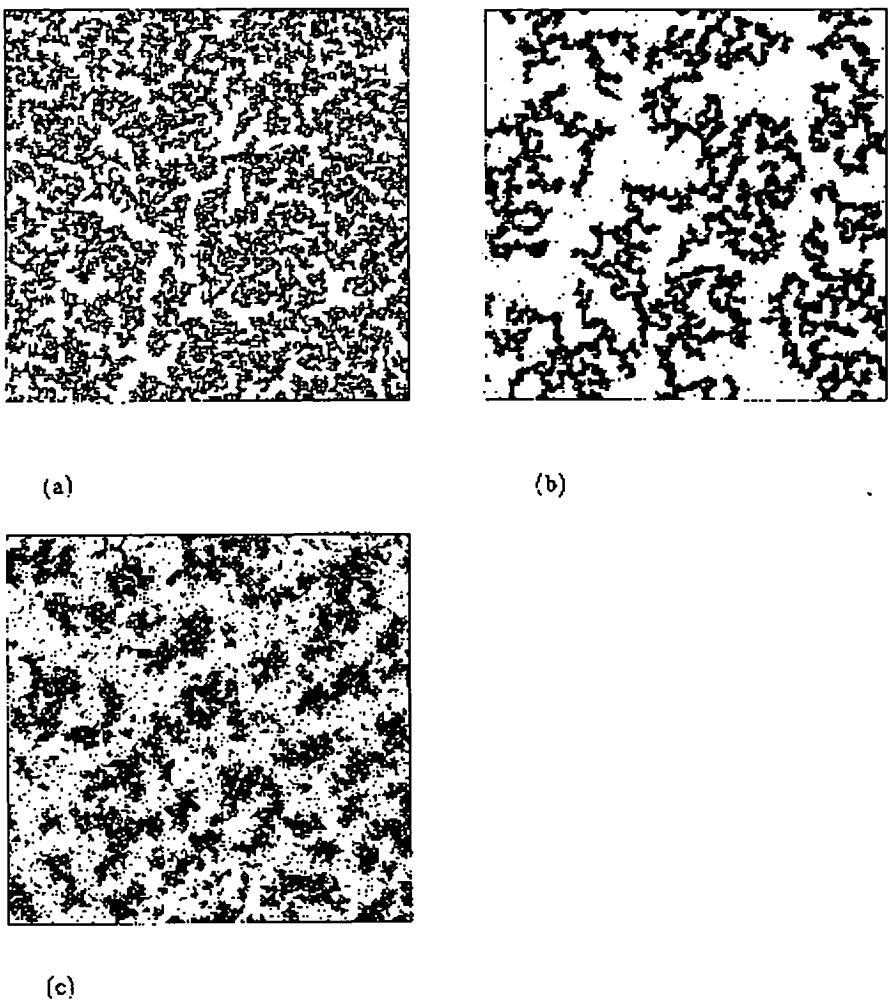

Figure 3.17: $2D$ reversible DLCA simulation of particle aggregation with varying bond strength. (a) $U_{dep} \gg k_B T$, (b) $U_{dep} \sim 3k_B T$, (c)$U_{dep} \simeq k_B T$, [35].

cles. Figure 3.17(a) shows the formation of a gel network when $U_{dep} \gg k_B T$, i.e. irreversible DLCA. The network is formed of single particle links. This is the kind of structure one might expect to see in the absence of gravity and with strong particle attractions.

For lower bond strengths, figure 3.17(b), thermal fluctuations can cause the clusters to compact on small length scales. However, the clusters can still grow fast enough to span the system. The gel network is made up of double or even triple bonds, making the arms of the gel look fatter than in the previous case. As time progresses the structure is seen to break into two or three larger clusters and then reform due to the thermal motions of the particles. The large channels formed between the arms of the network should also be noted. In a real system these would be

filled with solvent and polymer. In real systems the thermal rearrangements, the flow of fluid through these channels, and gravity could cause these types of structures to collapse.

At even lower bond energy, figure 3.17(c), compaction of the clusters due to thermal fluctuations wins over aggregation. The clusters formed cannot grow fast enough to form a space spanning network.

3.6.3 Percolation

In its simplest form percolation can be described as follows. On an infinite lattice, sites are occupied *at random* by particles with probability p (where p could also be interpreted as the particle density). This is known as random site percolation [103, 72, 25]. Each group of neighbouring particles (or occupied sites) is called a cluster. Percolation theory investigates the statistical properties, for example the size distribution, of the resultant clusters. As well as site percolation, it is possible to consider bond percolation. In this case, instead of the sites being occupied at random, the points have fixed positions and links are made between them at random. An important modification can be made to random site (or bond) percolation if the particles, instead of occupying sites (or forming bonds) at random, are correlated due to the presence of interactions. This is known as correlated percolation [25].

A quantity of particular interest for the study of gelation transitions is the percolation threshold p^*, at which an infinite cluster first appears. This percolation threshold p^* is found to be dependent on spatial dimensions as well as the symmetry of the lattice [103, 72]. At concentrations below the percolation threshold small clusters are predicted, but when the concentration reaches p^* the percolation transition is encountered and an infinite percolating cluster appears.

The percolation transition line can be continued inside the two phase (gas-liquid) region of the phase diagram, but only as a transient time dependent phenomenon. The system percolates for a finite time interval, after which the percolating cluster disintegrates into a set of finite clusters. This is known as Dynamic Percolation [38].

In some cases it is necessary to consider the property of rigidity of a percolating cluster, and the concept of rigidity percolation arises. To obtain a mental picture of rigidity percolation consider two large clusters that are connected via pivot joints. Even if the two clusters are connected, the network could still be 'floppy' rather than rigid. Essentially, a cluster is considered floppy when finite motions exist within that cluster which do not cost energy. Conversely, a cluster is considered rigid when no relative motion within that cluster can be achieved without a cost

in energy. Figure 3.18(a) shows two rigid clusters joined together by two rods (that could represent smaller rigid clusters or bonds) connecting at pivot points (open circles). Despite being connected, this is a floppy network. However, if a third connection is made between them, the network is no longer floppy but becomes rigid, as in figure 3.18(b). Predictions can then be made about the *rigidity* percolation threshold for a system [47].

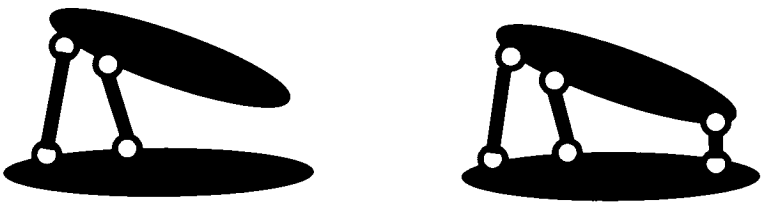

Figure 3.18: Schematic illustration showing (a) a floppy piece of network with four distinct rigid clusters and (b) the placement of an additional link that can lock the previous four clusters into a single rigid cluster [47]

Colloidal gels are characterised by ramified structures with particles located predominantly in clusters, so it seems natural to attempt to describe this phenomenon with percolation theories. However, the relevance of this idea to the interpretation of real experimental data is still subject to dispute [32, 107].

3.6.4 Mode Coupling Theory

When Mode Coupling Theory (MCT) was first applied to colloidal systems it was with the aim of providing a dynamical description of the hard-sphere glass transition. A physical interpretation of the MCT results for hard spheres is given by the caging effect [6]. At high volume fractions particles are trapped in the surrounding cage of neighbouring particles. In a liquid the particles can escape from their cage and the system relaxes, but in a glass the particles become permanently trapped in their cages. The MCT prediction of a transition from an ergodic (free to relax) state to a non-ergodic state is thought relevant to the experimentally observed liquid-glass transition in hard-sphere colloidal systems.

Recently MCT has been applied to the problem of gelation in colloidal systems with a short ranged attraction [7, 6, 8]. It is suggested that gels form as a result of an arrested structural relaxation, in a similar way as in the liquid-glass transition. According to MCT, if the short-ranged attractions are sufficiently strong, aggregation can lead to structural arrest of the long-time dynamics despite the bulk density being much lower than the hard sphere glass transition

density. In contrast to the hard-sphere glass transition, where the non-ergodicity transition predicted is a consequence of excluded volume effects, the low-density non-ergodicity transition is dominated by very short ranged correlations comparable to the range of the inter-particle attraction. This suggests the particles become stuck to their neighbours with long-lived bonds. The non-ergodicity transition line at low densities appears only for sufficiently short ranges of the attraction, and its precise path depends on the range of the interaction.

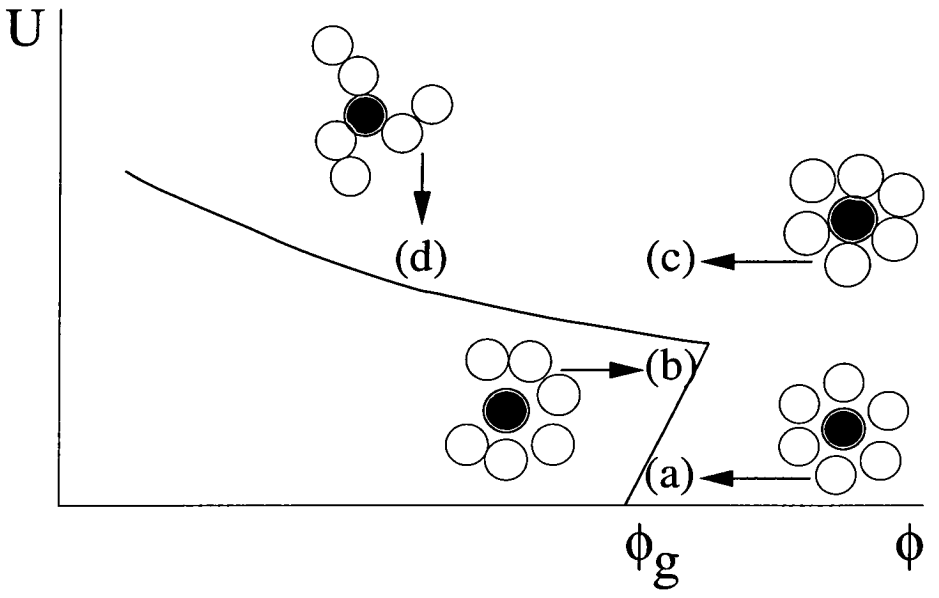

Figure 3.19: Schematic illustration showing predicted non-ergodicity transition and particle configurations for a colloid-polymer mixture of size ratio $\xi \sim 0.08$ which is (a) a repulsive glass, having crossed the non-ergodicity transition line, (b) a fluid at the same volume fraction as the glass but with a stronger attraction and (c) an attractive glass. Above the non-ergodicity line at high inter-particle attraction and lower volume fraction a gel might be expected (d).

Figure 3.19 shows a schematic diagram illustrating the non-ergodicity transition line predicted by MCT for a system with a short ranged inter-particle attraction. As the short ranged attraction is increased the cage surrounding a typical particle can be distorted due to the aggregation of particles forming the cage. The system can then relax because particles can escape from their cage. As the colloid density increases the particles again become trapped within cages of neighbouring particles, which leads to a glass transition that moves initially toward higher densities with increasing attraction, as observed in experiment [68]. For a colloid-polymer mixture where the size ratio is $\xi \simeq 0.08$, there is cross over from a 'repulsive glass', figure 3.19 (a), to a dense fluid (b), and to an 'attractive glass' (c), as the inter-particle attraction increases at constant colloid volume fraction [68]. The transition from a repulsive to an attractive glass vanishes at high size ratios in favour of a smooth curve [98]. Where MCT predicts the system

will be non-ergodic at low densities, one might expect the particles to become stuck together in ramified clusters (d) and ultimately gel.

Many qualitative aspects of the gel transition were found to be reproduced by the MCT calculations for a hard-core attractive system [6]. The calculated phase diagrams were found to exhibit gel transition which connected with the hard-sphere glass transition, and the phase diagram obtained by Verduin and Dhont [107] is qualitatively reproduced by MCT when the attraction is of intermediate range. For shorter ranged attractions MCT predicts that the gel transition passes below the critical point in the $(\phi, n_p^{(R)})$ phase diagram, so that structural arrest may occur instead of gas-liquid phase separation, which agrees with some experimental measurements [82].

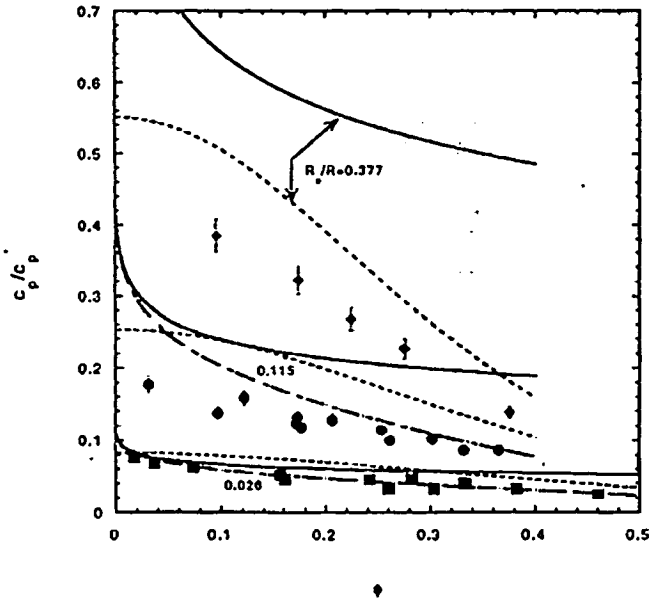

Figure 3.20: Predictions of the gel line from percolation and MCT compared to experimental results [82]. Solid symbols are the experimental points delimiting the stable fluid regions for different size ratios. At size ratios of $\xi = 0.026$ (squares) the samples gelled, at $\xi = 0.115$ (circles) fluid-crystal coexistence was observed, and at $\xi = 0.377$ (diamonds) the liquid-liquid coexistence curve was the phase boundary crossed. The solid curves are the MCT gel line, the long-short dashed curves are the MCT gel lines taking into account a polymer free volume correction (for details see [82]), and the short dashed curves are the static percolation lines. The corrected MCT line at size ratio of 0.337 lies well below the data points for that size ratio (diamonds) and was not shown for clarity.

MCT is different from approaches using a percolation transition to describe gelation, because it predicts the structural arrest to be driven by the slowing down of the local dynamics. The predictions from both percolation theory and MCT were discussed and compared to experimental results by Ramakrishnan [82], figure 3.20. The MCT prediction of an ergodic to non-ergodic

transition lies closer to the experimental gel line than the percolation line, although neither line corresponds well to the experimental situation at the high size ratios.

3.6.5 Sedimentation and the Influence of Gravity

The effects of gravity on colloidal suspensions can also be considered. The extent to which the collapse of transient gels is dependent on gravity is not yet understood, but it is generally accepted to be an important factor when considering their behaviour [101]. It has been suggested that due to the effects of gravity there is a threshold volume fraction $\phi^\star$ below which gelation does not occur. Below this threshold volume fraction the clusters cannot diffuse fast enough to form a space-spanning network, but instead the clusters would sediment. The gravitational Peclet number is the ratio of two timescales; the time it takes a fractal cluster of radius R to traverse a distance of the order of its own size by Brownian diffusion τ_b, and the time it takes the cluster to traverse the same distance by gravitational settling τ_s:

$$\mathrm{Pe}_g = \frac{\tau_b}{\tau_s} \sim \frac{2\pi\Delta\rho g a^4}{9k_BT}\left(\frac{R}{a}\right)^{d_f+1}, \tag{3.14}$$

where $\Delta\rho$ is the difference in density between the particles and the solvent, and a is the particle radius [72]. If individual clusters grow so large that they undergo significant sedimentation before the clusters meet and span space, gelation will not occur. These sedimentation limited clusters then deposit on the bottom of the sample cell to give a slightly expanded sediment. On the other hand, if $\mathrm{Pe_g} < 1$ when $R \sim R_{gel}$, where R_{gel} is the cluster size at gelation calculated in the absence of gravity, then gelation will happen. The threshold volume fraction between these two regimes is obtained by substituting the value of R_{gel} (using $\frac{R_{gel}}{a} \sim \phi^{1/(d_f-D)}$ from the DLCA model of gelation [72]) into the expression for the gravitational Peclet number and equating it to unity, giving [72, 2]:

$$\phi^\star \sim \left(\frac{9k_BT}{2\pi\Delta\rho g a^4}\right)^{\frac{d_f-3}{d_f+1}}, \tag{3.15}$$

where $\Delta\rho$ is the difference in the density between the particles and the suspending solvent, g is the gravitational acceleration constant, a is the radius of the particles, and d_f is the fractal dimension of the clusters. The effect of increasing the influence of gravity in this model is to increase $\Delta\rho g$ and thus increase $\phi^\star$. Therefor the onset of gelation would be expected to occur at higher volume fractions than those predicted by just considering the competition between

aggregation and thermal fluctuations. By suspending colloids in a solvent of the same density as the colloids themselves, the effects of gravity can be neglected and the phase behaviour studied in a close to zero gravity system.

3.7 Summary: Colloid-Polymer Mixtures

For the case of sterically stabilised colloids, the interaction potential is built up as follows. The constant components of the potential are a hard sphere repulsion, a steric repulsion, and a Van der Waals attraction. On the addition of polymer to the suspension the variable component of the potential is given by the depletion potential. The strength and range of this depletion attraction can be varied by changing the concentration and size of polymer. The effects of gravity can also be considered, and can be controlled by matching the density of the solvent to the colloidal particles.

The phase behaviour of a system can be changed by tuning the strength and range of the depletion attraction. It is known from both experiment and theory that the topology of the phase diagram of sterically stabilised colloid-polymer mixtures is dependent on the polymer to colloid size ratio. The equilibrium phase behaviour can be predicted using the lowest common tangent construction. Fluid and crystal are the only two equilibrium phases at low size ratios, and at higher size ratios there are also stable gas and liquid phases.

Various types of non-equilibrium behaviour are observed in colloid-polymer mixtures, some of which are associated with a metastable gas-liquid binodal within the fluid-crystal coexistence region. The experimental phenomenon of transient gelation has been discussed and three models of gelation, DLCA, Percolation and Mode Coupling Theory, have been considered. However, the nature of gelation in colloid-polymer mixtures is still the subject of much debate.

Chapter 4

Charged Colloidal Suspensions

4.1 Introduction

In this chapter the interaction potential and phase behaviour of charged colloidal systems will be considered. This includes suspensions of charged stabilised colloids and charged colloids that are sterically stabilised.

Charged colloidal particles can have a long ranged repulsive potential, and have a different phase behaviour to uncharged colloids. Commonly used charged colloids are charge-stabilised particles in aqueous solutions, for example polystyrene spheres. In the case of these systems the charge arises due to ionisable groups on the particle surfaces which mostly dissociate if the particles are dispersed in a polar solvent. More recently it has been demonstrated that sterically stabilised PMMA colloids carry a charge when suspended in certain organic solvents, for example cycloheptyl bromide (CHB). Here the charging mechanism is unknown. Under certain conditions, globular proteins can also be used as a system in which to study the phase behaviour of charged colloids. The interaction potential and phase behaviour of globular proteins will be discussed in detail in detail in chapter 5.

4.2 The Nature of Charged Colloids

In a vacuum, electrostatic repulsion between two like-charged particles would still be present at infinite separation. However, in solution there are free ions i from the dissociated ion-pairs on the particle surface, molecules of the solvent, and any additional salts. These free ions gather round the oppositely charged particles and create the electrical double layer (section 2.3, figure 2.3(a)).

The double layer can be modelled in terms of the Gouy-Chapman-Stern Model, where it is treated as consisting of two parts. At the particle surface there is a layer of ions that are specifically adsorbed (temporarily) with a force strong enough to overcome thermal agitation. This is known as the Stern Layer. Ions with centres beyond the Stern Layer form the diffuse part of the double layer, as illustrated schematically in figure 4.1. The Debye screening length κ^{-1} is the distance over which the potential decreases by an exponential factor, giving a measure of the thickness of the diffuse layer.

Thus, the electrical double layer screens the charge on the particle surface, so that the electrostatic repulsion decays exponentially, and the Debye screening length κ^{-1} provides a measure of the length over which the electrostatic repulsion decays.

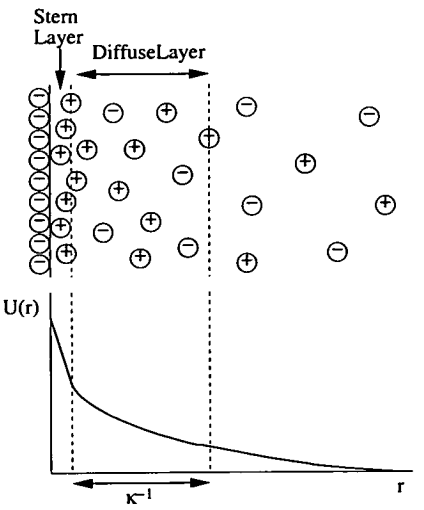

Figure 4.1: Schematic illustration of the electrical double layer of a charged colloid in solution.

4.3 Phase Behaviour of Charged Colloidal Suspensions

Hard sphere suspensions are fluid at low particle volume fractions ϕ but crystallise into a close-packed crystal at $\phi > 0.545$. Random hexagonal close packing is experimentally observed, although face centred cubic is the lowest free energy packing [97]. When the colloids are charged the electrostatic repulsion between the particles contributes to the interaction potential (the potential is made 'soft') and crystallisation occurs at smaller volume fractions. The crystal structure is then face centred cubic or body centred cubic. At higher volume fractions a glass is observed [93]. The range of the electrostatic repulsion due to the charge on the colloids can be controlled by the addition of salt to the suspension.

The crystallisation of charged colloidal systems has been studied by experiment [93, 97] and computer simulation [85]. Figure 4.2 shows the experimental phase diagram as a function of salt concentration for charged polystyrene spheres in a methanol-water solvent. The estimated charge on the colloids is $\sim$ 135 electronic charges per sphere [93].

In the limit of low salt, the crystallisation of charged colloids occurs at low volume fractions, in some cases as low as $\phi = 0.01$ [116]. As the salt concentration is increased the charge on the colloids is screened, and the effective range of the repulsion decreases. At high enough salt crystallisation occurs at volume fractions similar to that for uncharged hard spheres.

A glass transition is observed in charged colloidal suspensions at sufficiently high colloid volume fraction, figure 4.2 [93]. This is reminiscent of the glass transition for hard spheres which

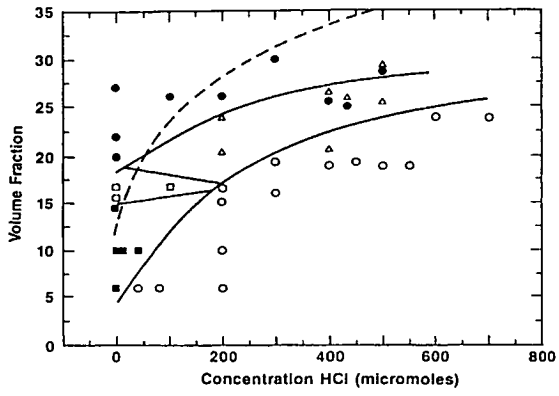

Figure 4.2: Phase diagram for charged polystyrene spheres on the addition of HCl. Symbols denote the following: ■ = *bcc* crystal, △ = *fcc* crystal, □ = *fcc* + *bcc* coexistence, • = *glass*, ○ = *fluid*. The bold lines are drawn as guide to the eye phase boundaries. The dashed line is the liquid-fcc phase boundary as predicted by computer simulation using a Yukawa potential [85]. To give an estimate of the range of the potential, note that the radius was 46nm, and the Debye screening length varied from 40nm (at zero salt concentration and volume fraction $\phi = 0.1$) to 9nm (at 500μ M salt concentration and $\phi = 0.3$), [93].

suppresses crystallisation at volume fractions ~ 0.58, but in the charged system the glass transition appears at volume fractions as low as $\phi = 0.2$ when there is no added salt.

4.4 DLVO potential

The phase behaviour of a charged colloidal suspension depends on the interplay between the inter-particle repulsion and attraction. For charged colloidal suspensions in a 1:1 electrolyte, the pair interaction potential between two colloidal particles can be modelled by the Derjaguin-Landau-Verwey-Overbeek (DLVO) potential. This includes a van der Waals attractive potential $U_A(r)$, a Coulomb repulsion potential $U_C(r)$, and a hard-sphere repulsion $U_{HS}(r)$:

$$U_{DLVO}(r) = U_A(r) + U_C(r) + U_{HS}(r), \tag{4.1}$$

where r is the centre to centre separation. The Van der Waals component of the potential $U_{VdW}(r)$ is given by equation 4.2:

$$U_{VdW}(r) = -\frac{A}{12}\left(\frac{4R^2}{r^2 - 4R^2} + \frac{4R^2}{r^2} + 2ln[1 - \frac{4R^2}{r^2}]\right), \tag{4.2}$$

where R is the radius of the particles and A is the Hamaker constant. This expression comes from integrating the Van der Waals interaction between pairs of atoms on the two particles.

The screened Coulomb repulsion term $U_C(r)$ is obtained by solving a linearised Poisson Boltzmann equation (known as the Debye Huckel equation) for particles with constant charge:

$$U_C(r) = \frac{(Qe)^2}{4\pi\epsilon_0\epsilon r}\frac{exp[-\kappa(r-2R)]}{(1+\kappa R)^2}, \tag{4.3}$$

where Q is the charge per particle, e the electronic charge, ϵ_o is the permittivity of a vacuum, ϵ is the dielectric constant of the solvent, and κ^{-1} is the Debye screening length. The Debye screening length κ^{-1} provides a measure of the length over which the electrostatic repulsion decays (i.e. the size of the electrical double layer), and is given by equation 4.4:

$$\frac{1}{\kappa} = \left(\frac{\epsilon\epsilon_0 k_B T}{e^2 \sum z_i^2 n_i}\right)^{\frac{1}{2}}, \tag{4.4}$$

where n_i is the number density of i-type of counter-ions in the bulk solution, k_B is Boltzmann's constant, T is the temperature, z_i is the valence of the i-type ionic species, and the sum is taken over *all types* of electrolyte ions i. As the ion concentration is increased, for example by adding salt, the Debye screening length gets shorter and the effective range of the electrostatic repulsion decreases. In the limit of high salt, where the Debye screening length (and hence the effective range of the electrostatic repulsion) is short, the behaviour tends toward that of uncharged particles.

Figure 4.3 shows a schematic example of a DLVO potential together with the van der Waals attraction, Coulomb repulsion and Hard Sphere repulsion components to the potential.

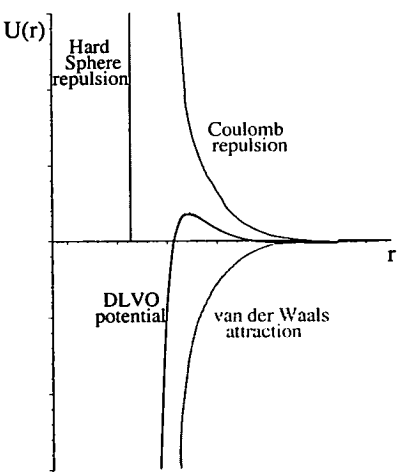

Figure 4.3: Schematic illustration of the DLVO potential and of the van der Waals and Coulomb components.

In this way the DLVO theory captures the essential physics of the interaction between charged colloidal particles. However, it is only a model and contains approximations which must be kept in mind when applying it to experimental situations. The main assumptions of DLVO theory are summarised below [65].

1. The surfaces of the particles are molecularly smooth and solid.
2. An intervening solvent has bulk liquid properties up to the interface.
3. Electrical double layer forces and van der Waals forces are treated independently and assumed additive.
4. The boundary conditions for the double layer are constant charge or constant potential.
5. The double layer interaction is computed using a Poisson Boltzmann equation for point ions. The Debye Huckel approximation is used to linearise the PB equation, which is valid at small surface potentials (or high electrolyte concentrations).
6. The attractive Van der Waals forces are calculated on the assumption that the solvent has a uniform density and orientation profile.

4.4.1 Van der Waals Component

In this section the Van der Waals component of the DLVO potential, and what effect the parameters within this term can have on the full interaction potential predicted by DLVO theory, will be considered.

The variable parameter to be considered is the Hamaker constant A. The value of the Hamaker constant depends on the material properties of the particles and solvent considered, in particular on their frequency-dependent polarisabilities, and has typical values in the range $A \simeq 10^{-18} - 10^{-21} J$ [87]. The Hamaker constant is small in systems where the polarisabilities of the particles and solvent are similar.

The effective Hamaker constant for particles in a solvent can be calculated from the Hamaker constants of the material and solvent in a vacuum using equation 4.5:

$$A_{121} = \left(A_{11}^{1/2} - A_{22}^{1/2}\right)^2, \tag{4.5}$$

where A_{11} and A_{22} are the Hamaker constants of the particle and solvent in vacuum [41, 89]. A lower value of the Hamaker constant and hence a weak interaction will arise when the particles and solvent are made of similar materials.

Figure 4.4 shows the effect of varying the Hamaker constant. Decreasing its value has the effect of shortening the range of the van der Waals potential. Conversely, the predicted range of the van der Waals interaction in systems with a high Hamaker constant would be long relative to systems with a lower Hamaker constant.

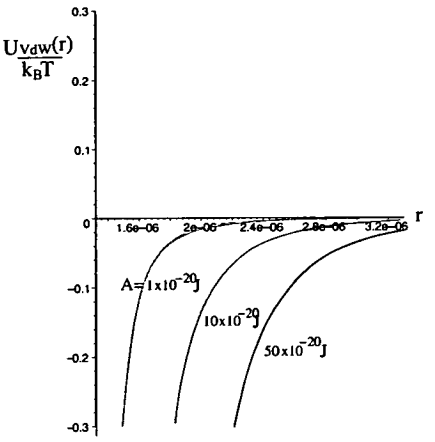

Figure 4.4: Predictions of the Van der Waals component using values of $R = 660$nm and $T = 295.15$, and plotting for values of the Hamaker constant of $50 \times 10^{-20}, 10 \times 10^{-20}$ and 1×10^{-20}J, as labelled. For calculations, written in Maple, see Appendix A.

4.4.2 Screened Coulomb Potential

Now consider the parameters in the screened Coulomb component of the potential. These are the charge on the particles Q and the Debye screening length κ^{-1} which in turn depends on the concentration of counter-ions in the solution.

Firstly consider varying the charge on the particles. Figure 4.5 shows that the effect of increasing the charge is to increase the strength and range of the repulsion.

Consider now varying the Debye screening length κ^{-1}. The competition between repulsion and attraction in the DLVO potential depends strongly on the salt concentration. At low salt concentrations the Debye screening length is long, so the repulsion dominates the interaction potential. This is the regime of colloidal stability. At intermediate salt concentrations the ranges of the repulsion and attraction are comparable. At high salt concentrations, the Debye screening length is short (and so the range of the Coulomb repulsion is short) compared to the range of the attraction, so attraction will dominate. In this case suspensions would be unstable and show irreversible flocculation.

These three cases are illustrated in figure 4.6 for the case of aqueous suspensions of small

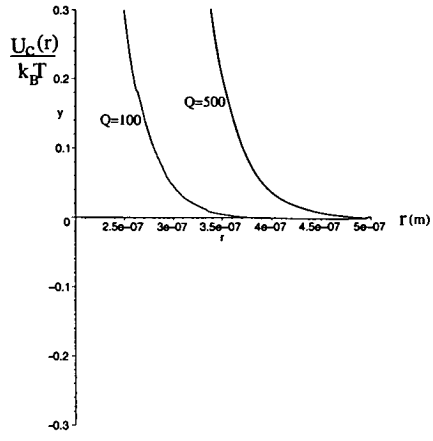

Figure 4.5: Predictions of the Coulomb component of the DLVO potential for different values of the charge on the particle. These plots are for the case of aqueous solutions of small charged colloids. Values used were $T = 295.15$, $R = 100nm$, $\epsilon = 80$, $c = 0.1mM$, and plotting for charges of $q = 100$ and $Q = 500$. The Hard sphere component of the potential is not shown for clarity, but provides an infinite repulsion at the point of contact $r = 2R$.

charged colloids of radius $R = 100$nm (for example polystyrene spheres in water). The Coulomb potential U_C and the DLVO potential U_{DLVO} are shown for the cases of low screening where the repulsion dominates the DLVO potential (salt concentration $c = 0.05$mM, Debye screening length $\kappa^{-1} = 50$nm), intermediate screening where the attraction and repulsion are balanced ($c = 0.2$ mM and $\kappa^{-1} = 2$nm), and high screening where the van der Waals attraction dominates the DLVO potential ($c = 5$mM and $\kappa^{-1} = 0.5$nm).

It is worth mentioning another potential often used in the literature to model the electrostatic interaction between charged colloids, the Yukawa potential, which is given by equation 4.6:

$$U_Y(r) \propto \frac{Z^2 e^2}{\epsilon} \frac{e^{-\kappa r}}{r} \tag{4.6}$$

This is similar to the expression used in the DLVO potential for the screened Coulomb interaction, but without a 'Geometrical Factor' of $(e^{\kappa 2R}/[1-\kappa R]^2)$. This factor takes into account that the part of the volume of the suspension occupied by colloids is not available to the screening ions. This Yukawa potential is only valid for dilute suspensions at low ionic strengths where $\kappa R \ll 1$. Some theoretical predictions made using the simple Yukawa model are incorrect, for example the prediction of a reenterant melting transition, which is not observed experimentally and is not predicted when the geometrical factor is included. Thus the more complete DLVO potential is a better model of the interactions of charged colloids [97].

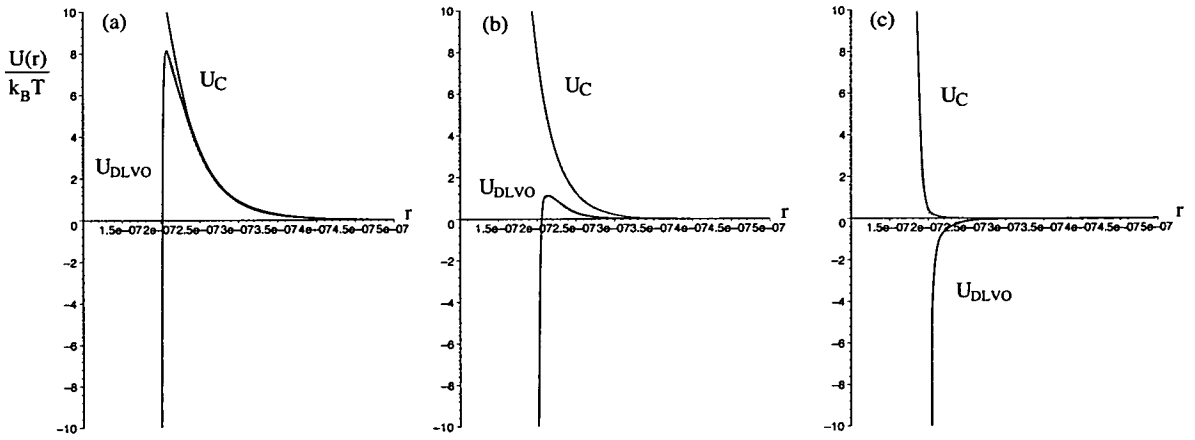

Figure 4.6: Predictions of the DLVO potential and the Coulomb component, using values of $T = 295.15$, $R = 100$nm, $\epsilon = 80$, $A = 1.3 \times 10^{-20}$ [89], $Q = 200$ electronic charges and varying the concentration of salt. The three salt concentrations plotted are (a) the low screening case $c = 0.05$ mM, (b) intermediate screening $c = 0.2$ mM and (c) the high screening case $c = 5$mM. For details of the calculation performed in Maple see Appendix A.

4.4.3 Applicability of the DLVO Potential

The DLVO potential has been applied to the study of colloidal systems with success. The competition between repulsion and attraction in the DLVO potential, which depends strongly on the salt concentration, can explain experimental observations on colloidal stability. At high salt concentrations, where the Debye screening length $\kappa^{-1} \ll 1$nm and DLVO theory tells us that attraction dominates over repulsion, suspensions are indeed unstable and show irreversible flocculation. At intermediate salt concentrations where $\kappa^{-1} \sim 1$nm the attraction balances the repulsion and reversible gas-liquid coexistence is possible [87]. At low salt concentration where $\kappa^{-1} \gg 1$nm the repulsion dominates the potential and the colloidal suspensions are stable.

The success of DLVO theory is not limited to a description of colloidal stability. Monovoukas and Gast [61] compared their experimental phase diagram of charged polystyrene spheres as a function of colloid volume fraction and ionic strength to the molecular dynamics results of Robbins *et.al* [85], who use a DLVO potential to model the particle interaction. The experimental results are shown in figure 4.7 (note that these authors used a renormalised surface charge density in the comparison of experimental data to MD simulations). The simulations using a DLVO potential show convincing agreement with the experimental data.

Due to the successes of the theory the classic DLVO potential is widely known and used, but its applicability is still a burning issue [65]. The continuum approximation upon which $U_A(r)$

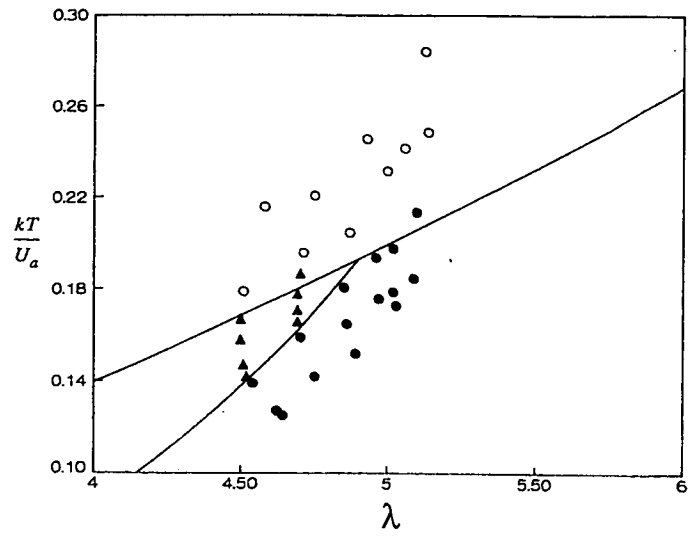

Figure 4.7: Experimental phase diagram of charged polystyrene spheres, where kT/U_a is a dimensionless temperature and λ is the Debye screening length multiplied by the average interparticle spacing. Symbols denote the following, ○, fluid phase, ▲, BCC crystal, ●, FCC crystal. Solid lines are MD simulation results using the DLVO potential from Robbins *et.al* [85]. Phase diagram taken from [61].

is based breaks down at atomic dimensions. It is assumed that the solvent has uniform bulk properties right up to the interface, a very serious approximation which must be overcome by putting in a cutoff for the Van der Waals force of the order of a molecular distance. It is well known that DLVO theory cannot be applied to systems with a very low Hamaker constant, for example oil in water, and indeed DLVO theory never claimed to be applicable to such systems [65].

The Debye-Huckel approximation used to describe the Coulomb repulsion U_C relies on small surface potentials ($\leq$ 25mV) which is unlikely to be the case for real colloidal systems. Furthermore, it has been shown that DLVO theory does not describe experimental results at low volume fractions and low salt [46], and new descriptions for the interaction have arisen. A modified form of DLVO with an additional term describing the low salt interactions has been published [87], and the existence of effective attractive forces between like charged particles has been suggested [46, 97, 111]. The Hofmeister series of ion specificity remains beyond the scope of DLVO theory, and indeed a full understanding of Hofmeister effects has proved elusive (for a full discussion see chapter 5.7). However, DLVO theory remains a useful model for the interaction between charged particles in systems where the assumptions involved are applicable, and it provides an essential platform from which to build a deeper understanding.

4.5 Phase Behaviour of Charged Colloid-Polymer Mixtures

Thus far only suspensions of charged colloids on the addition of salt have been discussed. Consider now what may happen if an additional attraction is present between the particles. This may be the case in suspensions of charge stabilised colloids mixed with uncharged polymer.

On the addition of polymer to a colloidal suspension the preliminary observation is that at low polymer concentration the suspension remains a single phase fluid, but above a critical polymer concentration the system separates into a dense phase in equilibrium with a dilute phase. As well as being reported for sterically stabilised colloidal suspensions (as discussed in chapter 3), this phenomenon has been reported for electrostatically stabilised suspensions of latex and a non-ionic water soluble polymer [100].

Sperry *et.al.* conducted a study on the flocculation of aqueous solutions of latex on the addition of the polymer Hydroxyethyl Cellulose (HEC) [100]. In suspensions with no HEC added, rapid Brownian motion of the particles was reported, and no flocculation or phase separation was observed. On the addition of HEC, particles aggregated above a critical concentration. The critical concentration at which flocculation is first reported decreased with increasing particle size (corresponding to a decrease in the polymer to colloid size ratio ξ) [99]. The morphology of the phase-separated dispersions were also studied, and the series of micrographs are shown in the figure 4.8. With hindsight, it can be seen that gas-liquid phase separation was observed, and on increasing the polymer concentration the colloids aggregated.

Since the colloidal latex particles are charged, they further characterised the system by varying the electrolyte concentration in the system and observing the effects this has on the concentration of polymer required for flocculation. In general, their observations are that increasing the ionic strength will decrease the critical concentration of HEC required to induce flocculation.

Gast *et.al* [29] developed a statistical mechanical analysis of the phase separation resulting from a volume exclusion mechanism in colloidal suspensions containing dissolved polymer. They used a perturbation approach to predict phase boundaries (for details see [89, 29]), using as the interaction potential a hard-sphere infinite repulsion and a depletion attraction as originally derived by Asakura and Oosawa [3] (see chapter 3.2).

Sperry discussed the interaction potential between charged colloids on the addition of non-adsorbing polymer, modelling it with a DLVO-like potential plus a depletion potential. The DLVO-type potential models the Van der Waals interaction and the screened Coulomb repulsion, and the depletion potential models the attraction due to the addition of polymer. In a

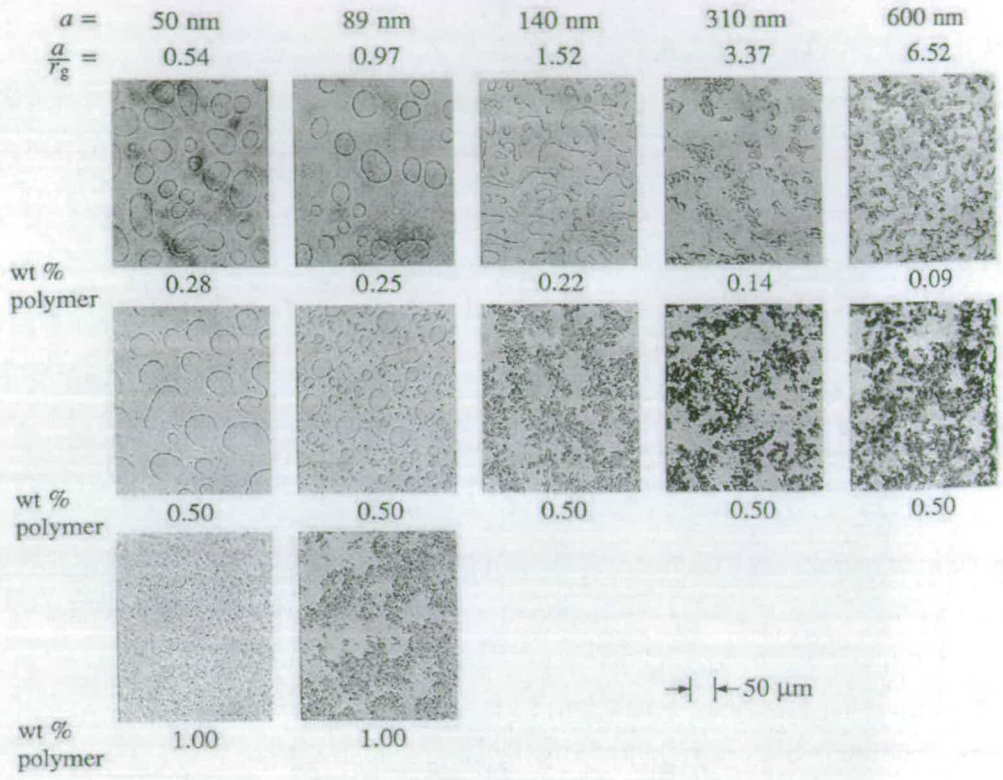

Figure 4.8: Morphology of phase-separating latex particles on the addition of HEC, taken from [99].

further paper, Gast *et.al* [30] extended their approach to predict the phase behaviour of charged colloidal suspensions on the addition of polymer, where the electrostatic interaction between the colloids is accounted for by including a screened Coulomb repulsion, of the same form as that used in the DLVO potential (although in this case the Van der Waals interaction is neglected). The data of Sperry [99] showing phase-separation as a function of colloid to polymer size ratio and polymer concentration, can be compared to the predictions from this theory [30], as shown in figure 4.9.

A more recent experimental investigation was made by L.A. Galloway [28], with the difference that surfactant worm-like micelles were used instead of the non-adsorbing polymer in the studies of Sperry and Gast *et.al*. The system was first studied in the presence of salt, using salt concentrations from $0.1 - 1.2\%$ by weight. As the surfactant concentration was increased the behaviour of the suspension changed from a single phase fluid to a region of gas-liquid coexistence. At higher surfactant concentrations a gel phase was observed. This behaviour is

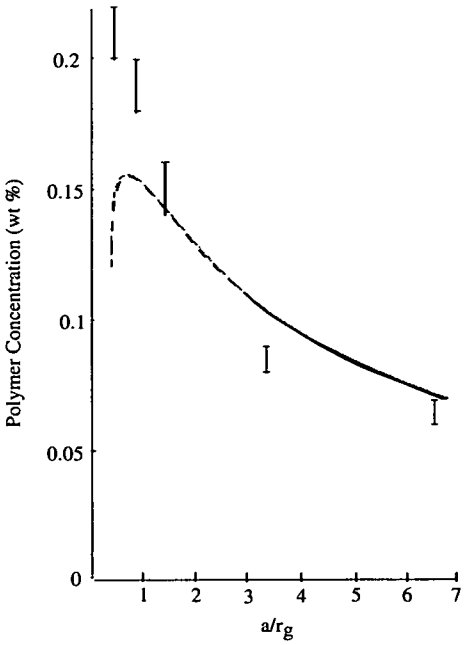

Figure 4.9: Comparison of experimental data [99] and predictions [29] of the phase behaviour of polystyrene latex on the addition of HEC. The fluid solid transition, indicated by the solid line, is predicted for $a/r_g > 3$ while the fluid-fluid transition, indicated by the dashed line, emerges for $a/r_g < 3$. Taken from [89].

reminiscent of that observed for uncharged colloid-polymer mixtures as discussed in chapter 3.

The same system was then studied with no added salt. It was reported that increasing the surfactant concentration at an intermediate colloid volume fraction $\phi \sim 0.05$ the following behaviour was observed. At low concentrations the suspensions were single phase fluid, but on increasing the surfactant concentrations crystals nucleated and a region of fluid-crystal coexistence is reported. On increasing the surfactant concentration further gel-gas phase coexistence is observed, and at the highest surfactant concentrations studied the colloids aggregated into a sample spanning gel.

In comparison to uncharged colloid-polymer mixtures the existence of a fluid-crystal coexistence region rather than gas-liquid phase separation implies a size ratio below the cross-over size ratio $\xi \sim 0.3$. This would suggest that for charged colloids the effective radius of the colloid is the colloid radius plus the Debye screening length, which must be used in calculating the size ratio and interaction potential of the system. However, differences to colloid-polymer mixtures were observed. The gels were permanent not transient, and in some cases a 'restabilisation' is reported at higher colloid volume fractions. Furthermore it was noted in this work

that the validity of comparison to colloid-polymer mixtures is unclear due to the high surfactant concentrations involved.

The behaviour of charged-colloids on the addition of *charged* polymer or worm-like micelles has also been studied [28, 89], but the complexities of such systems are beyond the scope of this thesis.

4.6 Beyond the DLVO Potential

There are some aspects of charged colloidal suspensions that are not captured by the simple DLVO model. In some cases DLVO like potentials can be used if some parameters such as the particle charge are *renormalised.* In fitting a DLVO potential to experimental data using adjustable (effective) parameters, it is found that the effective charge obtained is considerably smaller than the surface charge that is experimentally determined [81]. The DLVO potential could describe the interactions between charged particles if parameters within the Debye-Huckel (DH) approximation used to describe the Coulomb repulsion, in particular the charge, were renormalised with respect to their true value. In this way the charged colloid and its electrical double layer are treated as one composite object. There have been many approaches to this renormalisation [81], but a simple model for calculating the renormalised charge is still missing.

The screened Coulomb component of the potential, traditionally modelled using the Debye Huckel approximation to linearise the Poisson-Boltzmann equation, could be modelled more accurately. The full nature of the interactions of electrical double layers are still an active area of research. For a discussion of the different approximations which can be used in modelling the electrical double layer under different conditions see Russel [89].

The validity of DLVO-like potentials is not universally accepted. In the above discussion all the electrostatic forces between isolated colloidal particles with the same charge have been repulsive. However, experiments performed at low salt concentrations have revealed evidence for coexistence of a very dilute colloidal gas phase with a much denser colloidal liquid or crystal [46]. Since the Van der Waals attraction would be completely masked by the electrical double layer at these low salt concentrations, these results cannot be explained using the Van der Waals attraction in the DLVO potential. This has led some researchers to suggest the existence of attractive electrostatic interactions between similarly charged particles [46, 96].

Other suggestions have also been made to explain the experimental observations at low salt

concentrations [87]. Instead of using the DLVO pair potential (the effective potential between two colloidal particles in the presence of a bath of micro-ions), the total free energy of a three component mixture of charged hard spheres and positive and negative point ions can be calculated. In doing so the electrostatic screening at low salt concentrations is found to be dependent on the *density* of the colloids, so that the Debye screening length is substantially smaller in a dense phase. This leads to the prediction of gas-liquid coexistence at extremely low salt concentrations. The physical picture is that oppositely charged particles tend to be closer to each other than particles of similar charge, and the entities which exhibit DLVO pairwise interactions are colloids *surrounded by* a cloud of micro-ions with a compensating net charge. At low salt concentrations, the size of this ion cloud depends on the colloid density in such a way that in a dense phase the electrical double layer will be smaller. This can give rise to the required excess cohesive energy which stabilises a liquid phase in coexistence with a gas at low salt concentrations.

DLVO potential is an effective *pair* interaction potential, and does not take into account many-body effects. Attractive forces can result from many-body effects even in the case of a purely repulsive pair potential [81]. Other effects such as ion-ion correlation effects and specific ion effects (differing experimental results when different ions of equal valence are used) should also be taken into account when considering effective attraction between similarly charged particles. As this multitude of ideas would imply, the nature of the interaction between similarly charged particles is still an open question.

A recent publication [111] demonstrates the applicability of a (renormalised) DLVO theory at relatively high salt concentrations, which is no longer valid at low salt. At low salt concentrations it is demonstrated that the macro-ions (charged colloids) contribute to the screening length. To demonstrate the importance of this idea, two length scales are defined. κ^{-1} is the Debye screening length from the small ions, and κ_T^{-1} is the Debye screening length when the macro-ions also contribute. Note that $\kappa_T^{-1} < \kappa^{-1}$. The phase behaviour depends on the relative magnitudes of κ^{-1}, κ_T^{-1} and r_0, a measure of the typical distance between macro-ions.

If there is no salt added, then at low macro-ion concentrations $\kappa_T^{-1} > r_0$, and the macro-ions interact with an effectively unscreened Coulomb law in a neutralising background of electrolyte solution. As the macro-ion concentration increases, the spacing between macro-ions becomes larger than the associated screening length, that is $\kappa_T^{-1} < r_0$. In this case the macro-ions are too far apart to contribute to the screening length and κ_T^{-1} is no longer valid. However, since the screening length due to the small ions $\kappa^{-1} > r_0$, the macro-ions still interact with an effectively unscreened Coulomb law. Increasing the concentration of macro-ions further, the

screening length becomes less than the distance between neighbouring macro-ions ($\kappa_T^{-1} < r_0$), which results in a screened macro-ion interaction. The macro-ions become surrounded by a double layer of ions, and the DLVO interaction is recaptured.

If salt is added it reduces both screening lengths inducing a similar transition to the regime of screened Coulomb (DLVO) interactions at moderate salt concentrations. These considerations lead to a prediction of a phase instability occurring at low salt and colloid volume fraction within the phase diagram, as is observed experimentally.

It is discussed that the predicted phase instability is due to a long ranged net attraction, despite the repulsion between a pair of particles. The only force acting over such long distances would be the Coulomb force, but this is exactly cancelled by the net charge of the small ions since the bulk is electrically neutral. The macroion-macroion contribution is thus a correlation effect: the electrostatic repulsion between a particle and its neighbouring particles causes them to move away, leaving an excess of counter-ions. The particle is then attracted to this 'correlation hole', the centre of which is displaced toward the other macro-ions. This picture is illustrated schematically in figure 4.10.

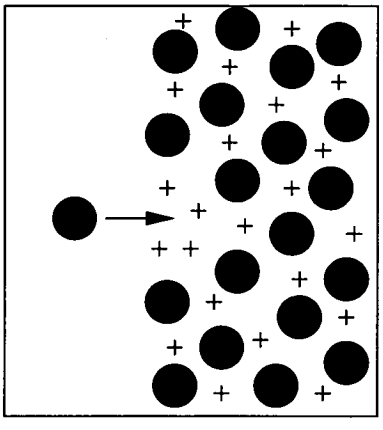

Figure 4.10: Schematic illustration of the resulting effective attraction of a negatively charged colloid to other like-charged colloids despite the electrostatically repulsive pair potential [111].

4.7 Gelation in Charged Colloid-Polymer Mixtures

The effect that charge may have on the gelation of colloid-polymer mixtures, for the case of charged colloids and uncharged polymer, will now be discussed. Insights into the effect of charge on the gelation transition can be gained through a theoretical description by Groenwald and Kegel [33]. They consider an uncharged aggregating colloidal system, and then ask what

the effect would be of adding a small charge on each of the aggregating particles. The general model is that the free energy of a cluster $f_n(Z)$, composed of n particles and with total charge Z, is assumed to be composed of a part due to the Van der Waals (dispersion) attractions $f_{VdW}(n)$, and a part due to the charge on the cluster $f_{charge}(n, Z)$:

$$f_n(Z) = f_{VdW}(n) + f_{charge}(n, Z) \tag{4.7}$$

Various assumptions underlie the theory, including that the cluster distribution is assumed to be monodisperse both in charge and size, which is valid for the charge on the cluster $Z \gg 1$ and the aggregation number $n \gg 1$. The interactions between clusters is also neglected. Furthermore the interactions between counter-ions and the surface charge are neglected. This assumption is valid only if the effective screening length is larger than the linear size of the cluster.

The free energy due to the charge on a particle is modelled using the Linearised Poisson-Boltzmann equation to describe the interaction between charges, and terms describing the energy and entropy associated with dissociating the ion pairs on the colloids. They extend this idea to include the free energy of a cluster made up of n charged particles. By minimising the expression for the free energy per particle of a cluster, they find an equilibrium aggregation number n_*, giving the number of particles that will make up a stable equilibrium cluster. The charge per particle depends on the volume fraction, such that the charge per particle decreases with increasing volume fraction, due to an increase in the translational entropy of the dissociated ions upon diluting the system. Following from this they make the prediction that the radius of the stable clusters R_* will be dependent on the initial volume fraction of the colloids in the following way:

$$R_* \simeq K \left(\frac{\gamma \nu b^3 e^{\Delta\epsilon}}{l_B \sigma s} \right)^{1/3} \phi^{1/3}. \tag{4.8}$$

l_B is the Bjerrum length, given by $l_B = e^2/4\pi\epsilon_0\epsilon_r k_B T$, where e is the elementary charge, ϵ_0 is the permittivity of a vacuum, ϵ_r is the dielectric constant of the solvent. The charge density is σ and s is the surface of the particle, so σs is the number of dissociation sites on the surface. b is the distance between opposite charges of an ion pair, and ν is the particle volume. $\Delta\epsilon = l_B/b$ is the dissociation energy, and γ is the surface tension scaled by $k_B T$, and is given by $\gamma \simeq \epsilon/s$, the energy of a particle in a cluster divided by the total surface of the particle. The constant K

depends on the *shape* of the clusters, for example for disk shaped clusters $K = 2.23$ and for spherical clusters $K = 1.52$.

They also predict the preferred shape of the clusters by minimising the free energy for different cluster shapes, and they find that disk shaped clusters are favourable.

Thus, by using a combination of dispersion attraction and electrostatic repulsion, an equilibrium phase of clusters is predicted. If the electrostatic repulsion were not present the system would continue aggregating into a non-equilibrium gel and no stable cluster phase would be observed. The number of charges per particle must be low enough to let the clusters grow sufficiently, but high enough to prevent large scale aggregation. In this cases one would expect to see a stable and long lived *equilibrium* cluster phase, where the preferred cluster shape is a disk, figure 4.11, and the radius of the clusters is dependent on the colloid volume fraction. Thus, the effect of adding a charge onto the particles in an otherwise aggregating system, is to stabilise the clusters at a given size against further aggregation, resulting in a long lived equilibrium cluster phase. In this way the gel transition line is moved relative to the uncharged case, due to the existence of an electrostatic repulsive term in the potential, and the system may be expected to gel at higher inter-particle attractions.

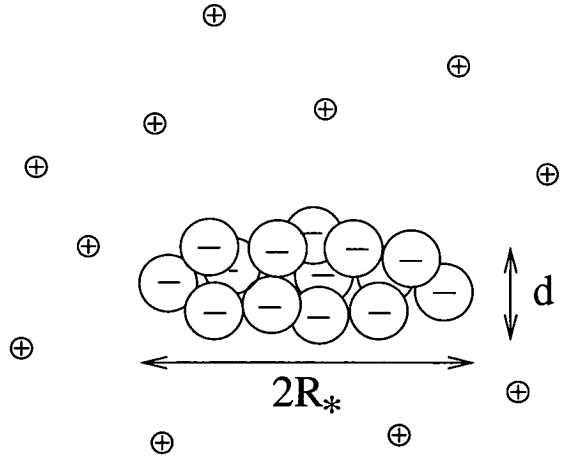

Figure 4.11: Schematic illustration of the stable cluster phase predicted for charged colloidal suspensions. Effect of the charge is to stabilise clusters of radius R_* against further aggregation.

4.8 Chapter Summary

In Chapters 3 and 4, two types of colloidal dispersions have been discussed, suspensions of sterically stabilised (uncharged) colloids and suspensions of charged colloids. The latter includes

suspensions of charged stabilised colloids and sterically stabilised charged colloids. The phase behaviour of these systems depends on the interaction potential of the particles.

Charged colloids have an interaction potential which is built up as follows. The constant components of the potential are the hard sphere repulsion and the Van der Waals attraction. The variable part of the potential can have two components. Firstly, an electrostatic interaction, the strength and range of which can be varied by changing the charge on the particles and adding salt to the system. For most cases this is a repulsion, but under some conditions (particularly very low salt) there can be an effective attraction between the particles. Secondly, a depletion attraction induced by adding polymer to the system, the strength and range of which can be controlled by varying the concentration and size of the polymer. The effects of gravity can be controlled by matching the density of the solvent to that of the particles.

The phase behaviour of a system can be changed by tuning the strength and range of the depletion attraction and electrostatic interaction.

The detailed phase behaviour of charged colloids is less understood than that of uncharged colloids. The crystallisation of charged colloidal suspensions as a function of salt concentration has been studied showing that, at low salt, crystallisation occurs at low volume fractions, but as the salt concentration is increased the behaviour tends toward that for uncharged colloids. A DLVO potential can be used to model the particle interaction potential of charged colloids, but this theory has limitations and cannot describe the experimental observations at low salt concentrations. The phase behaviour of charged colloidal suspensions on the addition of polymer is not understood in detail. It has been suggested that charge may have a stabilising effect on aggregating colloidal suspensions leading to an equilibrium cluster phase. However, a full understanding of the phase behaviour of charged colloidal suspensions has not yet been reached.

Chapter 5

Protein Solutions

5.1 Introduction

Proteins come in variety of shapes and sizes, and have evolved to perform specific functions, and as such they exhibit an extensive range of complex behaviour. In this chapter one particular class of proteins, globular proteins, are considered. Their shape, and the way their charge can be controlled is discussed. The DLVO potential is outlined as a possible model for protein interactions, and its successes and failures are highlighted. Finally the current understanding of the phase behaviour of the globular protein system studied here, lysozyme on the addition of NaCl, is described.

5.2 Protein Structure

The proteins observed in nature have evolved to have a specific function. The functional properties of proteins depend partly on their three dimensional structure. On the simplest level, proteins are made up of a series of amino acids. The sequence of the amino acids of each protein can be inferred from the gene sequence of DNA. This amino acid sequence is referred to as the primary structure of the protein, and in itself tells us very little about the function or three dimensional structure of the protein.

The particular sequence of amino acids in a protein will fold to create structures such as α helices or β strands, called the secondary structure of the protein. The tertiary structure is formed by the packing of these elements into one or several compact globular units, called domains. The final protein may contain several different domains arranged in the quaternary structure. The protein thus folds into a compact and complex structure.

The extent to which nearly-hard-sphere charge stabilised colloids can be modelled as interacting with a hard sphere repulsion, Van der Waals interaction and a screened Coulomb repulsion (collectively the DLVO interaction) has been discussed in the previous chapter. Whether this model can also be applied to proteins is discussed in this chapter. Firstly, is it valid to attribute a hard sphere repulsion to proteins? The compact structure of globular proteins implies that, in their folded native state, they perhaps may be treated as rigid bodies for some purposes. To determine if the proteins have a spherical shape, the quaternary structure of the proteins is of paramount importance. The class of proteins of interest here is globular proteins which, as the name suggests, are approximately spherical. We shall see in the following chapters how good an approximation this is for the globular protein studied here, lysozyme.

5.3 Controlling the Charge

Most proteins in aqueous solutions carry a charge. Hydrogen ions bind covalently to, or dissociate from, the side chains of acidic and basic amino acid residues and at the carboxyl and amino termini of the amino acid chains of the protein. The ionisation of these groups, and so the net molecular charge, depends on the pH of the solution. In order to predict the protein interaction using the DLVO potential, the charge on the proteins must be maintained at a constant, known value. To do this the pH of the solution must remain constant as the concentration of the protein and other components of the solution are varied.

5.3.1 Importance of pH

The pH is a measure of the concentration of protons (hydrogen ions) in solution, and is given by equation 5.1:

$$pH = -\log a(H^+), \tag{5.1}$$

where $a(H^+)$ is the activity of hydrogen and is given by:

$$a(H^+) = \gamma[H^+], \tag{5.2}$$

where $[H^+]$ is the concentration of hydrogen ions in moles per litre. Assuming that the solution can be treated as an ideal solution, the activity constant $\gamma = 1$ [5] and the pH of the solution is the negative logarithm of the concentration of hydrogen ions in moles per litre pH$= -\log[H^+]$. In a solution with low pH a protein would be positively charged, and in a solution with high pH it would be negatively charged. The pH at which the net charge is zero is called the isoelectric point, and the isoelectric pH of lysozyme is 11.0 . The variation of the charge on a protein with pH can be experimentally determined, and the plot of the proteins charge against solution pH is called a protein titration curve. Experimental determination of the lysozyme titration curve was carried out by Kuehner *et. al.* [50]. Their experimental measurement of the titration curve of lysozyme is shown in figure 5.1, and compared to the titration curves of lysozyme reported by other authors [37, 105].

The protein titration curves are dependent on the ionic strength of the solution. All the solutions used for the lysozyme titration curves in figure 5.1 had an ionic strength of 0.1M. The variation

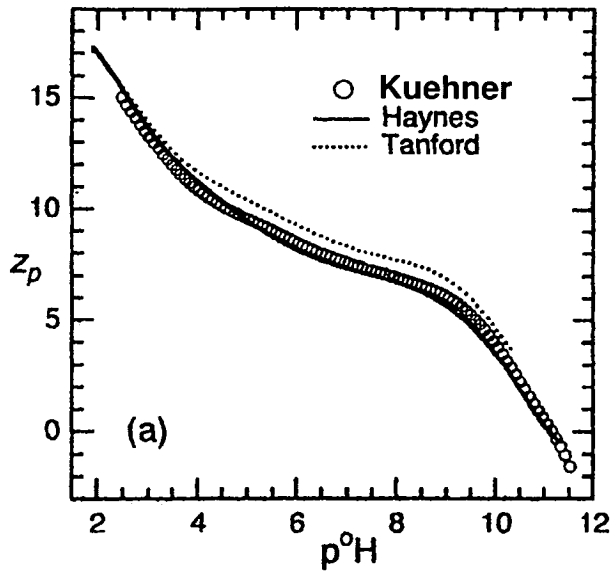

Figure 5.1: Experimental titration curve for the globular protein lysozyme, from Kuehner *et. al.* [50], Tanford *et. al.* [105] and Haynes *et. al.* [37]. Taken from [50].

of the titration curves with ionic strength was also measured by Kuehner [50], and are shown in figure 5.2 for potassium chloride solutions ranging from $0.1 - 2$M.

The pH of a solution can be maintained at a constant level by using a buffer. Buffers make use of the chemical equilibrium that exists when acids and bases are both present in the solution, due to the transfer of protons (hydrogen ions) between species. The pH of a buffer solution depends on the concentration ratio of acidic to basic species in the solution. I will discuss this in more detail in the following sections.

5.3.2 Acids and Bases

According to the Bronsted-Lowry theory of acids and bases [5], an acid is a species which tends to lose a proton (in this case a hydrogen ion H^+), and a base is a species which tends to accept a proton, and they are expressed in the following way:

A Bronsted acid HA is a proton donor: $HA \rightarrow H^+ + A^-$
A Bronsted base B is a proton acceptor: $B + H^+ \rightarrow BH^+$

When dissolved in water, an acid HA takes part in the following proton transfer:

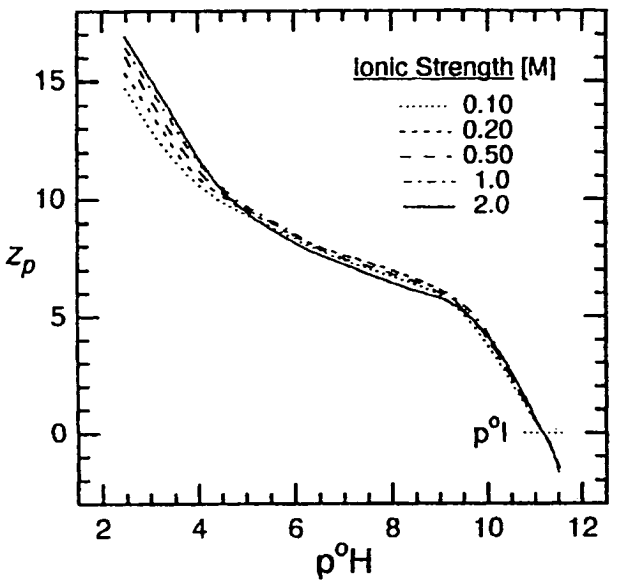

Figure 5.2: Experimental titration curves for the globular protein lysozyme in potassium chloride solutions of ionic strength ranging frome 0.1 – 2 Molar. Taken from [50].

$$HA + H_20 \rightleftharpoons H_3O^+ + A^- \tag{5.3}$$

In the forward reaction the H_20 molecule accepts a proton from the acid HA and therefore acts as a Bronsted Base. In the reverse reaction, the A^- ion accepts a proton from H_30^+ and is converted back into the acid HA. Therefore, in the reverse reaction, H_30^+ acts as the Bronsted acid and A^- acts as the Bronsted base.

The proton donor that results from the transfer of a proton to a species is called the **conjugate acid** of the original base. In the above reaction H_30^+ is the conjugate acid of the base H_20. Similarly, A^- is called the conjugate base of the acid HA. The basic form of the proton-transfer equilibrium in water is therefore:

$$\text{acid}_1 + \text{base}_2 \rightleftharpoons \text{acid}_2 + \text{base}_1. \tag{5.4}$$

A similar reaction can be written for a base B in water:

$$H_20 + B \rightleftharpoons BH^+ + OH^- \tag{5.5}$$

The fact that water can act as both an acid and a base means that there exists H_30^+ and OH^- ions in water (1.0×10^{-7} mol l^{-1}), as a result of the autoprotolysis equilibrium, equation 5.6. From this follows the concept of a neutral solution as having the same pH as water at $25°C$, i.e. $pH = -\log(1 \times 10^{-7}) = 7.00$.

$$H_20 + H_20 \rightleftharpoons H_30^+ + OH^-. \tag{5.6}$$

The proton-transfer equilibrium of a Bronsted acid in an ideal aqueous solution can be expressed in terms of an equilibrium constant, the dissociation constant (or acidity constant) K_a:

$$K_a = \frac{[H^+][A^-]}{[HA]}. \tag{5.7}$$

Acidity constants are widely reported by their logarithms, and by analogy with the definition of pH the pK_a is defined as:

$$pK_a = -\log K_a. \tag{5.8}$$

It follows that the pH can be expressed in terms of the acidity constant by equation 5.9:

$$pH = pK_a + log\frac{[base]}{[acid]}. \tag{5.9}$$

Acidity constants are used to classify acids as either weak or strong. A strong acid is one which has an activity constant $K_a > 1$, for example hydrochloric acid HCl, and at normal concentrations its molecules are fully ionised. The stronger the acid the weaker its conjugate base, and vice versa.

5.3.3 Amino Acids and Proteins

Amino acids, like water, behave as both acids *and* bases. For example, when the amino acid glycine is titrated with hydrochloric acid it behaves as a base, but when it is titrated with sodium hydroxide it behaves as an acid. The pK_a values of all 20 amino acids are known, and listed in [17].

Turning now to proteins, the situation becomes complex since a protein has numerous ionisable protons. The overall pK_a value of the protein depends not only on the different pK_a values of

all the amino acids, but also on the environment of the protein and each amino acid. Therefore knowing the individual pK_a values for all the amino acids in a protein is not sufficient to determine the pK_a of the protein itself. Theoretical treatments are attempted, but show some disagreement with experimental results [50, 105]. Therefore it is necessary to experimentally determine the titration curves for proteins in different environments. The titration curve of lysozyme was shown in figure 5.1.

5.3.4 Buffer Action

Consider an acidic solution to which a base is being added. A plot of the pH against the volume of the base added is called the pH titration curve [5, 24, 17], where the *titrant* is the species being added to a solution to change its pH, figure 5.3. Consider an acidic solution which initially has a low pH. As the volume of the base added is increased, there comes a point when a stoichiometrically equivalent amount of base has been added to a given amount of acid. This is called the stoichiometric point. Increasing the volume of added base around this point increases the pH steeply. The exact shape of the titration curve depends on the strengths of the acid and base used.

The addition of the titrant to the solution converts some of the acid into its conjugate base. When the concentrations of the conjugate acid and base are equal (that is, then pH $=pK_a$), the pH only changes slowly when small amounts of acids or bases are added. This is half way to the stoichiometric point on the pH titration curve, as illustrated in figure 5.3.

$$HA + H_20 \rightleftharpoons H_3O^+ + A^- \tag{5.10}$$

$$H_20 + B \rightleftharpoons BH^+ + OH^- \tag{5.11}$$

The slow change in pH when small amounts of acids or bases are added when the pH is near pK_a is the basis for buffer action. Recall the reaction of the acid HA and the base B in water, equations 5.10 and 5.11. The physical basis of acidic buffer action is that the existence of an abundant supply of A^- ions can remove any H_30^+ ions brought by the additional acid. The abundant supply of HA molecules can supply H_30^+ ions to react with any base that is added. Similarly, for the case of a base buffer, the supply of BH^+ ions can remove any OH^- ions brought by the additional base, and the supply of B molecules can supply OH^- ions to interact with any added acid.

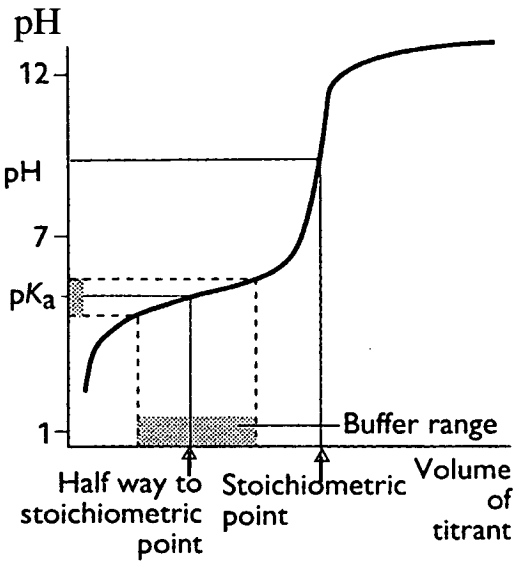

Figure 5.3: Schematic titration curve, showing the buffering region around the pK_a value, taken from [5].

Buffers have an ionic strength I, given by:

$$I = \frac{1}{2}\sum_i (c_i z_i^2) \tag{5.12}$$

where c_i is the concentration of ions (in moles) and $z - i$ is the charge on each ion, and the sum is taken over all species i. This must be taken into account when calculating total ionic strength of the solution, chapter 9.2.3. For the experiments reported in this thesis the protein lysozyme was dissolved in a sodium acetate (NaAc) buffer, titrated by hydrochloric acid (HCl) to a pH of 4.5. The following equations describe the processes that take place when the NaAc powder is dissolved in water:

$$NaAc + H_2O \rightarrow Na^+ + Ac^- + H_2O \tag{5.13}$$

$$Ac^- + H_2O \rightleftharpoons HAc + OH^- \tag{5.14}$$

The NaAc dissociates to produce acetate (Ac^-), which reacts with the water to form acetic acid (HAc). The acetate is the base, and acetic acid is the conjugate acid, with a pK_a value of 4.74. Titration with hydrochloric acid then has the effect of changing the ratio of [HAc] to [Ac^-]. It increases the concentration of [HAc] and decreases that of [Ac^-], thus lowering the pH. This reaction is shown in equation 5.15.

$$Na^+ + Ac^- + H^+ + Cl^- \rightleftharpoons Na^+ + Cl^- + HAc. \tag{5.15}$$

5.4 Phase Behaviour of Proteins

Under certain conditions, some globular protein solutions can be used as a model system to study equilibrium phase behaviour. The complicating effects of polydispersity (chapter 2.3) are not present since proteins are monodisperse, and with a radius of order nm sedimentation due to gravity is less pronounced. The addition of salt to a solution of charged proteins will screen the charge, inducing an effective short ranged attraction between the proteins. In this way globular proteins on the addition of salt might be used as a system to study the phase behaviour of particles as the strength of the short ranged inter-particle attraction is increased.

Protein phase behaviour is also of biological relevance. A key element in analysis of the function, or malfunction, of proteins is the determination of their structure. Whilst recombinant DNA techniques are used to infer the amino acid sequence of proteins, their 3-D structure is experimentally determined by crystallography. Thus understanding the growth of protein crystals is of biological importance, and has been the subject of extensive research [58, 114, 31].

The first published observation of the crystallisation of a protein was by Hunefeld in 1840. The protein was hemoglobin from the earthworm, and crystals were obtained when earthworm blood was pressed between two glass slides and allowed to dry [58]. This demonstrated for the first time that protein crystals can be obtained by the evaporation of a concentrated protein solution. Fifty years later, Osborne and others (see [58] and references therein) reported that plant seed proteins, principally globulins, were crystallised by the extraction of proteins into a salt solution of about 1M NaCl followed by a slow cooling to 20°C. Soon after, the protein albumin was crystallised by the addition of salt until turbidity, followed by adjustment of the pH. These early reports, often in more subtle forms, are the basis of protein crystallisation techniques used today.

The solubility (and hence crystallisation) of a protein depends on properties such as temperature and pH, as well as the concentration of protein and any additives used such as salts or polymers. Many reports of protein crystal growth describe the nucleation of crystals at a given set of conditions, sometimes followed by changing these conditions (for example, temperature for the case of globulins and pH for the case of albumin). Throughout the literature many different conditions for protein crystallisation are reported. However, all these techniques are

a way of manipulating the position of the protein solution within the phase diagram. In the discussion that follows I concentrate on the location of the crystallisation boundary of globular protein solutions as their inter-particle potential is varied by changing temperature, pH or salt.

It has been suggested by George and Wilson [31] that many globular proteins show a universal crystallisation boundary when plotted in the (ϕ, B_2) plane, where ϕ is the protein volume fraction and B_2 is the second virial coefficient of the osmotic pressure. For particles interacting with pair potential $U(r)$ when their centres are separated by distance r, B_2 is given by:

$$B_2 = 2\pi \int_0^\infty (1 - e^{-U(r)/k_B T}) r^2 dr. \tag{5.16}$$

In general, a negative B_2 results from an attractive particle interaction, whereas a positive B_2 would imply a repulsive interaction. B_2 values were experimentally determined by static light scattering, and it was found that at a constant volume fraction crystallisation falls within a favourable crystallisation window between B_2 values of -3.2 and -0.85 for all globular proteins studied. Further evidence was provided by Rosenbaum *et.al.* [88] and Poon [70], and the collective data shows that 20 globular proteins and related macromolecules, as well as a model colloid-polymer mixture, have a common crystallisation boundary in the (B_2, ϕ) plane.

5.5 DLVO Potential

As described in section 4.3, the interaction potential between charged colloids can be modelled by the Derjaguin-Landau-Verwey-Overbeek (DLVO) potential. The addition of salt to a protein solution has the effect of screening the charge on the proteins. This charge screening can be modelled using the screened Coulomb repulsion term of the DLVO potential, equation 5.17, where κ^{-1} is the Debye screening length:

$$U_C(r) = \frac{(Qe)^2}{4\pi\epsilon_0\epsilon r} \frac{exp[-\kappa(r - 2R)]}{(1 + \kappa R)^2}, \tag{5.17}$$

$$\frac{1}{\kappa} = \left(\frac{\epsilon\epsilon_0 k_B T}{e^2 \sum_i (z_i^2 n_i)} \right)^{\frac{1}{2}}, \tag{5.18}$$

where n_i is the number of ionisable groups per unit volume in the bulk solution, k_B is Boltzmann's constant, T is the temperature, z_i is the valence of the ionic species, and the sum is taken over the electrolyte ions i. Since the sum must include all electrolyte ions, the ionic

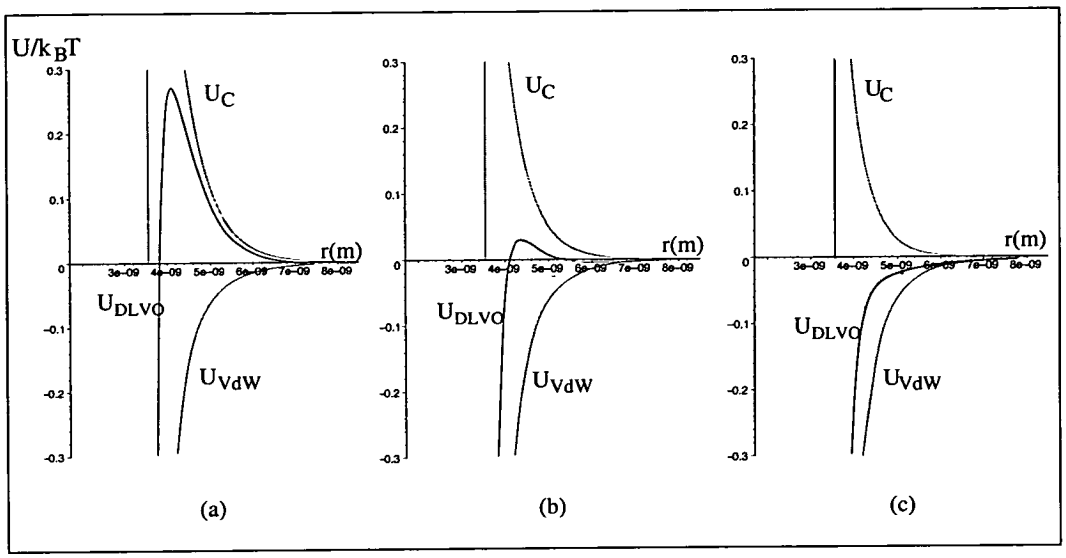

Figure 5.4: Predictions of DLVO theory showing the Coulomb component of the potential U_C, the van der Waals component U_{VdW} and the resultant DLVO potential U_{DLVO}, for a pH of 4.5 and typical experimental NaCl concentrations of (a) 0.15 M, (b) 0.25 M and (c) 0.5 M.

strength of the buffer solution must be taken into account. The total ionic strength is given by $I_{total} = \frac{1}{2}\sum_i (c_i z_i^2)$, where c_i is the concentration of ions, so the Debye screening length could be re-written as:

$$\frac{1}{\kappa} = \left(\frac{\epsilon\epsilon_0 k_B T}{2e^2 I}\right)^{\frac{1}{2}}, \tag{5.19}$$

The DLVO prediction for the protein interaction potential for the case of lysozyme on the addition of NaCl is illustrated in figure 5.4 for pH= 4.5, where the Hamaker constant $A = 8.3k_BT$ [71], and the charge $Q = 11.4$e [50]. For the Maple code used to calculate the DLVO potential see appendix A. Predictions of the Coulomb and Van der Waals components to the potential are shown, together with the resultant DLVO potential for typical experimental salt concentrations of (a) 0.15 M, (b) 0.25 M and (c) 0.5 M [71]. The DLVO interaction potential changes from repulsive to attractive as the salt concentration increases.

The DLVO pair potential $U_{DLVO}(r)$ can be used to calculate the second virial coefficient B_2, equation 5.16. However, the continuum approximation upon which $U_{VdW}(r)$ is based breaks down at atomic dimensions. This is reflected in the divergence of the integral if the lower limit is $r = 2R$. i.e. the model no longer functions when the particles touch. Therefore the lower integration limit must be taken as $r = 2R + \delta$. Consistency demands that the hard sphere interaction radius is taken to be $2R + \delta$. The value of δ used would depend on the system

under consideration, for lysozyme on the addition of NaCl a value of $\delta = 0.1437$nm was used, following the approach of Poon *et.al.* [71]. The successes of using the DLVO potential as a model of the protein interaction potential in this case are described in section 5.8.

On closer consideration of figure 5.4, the electrostatic repulsion even at experimentally low salt concentrations (see phase diagram in [71], and chapter 10) is less than $1k_BT$. This is consistent with the favourable crystallisation window at small but *negative* B_2, implying the overall potential must be attractive before crystallisation will begin. It was noted by Broide *et.al.* [12] that the electrostatic repulsion predicted in the DLVO potential is not sufficient to stabilise the protein against aggregation, and they speculate that the repulsive hydration force may be relevant.

Other possible interactions between protein molecules are not included in the DLVO potential. The non-polar groups of some amino acids in a protein in aqueous solution are hydrophobic. Although the protein folds in such a way as to minimise the number of hydrophobic groups on its surface, there are some hydrophobic patches on the surface of proteins. Hydrophobic interactions which will arise from the interaction of these hydrophobic groups are neglected in the DLVO potential. The use of a Hamaker constant that has been determined by scattering measurements provides something of a cheap fix, as it would incorporate other forces between the proteins as well as the Van der Waals dispersion forces. However, as other parameters in the system such as temperature are varied, the strength and range of interactions that are not explicitly included in the DLVO potential might change, as discussed further in chapter 10. This would change the protein interaction potential in a way that is not predicted by the DLVO model.

Indeed, the DLVO potential cannot account for all the effects observed in protein solutions. Most globular proteins exhibit a non-crystallisation boundary above which crystallisation is suppressed, and the protein comes out of solution as various forms of amorphous aggregates [63, 70, 104]. This non-equilibrium behaviour can not be modelled using the DLVO potential. Furthermore other effects such as salting-in and the Hofmeister series cannot be explained using the DLVO model. I shall go on to describe these effects in the following sections.

5.6 Salting-In

So far only salting-out effects in protein solutions have been discussed. That is, the protein is assumed to be stable in solution with no salt, and as salt is added the protein comes out of

solution, either in the form of crystals or as various other forms of aggregates. However, for some proteins the opposite effect is observed, where salt needs to be added before the protein can be stable in solution. Thus adding salt encourages the protein to go into solution rather than bringing it out. This effect is called salting-in, and is not predicted by DLVO theory. However a recent description of charged colloidal particles by Warren [111] has predicted regions of instability at very low ionic strengths. This prediction was discussed in detail in chapter 4.7, and may have some relevance to the salting-in of some proteins at low ionic strengths.

5.7 The Hofmeister Series

Franz Hofmeister first described the different effects of neutral salts on the solubility of proteins in 1888. Since then they have been extensively studied, but are yet to be fully understood [19, 14].

Early studies showed that protein solubility depended on the type of salt used [14]. The Hofmeister series, shown in figure 5.5, shows the difference in the minimum concentration of various neutral salts required to precipitate a given protein from aqueous solution. The Hofmeister series would predict that the solubility of a protein will be at the lowest salt concentration for the most efficient salting-out salts (to the left of figure 5.5).

Hofmeister effects are not only manifested in protein solubility, but by many different measurements including protein conformational stability, the dielectric relaxation time of water, and polymer cloud points (for a full discussion see [19]). Different measurements of the Hofmeister series generally give a similar, characteristic ranking order (but with slight alterations).

	(SALTING-OUT)										
Anions:	F^-	PO_4^{3-}	SO_4^{2-}	CH_3COO^-	Cl^-	Br^-	I^-	CNS^-			
Cations:	$(CH_3)_4N^+$	$(CH_3)_2NH_2^+$		NH_4^+	K^+	Na^+	Cs^+	Li^+	Mg^{2+}	Ca^{2+}	Ba^{2+}
					(SALTING-IN)						

Figure 5.5: Schematic illustration of the Hofmeister series, taken from [14]

It is interesting to compare the Hofmeister series to the difference in experimentally determined crystallisation boundaries of proteins on the addition of different salts. For some proteins the effect of salts is in agreement with the Hofmeister series (for example the protein *hypoderma lineatum* collagenase) [14]. However, for lysozyme at pH 4.5 the effects of different salts are

in the reverse order to the Hofmeister series, implying the relative effectiveness of the salts to promote protein crystallisation is dependent on the net charge of the protein: for acidic proteins it follows the Hofmeister series but for basic proteins the order is reversed.

Using a simple DLVO potential no such series would be predicted. The Hofmeister series has been linked to a variety of effects including water solvation, water structure, and ion-dipole interactions [14]. A recent publication by Bostrom *et.al.* [13] suggests the failure of DLVO to capture the Hofmeister (and other) effects in biological systems may be because the theory ignores the dispersion forces acting on the ions. However a complete interpretation of all the Hofmeister effects has yet to be given.

5.8 The Lysozyme-NaCl System

In this work the phase behaviour of the globular protein lysozyme is studied on the addition of NaCl. There have been a number of studies of this system, mostly concentrating on the equilibrium crystallisation boundary of lysozyme.

Poon *et. al.* [71] studied the phase behaviour of lysozyme on the addition of NaCl in a range of solutions of different pH. Using the DLVO potential to model the lysozyme pair potential, they found a universal crystallisation boundary for lysozyme in different pH solutions when the data is scaled by the salt concentration and normalised by the square of the charge at the appropriate pH, figure 5.6.

This c_s/Q^2 scaling is shown to map on the the B_2 scaling described by George and Wilson [31], and the conditions for crystallising lysozyme using NaCl at any pH are within the crystallisation window described by these authors. Thus for lysozyme, as well as a variety of other globular proteins, the fluid-crystal coexistence boundary is *universal* if $U(r)$ is quantified by the second virial coefficient, $B_2 = 2\pi \int_0^\infty \left(1 - e^{-U(r)/k_BT}\right) r^2 dr$.

The situation is quite different when we turn to *non-equilibrium* behaviour. There is a non-crystallisation boundary above which the proteins form various types of non-equilibrium aggregates instead of the equilibrium crystals. It has been suggested that this non-crystallisation boundary can be associated with a metastable gas-liquid binodal within the fluid-crystal region of the phase diagram [70], as is the case for colloid-polymer mixtures at size ratios $\xi < 0.3$ (chapter 3.3.6 and 3.2).

There have been detailed reports of gas-liquid phase separation [106, 63, 44, 12], and it has been suggested that a metastable gas-liquid binodal may be used to *enhance* protein crystal growth

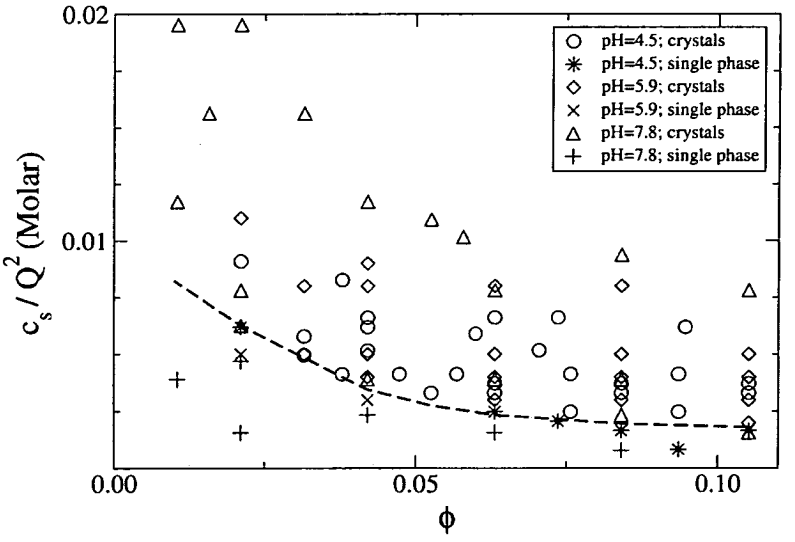

Figure 5.6: Phase diagram of lysozyme on the addition of NaCl at pH= 4.5, pH= 5.9 and pH= 7.8, in the scaled (c_s/Q^2, ϕ) plane, taken from [71].

[114] as well as inhibit it. Furthermore, various amorphous aggregates have been reported, including 'oily drops' of uncertain structure and origin [104, 52] and occasionally gelation [63, 51]. However, no comprehensive study of the non-equilibrium behaviour of protein solutions exists.

5.9 Summary

In this chapter the principles of buffer action have been outlined. The application of the DLVO potential to protein solutions has been discussed and its successes and failures highlighted. Finally the phase behaviour of proteins, in particular the lysozyme-NaCl system studied here, have been discussed.

In this and the preceding three chapters the current understanding of the interaction potential and phase behaviour of colloid-polymer mixtures, charged colloidal suspensions and protein solutions, has been discussed. The experimental techniques used in this work will now be described.

Chapter 6

Experimental Techniques

6.1 Introduction

In this chapter the experimental techniques used to study the phase behaviour of colloid-polymer mixtures and protein solutions are outlined. Firstly, the basic principles of microscopy are described, followed by the modifications that lead to the confocal microscope. Secondly, the principles of nuclear magnetic resonance are discussed.

6.2 Microscopy

6.2.1 Basic Principles

The eye is the most efficient image processing system there is. A sharp image is provided by the flexible lens, the focal length of which is changed by muscles, so that focusing is possible on any subject at distances between $\sim 20cm$ and infinity. However, if we want to look at something with dimensions of micrometres the viewing angle becomes very small, so we are unable to see any detail. A single lens, figure 6.1, can magnify up to $\sim 10\times$, but to achieve higher magnification a microscope is needed. In this section I give a non-mathematical introduction to the principles of microscopy. For mathematical details see [23, 21, 62, 56], and for further practical details consult references [11, 84].

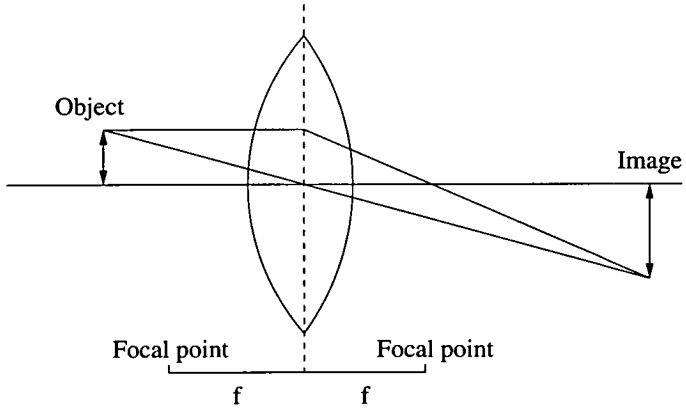

Figure 6.1: Magnification by a converging lens of focal length f.

The Optical Bright Field Microscope

In a compound microscope several lenses are arranged one behind another, so that the magnifying effect is multiplied. The classic microscope magnifies in two steps: the objective produces a

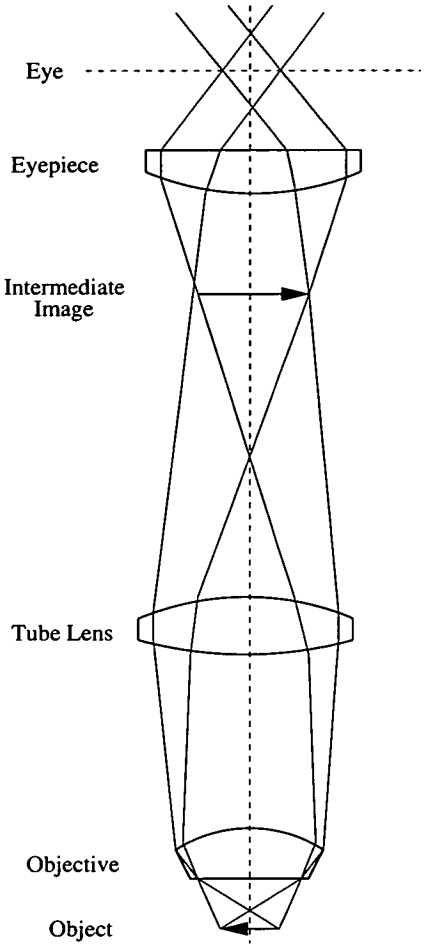

Figure 6.2: Magnification by an infinite tube length compound microscope.

magnified image of the object in the intermediate image plane, and the eyepiece then magnifies this intermediate image.

A third step is included in the infinite tube length compound microscope: a tube lens is added to support the objective. The objective projects a real magnified image at an infinite distance. Therefore, the light rays originating from one point of the object run parallel behind the objective. The tube lens then produces a magnified intermediate image from these parallel beams. The eyepiece serves as a magnifying lens to make the intermediate image further magnified to the eye. Figure 6.2 shows how light is emitted from the object and processed in the three lenses.

The traditional compound microscope (which does not incorporate the tube lens) uses the objective to form a real magnified inverted intermediate image at the front focal plane of the

eyepiece, which in turn forms a further magnified, still inverted, final image at infinity. Having the image at infinity means that the eye of the observer can be relaxed when focusing on the final image. With this two lens system, maintaining the correct distance between the lenses is critical. However, using an objective which forms an image at infinity and adding a tube lens behind it to form a real intermediate image, means that the exact axial position of the objective becomes relatively unimportant, and focusing can be achieved by moving the objective alone.

The overall magnification of the infinite tube length compound microscope is built up in three steps: transverse (objective) magnification, visual (or eyepiece) magnification, and the tube lens factor. The transverse magnification is provided by the objective, and is equal to the ratio of the image size to the object size, $M_{OB} = \frac{imagesize}{objectsize}$. The eyepiece magnification M_{EP} compares the angular size of the image with the angular size of the object when viewed unaided. The tube lens magnification is measured in terms of the tube lens factor Q. The total magnification of the microscope is the product of these three effects.

$$M = M_{OB} \times Q \times M_{EP} \tag{6.1}$$

However, magnification alone is not enough, it is the resolution of the microscope that determines what is seen. Resolution is defined as the least distance between two points at which they can still be recognised as two separate entities. The resolving power of a microscope cannot be increased indefinitely because it is critically limited by two factors, the light gathering power (described by the numerical aperture) of the lens and the wavelength λ of light used.

Numerical aperture (NA) can be thought of as the size of the cone of light coming from each point in the specimen that can get into the lens, figure 6.3, and is given by equation 6.2:

$$\mathrm{NA} = \mathrm{n} \times \sin\alpha, \tag{6.2}$$

where n is the refractive index of the medium between the specimen and the lens and α is the angle between the edge of the cone of illumination and the vertical.

If the medium between the specimen and lens is air, which has a refractive index of $n \simeq 1.0$, then the maximum possible numerical aperture will be $NA = sin\alpha$. However, the resolving power can be increased by using an immersion liquid between the objective and cover slip. An oil is used with a refractive index $n = 1.515$, matched to the refractive index of glass. All refraction on the path from the object to the objective is eliminated, and a higher numerical aperture is achieved.

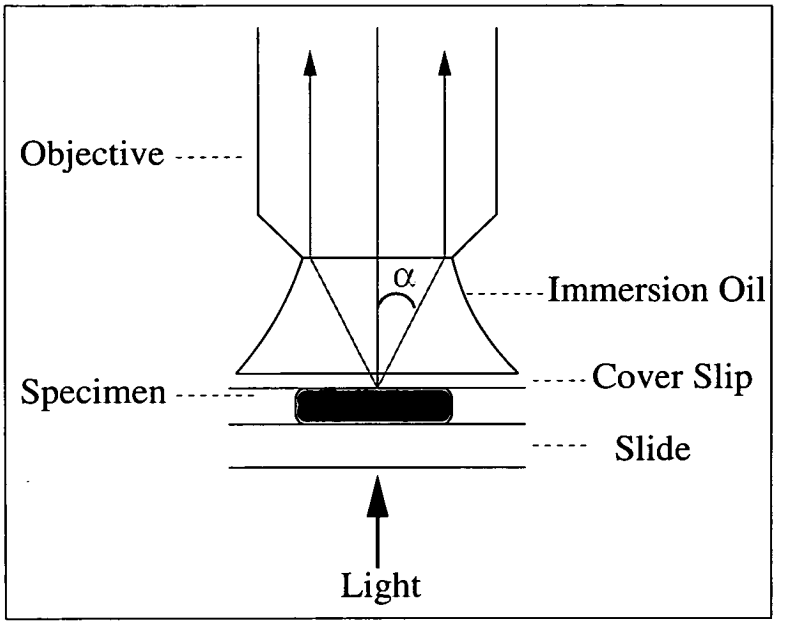

Figure 6.3: Illustration of the numerical aperture of an objective lens [84].

When a light wave passes through a circular aperture of finite diameter the light will be diffracted. This means that a point object will not result in a point image, but rather the interference maxima and minima will form a diffraction pattern known as the point spread function. For an imaging system with circularly symmetric pupils this is a concentric circular pattern known as the Airy disk.

Two completely separate points would produce two such independent diffraction patterns. If the point objects are brought closer together, then at some stage the Airy disk patterns overlap so much that it is not possible to say whether it is one object or two that is being imaged. Lord Rayleigh established an arbitrary criterion for determining resolution in this case when he said that resolution occurs when the first dark ring of one Airy disk coincides with the centre of the second. This is illustrated in figure 6.4, showing the intensity across the Airy disk pattern for two points that are just resolved. This minimal separation in the object plane (i.e. the resolving power) is given by:

$$r \simeq \frac{0.61\lambda}{nsin\alpha}, \tag{6.3}$$

where λ is the wavelength of the light. From this expression the two limiting factors of microscope resolution can be considered. The resolving power is dependent on the wavelength of light used. If the wavelength of light is made shorter, the distance between the interference

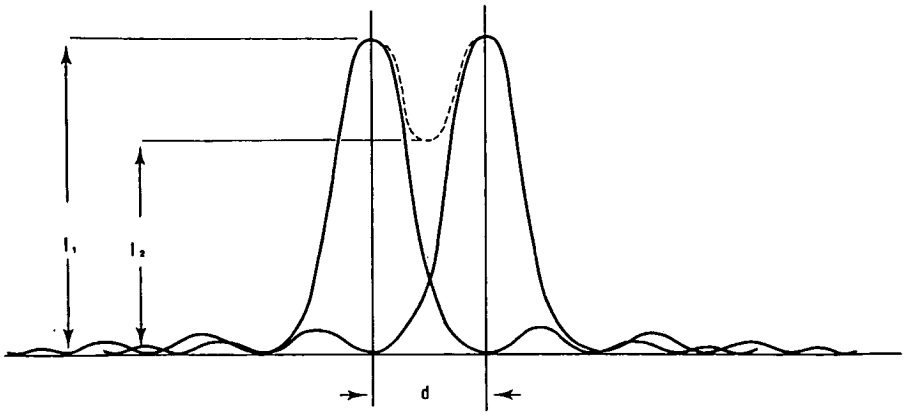

Figure 6.4: Diagram of the intensity across the Airy disk pattern of two points separated by a distance d just satisfying the Rayleigh criterion and hence just resolved. I_1 represents the intensity of each central maximum and I_2 the intensity of the resultant central trough.

maxima and minima is decreased, and so the two separate points can be distinguished when they are closer together. But, of course, there is a limit to how short the wavelength of light can be made. The numerical aperture of the objective, $nsin\alpha$, also limits the resolving power of the microscope. In order to distinguish the two points as separate, at least two primary maxima must enter the objective and interfere. As the two points are brought closer together the angular separation between their diffraction maxima increases and may not fall within the acceptance angle of the objective. In this case they will not be distinguished as two separate points.

Kohler Illumination

Kohler illumination is the basic mode of operation for the transmitted light microscope. It is a method for setting up the microscope for bright field illumination, which is designed to produce a large area of even illumination from a light source that need not itself be homogeneous. There are two lenses placed behind the objective. A collector lens is attached to the front of the lamp housing to collect as much as possible of the lamp light. A condenser lens then focuses a cone of light of uniform intensity onto the specimen.

To understand how Kohler illumination works, it is useful to consider two sets of light rays that coincide but do different jobs; the illuminating rays and the image forming rays, figure 6.5.

Consider first the illuminating rays, whose purpose is to form a wide area of even illumination over the sample. Light from a point on the bulb filament is focused to a point at the condenser

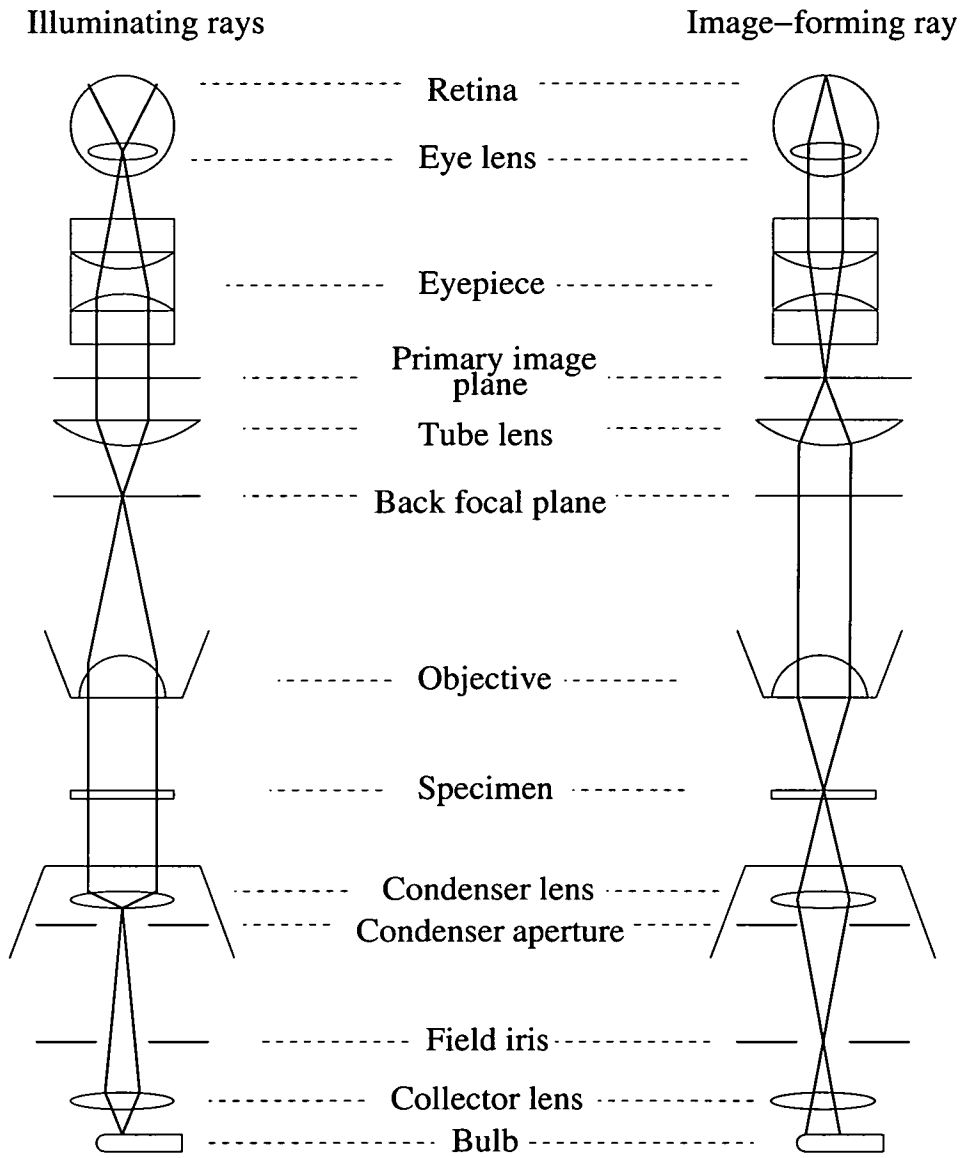

Figure 6.5: Kohler illumination. The illuminating and images forming rays are shown separately.

aperture. Meanwhile, at the field aperture there is just a wide area of illumination, not a focused image. From the condenser aperture the light is next focused at a point inside the objective called the back focal plane. As before at the intermediate position (this time the specimen) there is a wide area of illumination. The final point at which the light from the filament is focused is the eye lens, which projects the wide area of illumination onto the retina.

Consider now the image forming rays. The specimen should now be illuminated by an even source of light. Light coming from the specimen will be focused by the objective at tube lens at the primary image plane. At this point it is magnified but upside down. The eyepiece lenses turn it the right way up again, and form an image a small distance from the top lens of the eyepiece. Looking at this point, a focused image will appear on the retina, and the specimen will be seen. The procedure for setting up Kohler illumination is as follows:

1. Move the condenser close to the object plane.
2. Focus on the object plane.
3. Close the field iris enough to obstruct part of the field of view.
4. Focus to form a sharp image of the field iris, and if necessary use the centring screws on the condenser to centre the image.
5. Open the field iris so that slightly more than the area of interest of the object is illuminated.
6. Adjust the size of the condenser iris till maximum contrast is reached, typically illuminating about 80% of the pupil diameter.

This method of illumination, combined with the use of immersion oils, can resolve particles on the sub-micron scale, and if the sample has good contrast high quality optical micrographs can be produced [23, 11, 84]. Colloidal suspensions with closely matched refractive indices of particles and medium produce very low contrast images under bright-field methods. However, if they are not index matched the samples are too turbid for optical measurements. Confocal microscopy and fluorescence can be used to overcome these problems.

6.2.2 The Confocal Microscope

In this section the principles of confocal microscopy are outlined, and the main advantages over conventional optical microscopy are highlighted. Further information on the practical and mathematical details is given by T.Wilson [112].

Fluorescence Microscopy

Some molecules absorb and emit light at different frequencies. This is called fluorescence. The molecules absorb at high energy and become excited. Some of this energy is lost non-radiatively, and the molecule then emits a photon of lower energy to return to its ground state.

Figure 6.6 shows an illustration of the fluorescence microscope. The microscope uses a dichroic (dichromatic) mirror which reflects light shorter than a certain wavelength, and passes light longer than that wavelength. Thus your eye only sees the emitted light from the fluorescent dye and not the scattered incident light.

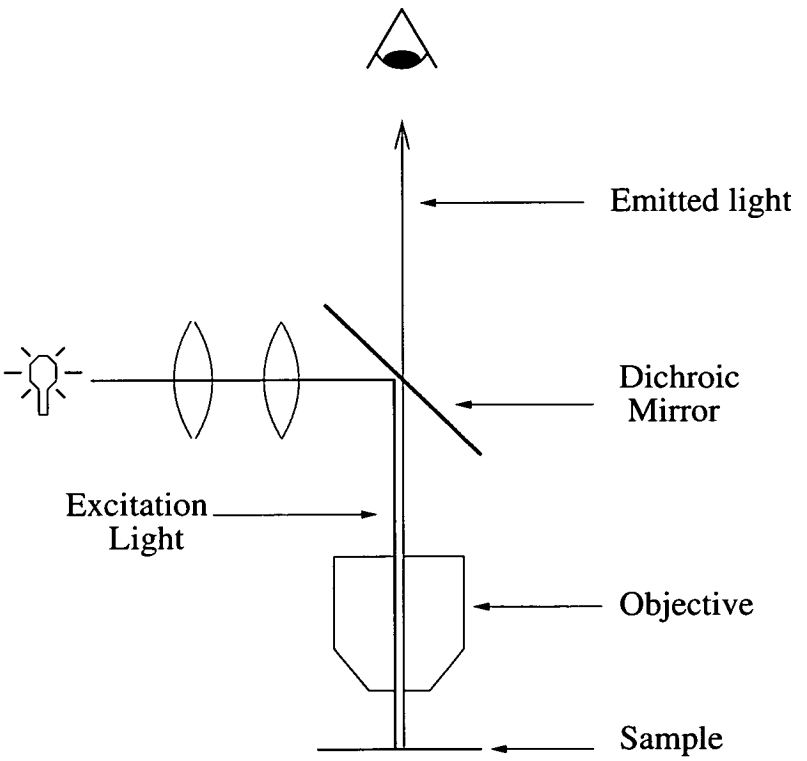

Figure 6.6: The fluorescent microscope.

The Scanning Microscope

The conventional microscope images the entire object field simultaneously. This is a very severe requirement for the optical components. However, we can relax this requirement if we no longer try to image the whole object at once. The limit of this is to obtain an image of only one object point at a time. In this case, all we ask of the optics is to provide a good image of

one point. In order to build up a picture of the entire field we must scan across the sample.

The essential components in a scanning microscope are some form of mechanism for scanning the light beam (usually a laser) relative to the specimen, and appropriate photo-detectors to collect the reflected or transmitted light. It is usual to use a computer both to drive the microscope and display and collect the image. The image is obtained in electrical form, allowing image enhancement processes such as contrast enhancement to be undertaken.

In the following sections it will be shown that relaxing the requirement to simultaneously image the whole object leads to a simple modification of the optical system resulting in the confocal scanning microscope.

Enhancing Resolution

Consider first a simple model of how image formation takes place in a conventional microscope. From here an equivalent form of (conventional) scanning microscope will be described, from which follows the modifications which lead to the confocal scanning microscope.

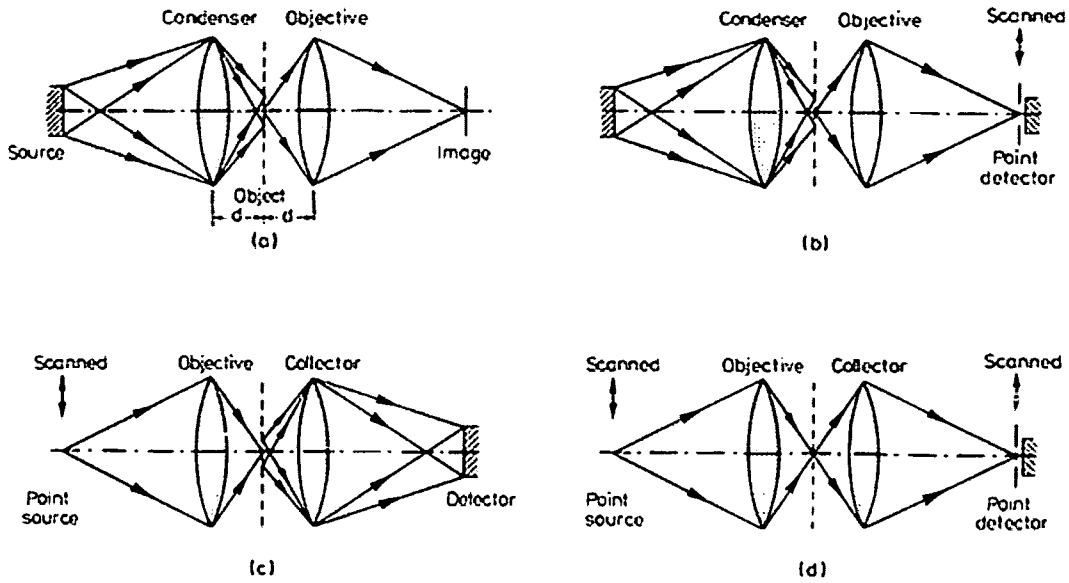

Figure 6.7: Illustration of the development of the confocal scanning microscope from the conventional microscope, (a) shows the optical system of a conventional microscope, (b) a form of the conventional scanning microscope, (c) Another form of conventional scanning microscope, and (d) The confocal optical system. Taken from [112].

Figure 6.7(a) shows the key elements of the optical system of a conventional microscope. The object is illuminated by a patch of light from an extended source via a condenser lens. The

condenser lens provides a wide area of even illumination at the object. The illuminated patch of the object is focused by the objective lens into the image plane, and then viewed via an eyepiece. The resolution results primarily from the objective lens, and the condenser is much less important.

A conventional scanning microscope could be built by scanning a point detector through the image plane, so that the image is built up point by point, figure 6.7(b). Figure 6.7(c) shows an analogous system which uses a point source and a large area incoherent detector. The objective lens probes the specimen point by point with a finely focused spot of light while the second lens merely serves to collect all the transmitted light. This collector lens is analogous to the condenser lens in conventional microscopy, and plays only a minor role in determining the resolution.

To make the second lens contribute to the resolution we need to make it an imaging lens rather than merely a collector lens. This is achieved by using a point detector rather than a large area one. This is the form of the confocal scanning microscope, figure 6.7(d). Light from the point source probes a very small region of the object, and the point detector ensures that only light from that same very small region is detected. In the figure, one would have to scan the source and detector together, but in practise it may be more convenient to scan either the light beam or the object.

In this confocal configuration both lenses play an equal role in the imaging. The point detector has caused the second lens to image only the region of the object probed by the first lens. Since the two lenses are employed simultaneously to image the object, the resolution will be improved. Essentially, the effective point spread function of the confocal imaging system is given by the product of the point spread functions of the two lenses [112]. The resultant resolution is increased at the expense of the field of view, and a wide field of view can then be regained by scanning.

Optical Sectioning

As well as enhancing the lateral resolution the confocal microscope also enhances the longitudinal resolution, leading to the property of depth discrimination known as optical sectioning. One of the problems of regular fluorescence microscopy is that all of the sample is illuminated and fluoresces, which results in a background haze in the image. However, a confocal microscope solves this problem.

The principle of optical sectioning can be understood from figure 6.8. The bold vertical line represents the focal plane of the lens, and the full lines show the optical path when an object feature lies in this focal plane. Incoming light is focused onto the object feature that lies in the focal plane. The transmitted light (or, in the case of fluorescent microscopy the emitted light) from this feature is then focused onto the pinhole (or point detector) and detected.

Consider now an object feature that lies on the vertical dashed line, out of the focal plane of the lens. The emitted light from this feature arrives at the pinhole as a defocused blur, only the central portion of which is detected and contributes to the image. In this way the system discriminates against features which do not lie in the focal plane of the lens.

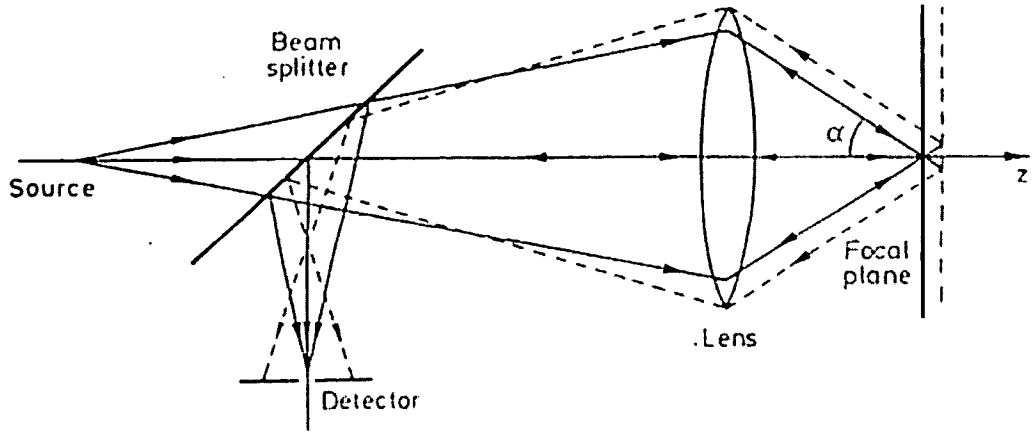

Figure 6.8: The optical sectioning property of the confocal microscope [112].

Putting all this together we can see how the confocal microscope works, figure 6.9. The laser light reflects off a dichroic mirror. From there two mirrors which are mounted on motors scan the laser across the sample. The laser beam is focused by the objective to illuminate one point of the object. Dye in the sample fluoresces and the emitted light is focused by the objective and gets descanned by the same mirrors. The emitted light then passes through the dichroic mirror and is focused onto the pinhole. The illuminated point (on the object) and the observed point (the image) lie on conjugate planes, i.e. they are focused onto each other. Light coming from planes above or below the focal plane will be out of focus when it reaches the pinhole so most of it cannot pass through and so does not contribute to the final image. The light that passes through the pinhole is then measured by the detector. There is never a complete image of the sample since at any given instant only one point in the sample is observed. The detector is attached to a computer which builds up the image one pixel at a time.

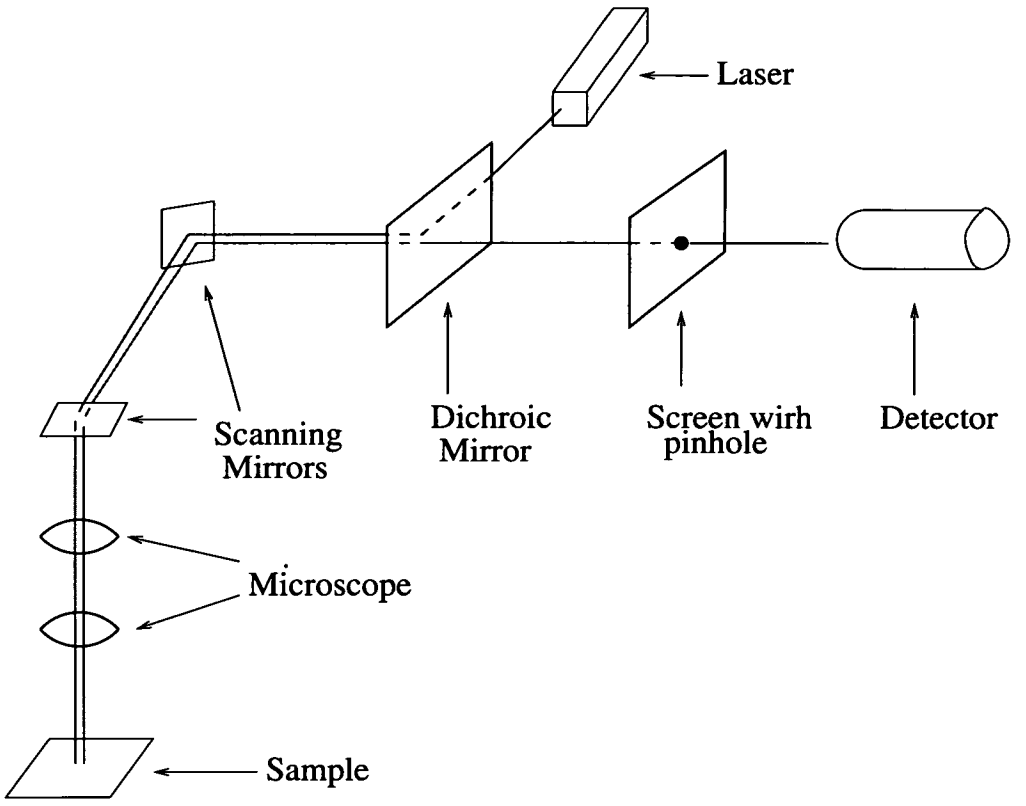

Figure 6.9: The confocal microscope.

The confocal microscope thus allows the imaging of one in-focus plane with a much suppressed background haze from out-of-focus information from surrounding panes, and at the same time provides enhanced lateral resolution. Optical sectioning has become the major motivation for using confocal microscopes. By scanning many thin, in-focus, sections a very clean 3-D image of the sample can be built up.

6.3 Nuclear Magnetic Resonance

Spectroscopy is the energy resolved study of the interaction between matter and radiation. Nuclear Magnetic Resonance Spectroscopy (NMR) uses the transitions that occur when nuclei are placed in a magnetic field. The end result of an NMR experiment is a spectrum, which can be described in terms of the frequency, intensity, and shape of the spectral lines. In this section the basic principles of nuclear spin and magnetic moments are outlined, and how these are affected when placed in a magnetic field is discussed. The experiments through which results are obtained using NMR spectroscopy are then described.

6.3.1 Nuclear Magnetic Effects

In this section a semi-classical picture of the interaction between nuclei and an applied magnetic field is presented. Consider first a single atomic nucleus. This nucleus has an intrinsic angular momentum which is usually referred to as spin, and an associated nuclear magnetic moment. The spin quantum number is I, and the spin is restricted to $(2I + 1)$ possible values. The nuclei used in an NMR experiment (e.g. hydrogen) have a spin angular momentum quantum number of $1/2$ and so the spin of each nuclei is restricted to two possible values. The energy of the spin values is degenerate, but the application of a magnetic field will split the energy, resulting in $(2I + 1)$ separate energy levels. Let the applied field be B_0, figure 6.10(a). In a semi-classical visualisation, the magnetic field causes precession of the spin axis of the nucleus about the direction of the field. The precessional motion occurs at a rate called its Larmor frequency, which depends on the type of nucleus and is directly proportional to the strength of the applied field. Information about the molecule can be gained by irradiating it with electromagnetic radiation with a frequency equal to the Larmor frequency. This induces transitions between the energy states in the following way.

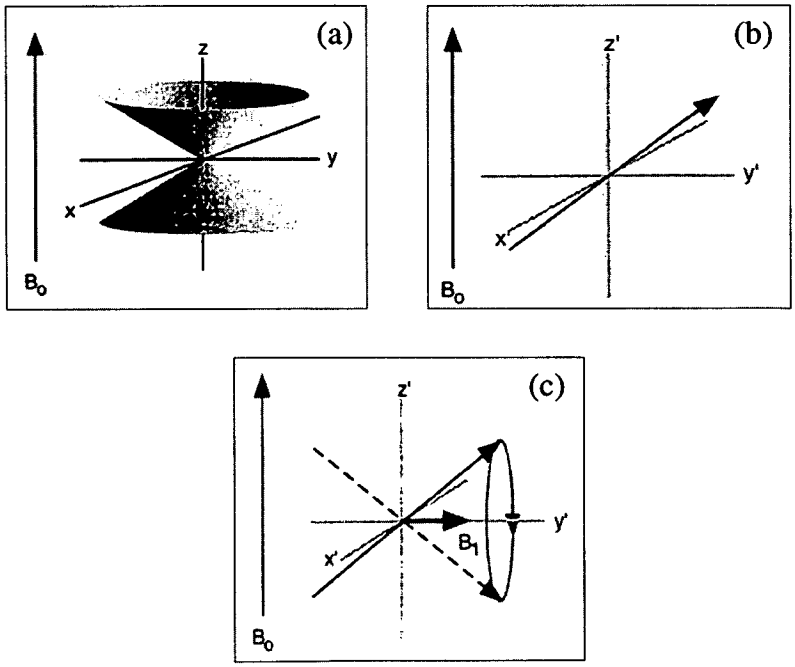

Figure 6.10: Illustration of (a) Precessing spin viewed in the laboratory (stationary) frame of reference, and (b) Precessing spin viewed in the rotating frame of reference so it appears stationary. The application of a rotating magnetic field B_1, which appears stationary in the rotating frame of reference, induced transitions between the two allowed states, (c). Taken from [83].

As each individual nucleus precesses about B_0 its magnetic moment can be resolved into a z-component which is constant and an $x - y$ component that rotates at the Larmor frequency. If a second field B_1 is applied, which is perpendicular to and rotating (with the nucleus) about the z axis of B_0, then the spin axis of the nucleus will start to precess about the field B_1, figure 6.10(c). Such a field can be produced by simply applying electromagnetic radiation at the Larmor frequency: B_1 will be one of the components of this radiation. As the spin precesses about B_1 it will pass between the upper and lower energy levels, undergoing a transition between its two allowed orientations.

The collective behaviour of a large number of nuclei together produces observable effects. In the absence of a magnetic field, the nuclear spins are randomly aligned, figure 6.11(a). When the magnetic field B_0 is applied, the spins become aligned in the direction of the field, figure 6.11(b). At equilibrium the populations of the two energy states are nearly equal, but a small excess in the lower energy level results in a net magnetisation in the z direction called M_z. There is no net magnetisation in the $x-y$ plane since these components are randomly arranged.

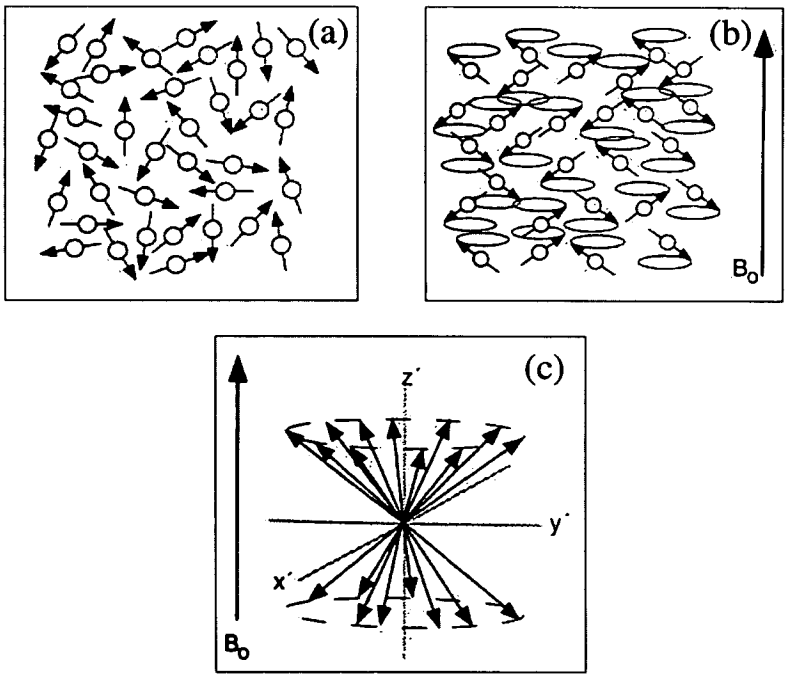

Figure 6.11: Population of spins:top, disordered in the absence of a magnetic field; middle, aligned and precessing in an applied field; bottom, brought to a common origin. Taken from [83]

Now apply a short, intense pulse of radiation B_1 at the Larmor frequency. The nuclei will undergo a large number of transitions between their two energy states, with a transition probability that is the same in both directions. This has two effects on the system. Firstly, more

transitions will be from low to high energy, because there were more nuclei in the low state to begin with. The population difference will be reduced or inverted, as will M_z. Secondly, the spins start to precess in phase with each other. This effect is called phase coherence, and results in a net magnetisation in the $x - y$ direction, M_{xy}, which rotates in the $x - y$ plane at the Larmor frequency, figure 6.12. An NMR spectrometer detects this rotating magnetisation and its decay.

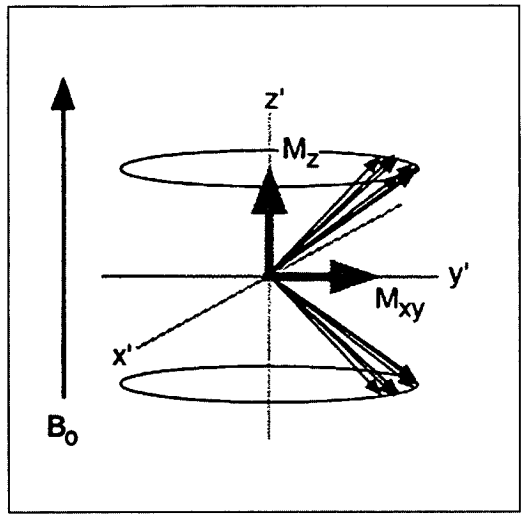

Figure 6.12: Magnetisation M_{xy} produced by phase coherence between spins after an applied radio frequency pulse. Taken from [83]

Thus the pulse has reduced or inverted M_z and created M_{xy}. The resultant magnetisation can be thought of as an angle away from the z axis. For example, a 90 degree pulse would result in zero M_z and non zero M_xy, and 180 degree pulse inverts M_z and has zero M_{xy}. When the pulse ends, the system relaxes to its original state.

6.3.2 Principles of relaxation

After the system has been perturbed by a pulse, it relaxes to its equilibrium state. M_z returns exponentially to its original state in a characteristic time T_1, called longitudinal relaxation. M_{xy} decays exponentially to zero by transverse relaxation with a characteristic time of T_2.

Longitudinal Relaxation

The Boltzmann equilibrium nuclear magnetisation is represented by M_0. Any deviation of the longitudinal magnetisation M_z away from the equilibrium value M_0 is followed by an

exponential recovery according to the equation:

$$(M_z - M_0)_t = (M_z - M_0)_0 \exp \frac{-t}{T_1}, \tag{6.4}$$

where T_1 is the *longitudinal* relaxation time [86]. The relaxation of the magnetisation requires a transition between the two energy levels of the nucleus, which returns it to its original energy level. The energy is transfered from nuclear spins to the sample lattice. The transition between energy states requires a magnetic field at the nucleus fluctuating at the Larmor precession frequency. For relaxation, this field originates from magnetic dipoles in the sample lattice which is in thermal agitation. The rotation of the molecules in the sample induces a magnetic field fluctuating at a frequency approximately equal to the Larmor frequency, which induces transitions between the two energy levels. The energy is transfered from the nuclear spins to the environment and the magnetisation relaxes back to its original value. In general a short T_1 (i.e. fast relaxation) favours sensitivity.

Transverse relaxation

Small magnetic interactions between the nuclei interfere with the exact nuclear precession frequencies, so spins that precess in phase at time zero gradually lose their phase coherence with a time constant called the spin-spin relaxation time T_2. This relaxation time is the decay constant of *transverse* nuclear magnetisation. T_2 can be identified as the inverse of the natural line width, so a very short T_2 relaxation time would lead to very broad line widths in the NMR spectrum.

It is important to make the distinction between the longitudinal (T_1) and transverse (T_2) relaxation times. T_1 is the spin-lattice relaxation time, which is the lifetime of the spins in a given excited state, and measures the time constant for the transfer of energy from the spin system to the environment. However T_2 is the spin-spin relaxation time, dependent on how fast spins can be exchanged between nuclei, and there is no energy change in the spin system since interactions between spins maintain a true thermal equilibrium with the spin system.

Sometimes the same physical mechanisms determine both T_1 and T_2. However, there are often *additional* mechanisms for spin-spin relaxation, loosely referred to as T_2 mechanisms. The most important of these is chemical exchange, where an atom moves from one chemically distinguishable site to another, and is replaced by a similar atom whose precession phase is random.

6.3.3 NMR experiments

Collecting an NMR Spectrum

In an NMR experiment a pulse is applied, and the resultant magnetisation M_{xy} is detected via a small wire coil near the sample, in which a current will be induced and decay as the system relaxes back to equilibrium. The signal is called the Free Induction Decay FID.

The Larmor frequency of a given nucleus is proportional to the total magnetic field at the nucleus. If the nucleus is surrounded by an electron cloud, the motion of the electrons will alter the local field at the nucleus. The exact magnitude of this shielding depends on the distribution and density of the electron cloud, so that the same nucleus in a different chemical environment will have a different Larmor frequency. Therefore the FID is usually a mixture of many different frequencies corresponding to the different chemical environments of the nuclei. A Fourier transform of the FID gives a spectrum, a plot of intensity vs frequency, in which the Larmor frequency of each nuclei corresponds to a different peak. The line width will depend on the rate of decay, which is determined by T_2, where fast T_2 relaxation leads to broad spectral lines.

Analysing Spectra

Having collected and transformed the FID a one-dimensional NMR spectrum is obtained, shown schematically in figure 6.13.

The spectrum is characterised by five parameters:

1. Chemical shift, or position of the resonances on the frequency scale, usually expressed in parts per million of the Larmor frequency.
2. Area under each resonance signal. The area under peak is proportional to the number of nuclei in the sample which contribute to that resonance.
3. Width of the resonances, measured in Hz at half the peak height. The width of the line is proportional to $1/T_2$.
4. Multiplicity of each resonance, that is whether it is a doublet or triplet etc. Due to the interaction between spins which are close together in the same molecule.
5. The separation of the components of each multiplet. This is known as the coupling constant and given the symbol J Hz.

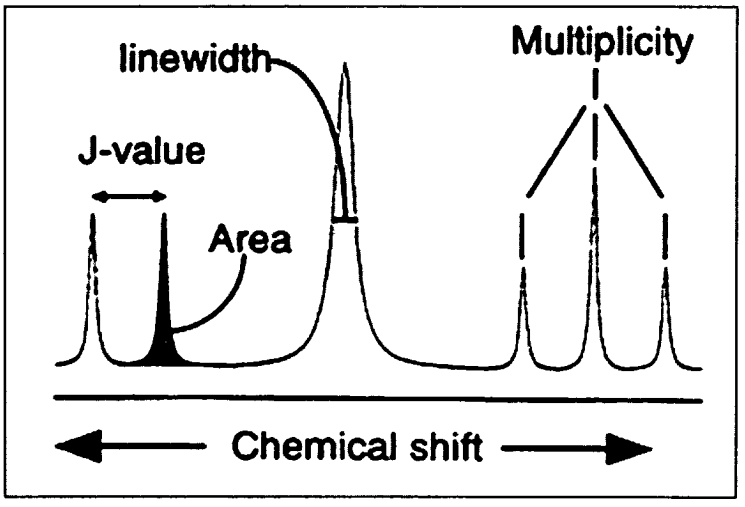

Figure 6.13: The five parameters of a high resolution NMR spectrum, taken from [83].

Measurement and Analysis of Relaxation Times

The longitudinal relaxation time T_1 can be experimentally determined using a method called inversion recovery. A series of pulses are applied separated by a time interval, of the form $180° - \tau - 90°$, where τ is a small time which is varied from one pulse sequence to the next. The first, 180° pulse inverts M_z, which then decays exponentially toward its original value. After time τ the magnetisation will have relaxed to a value M which can be measured by applying a 90° pulse which tips it into the $x - y$ plane so it can be detected. A series of FID's corresponding to different values of τ are accumulated and transformed. In the resulting set of partially relaxed spectra, the size of each individual peak is a function of its own T_1 value. T_1 can be found by equation 6.5:

$$M = M_0(1 - 2e^{-\frac{\tau}{T_1}}), \tag{6.5}$$

which derives from equation 6.4 given that M_0 is a constant and M_z at time $t = 0$ is equal to $-M_0$. Rearranging equation 6.5 shows that the relaxation time T_1 can be determined from a plot of $ln(1 - \frac{M}{M_0})$ vs $\tau(ms)$, where the gradient of the line will be $\frac{1}{T_1}$, equation 6.6:

$$ln(1 - \frac{M}{M_0}) = ln2 - \frac{\tau}{T_1}. \tag{6.6}$$

As well as the traditional uses of NMR spectroscopy, for example providing information about the position of nuclei within a molecule and detecting conformational changes of the molecule,

relaxation times can also provide information about the state of a sample. Typically, large molecules (for example proteins) dissolved in solution have T_1 values of a few hundred ms. However, as the molecules solidify the molecular motions become increasingly restricted, which has two effects on the relaxation. Firstly the molecules spend more time closer together, so they undergo more spin-spin relaxation. Therefore the T_2 values become very short and the observed spectra becomes very broad. Secondly, there is less molecular motion, so magnetic noise (the key mechanism for spin-lattice relaxation) decreases and the T_1 values become longer. Therefore a solid sample would have shorter T_2 (thus a broader spectra) and a longer T_1 than the same molecules in a fluid phase.In this way relaxation time can provide useful information about the state of a sample, which will be discussed in detail in chapter 10.

6.4 Summary

In this chapter the basic principles of conventional microscopy, confocal microscopy, and nuclear magnetic resonance spectroscopy have been outlined. In the following chapters the experimental systems used in this work are characterised and the results presented, firstly for the colloid-polymer mixture studied and secondly for the protein solution.

Chapter 7

Experimental System 1:
Colloid-Polymer Mixtures

7.1 Introduction

Under appropriate conditions, sterically-stabilised spherical colloidal particles can provide good experimental models of hard spheres. This chapter gives details of the different systems used to explore the effect of gravity and charge on the behaviour of colloidal suspensions.

Four colloidal systems were used in this work, two with charged colloids and two with uncharged colloids. Both the uncharged and charged colloids were studied in a density matched solvent and in gravity. In all cases the colloids used were sterically-stabilised poly-methyl-methacrylate (PMMA) colloids and the polymer was linear polystyrene (PS).

The particles were dispersed in solvents of similar refractive index so as to minimise van der Waals interactions and make the sample virtually transparent. Two different solvents were used in this work; *cis*-decalin and cycloheptyl bromide (CHB). The different solvents have the effect of swelling the colloid radius and the polymer radius of gyration by different amounts. In addition to this, it has recently been reported [116] that PMMA colloids carry a charge when suspended in certain organic solvents, including CHB. The charge on the colloids can be screened by the addition of a salt that is soluble in the appropriate organic solvents.

In this chapter each system is characterised by determination the size ratio and charge. The effect of the different solvents used on the particles is discussed. Determination of the final sample composition is described, and finally the errors associated with the sample characterisation and preparation are highlighted.

7.2 Colloid-Polymer Mixtures in *Cis*-Decalin

7.2.1 Colloids

The colloidal particles used in this work consist of nearly monodisperse spheres of fluorescently labelled poly-methyl-methacrylate (PMMA), sterically stabilised by a chemically-grafted monolayer of poly-12-hydroxystearic acid (PHSA) polymer chains. They were synthesised in Edinburgh University School of Physics by Dr. A.B. Schofield. The particles were fluorescently labelled using the dye nitrobenzoxadiazole (NBD), which is excited at a wavelength of 488 nm and emits at a wavelength of 525nm. Figure 1 shows a schematic representation of a particle. The radius of the particles are in the range of $\sim 500 - 700$ nm. The polydispersity varies from batch to batch, and in this work polydispersities do not exceed $\sim 6\%$ unless otherwise stated.

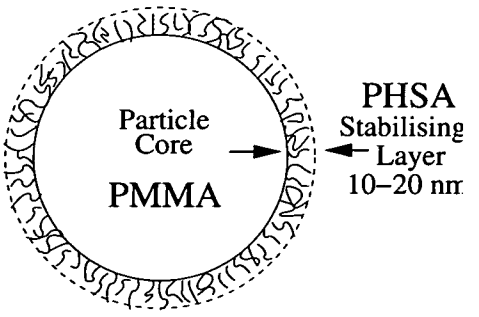

Figure 7.1: Schematic plot of a sterically stabilised PMMA colloid

As made the particles are suspended in a mixture of dodecane and hexane. However, the solutions appear cloudy due to multiple light scattering, which makes visual observations difficult. This mixture of solvents was replaced by solvents with a refractive index closer to that of the particles. A common solvent used for the study of PMMA colloids is *cis*-decalin. This solvent is primarily chosen to ensure the suspension behave as hard spheres. To satisfy this criterion, it has to be a poor solvent for PMMA polymer chains to ensure low swelling of the particle cores, but a good solvent for PHSA to force them into extended conformations. This layer of polymer 'hairs' at the surface provides steric stabilisation resulting in an almost hard sphere inter-particle potential. The solvent's refractive index is then chosen to match the particle. *Cis*-decalin is used for studies conducted in gravity. For studies in a density matched system *cis*-decalin was mixed with cycloheptyl bromide (section 7.3).

The radius of the colloid suspended in *cis*-decalin was found to be 526 nm when measured by optical imaging. This is consistent with dynamic light scattering measurements [67] showing the hydrodynamic radius of the colloids suspended in *cis*-decalin to be 527nm.

7.2.2 Polymer

The non-adsorbing polymer used in these experiments is polystyrene (PS), with a weight-averaged molecular mass of $M_w = 212,400$ g/mol. The behaviour of linear polystyrene in *cis*-decalin has been fully characterised by Berry [10], who performed extensive characterisation of polystyrene solutions.

The theta temperature for a particular solvent represents the temperature at which the steric excluded volume effect (repulsion) and attractions between monomers mutually cancel and the solution is ideal up to 2nd-virial level. At the theta temperature T_θ the polymer can be approximately described by a Gaussian coil. Therefore, to a first approximation the size of the

polystyrene molecule, at T_θ depends only on its molecular weight M_w. For linear polystyrene molecules, Berry has shown that the dependence of the radius of gyration R_g^θ on the molecular weight is given by:

$$R_g^\theta(nm) = 0.0276\sqrt{M_w(daltons)}. \tag{7.1}$$

This is only valid at the theta temperature, which for a solution of linear polystyrene in *cis*-decalin is at $T_\theta = 12.2°C = 285.2K$.

Because T_θ is lower than room temperature (which is typically $22°C$), we need to consider how the increase in temperature affects the properties of the polymer. Above the theta temperature, for a given solvent, the net interaction between polymer segments becomes repulsive; the solvent becomes a 'good' solvent so that the monomers prefer to contact with solvent molecules rather than themselves, and the steric repulsive interaction dominates. This net repulsive interaction swells the polymer, so the coil size of a chain with such an interaction is larger than that of the ideal chain which has no net interaction.

The radius of gyration of the expanded coil is expressed as a function of the Fixman parameter z, which accounts for the monomer-monomer interactions. At the theta temperature, where a polymer coil is at its most ideal, $z = 0$. The rate at which z increases from zero then gives a measure of the polymer non-ideality. It is governed by the molecular weight of the polymer molecule M_w and the temperature T. The expression for z for the case of linear polystyrene molecules suspended in *cis*-decalin is given by equation 7.2:

$$z = 0.00975\sqrt{M_W}\left[1 - \left(\frac{T_\theta}{T}\right)\right]. \tag{7.2}$$

According to Berry [10] the radius of gyration of a polystyrene coil suspended in *cis*-decalin at a temperature T (in Kelvin), to first order in z, is given by:

$$R_g = R_g^\theta\sqrt{1 + \frac{134}{105}z}. \tag{7.3}$$

However, as shown by Berry, this approximation is only accurate up to $z \sim 0.1$. This limits the accuracy of the equation to a small temperature range above the theta temperature from $12.2 - 20°C$, which must be kept in mind. The calculated values of z and R_g for polystyrene of molecular weight $M_w = 212,400$ for a range of temperatures are summarised in table 7.1.

Temp. $T°C$	Temp T $Kelvin$	z	$R_g(nm)$
12.2	285.2	0	12.7
15	288	0.044	13.0
20	293	0.120	13.6
22	295	0.149	13.7
25	298	0.193	14.1

Table 7.1: Radius of gyration for polystyrene in *cis*-decalin

Following this approach the radius of gyration of the PS in *cis*-decalin at room temperature of $22°C$ is found to be $R_g \simeq 13.7$nm. Together with the radius of the colloids which was measured to be 527nm, this gives a size ratio for this system of 0.026.

The molecular weight that has been used up to now M_w is the weight averaged molecular mass of the polymer. However, polymers have a certain degree of polydispersity in their molecular weight. The polydispersity of polymers is normally expressed as a ratio : M_w/M_n, where $M_w \equiv \frac{\overline{M^2}}{\overline{M}}$ represent the weight averaged molecular mass and $M_n \equiv \overline{M}$ represents the number averaged molecular mass. It follows that $\frac{M_w}{M_n} = \frac{\overline{M^2}}{\overline{M}^2}$. By definition the polydispersity in molecular weight σ_M can be written as

$$\sigma_M = \frac{\sqrt{\overline{M^2} - \overline{M}^2}}{\overline{M}} \tag{7.4}$$

Therefore, σ_M is directly related to the ratio M_w/M_n via equation 7.5:

$$\sigma_M^2 = \frac{\overline{M^2}}{\overline{M}^2} - 1 = \frac{M_w}{M_n} - 1 \tag{7.5}$$

The measurements performed by Berry [10] indicate that the relationship $R_g^\theta = 0.0276\sqrt{M_w}$ holds for ratios $M_w/M_n < 1.07$, and that the expansion coefficient R_g/R_g^θ was unaffected by polydispersity. The values of R_g quoted in table 7.1 represent weight averaged radius of gyration. For the polymer used, the value quoted by the manufacturer is $M_w/M_n = 1.06$. The polydispersity in the ideal radius of gyration, assuming a relatively symmetrical and narrow distribution of radii, can be expressed in terms of the polydispersity in molecular weight as [57]:

$$\sigma_{R_g^9} = \frac{\sigma_M}{2} = \frac{1}{2}\sqrt{\frac{M_w}{M_n} - 1}, \tag{7.6}$$

giving a corresponding polydispersity in the radius of gyration as $\sigma_{R_g} \sim 12\%$.

All the measurements performed by Berry were on dilute solutions of polystyrene. One may then ask whether it is valid to assume that the polymer solutions used here are dilute? The polymer overlap concentrations can give an estimate of the concentration at which the polymer is space filling. An approximate value for the polymer overlap concentration c_p^* for this system can be calculated. Assuming that the polymers can be treated as spheres, $c_p^* = \frac{3}{4\pi R_g^3}$. This equation gives the number of polymers per unit volume when the polymer coils fill space. The concentration in mass per unit volume can then be calculated using equation 7.7. As a rough approximation, this tells us that the polymer solution can no longer be treated as dilute as the concentration approaches this value. A thorough discussion on the variation of R_g as the polymer concentration is increased is presented in section 7.3.2.

$$c_p^* = \frac{M_w}{N_A} \times \frac{3}{4\pi R_g^3} = 32.7 mg/ml. \tag{7.7}$$

7.2.3 Sample Preparation

The particles of PMMA are synthesised in a mixture of dodecane and hexane. The refractive index of this mixture is $n \sim 1.40$, which is not close enough to that of PMMA ($n = 1.494$) for optical experiments, due to strong scattering. The suspension medium is therefore replaced by *cis*-decalin, which has a refractive index $n = 1.4810$, by repeated centrifugation of the samples, in between which the supernatant is discarded and replaced by the new chosen solvent.

The samples are centrifuged at a rate of $\sim$ 3000 rpm, and after $\sim 6 - 12$ hours (depending on the size of the colloids) the particles have all settled at the bottom of the cell into a dense sediment, leaving solvent on the top which is easily poured out. The speed is limited by the container used, plastic containers being more robust and less prone to breaking than glass ones.

The volume fraction of the sediment is in the vicinity of a random close packing volume fraction $\phi_{rcp} = 0.64$, although the exact nature of the sediment is expected to be particle size dependent and is not fully understood. Every time the sample is centrifuged a fraction of the solvent stays trapped in the sediment. To obtain suspensions with an almost pure solvent the procedure must be repeated many times until the desired solvent purity is reached. The washing process was repeated until the measured refractive index of the supernatant was unchanged

within experimental uncertainty from one wash to the next. Typically this required 6-7 washes. The final supernatant refractive index was measured using a refractometer ($\lambda = 589.3$ nm) and found to be $n = 1.4781$.

7.3 Colloid-Polymer Mixtures in Density Matched Solvents

7.3.1 Colloids

PMMA has a density of ~ 1.19 g.cm^{-3} [27], which is considerably denser than *cis*-decalin (0.897 g.cm^{-3}). Since the radii of the colloids studied here are large (500 − 700nm) gravity will have a large effect on their behaviour. It is possible to make a colloidal suspension of particles in a solvent of the same density as the colloids themselves. In this way, the effects of gravity can be neglected and the phase behaviour studied in a close to zero gravity system. The solvent used to do this is cycloheptyl bromide, which has a density of 1.289 g.cm^{-3}, and when mixed with *cis*-decalin at a ratio of approximately 4:1 can produce a suspending medium with a density approximately equal to that of the PMMA colloids themselves.

The density of the particles is one of the major quantities needed for the preparation of the samples. Values for the density of bulk PMMA can be found in the literature, and is typically 1.19 g.cm^{-3} for bulk PMMA at room temperature [27]. It is usually assumed that the core of the particles is impenetrable to the solvent (although, if the solvent and colloids have the same density then solvation will not change the density of the particles). However, experimentally different degrees of swelling have been observed depending on the solvent used. In order to quantify this, the degree of swelling of PMMA in the CHB *cis*-decalin solvent was studied by V. Martellozo [57]. An increase in the particle radius of $\sim 3\%$ was found compared to the PMMA colloids in *cis*-decalin alone. It was found that the CHB penetrates the shell (the polymer coating which provide steric stabilisation) and eventually also the core of the colloids. The penetration process took place over the first 2-3 weeks after preparation. The particles then remained unchanged after 1 and 3 months. To ensure the suspensions remained fresh for timescales of months all samples were kept in cold ($\sim 4°C$) and dark conditions (to stop decomposition of the CHB).

It has recently been demonstrated [116] that nearly hard sphere PMMA colloids carry a charge when suspended in certain organic solvents including CHB. Therefore fluorescently labelled PMMA colloids dispersed in a density matched solvent of chb and *cis*-decalin at a ratio of

535nm colloids		660nm colloids	
volume fraction	phase	volume fraction	phase
0.29	F	0.31	F
0.31	F	0.36	F+C
0.35	F+C	0.40	F+C
0.38	F+C	0.42	F+C
0.46	C	0.49	C
0.52	G	0.54	G

Table 7.2: Phase behaviour of Charged PMMA Colloids

approximately 4 : 1 was used to study the effect of charge on the gel transition with out the effects of gravity.

This system was studied using two different sizes of PMMA colloids (radii 660nm and 535nm). A sequence of samples were made, then left to equilibriate for two weeks. The samples were observed in bulk, and placed in microscope capillaries for closer observation. The phases observed were fluid (F), fluid-crystal coexistence (F+C), crystal (C) and glassy (G). The phase behaviour is illustrated in figure 7.2, and summarised in Table 7.2.

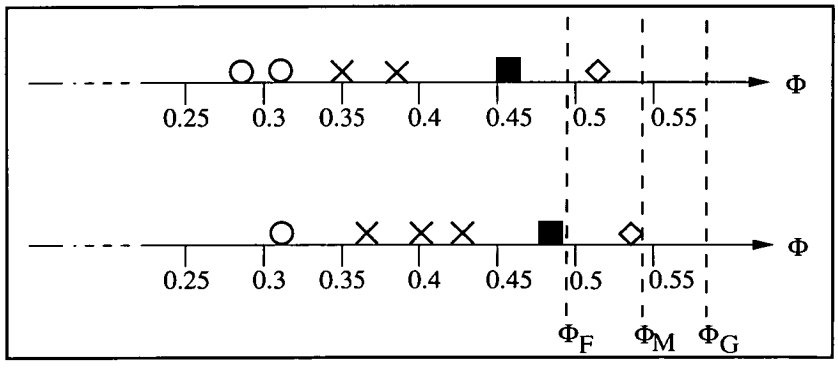

Figure 7.2: Phase behaviour of PMMA colloids of radius $535nm$ (top) and $660nm$(bottom). In each case the symbols denote the following: ○ =fluid, × =fluid-crystal coexistence, ■ =crystal and ◇ =glass. ϕ_F, ϕ_M and ϕ_G are the freezing, melting and glass transition volume fraction for hard spheres.

The freezing volume fraction for this system is found to be at $\phi \sim 0.33$, and that for hard spheres is $\phi_F^{HS} = 0.494$. Using this information, the charge per colloid can be estimated. Firstly, assume that all of the charges are ionised. For a known volume fraction ($\phi \sim 0.33$) the counterion concentration in the solvent as a function of charge per colloid Q can be calculated. To do this, the number of colloids n per unit volume at that volume fraction is calculated. The

number of counter ions in the same volume will be Qn. The number of ions in the *free* volume will be given by Qn/V_{free}, and since the colloid volume fraction is 0.33 we know the free volume fraction to be 0.67.

In order to calculate the Debye screening length (in terms of Q) the dielectric constant of the solvent is needed. The dielectric constant of CHB is $\epsilon^{chb} = 5.3$, and that of decalin is $\epsilon^{decalin} = 2.15$. In the solvent used here they were mixed together at a ratio of 4 : 1. The dielectric constant of the solvent mixture of CHB (solvent 1) and decalin (solvent 2), $\bar{\epsilon}$ can be calculated [20] using equation 7.8:

$$\frac{\bar{\epsilon}-1}{\bar{\epsilon}+2}\frac{M_1 f_1 + M_2 f_2}{\rho} = P_1 f_1 + P_2 f_2, \tag{7.8}$$

where M is the molecular weight of the solvent ($M_1 = 177.8$ and $M_2 = 138.2$), ρ is the density ($\rho_1 = 1.289 \times 10^3$ g/l and $\rho_2 = 0.897 \times 10^3$ g/l), f is the fraction of each solvent in the mixture $f_1 = 3/4$ and $f_2 = 1/4$, and P is the molar polarisation, given for each solvent by equation 7.9 [20]:

$$P_i = \frac{\overline{\epsilon_i}-1}{\overline{\epsilon_i}+2}\frac{M_i}{\rho_i}. \tag{7.9}$$

The molar polarisations are found to be $P_1 = 0.081$ and $P_2 = 0.043$, and the dielectric constant of the mixture is found to be 4.1.

The Debye screening length was defined in chapter 4.4, and can be calculated using equation 7.10:

$$\frac{\kappa_w}{\kappa_c} = \sqrt{\frac{\epsilon_c c_w}{c_c \epsilon_w}}, \tag{7.10}$$

where the dielectric constant of water $\epsilon_w = 81$, the Debye screening length of monovalent salt in water $\kappa_w^{-1} = 0.3$nm at a concentration of $c_w = 1$ Molar, and the dielectric constant of the solvent $\epsilon_c \sim 4.1$. For the 660nm colloids, the Debye screening length is calculated to be $2586/\sqrt{Q}nm$. Crudely, the Debye screening length is added to the hard-sphere radius to get a renormalised radius $R^{effective}$. Since the freezing volume fraction using this renormalised radius should be approx 0.494, then

$$(R^{effective}/R)^3 = \frac{0.494}{0.33} = 1.5. \tag{7.11}$$

Rearanging equation 7.11 for the case of the 660nm colloids gives a value of the Debye screening length to be $\kappa^{-1} \sim 100$nm, and solving for Q gives an estimate of the charge per particle $Q \sim 700$ electronic charges. A similar calculation can be performed for the smaller colloids of radius $535nm$ and the charge on these colloids is found to be $Q \sim 300$ electronic charges per colloid.

7.3.2 Polymer

The coil dimensions of polystyrene in a mixture of decalin and cycloheptyl bromide has been studied by Prasad [77]. Static light scattering was used to determine the radius of gyration of polystyrene with molecular weight $2,000,000gmol^{-1}$. It was found that the solvent was a good solvent for polystyrene, and the radius of gyration of the polymer was found to be $R_g = 50 \pm 5nm$.

Using the data of Berry [10], the radius of the polystyrene under theta conditions is calculated to be $R_g^\theta = 39nm$, and the swelling of the polymer in *cis*-decalin at room temperature increases the radius of gyration to $R_g^{decalin} = 47nm$. Within the experimental uncertainties quoted by Prasad [77], the radius of gyration of polystyrene is the same in both *cis*-decalin and CHB. The radius of gyration of the polystyrene used in this work is therefore calculated to be 13.7nm in both solvents used.

Consider now how the radius of gyration may change as the polymer concentration is increased. Wiltzius [113] has performed a study showing that solutions of linear and flexible polymers can be characterised by a *concentration dependent* characteristic length. Using this approach corrections to the radius of gyration as the polymer solution becomes more concentrated can be made. A reduced concentration X is defined following the work of Ohta and Oono [66]. X is proportional to c/c^* and to a first order approximation is given by:

$$X\left[\frac{9}{16} - \frac{\ln(M_w/M_n)}{8}\right] = B_2 \times c, \tag{7.12}$$

where c is the concentration of the polymer solution (in the *free* volume), and B_2 is the second virial coefficient of the osmotic pressure. If the second virial coefficient B_2 is known, then the reduced concentration X can be calculated. The second virial coefficient was measured by Berry [10] for solutions of polystyrene in *cis*-decalin. A value $A_2\sqrt{M_w}$ was measured as a function of the Fixman parameter z, so that for a given Fixman parameter the value of $A_2\sqrt{M_w}$

is known. The second virial coefficient B_2 can then be calculated since $B_2 = A_2 \times M_w$. For the polystyrene used here, with $M_w = 212400$, $A_2\sqrt{M_w} = 0.32$ giving $B_2 = 14.75cm^3g^{-1}$.

Wiltzius [113] then measured a reduced length Δ/R_g (where R_g is the radius of gyration of a single polymer coil in solution) as a function of X. By comparison to this data (Fig.3 in reference [113]), an estimate of the reduced length can be made for a particular concentration of polystyrene. The reduced length can then be converted into an effective radius of gyration using an approximate scaling (multiplication by a factor of $\sqrt{3}$). A table containing all the corrected radii of gyration and size ratios for each sample observed is given in appendix B. The reduced size ratio and polymer radius of gyration can then be taken into account when calculating the depletion potential.

7.3.3 Screening the Charge

The effective range of the electrostatic interaction can be tuned by the addition of salt. To approximate the colloids as hard spheres, tetrabutylammonium chloride ($(C_4H_9)_4NCl$, $M_W =$ 277.92 g/mol, purchased from Fluka) is added to the suspension at a concentration of 1 mg/ml ($\sim$ 4mM). The Debye screening length of the tetrabutylammonium chloride can be calculated following the description in section 7.3.1for a solvent of dielectric constant $\epsilon = 4.1$, giving:

$$\frac{\kappa_w}{\kappa_c} = \sqrt{\frac{\epsilon_c c_w}{c_c \epsilon_w}} \Longrightarrow \frac{1}{\kappa_c} = \frac{0.07}{\sqrt{c_c}} nm. \tag{7.13}$$

where c is the salt concentration in Molar. A concentration of 1mg/ml corresponds to a Debye screening length of $\sim$ 1 nm. However, it has been estimated by Yethiraj and van Blaaderen [116] that the degree of salt dissociation in this system is $< 1\%$. This would give an ion concentration of $\sim 40\mu$M for an added salt concentration of 1 mg/ml, resulting in a Debye screening length of $\sim$ 10 nm.

7.3.4 DLVO Potential

Consider now the DLVO potential (chapter 4.4) for the specific system used in this work, PMMA colloids in a solvent mixture of CHB at *cis*-decalin at a ratio of 4:1.

The radius of the colloids used in this work are $\sim$ 660nm, the dielectric constant of the solvent is $\epsilon = 4.1$ as calculated in section 7.3.1, and the charge per colloid was estimated to be $Q \sim 700$ electronic charges for a volume fraction of $\phi = 0.33$. The charging mechanism is unknown.

However a publication by Nazareno *et.al.* [64] has shown that the bond between cycloheptyl and bromine in a molecule of CHB can break, leaving a positive cycloheptyl ion and a negative bromine ion. The probability of bond breaking increases as both heat and light are applied to the sample. I suggest that this bond breaks to some extent in the solvent, and that the cycloheptyl ions bond with the PMMA colloids. This is consistent with positive charge on the particles [116]. The bromine ion remains in the solvent as a counter-ion. If this charging mechanism is correct, the ionic strength of the solvent can be calculated using $I_{total} = \frac{1}{2}\sum_i (c_i z^2)$ M, where c_i is the concentration of ions in mol/l, and the molecular weight of bromine is $M_w = 79$ g/mol. The number density of ions is found to be 2.9×10^{14} ions per ml, giving an ionic strength of the solvent to be $I = 5 \times 10^{-7}$Molar.

Now consider screening the charge by the addition of a specific amount of the salt tetrabutylammonium chloride. The Debye screening length can be calculated as discussed in section 7.3.1, and is given by:

$$\frac{1}{\kappa}(\text{nm}) = \frac{0.07}{\sqrt{\text{c}}}, \tag{7.14}$$

Figure 7.3 shows the DLVO potential, the Coulomb repulsion and the van der Waals attractive terms (shown on separate graphs for clarity). For the case of high screening (figures (a) to (c)), the van der Waals attraction will dominate and the behaviour will resemble that of uncharged colloids. L represents the length of the stabilising polymer layer (assuming it to be $L \sim 20$nm), so the steric repulsion will prevent flocculation due to the van der Waals attraction. For the case of low screening (figures (d) to (f)) the electrostatic repulsion will dominate the DLVO potential.

7.3.5 Sample Preparation

Colloidal samples were first washed in *cis*-decalin as described in section 7.2. Density matching was achieved by the repeated addition of a 4 : 1 ratio solution of CHB:*cis*-decalin followed by sedimentation in the centrifuge. The density matching can then be perfected by adjustment of the solvent by adding CHB or *cis*-decalin as appropriate until the colloids no longer sediment over long timescales in the centrifuge. Density matching was assumed sufficient when there was no sedimentation in the centrifuge at speeds of $\sim 3000rpm$ after 24 hours.

The almost-density-matched solution was then spun down over many days in the centrifuge. The lower half was used as a colloidal stock solution, and some of the remaining solvent was taken off the sample and used as the solvent in which to dissolve the polystyrene.

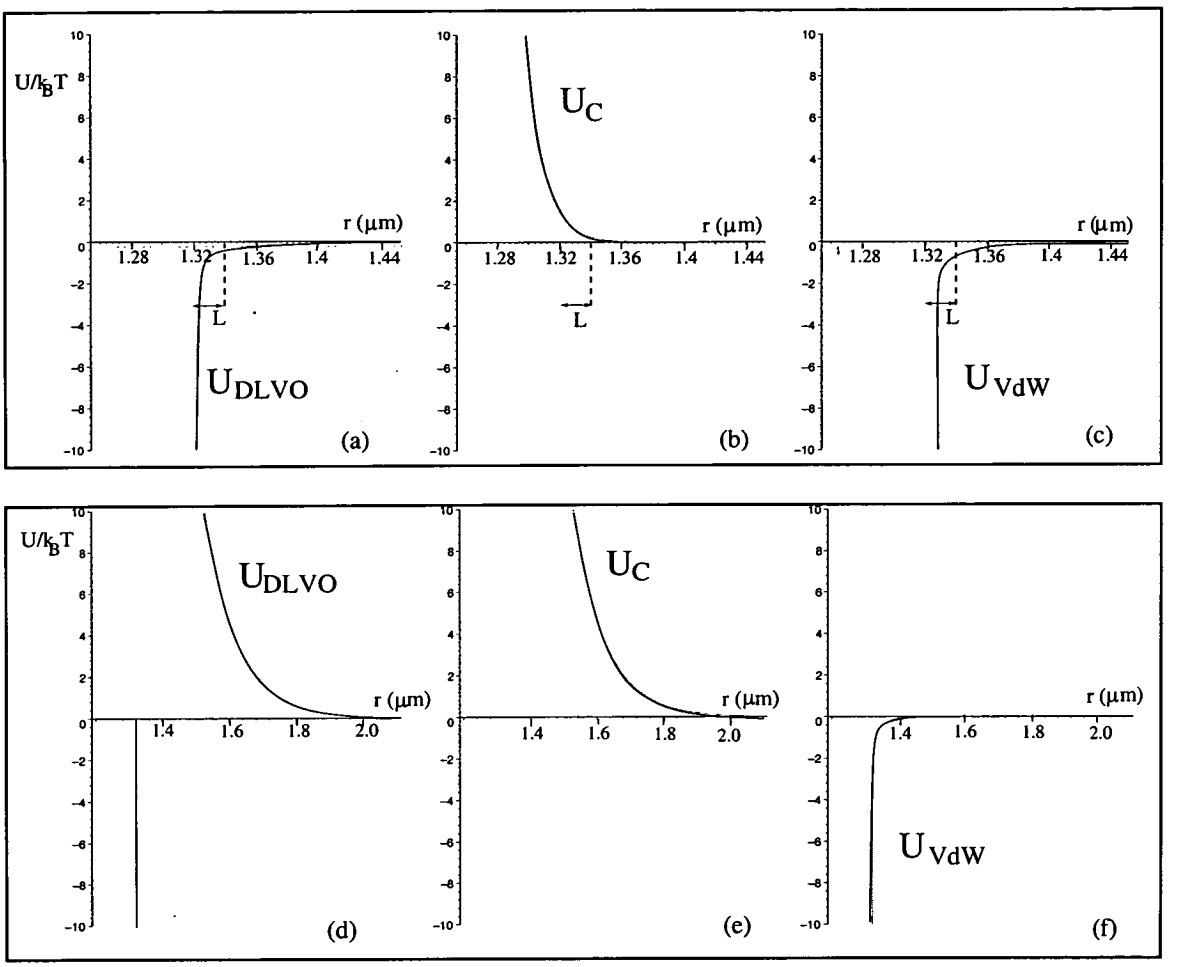

Figure 7.3: Predictions of DLVO theory, using values of $T = 295.15$, $A = 0.105x10^{-20}$J, $R = 660nm$ and $\epsilon = 4.1$, as discussed in section 4.3.1. Figures (a) to (c) show the high screening case where a salt concentration of 40μM has been used. The full DLVO potential (a), the Coulomb repulsion (b) and the van der Waals attraction (c) are shown separately for clarity. The van der Waals attraction dominates the DLVO potential in this high screening case. Figures (d) to (f) show the case of low screening, using an ion concentration of 5×10^{-7}M. This value is an estimate of the ion concentration when no salt is added, for colloidal particles with a charge of 700 electronic charges per particle. The full DLVO potential (d), the Coulomb repulsion (e) and the van der Waals attraction (f) are shown separately. For the Maple code used in calculating these potentials see Appendix A.

Solvent	Ratio	Density ($g.cm^{-3}$)
CHB	1	1.289
cis-decalin	1	0.897
CHB-*cis*-decalin	4 :1	1.191
CHB-*cis*-decalin	1 : 2	1.0

Table 7.3: Values of the solvent density of the different solvents used.

7.4 Combining the Solvents: Charge and Gravity

A mixture of solvents at a ratio of approximately 1:2 CHB:*cis*-decalin was used. This gives a density of $1.0g.cm^{-3}$, half way between the density of cis-decalin alone and the density matched solution. The table below shows a summary of the solvents used and their densities.

7.4.1 Sample Preparation

Samples were first washed in *cis*-decalin as described in section 7.2. They were then washed in a mixture of CHB and *cis*-decalin at a ratio of 1 : 2. A different batch of colloids were used for the experiments in this solvent. Due to the high polydispersity of the particular batch of colloids used for this experiment ($\sigma \geq 8\%$) no crystalisation data could be obtaied.

7.5 Summary of Experimental Systems

In summary, four experimental systems were studied, two using uncharged colloids and two using charged colloids. Uncharged colloids were studied in *cis*-decalin, where the effects of gravity are present. Uncharged colloids were also studied in a density matched solvent of CHB and *cis*-decalin, with tetrabutylammonium chloride added to screen the charge on the colloids. In these two systems the behaviour of effectively uncharged colloids was studied with and without gravity.

The phase behaviour of charged colloids was also studied. Firstly charged colloids were studied in the density matched system, so the effects of charge could be studied without the complicating effects of gravity. Finally, charged colloids in a mixture of CHB and *cis*-decalin at a ratio of 1 : 2 were studied, where the combined effects of charge *and* gravity could be observed. The four systems studied are summarised in table 7.4.

System	Solvent	Colloid radius	Polymer R_g	Size ratio	Charge	Gravity
1	CHB-*cis*-decalin 4:1 + salt	$535nm$	$13.7nm$	0.026	N	N
2	*cis*-decalin	$527nm$	$13.7nm$	0.026	N	Y
3a	CHB-*cis*-decalin 4:1	$535nm$	$13.7nm$	0.026	Y	N
3b	CHB-*cis*-decalin 4:1	$660nm$	$13.7nm$	0.021	Y	N
4	CHB-*cis*-decalin 1:2	$527nm$	$13.7nm$	0.026	Y	Y

Table 7.4: Full characterisation of the four experimental systems studied.

7.6 Colloid-Polymer Sample Composition

For all of the colloid systems studied the sample volume fraction and polymer concentration were calculated in the same way. The colloids were washed in the desired solvent as described above and the volume fraction of the stock colloid solution was then calculated. A quick method to determine the effective volume fraction of a suspension of colloids consists of centrifuging it until all the particles have formed a sediment at the bottom of the container, and assuming this sediment has the volume fraction of a random close packed solid [57]. However, this method lacks accuracy and should only be used for rough calibrations. It is likely that the sediment is not completely random close packed. Small particles may have time to rearrange themselves in a crystalline manner, or alternatively kinetic arrest due to the glass transition or jamming may prevent the volume fraction ever reaching that of a random close packed solid.

A more accurate way of determining the effective volume fraction is to make a sample of volume fraction within the fluid crystal coexistence region. One can measure the height of the fluid-crystal interface with time, and extrapolate the linear compaction of the sediment back to zero time to obtain a value of the crystal height divided by the total height of the sample, X. The relative fraction of the sample occupied by crystallites can then be related to the colloid volume fraction by:

$$\phi = \phi_F(1 - X) + \phi_M X, \tag{7.15}$$

where ϕ_F and ϕ_M are the freezing and melting volume fractions for hard spheres. However, this calibration method requires sedimentation of the crystallites over time. In density matched samples the effects of gravity have been reduced to such an extent that there is no visible sedimentation over many weeks. Since no macro-phase separation is observed, this calibration

method cannot be used. Therefore, measurement of volume fraction of density matched colloidal suspensions was achieved by weighing the colloidal samples. A drop of known mass is allowed to dry until all the solvent has evaporated. The weight of the remaining colloid is then measured, and the weight fraction is calculated as the weight of the dry colloids divided by the weight of the total drop:

$$\phi_w = \frac{m_{dry}}{m_{total}}. \tag{7.16}$$

In calculating the weight fraction of the colloids several experiments were carried out and an average of the resultant weight fractions used. The effective hard-sphere volume fraction of the colloids ϕ must then be calculated. The simplest method to calculate the volume fraction is to assume a density of 1.19 g.cm^{-3} for all components in the system whilst the colloids are in solution, including the core, shell and solvent. This is not unreasonable since the samples are density matched. However, when the colloids are dry the stabilising layer will not contribute significantly to the mass. The length of the stabilising layer in solution is $\sim 10 - 20$nm. A 10nm stabilising layer is 6% of the colloidal core volume. This must be taken into account when calculating the effective volume fraction ϕ of the colloids in solution. However it must be noted that the uncertainty in the length of the stabilising layer will lead to large uncertainties in ϕ, since the length is cubed when converted into a fraction of the colloidal volume. The volume fraction not including the stabilising layer is given by:

$$\phi = \frac{V_{colloids}}{V_{total}} = \frac{m_{colloids}/\rho_{colloids}}{m_{total}/\rho_{total}}, \tag{7.17}$$

where $\rho_{colloids}$ and ρ_{total} are the densities of the colloids and total solution respectively. Since the density of the solvent is matched to the colloid density, then without including the volume occupied by the stabilising layer $\phi = \phi_w$. To take into account the volume occupied by the stabilising layer of polymer 6% of the volume fraction must be added on, so:

$$\phi = 1.06\phi_w. \tag{7.18}$$

It is also possible to calculate the conversion factor experimentally for uncharged PMMA colloids in *cis*-decalin, which leads to a scaling factor as reported by Pusey [1] of $\phi = 1.04\phi_w$. This scaling was experimentally determined in the following way. A non-density matched suspension of colloids was prepared, and the weight fraction measured by drying. The volume fraction of the same sample was experimentally measured by calculating the percentages of the

fluid and crystal phases once the sample had phase separated. The difference between these two values was found to be the factor of 1.04. However, this scaling factor has its limitations, since it is only valid at the volume fraction of this one sample, and only valid in *cis*-decalin not density matched solvents. Due to the complications introduced to the density matched system due to the mixture of two different solvents, it was decided that the approximate value for the volume fraction obtained using equation 7.18 would be used.

The polymer stock solutions were prepared by dissolving a known mass of dry polymer into a known mass of solvent by prolonged tumbling. The corresponding polymer concentration c_p (in mg/ml) was obtained directly by dividing the polymer mass by the volume of solvent, calculated from the literature value (and subsequent calculation for the mixtures) for the density of the solvent. The polymer contribution to the overall volume is very small and was neglected.

The colloid-polymer samples were then prepared by mixing calculated masses of colloid and polymer stock solutions with pure solvent. The volume fraction ϕ and the polymer concentration c_p can be calculated from the equations:

$$\phi = \frac{V_{cs}}{V_{cs} + V_{ps} + V_{ss}} \phi_{cs}, \tag{7.19}$$

$$c_p = \frac{V_{ps}}{V_{cs} + V_{ps} + V_{ss}} c_{ps}, \tag{7.20}$$

where V_{cs}, V_{ps} and V_{ss} are the volumes of the colloid, polymer and solvent solutions added to the sample. ϕ_{cs} and c_{ps} are the volume fraction of the colloid stock and the polymer concentration of the polymer stock solutions.

7.6.1 Errors

Uncertainties in the final sample composition (ϕ, c_p) arise from (1) uncertainties in the concentration of colloid and polymer stock solutions and densities of solvent mixtures, (2) preparation errors for example weighing and pipetting of solutions, and (3) solvent evaporation from the sample once it has been placed in the sample cell.

Colloid Stock Solution Composition

In calculating the weight fraction of the colloids several experiments were carried out and an average of the resultant volume fractions used. A standard deviation in these values can be calculated, using

$$s^2 = \frac{1}{N}\sum_{i=1}^{N}(x_i - \overline{x})^2, \tag{7.21}$$

where s is the standard deviation, which was calculated to be 0.004, a relative error of $\pm 1\%$, which in turn gives a standard error in the mean of $\sim \pm 0.5\%$. However, the transformation from a weight fraction to a volume fraction contains errors due to the fact that the density and length of the stabilising layer in the solvents used are not precisely known. I estimate the error in the volume fraction to be $\sim 5\%$. This is an error in the volume fraction of the stock solution, so would lead to a *systematic*, not random, error in the sample volume fraction. The *relative* volume fractions may be believed with a confidence determined by the sample preparation uncertainties discussed below. But it must be remembered that the absolute values of the volume fraction are subject to a $\sim 5\%$ systematic error.

Polymer Stock Solution Composition

Uncertainties in the composition of the polymer stock solution can arise from errors in weighing the dry polystyrene. Making the polymer stock requires the weighing of a small amount of dry polystyrene ($\sim 0.1g$). It is estimated that all masses on the balance are accurate to $\pm 0.001g$. This leads to an uncertainty in the mass of the dry polymer of $\pm 1\%$. This uncertainty result in absolute or systematic errors, not relative errors.

Because the effect of CHB on the size of the polymer coils has not been fully characterised to date, the radius of gyration (and consequently the size ratio of the system) has an associated uncertainty. Following on from the measurements by Prasad [77] I estimate the error in the radius of gyration calculated to be $\pm 10\%$.

Sample Preparation

Weighing errors in the preparation of colloid samples must be considered. Samples were prepared with volumes of $\sim 0.4g$ of the stock solutions, leading to a percentage error in the final colloid volume fraction and polymer concentration of $\pm 0.25\%$. The volume fraction of the colloid solution may also be affected by using a pipette to transfer stock solution into the sample. Jamming at the entrance to the pipette tip reduces the colloid volume fraction by hindering the flow of colloidal particles. However, the suspensions used in these experiments are of volume fraction ~ 0.5, where these effects should be small.

Errors Introduced During Observation

Solvent evaporation was accounted for by recalibration of the stock solutions, and in general proved to be negligible over periods of weeks. Evaporation of the solvent during observation was quantified by measuring the change in mass of a sample (with volume fraction $\phi = 0.03$ and polymer concentration $c_p = 6.2$mg/ml) with time. Figure 7.4 is a plot of the mass of the sample expressed as a percentage of the original mass, and shows that there was no evaporation of the sample over two hours, the typical timescale of the experiments.

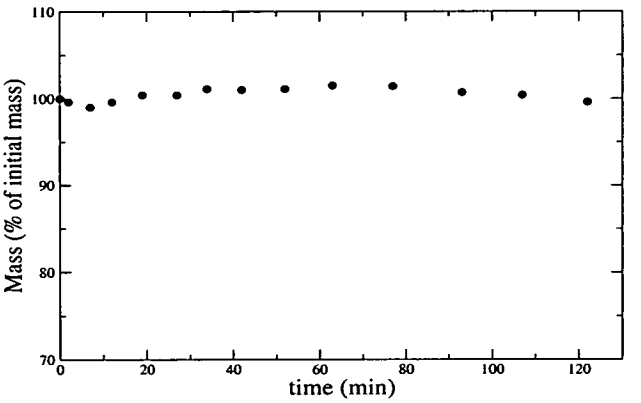

Figure 7.4: Plot showing the percentage decrease in the weight of a sample over two hours.

In order to ensure that the bulk properties of the system are being observed, and that edge effects are negligible, viewing too close to the sample cell edge must be avoided. It was observed that edge effects could extend into the sample as far as 20 colloid diameters (corresponding to about 20μm). Samples were observed into depths of 60μm.

Chapter 8

Results 1:
Colloid-Polymer Mixtures

8.1 Introduction

The addition of non-adsorbing polymer to a suspension of colloids induces an effective short ranged inter-particle attraction between the colloids, as discussed in chapter 3. If this attraction is sufficiently strong, the colloids can aggregate to form a space filling gel even when the colloid volume fraction(ϕ) is very low. Colloidal gels have been studied in the past using a variety of techniques including direct observation and light scattering [102, 76, 101, 73], and a confusing 'zoo' of observations have been reported, including 'clusters' at weaker attractions than those needed for gelation [91]. These phenomena have been found in different experimental systems, and no unified understanding has been reached.

The phase behaviour of a colloid-polymer mixture is dependent on the polymer to colloid size ratio. For small size ratios $\xi \lesssim 0.03$, it has been reported that gelation is the first transition encountered on increasing the attraction beyond the fluid phase [82, 92]. The size ratios used in all the systems studied are below $\xi = 0.03$.

In this chapter results from a single well-characterised model colloid-polymer mixture are presented, in which the effects of gravity and charge on the aggregation of the colloids have been studied. Furthermore, the enhanced resolution obtainable using the confocal microscope enables direct imaging of the colloidal particles during the formation and evolution of the aggregates.

Four different experimental phase diagrams are obtained using the single colloidal system. By varying the solvents used, the colloids have been studied both in gravity and in a density matched (close to zero gravity) system. In certain organic solvents the colloids carry a charge, so that the phase behaviour of charged colloids in gravity and in a close to zero gravity system can also be studied. The gel transition is first studied in its simplest form, in an uncharged and density matched system. The effects of charge and gravity on the gel transition and aggregation of colloids are then each be studied in turn. For each system the results are interpreted and compared with other results from the literature and a range of theoretical predictions.

8.2 System 1

Uncharged Colloids in a Density Matched Solvent

8.2.1 Phase Diagram

The first experimental system that will be discussed is that of effectively uncharged colloids in a density matched solvent. This system is the 'standard model' with which phase behaviour can be studied without the complicating effects of charge or gravity. The colloidal particles used in this work are fluorescently labelled PMMA colloids dispersed in a mixture of cycloheptyl bromide (CHB) and *cis*-decalin. A mixture of these two solvents at a ratio of 4 : 1 is used to produce a suspending medium with a density approximately equal to that of the colloids themselves ($\sim$ 1.19 g.cm^{-3}, for details see chapter 7). The radius of the colloidal particles is 535nm, and the polymer used was polystyrene (PS) of molecular weight $M_w = 212,400$ daltons. The polymer radius of gyration in the density matched solvent is estimated to be $\sim$ 13.7 nm, giving a size ratio of $\xi = 0.026$. As discussed in chapter 7, PMMA colloids suspended in CHB are charged. To approximate the colloids as hard spheres the salt tetrabutylammonium chloride is added at a concentration of 1 mg/ml, which corresponds to a Debye screening length of $\sim$ 1 nm.

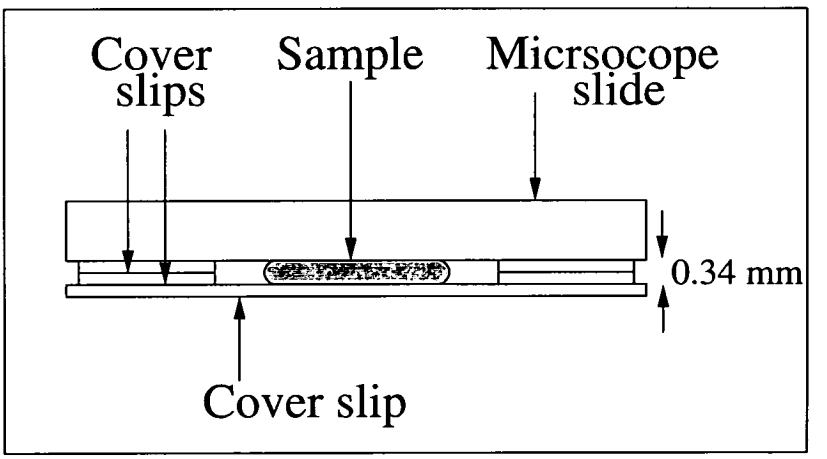

Figure 8.1: Experimental set up for sample observation in the confocal microscope.

The first step in understanding the phase behaviour of a colloid-polymer mixture is to determine the phase diagram of the system. A series of samples spanning a range of colloid volume

fraction $0.01 \lesssim \phi \lesssim 0.2$ and a range of polymer concentrations 2 mg/ml$\lesssim c_p \lesssim$ 10 mg/ml were prepared. Each sample was then set up for microscopic observation. The sample, initially in a glass sample cell, was shaken vigorously by hand and a small drop of the sample was pipetted onto a cover slip. The drop was covered with a microscope slide, which was prevented from squashing the sample by the placement of two cover slips either side of the sample. This set up is illustrated in figure 8.1. The samples were not sealed because immediate observation was required, but the effects of evaporation were monitored and shown to be negligible (chapter 7.6.1). Their behaviour was then studied by immediate observation with the confocal microscope.

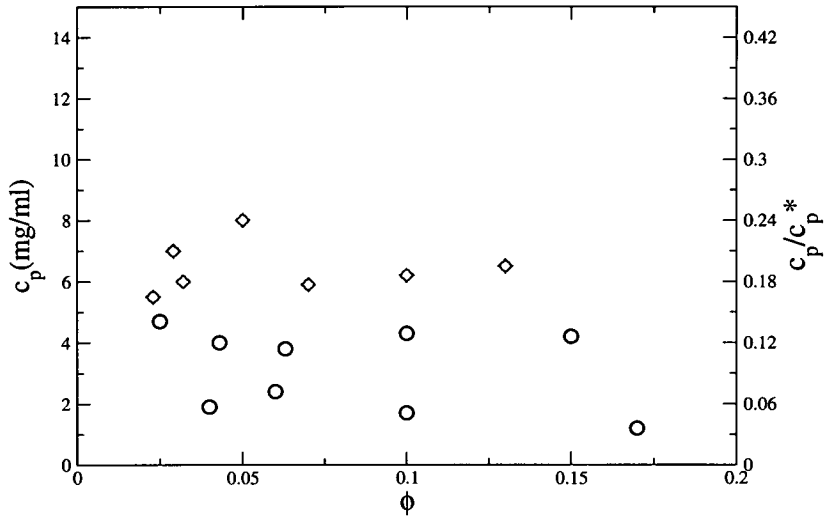

Figure 8.2: Phase diagram of uncharged PMMA-PS in a density matched solvent mixture of CHB and *cis*-decalin, showing phases of fluid (○) and large non-ergodic aggregates (◇).

Figure 8.2 shows the phase diagram for the 'standard model' system: effectively uncharged PMMA colloids in a density matched solvent, plotted in the (ϕ, c_p)-plane. Two states were observed in this system. At low polymer concentrations, samples remained in a single ergodic phase and appeared homogeneous (○), with a fluid-like arrangement of the colloidal particles. An example of this phase is shown in figure 8.3(a). On increasing the polymer concentration, aggregation was observed, which rapidly gave rise to large clusters ($\sim 25 - 50$ particle diameters, increasing with ϕ), ◇ in figure 8.2. These clusters appeared 'caged' by each other, so that the orientation and centre of mass of each cluster fluctuated without any net long-range motion. These fluctuations never disappeared during a two hour observation period for the clustering

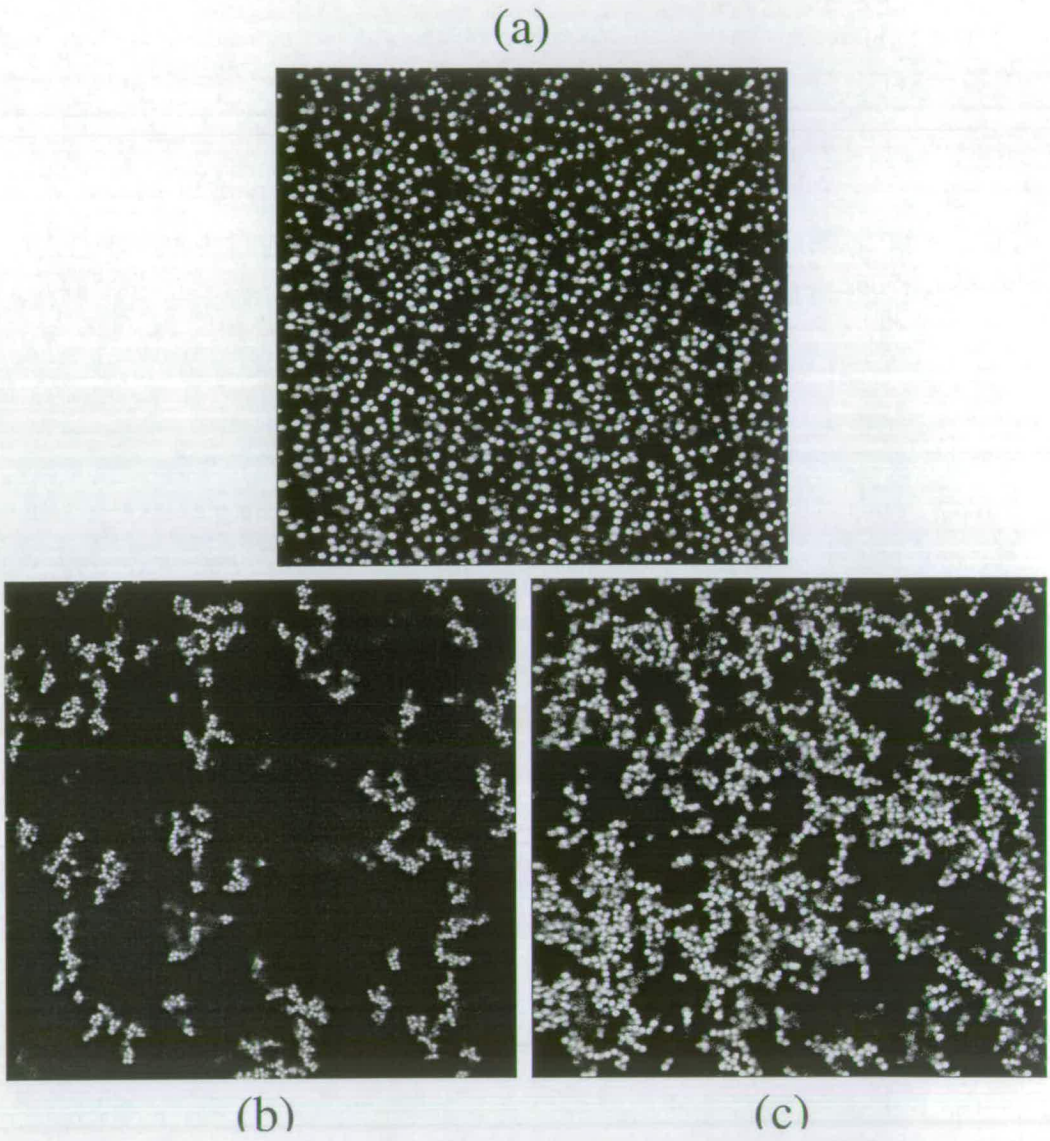

Figure 8.3: Confocal micrographs showing a samples (a) in the homogeneous fluid phase $\phi = 0.06$ and $c_p = 2.4$ mg/ml, (b) large non-ergodic aggregates at low volume fraction $\phi = 0.029$, $c_p = 7$ mg/ml and (c) large non-ergodic aggregates at higher volume fraction $\phi = 0.1$, $c_p = 6.2$ mg/ml. All images taken 1 hour after initial sample preparation.

sample with the lowest volume fraction and polymer concentration ($\phi = 0.024, c_p = 5.5$ mg/ml). In other clustering samples however, all discernible motion ceased after a time period τ, and the structure appeared frozen. The time interval τ varied from ~ 80 to ~ 5 minutes, rapidly decreasing as ϕ and c_p increased. Figure 8.3 shows two examples of this state, one at low colloid volume fraction $\phi = 0.029$, figure 8.3(b) and one at a higher volume fraction $\phi = 0.1$, figure 8.3(c).

A recent publication has reported the existence and position of a fluid-gel phase boundary at low size ratios in a silica-polystyrene mixture in decalin [92]. The silica particle radius is $a \sim 50$ nm, an order of magnitude smaller than that of the colloids used in this work. The rate of sedimentation due to gravity can be estimated using equation 8.1:

$$v_s = \frac{2\Delta\rho g a^2}{9\eta}, \tag{8.1}$$

where η is the viscosity, $\Delta\rho$ is the density difference between the particles and solvent and a is the particle radius. The density of the silica particles use was reported to be $\rho = 1.9\text{g.cm}^3$, giving a sedimentation velocity of $v_s \sim 0.2$nm/sec. This slow sedimentation velocity implies that the results reported by these authors may be comparable to those reported here. Indeed their results show the gelation boundary to be within the range of $c_p/c_p^* \sim 0.12 - 0.18$ for volume fractions $\phi \lesssim 0.2$, as reported here.

8.2.2 Detailed Observations

The aggregation of the samples was observed in more detail. Sample $\phi = 0.029$ and $c_p = 7$ mg/ml was observed from the initial sample preparation and for an hour subsequently by confocal microscopy, figure 8.4. Initial observation revealed small colloidal aggregates incorporating tens of particles. These aggregates had already formed when the first image was taken, so their formation takes place within the 2 minutes taken to prepare samples for observation. At first the aggregates appear 'stringy' and inhomogeneous, as seen in the image taken 1 minute after preparation (figure 8.4). They grow quickly and after typically $10 - 20$ minutes all the particles are incorporated into the aggregates. The aggregates grow to form a large clusters, as in the image taken after 50 minutes. After ~ 70 minutes the colloids appear to be very 'stuck', the lack of movement of the particles implying the sample is non-ergodic, and there is no noticeable change in the structure from $\sim 70 - 80$ minutes.

The time taken for the large clusters to form, and the time τ in which the samples became non-ergodic, depends on the sample volume fraction ϕ and polymer concentration c_p. At moderate

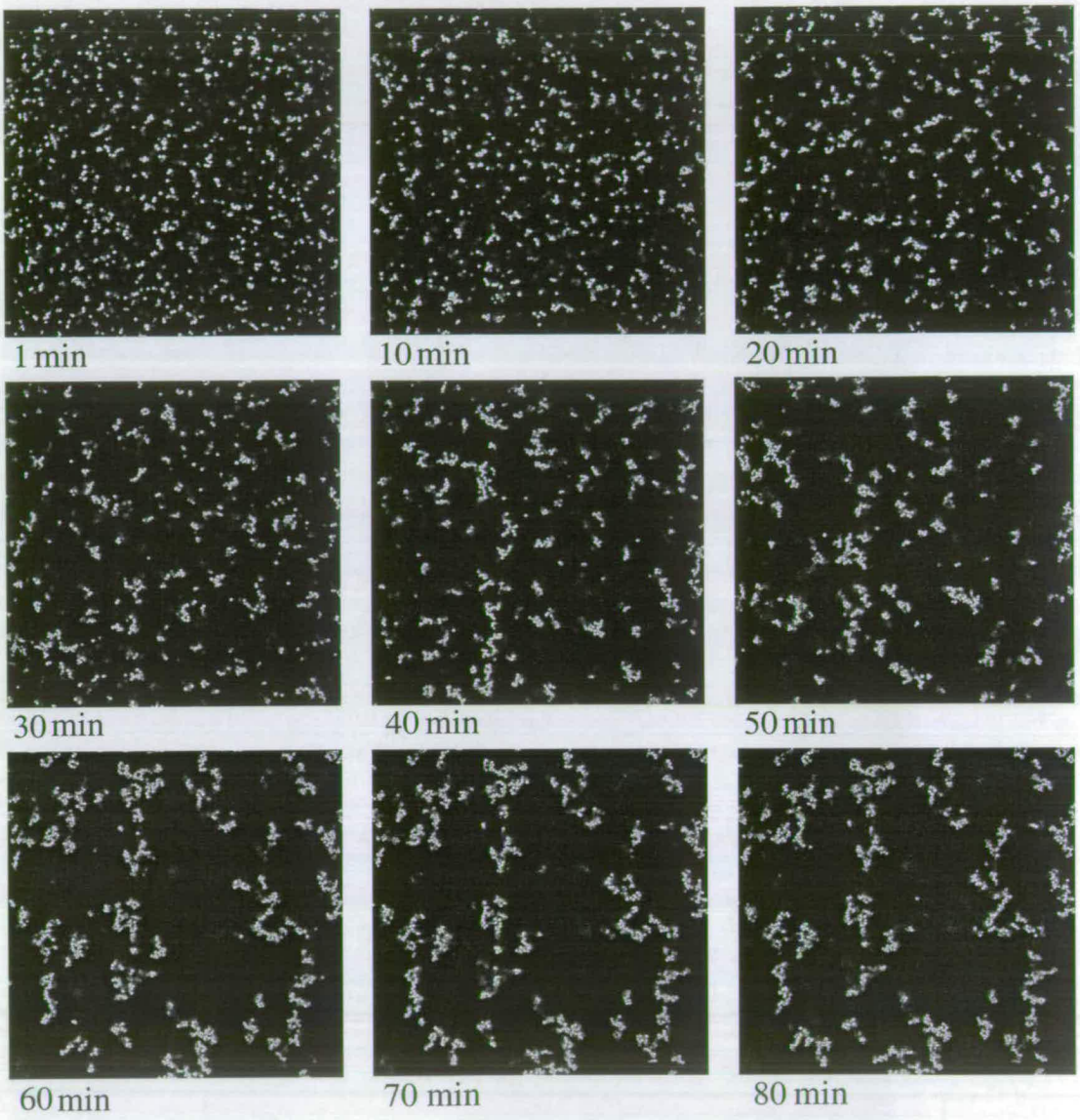

Figure 8.4: A time series of sample $\phi = 0.029$ and $c_p = 7$ mg/ml taken from 1 to 80 minutes after sample preparation, illustrating the formation of large aggregates at low volume fractions.

to high volume fraction $\phi \gtrsim 0.05$ all the particles are incorporated into aggregates within 5 minutes, and the sample appears to be non-ergodic within $\sim 5 - 15$ minutes. However, samples at low volume fractions ($\phi \sim 0.02$) take up to an hour to form large clusters. After ~ 1.5 hours most samples at low volume fractions appear non-ergodic, however the sample at $\phi = 0.024$ and $c_p = 5.5$ did not appear non-ergodic for the timescale of the experiment, ~ 2 hours.

In observing the sample $\phi = 0.029$ and $c_p = 7$ mg/ml its formation and evolution can be loosely grouped into three stages. Immediately after mixing the particles form small aggregates. At first aggregates and monomers are clearly visible, but after ~ 10 minutes almost all the monomers are incorporated into the aggregates. The second stage is the formation of these aggregates into large clusters, which are observed about 40 minutes after sample preparation. During the following 30 minutes the particles gradually appear to get more stuck. Finally, after ~ 70 minutes the colloids appear very stuck with very little movement observed.

8.2.3 Interpretation

The most striking feature of these observations is the *sharp* onset of aggregation across a 'clustering boundary' at $c_p \sim 5$ mg/ml. I now discuss the causes of this aggregation using the evidence presented in the previous section. First I consider predictions of a non-ergodicity transition from mode coupling theory (MCT). I then go on to discuss a renormalised variant of MCT known as cluster mode coupling theory (CMCT). I highlight the sedimentation that can arise when even a small degree of density mis-matching is present, and finally summarise two possible interpretations of the experimental data that has been presented here.

MCT Predictions of Non-ergodicity

Theoretically, gelation is often discussed in terms of diffusion limited cluster aggregation (DLCA) or percolation (chapter 3.5). However, these non-equilibrium approaches do not describe why the predicted equilibrium phase behaviour of the system is not reached. However, mode coupling theory (MCT) is an equilibrium statistical mechanics approach that predicts where the system would fall out of equilibrium, and therefore where non-equilibrium approaches such as DLCA start to become meaningful. MCT predicts a non-ergodicity transition at low volume fractions which has been thought relevant to gelation transitions [8, 7, 6]. Bergenholtz *et.al* describe a version of idealised mode coupling theory from which the gelation transition in colloid-polymer mixtures can be predicted [9].

Bergenholtz *et. al.* [9] model the colloid interaction potential by the depletion potential. This was described in full in chapter 3, however for low size ratios $\xi < 0.1$ and range of $\sigma < r < \sigma(1+\xi)$ (where σ is the particle diameter) an approximation to the full depletion potential is:

$$u(r) = -\eta_p^{(R)} k_B T \frac{3}{2} \frac{1+\xi}{\xi^3} \left(\frac{r}{\sigma} - 1 - \xi\right)^2 \tag{8.2}$$

Here $\eta_p^{(R)} = 4\pi n_p^{(R)} R_g^3/3$ is the polymer volume fraction in the free volume. Using this simple form of the depletion potential, the authors derive an analytic prediction of the MCT non-ergodicity boundary at low ϕ [9]. Dynamical arrest is predicted using an interaction parameter $\Gamma = K^2\phi/b$, where the parameters K and b are functions of the polymer volume fraction and the size ratio of the system (see details in ref [9] for full derivation). Using mode coupling theory to predict where the system will become non-ergodic they find a critical value for this interaction parameter of $\Gamma \sim 3.02$, above which the dynamics become arrested. By substituting the full expression for the parameters K and b, a prediction for the ergodic to non-ergodic transition in the phase diagram of a colloid-polymer mixture can be made. States with arrested long time dynamics are predicted for $K^2\phi/b \geq 3.02$:

$$3.02 \sim \frac{K_c^2 \phi_c}{b_c} = \frac{\xi^2 \phi_c}{3\eta_{p,c}^{(R)}(1+\xi)} \exp[3\eta_{p,c}^{(R)}(1+\xi)/\xi] \tag{8.3}$$

It is known that the *raw* MCT prediction for the hard-sphere glass transition $\phi_g^{MCT} \sim 0.516$ is lower than the value measured from dynamic light scattering $\phi_g \sim 0.58$, so a scaling of $\phi = (0.58/0.516)\phi^{MCT}$ is used to bring the theory in line with experimental data [9]. The same scaling is applied in what follows, so that the final calculated prediction for the non-ergodicity transition in the ϕ, c_p plane is scaled before plotting these values on the experimental phase diagram.

The next step in the comparison of the MCT predictions to my experimental data is the conversion of the polymer volume fraction in the free volume $\eta_p^{(R)}$ into the value of the mass concentration of polymer in the total sample volume c_p. The volume fraction of the polymer in the total sample volume is given by $\eta_p = \alpha\eta_p^{(R)}$, where α is the free volume fraction as defined in chapter 3.2. The density of the polymer is taken as $3M_w/(4\pi R_g^3 N_a)$ where M_w is the polymer molecular weight and N_a is Avogadro's constant, giving

$$c_p = 3[\alpha\eta_p^{(R)}]\frac{M_w}{4\pi R_g^3 N_a}. \tag{8.4}$$

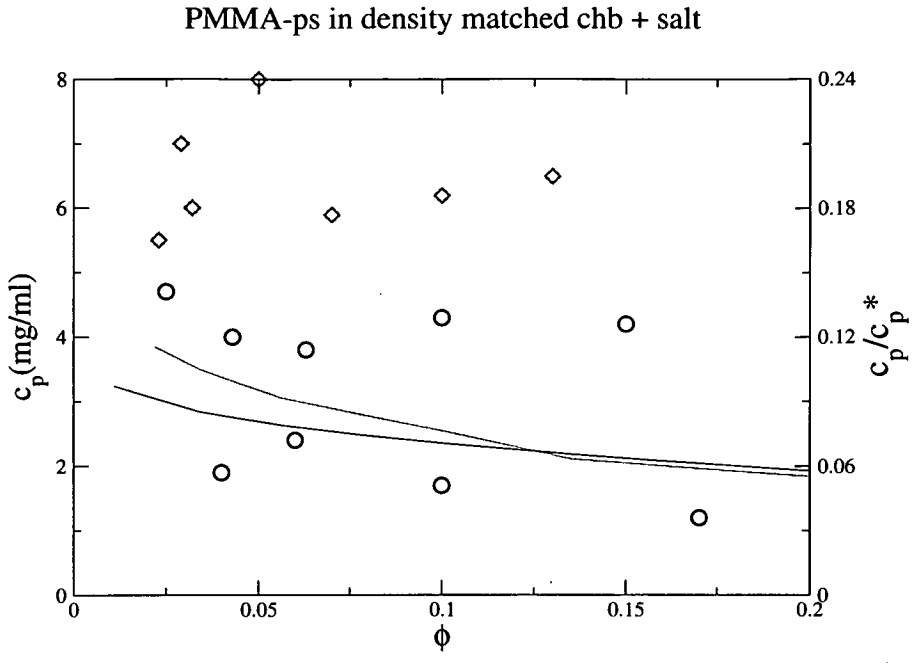

Figure 8.5: Phase diagram showing the experimental data presented in section 8.2 and the calculated non-ergodicity lines predicted using Mode Coupling Theory. The upper line includes the correction for the decrease in R_g and ξ at increasing polymer concentrations.

In this way the MCT predictions for the non-ergodicity transitions at low volume fractions and size ratio $\xi < 0.1$ can be calculated. The maple code used to calculate the MCT non-ergodicity transition is presented in appendix C and the results are plotted, together with the experimental data presented in the previous section, in figure 8.5.

As discussed in chapter 7, the radius of gyration of the polymer and hence the size ratio decrease as the polymer becomes more concentrated. These effects can be taken into account when calculating the MCT non-ergodicity transition line. The correction to the radius of gyration and the size ratio were performed in the same way as for my experimental data, as described in Chapter 7.3.2. The corrected values are listed in appendix B, and the corrected MCT line is also plotted in figure 8.5 (upper line).

CMCT Predictions of Non-ergodicity

Although the validity of the MCT non-ergodicity transition at high volume fractions has been demonstrated [68], the physical relevance of the MCT line itself at *low* volume fractions has

not been established. A recent publication has derived a renormalised variant of MCT which may be relevant [49], known as cluster mode coupling theory (CMCT).

MCT takes its structural input from equilibrium state theory, which means that it cannot address states where the structure is strongly perturbed. However, the gels observed at low volume fractions have a highly non-uniform, ramified structure. Cluster MCT treats the formation of these non-ergodic aggregated structures as irreversible cluster aggregation (ICA). The cluster aggregation process is invariant under coarse graining in the limit of δ, $\epsilon^{-1} \to 0$, and $\phi \to 0$, where δ is the attraction range, and the well depth is ϵ. This scaling limit is controlled by the ICA 'fixed-point'. For $\phi > 0$ the resulting clusters eventually form a percolating gel of locally ICA-like structure.

Consider a system at low volume fraction in which aggregation has begun. The parameters of the system, ϕ, δ and ϵ^{-1} must change upon coarse graining as ICA-like clusters begin to grow. This leads to a schematic description of the suspension in terms of an effective theory for a liquid of renormalised particles or coarse-grained clusters. Applying MCT to this theory, a new condition for the arrest *of the clusters* is obtained. This arrested state is identified with a weak gelled state. If this condition is not met, one has instead a fluid of clusters that is ergodic at large scales. Bond breaking and reconnection on the scale of entire clusters is allowed for in the model, but reconstruction on shorter length scales is not.

Within this scenario, weak colloidal gelation is a double ergodicity breaking. Firstly, above the MCT non-ergodicity transition line, the particles become kinetically unstable against aggregation. Secondly, the fluid of clusters crosses the CMCT non-ergodicity transition line and arrests. It is assumed that bonds can break with a small but finite probability. Initially this has no effect on the aggregation, which flows toward the ICA fixed point. But as the clusters grow the chances of fragmentation increase and the system flows away from it. The flow takes place in a parameter space comprising of the effective system variables $(\tilde{\phi}, \tilde{\delta}, \tilde{\epsilon^{-1}})$. These coarse grained parameters describe the density and interaction of the aggregated clusters and given by [49]:

$$\tilde{\phi} = \phi N^{3/d_c - 1}, \tag{8.5}$$

$$\tilde{\delta} = \delta N^{-\nu}, \tag{8.6}$$

$$\tilde{\epsilon} = \epsilon - \chi \ln N - f(N). \tag{8.7}$$

The combination of these three equations with mode coupling theory is called cluster mode

coupling theory, CMCT [49]. N is the number of particles in a typical cluster, and the three exponents are initially properties if the ICA fixed point ($d_c \sim 2$ and $\nu \sim \chi \sim 1/d_c$ in 3 dimensions). Although they will change with the flow, they are treated as negotiable constants in the theory. The resulting CMCT flow within renormalised parameter space is shown in figure 8.6. The ergodic region is the upper left of the diagram, below the dark dome is an attractive glass and to the right of the light sheet is a repulsive glass.

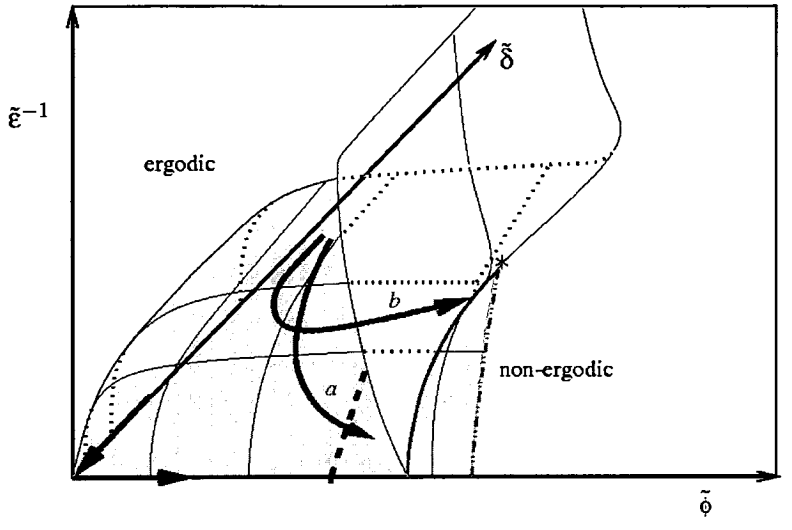

Figure 8.6: Schematic parameter flows (arrows) in the CMCT scheme. Flow (a) within the lower coordinate plane ($\epsilon^{-1} = 0$) gives percolation of ICA clusters on passing through a non-equilibrium percolation line. Trajectories starting from finite ϵ^{-1} flow upward to smaller ϵ, larger ϕ and smaller δ. Those that arrive on the dark surface result in a semi-ergodic cluster phase. The marginal gel trajectory (b) ends at the intersection line of the repulsive (light surface) and attractive (dark surface) branches of the MCT transition. Taken from [49].

Trajectories starting from finite ϵ^{-1} flow upward to smaller ϵ, larger ϕ and smaller δ. Those that arrive on the dark surface result in a semi-ergodic cluster phase. Aggregation of the clusters ceases because the clusters' effective parameters now correspond to an ergodic phase. A semi-ergodic fluid of finite clusters is expected. If a trajectory meets the intersection between the dark and light surfaces, the marginal gel trajectory (b), then aggregation ceases because the clusters form a repulsive glass. This repulsive cluster-glass is associated with the gel phase [49].

Phase diagrams can be predicted using this theory. The bare MCT line predicts where the initial suspension will become locally non-ergodic, that is where aggregation begins. The CMCT line then plots out the transition where the growing clusters will form a repulsive glass due the flow

through their renormalised parameters.

Thus, below the MCT one expects equilibrium, ergodic phase behaviour. Between these two lines one expects a fluid of cluster that is ergodic at large length scales. Above the MCT line one expects a non-ergodic state, which is essentially a repulsive glass of the clusters. A plot of the CMCT line and the bare MCT line for the parameters of my experimental system are shown in figure 8.7, together with my experimental data.

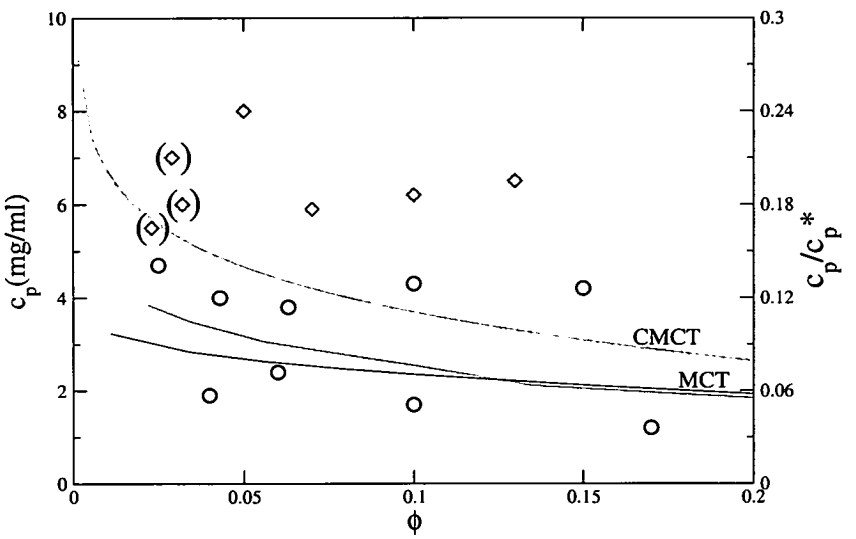

Figure 8.7: Phase diagram in the (ϕ, c_p) plane. The data points are those presented in chapter 8.2, the upper line is the predicted position of the CMCT non-ergodicity line, and the lower lines are the MCT predictions of the non-ergodicity line with and without the correction to the polymer R_g and size ratio ξ. Samples which took timescales of hours to form are bracketed (◊).

Consider now what differences between these two states might be observable. Above the MCT line but below the CMCT line, the clusters might be considerably larger than the field of view of the microscope, but one would expect diffusion on the scale of the clusters. However, samples above the CMCT should be truly arrested.

As described in section 8.2.2, some of the samples at low volume fraction took a long time to become non-ergodic, and the lowest sample ($\phi = 0.024$, $c_p = 5.5$) never appeared non-ergodic in the timescale of the experiment ($\sim$ 2 hours). In table 8.1 I list the time taken for the aggregated clusters to appear non-ergodic, for samples with different volume fractions.

The three samples with $\phi < 0.05$ take long times to become non-ergodic $\sim$ 80 minutes (if

ϕ	τ (min)
0.03	~ 80
0.05	~ 15
0.07	~ 10
0.1	~ 5
0.15	~ 3

Table 8.1: Table showing the time taken for clusters to appear non-ergodic (τ) for a range of volume fractions.

at all). These samples can be distinguished from the remaining samples (which became non-ergodic within $\sim 5 - 15$ minutes), and are bracketed in the phase diagram in figure 8.7. It is suggested that these samples may lie between the MCT and CMCT lines and so are an ergodic fluid of large, non-ergodic clusters, henceforth referred to as scenario 1.

However, non-ergodicity takes a finite time even at the higher volume fractions, so the CMCT picture of a cluster phase could also be applied to *all* the samples. In this case, the CMCT 'gel' (i.e. a repulsive glass of large clusters) may in fact lie at higher polymer concentrations than those observed, and all samples which aggregated lie between the MCT and the CMCT lines. This will be referred to as scenario 2.

Gravitational Effects

However, almost all of the samples (including some at low volume fraction $\phi < 0.05$) did eventually appear non-ergodic, as in the images shown in figure 8.4. If the samples at $\phi < 0.05$ are an ergodic fluid of clusters, as in scenario 1, (or indeed if *all* the samples are an ergodic fluid of clusters, as in scenario 2), then how can this eventual appearance of non-ergodicity be explained?

The simplest CMCT scheme outlined here neglects thermal fluctuations, and tacitly assumes that the system is perfectly density matched. In a real system, where thermal rearrangements will occur, and density matching is never perfect, the cluster phase would be expected to have a finite lifetime. Thus, for example, even a small amount of sedimentation would cause the clusters to jam.

To quantify the extent of sedimentation, the degree of density matching of the sample can be determined. As stated in chapter 7.3.4, the samples were centrifuged at 3000 rpm for 24 hours

with no sedimentation. After $\sim$ 48 hours there was typically $\sim$ 5mm of sedimentation visible. Using this rate, the difference between the density of solvent and particles can be estimated. The downward velocity of the particles in the centrifuge is given by equation 8.8:

$$v_s = \frac{2\Delta\rho g a^2}{9\eta}, \tag{8.8}$$

where η is the viscosity, $\Delta\rho$ is the density difference between the particles and solvent and a is the particle radius. The radius of the centrifuge is $r \sim$ 10cm and the speed is 50 revolutions per second, giving an angular velocity of $\omega = 50 \times 2\pi$ rad/s. The acceleration is then simply $\omega^2 r \sim 1000g$. Estimating now that the particles sediment by $\sim 5mm$ in 48 hours, the velocity of the particles is $\sim$ 30nm/s. Rearranging to find the density mismatch gives $\Delta\rho = 0.12kg.m^{-3}$. The sedimentation velocity of clusters of radius $\sim$ 25 particles in a sample that is being observed in the microscope is given by:

$$v_s = \frac{2 \times 0.12 \times g \times (25R)^2}{9\eta} \sim 20\text{nm/s}, \tag{8.9}$$

It is clear that even though the system is nearly density matched, the slight density mismatching could cause large clusters to sediment distances comparable to a particle diameter within a minute (note that a single particle would have a sediment velocity of only 0.03nm/s). In this calculation it has been assumed that the *cluster* density is the same as the colloid density, but in reality the solvent incorporated into the clusters would decrease the cluster density, decreasing the density difference in the calculation. However, it is possible that large clusters could sediment far enough within the timescale of an experiment to cross the CMCT transition line, and change from being an ergodic cluster-fluid to becoming a non-ergodic cluster-glass.

Having demonstrated that sedimentation of large clusters would be sufficient to cause eventual gelation of samples that were initially cluster-like, can a distinction be drawn between samples which became non-ergodic over long times $\sim$ 1 hour, and those that became non-ergodic within shorter times $\sim$ 15 minutes? It is tempting to identify the long-lived clusters, at $\phi < 0.05$, with the CMCT predicted cluster phase, and the eventual cessation of fluctuations as due to the imperfect density matching in the sample. However, a detailed interpretation of the results in terms of the MCT and CMCT lines is still speculative.

8.3 System 2

Charged Colloids in a Density Matched Solvent

8.3.1 Phase Diagrams

In this section the phase behaviour of charged PMMA colloids on the addition of non-adsorbing polystyrene is presented. Fluorescently labelled PMMA colloids were suspended in the CHB-*cis*-decalin density matched solvent. The colloids were observed to crystallise at volume fractions $0.31 < \phi < 0.36$, for a full description see chapter 7.3.1. Linear polystyrene with a molecular weight $M_w = 212400$ and radius of gyration of $R_g = 13.7$nm was used. The phase behaviour was studied using two different sized colloids, PMMA of radius 660nm and 535nm. The phase diagram was determined for each, figures 8.8 and 8.9.

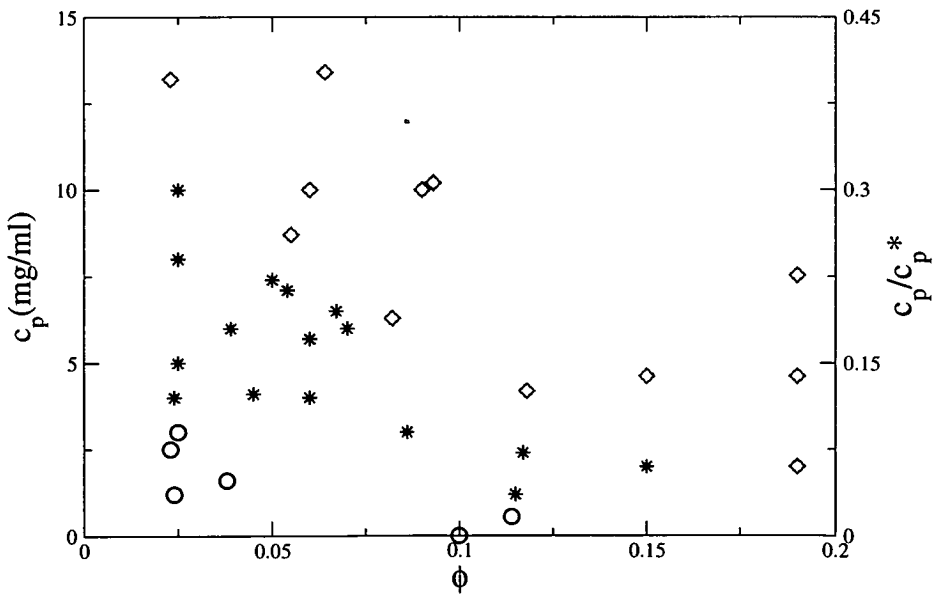

Figure 8.8: Phase diagram of charged and density matched PMMA on the addition of polystyrene, size ratio $\xi = 0.021$, showing regions of fluid(○), small clusters(⋆), and large non-ergodic aggregates(◇).

Three types of behaviour were observed in this system. At low polymer concentrations samples remained in an ergodic, homogeneous, single fluid phase (○, figures 8.8 and 8.9). A confocal micrograph of such a sample is shown in figure 8.10(a). On increasing the polymer concentra-

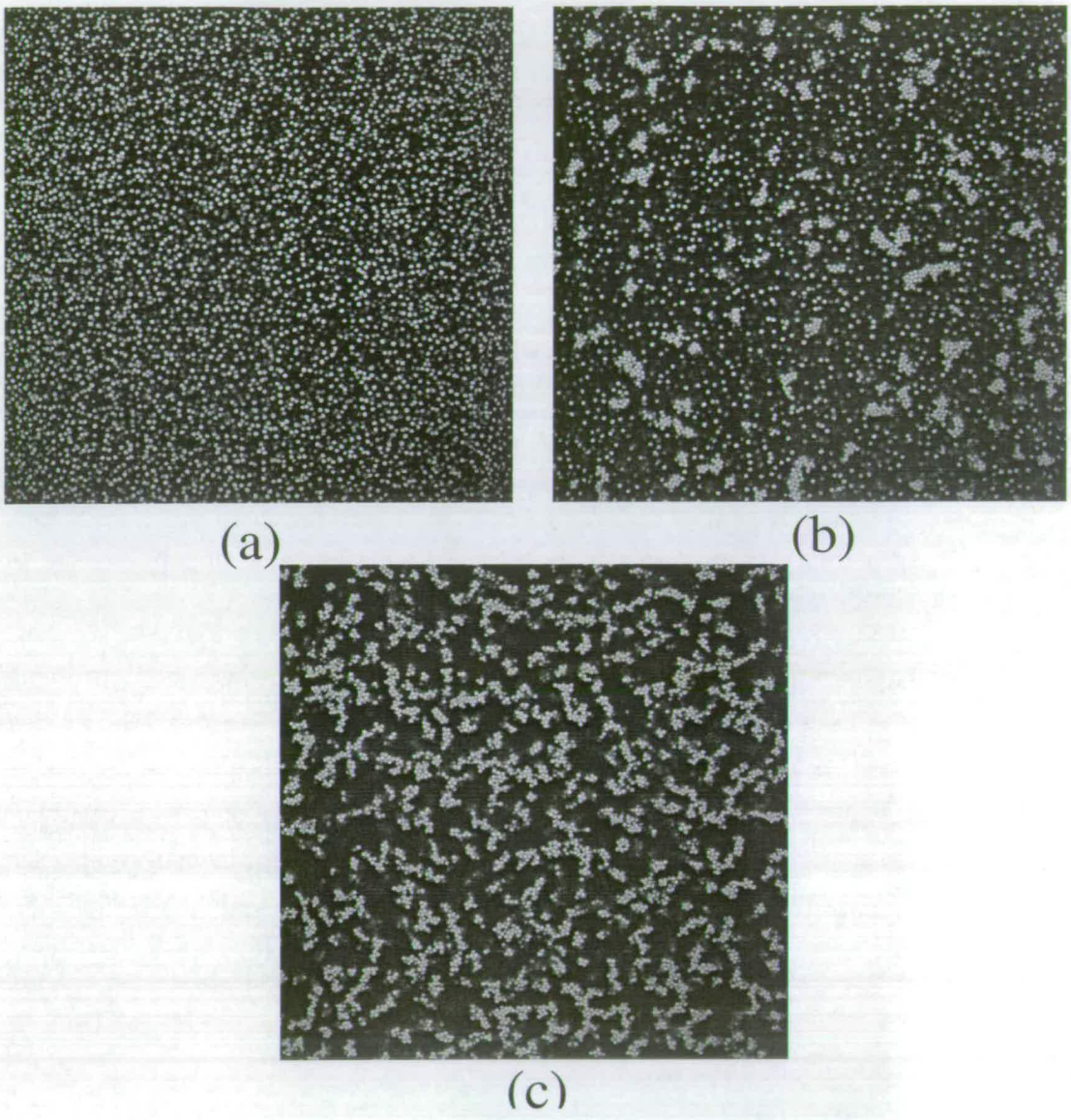

Figure 8.10: Confocal images of samples (a) $\phi = 0.01$, $c_p = 0.5$ mg/ml, (b) $\phi = 0.086$, $c_p = 3$ mg/ml and (c) $\phi = 0.082$, $c_p = 6.3$ mg/ml taken 1 hour after sample preparation.

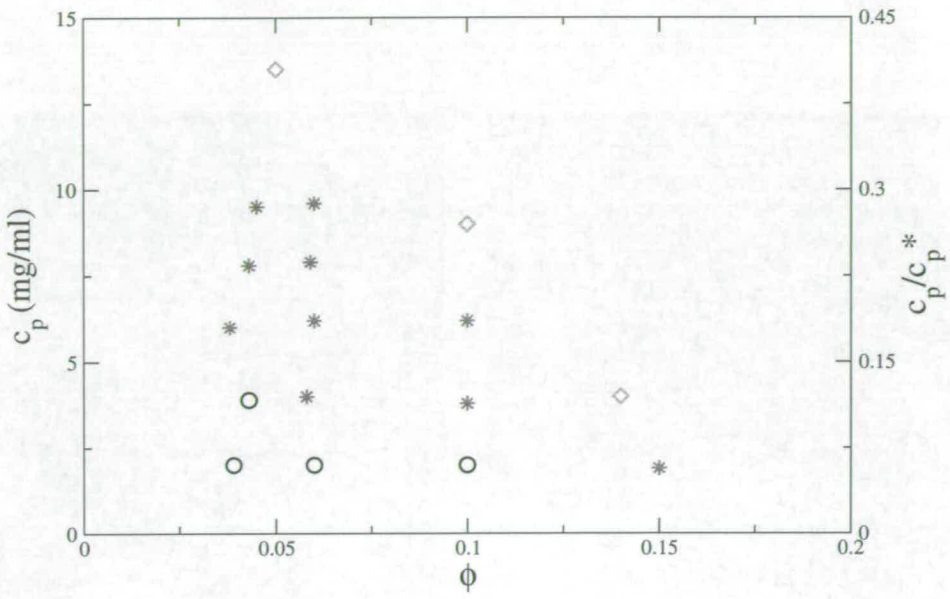

Figure 8.9: Phase diagram of charged and density matched PMMA on the addition of polystyrene, size ratio $\xi = 0.026$, showing regions of fluid(○), clusters(⋆), and gel(◇).

tion above a sharp transition (⋆, figures 8.8 and 8.9) the colloids aggregated into small, long-lived clusters of at most tens of particles, which remained mobile over timescales of at least hours and coexisted with a sea of monomers, figure 8.10(b). These observations are reminiscent of the 'cluster phase' identified by Segre *et.al.* [91]. At the highest polymer concentrations observed colloids aggregated into non-ergodic structures reminiscent of the non-ergodic samples observed in the uncharged system (system 1, section 8.2). These samples are shown as ◇ figures 8.8 and 8.9, and a confocal micrograph is shown in figure 8.10(c).

8.3.2 Detailed Observations

The topology of the phase diagrams for this system is different from the 'standard model' system previously discussed, in particular there exists a phase of small, long lived clusters (⋆ in figures 8.8 and 8.9). Figure 8.11 shows a short series of images of a sample in which these clusters were observed. The images were taken ten seconds apart, the sample volume fraction was $\phi = 0.086$ and polymer concentration $c_p = 3$ mg/ml, and the system had a size ratio $\xi = 0.021$. To illustrate their mobility two particular clusters have been highlighted. Following

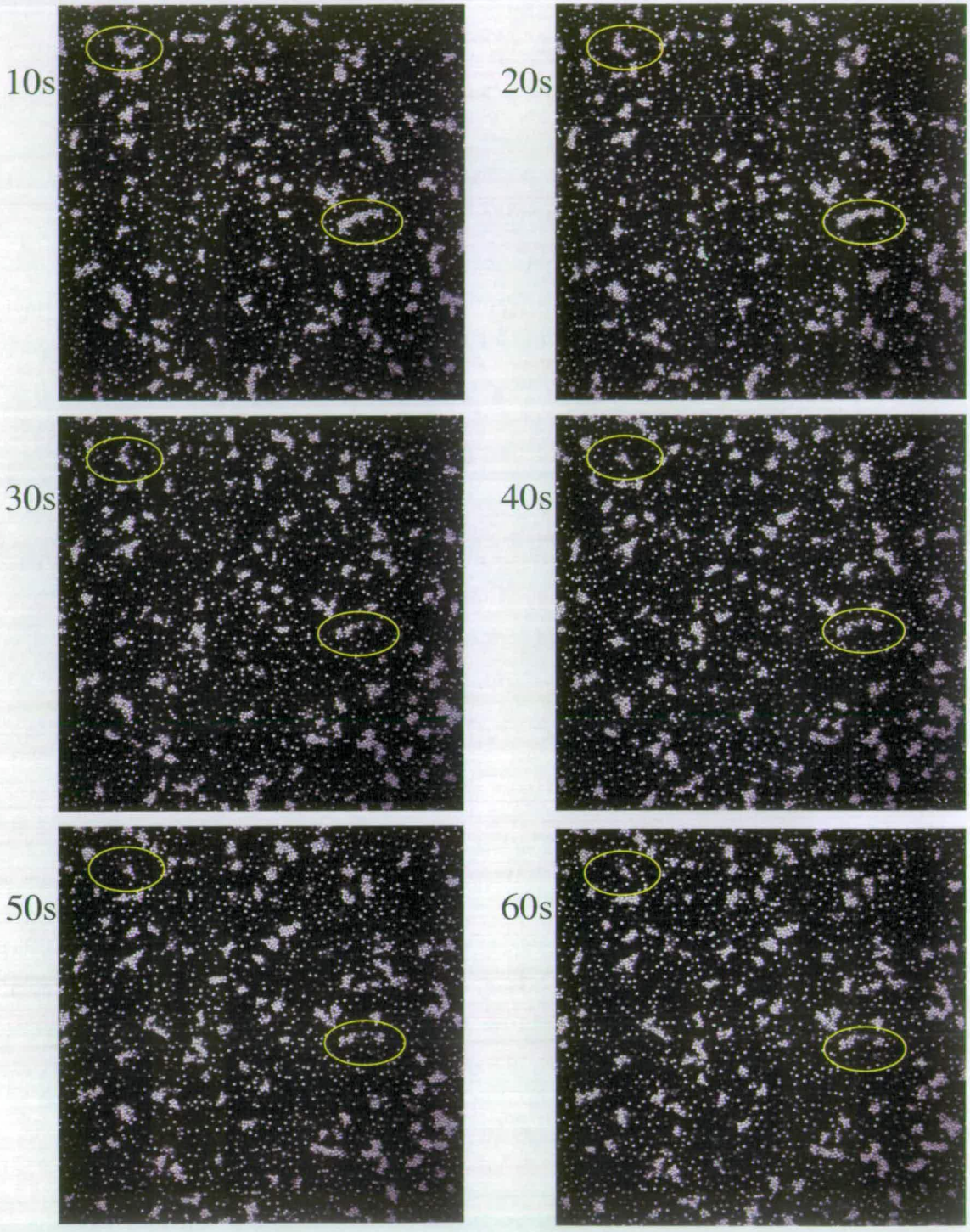

Figure 8.11: A time series of sample $\phi = 0.086$, $c_p = 3$ mg/ml showing a short time behaviour of a cluster sample. Images were taken 1 hour after sample preparation, and each image is separated by 10 seconds.

closely the shape and relative position of these clusters, it can be seen that they diffuse in three dimensions, and their position and orientation differs from one image to the next.

Figure 8.12 shows a similar series of images, again taken ten seconds apart, of a sample from the same system that became non-ergodic ($\phi = 0.082, c_p = 6.3$ mg/ml). In this case, the highlighted particles remain in the same position and orientation throughout this time series, illustrating the non-ergodic nature of this state.

To illustrate the behaviour of the cluster and gel phases over longer time periods, images taken after 1, 30 and 60 minutes are presented. Figure 8.13 shows such a time series for two samples at high volume fraction ($\phi = 0.15$), one in which clusters were observed, and the other which became non-ergodic, in the system of size ratio $\xi = 0.026$. Figure 8.14 shows a similar time series for examples of the cluster and non-ergodic states at a lower volume fractions ($\phi = 0.06$).

In the first image of each time series the two samples appear very similar. However, by the second image of each series the difference between the two states is apparent. The clusters remain a similar size to when they first formed, and coexist with a sea of monomers. In contrast, the samples at a higher polymer concentration have formed large, 3-dimensional networks incorporating the majority of the particles. Shorter time series of these samples illustrate that the small clusters are free to diffuse, but samples at the highest polymer concentrations are non-ergodic, as in figures 8.11 and 8.12.

8.3.3 Interpretation

Cluster Stabilisation

Comparison to the phase behaviour of the uncharged colloids implies that the small, long-lived clusters may be a consequence of the charge on the particles. The initial stages of aggregation look similar in the two systems. This suggests that the initial cause of aggregation in the two systems is the same, but that the clusters in the charged system are somehow stabilised against further aggregation.

In a theoretical treatment, Groenwold and Kegel [33] have explored the effect of charge on an aggregating system (discussed in depth in chapter 4.6). By first assuming an aggregating colloidal system with an attractive interaction, the consequences of adding a charge on the particles are predicted. The onset of aggregation results in the formation and growth of clusters of particles. However, when the clusters have reached a particular size (dependent on the parameters of the system) the electrostatic repulsion between the cluster and a nearby particle

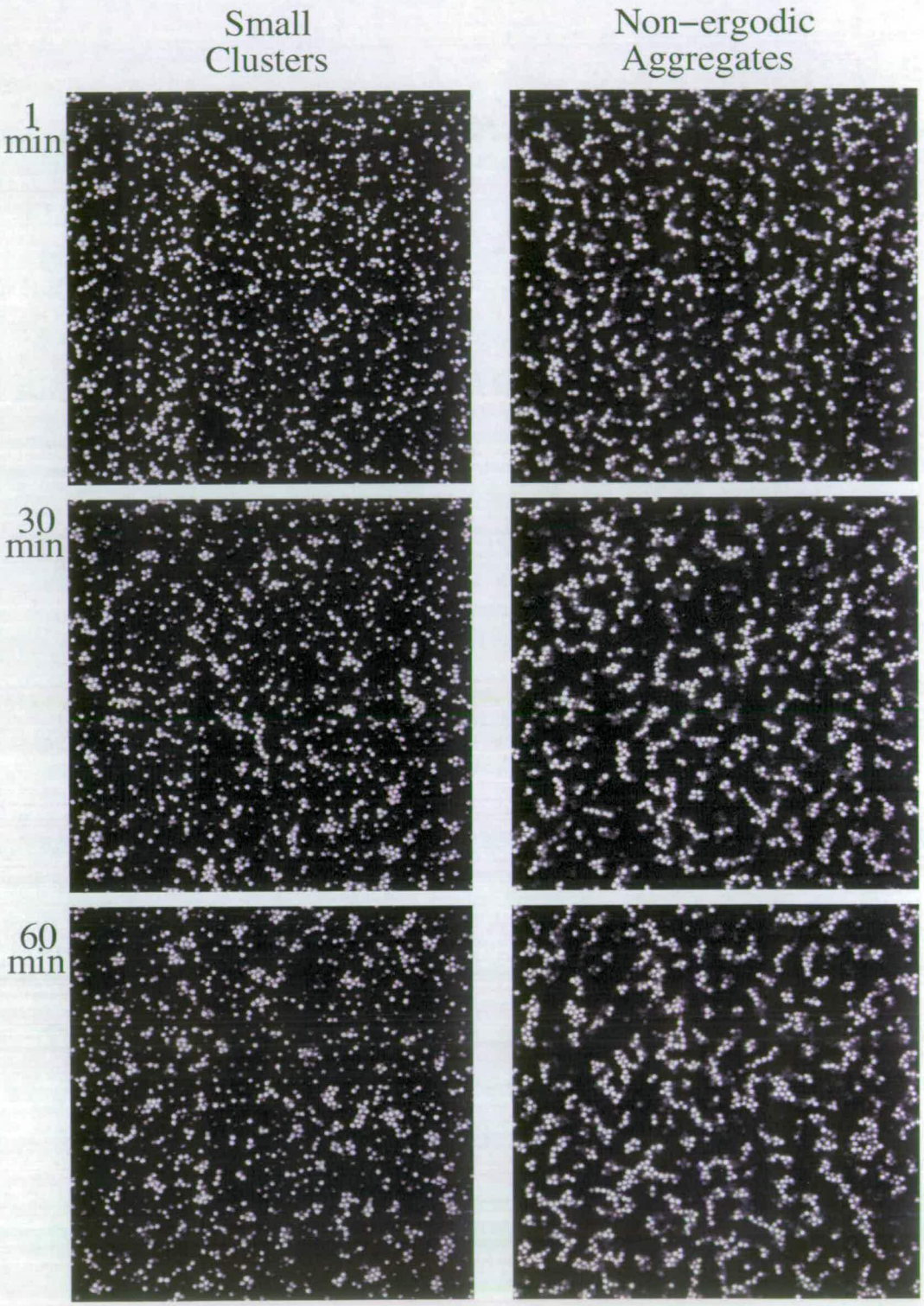

Figure 8.13: A series of images of sample $\phi = 0.15$, $c_p = 1.9$ mg/ml showing the behaviour of a cluster sample over time, and $\phi = 0.15$, $c_p = 4$ mg/ml showing the behaviour of a non-ergodic sample over time. Both samples had high volume fractions. Images were taken 1 minute, 30 minutes and 1 hour after sample preparation. The images have been enlarged for clarity.

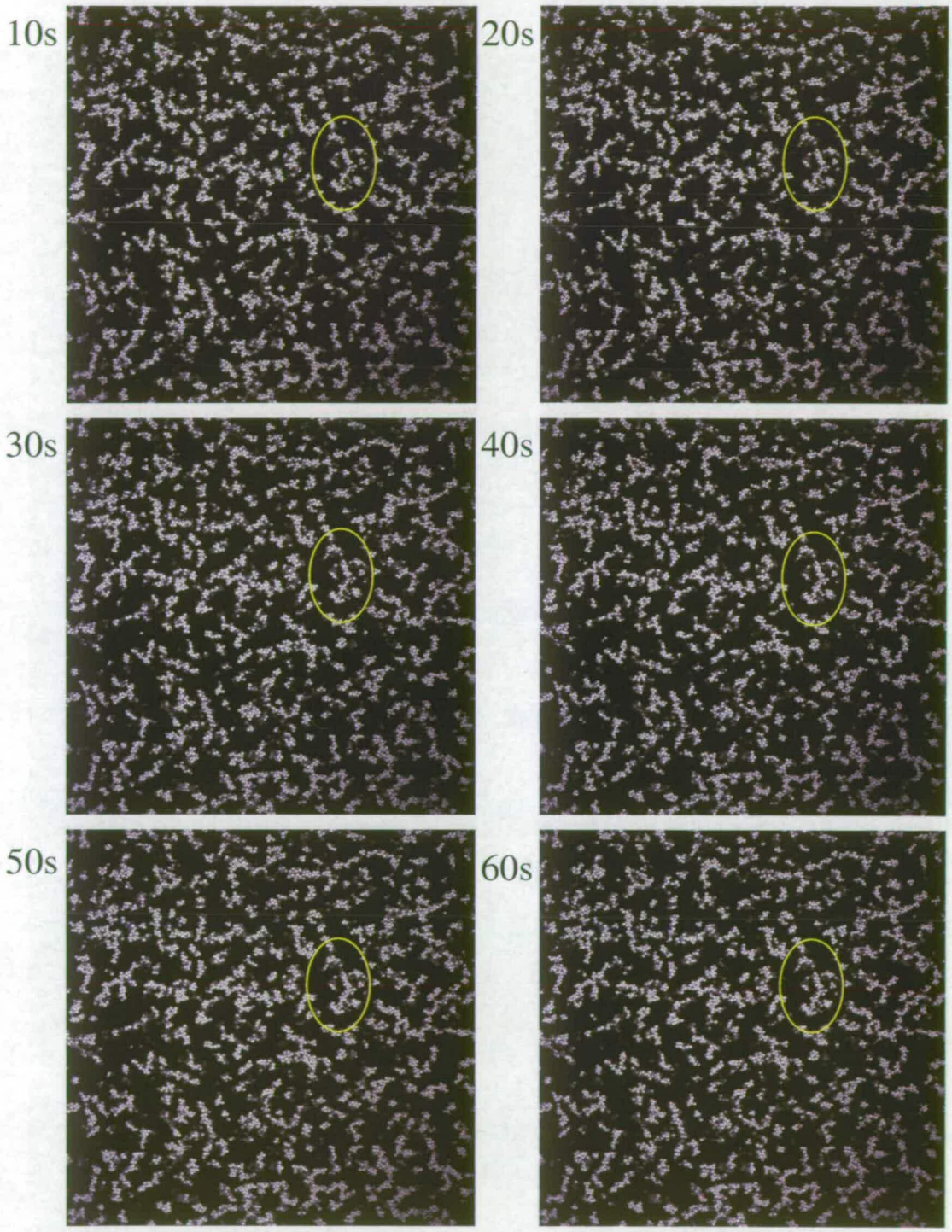

Figure 8.12: A time series of sample $\phi = 0.082$, $c_p = 6.3$ mg/ml, showing the short time behaviour of a non-ergodic sample. The images were taken 1 hour after sample preparation and each image is separated by 10 seconds.

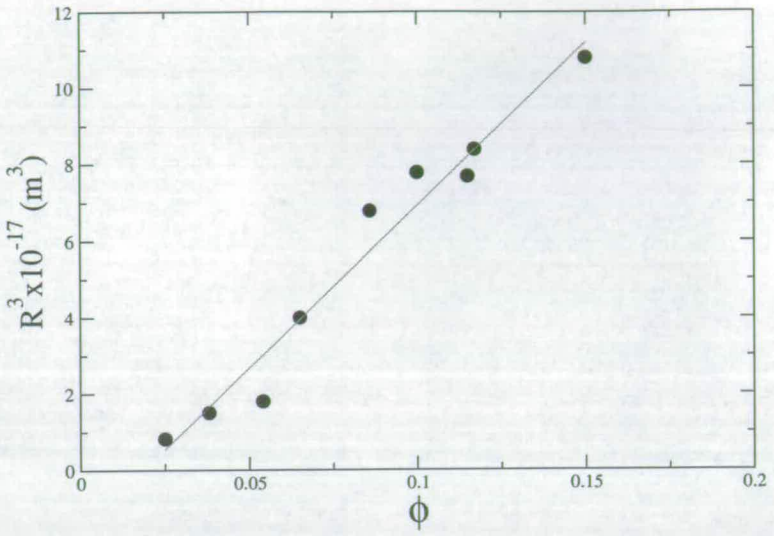

Figure 8.15: Plot showing the variation of cluster radius with volume fraction.

prevents further growth. In this way a stable and equilibrium cluster phase is predicted. The aggregation number (that is the number of particles per cluster when the electrostatic repulsion becomes great enough to prevent any further growth) is dependent on the charge per particle. The charge on each particle is dependent on the volume fraction, because of the increase in the free volume for the dissociated ions on diluting the system. From this they make the prediction that $R_\star \propto \phi^{\frac{1}{3}}$, where $R_\star$ is the cluster radius.

To compare their prediction to my experimental results the average cluster radius was determined in the following way. For each sample a sequence of images was taken through the sample in 0.3μm steps. From these sequences, the three dimensional structure of each cluster can be seen, and the axis of each cluster found. The diameter of each cluster was measured in pixels. This process was repeated for twenty clusters at each volume fraction, and at approximately constant polymer concentration of $2 - 4$ mg/ml. The average radius of the clusters was calculated for each volume fraction. A plot of $R_\star^3$(m) vs ϕ is shown in figure 8.15.

On first sight the theory appears to fit the experimental data well. However, the graph should go through the origin, since a sample with no colloids in must result in a cluster radius of zero, and for a finite number of colloids a negative cluster radius would be unphysical. Therefore it is now discussed why the gradient of the best fit line to the experimental data cannot be extrapolated to zero, but intercepts the x axis at a finite colloid volume fraction of $\phi = 0.02$.

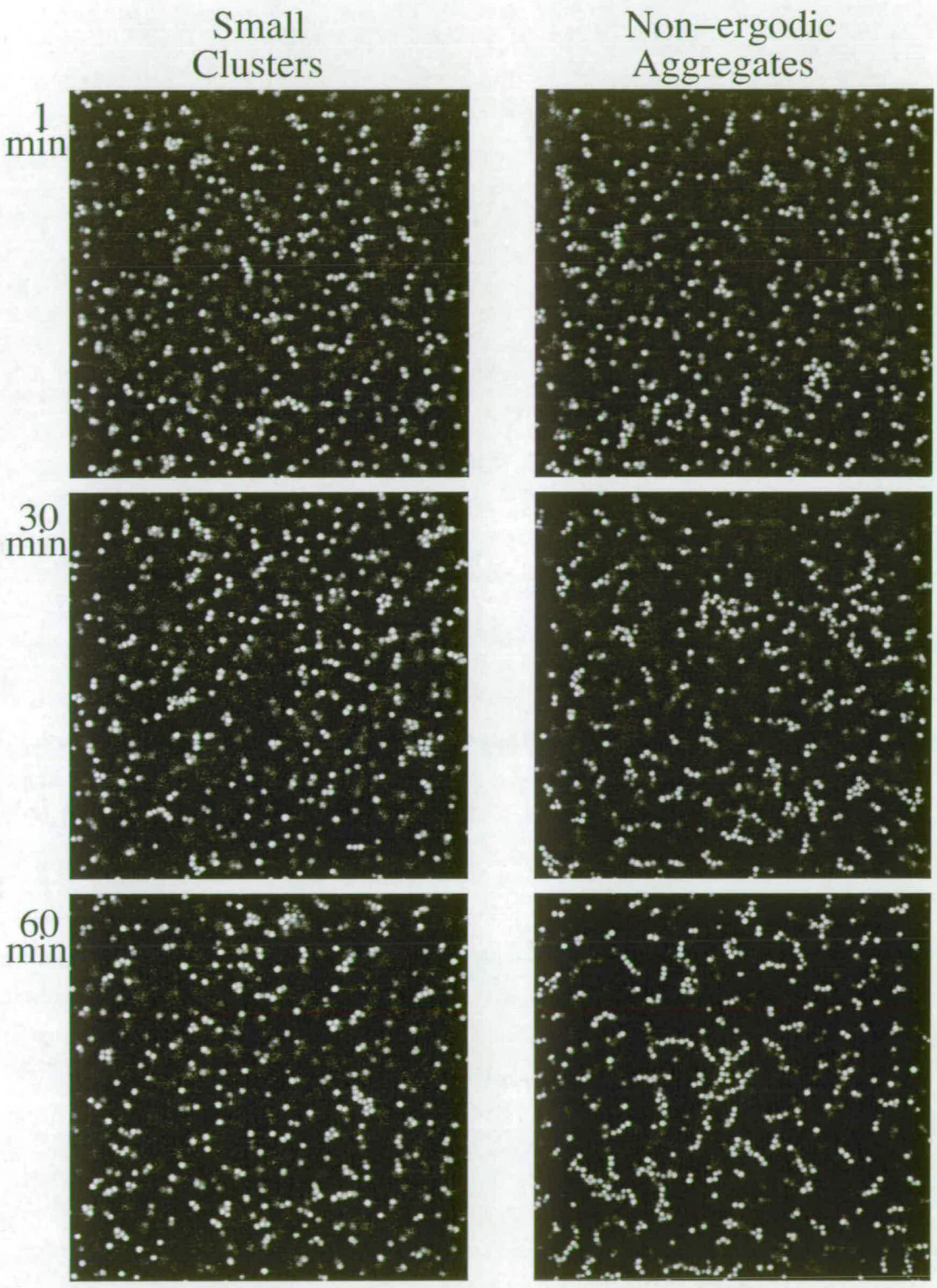

Figure 8.14: Sequence of images of sample $\phi = 0.06$, $c_p = 9.6$ mg/ml showing the behaviour of a cluster sample with time, and $\phi = 0.05$, $c_p = 13.5$ mg/ml showing the behaviour of a non-ergodic sample with time. Both samples have low volume fractions. Images taken 1 minute, 30 minutes and 1 hour after initial sample preparation. The images have been enlarged for clarity.

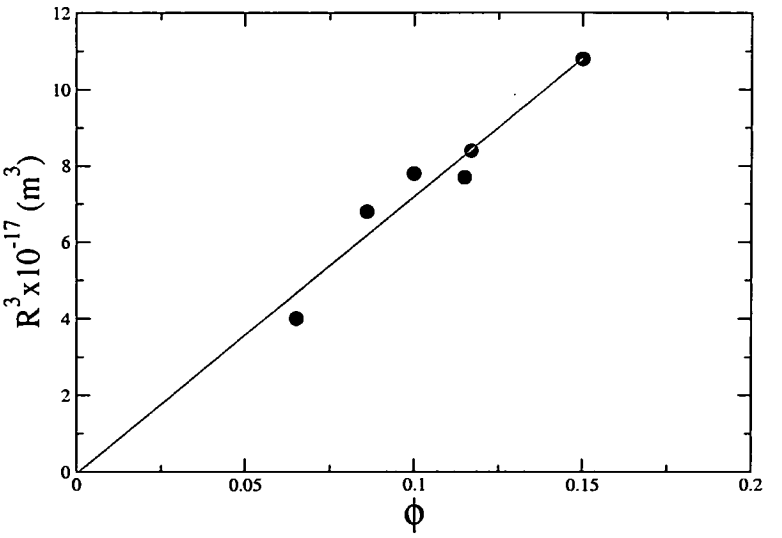

Figure 8.16: Plot showing the variation of cluster radius with volume fraction, for volume fractions $\phi \gtrsim 0.07$.

Consider first errors which may arise in the measurement of the cluster radius. Twenty cluster were measured at each volume fraction, giving as an example a standard error in the mean value of R^3 for the sample $\phi = 0.054$ as $\sigma = \pm 0.1\%$. Further consideration of the graph shows that the discrepancy is at samples of low volume fraction, where the cluster size appears to be too small. For the descrepancy to be a human error in counting, then all the biggest clusters must have been missed, an unlikely mistake to make since the biggest clusters are the most easily observed.

Therefore, we turn instead to the physics to find a reason why the cluster size should be lower than predicted at low volume fractions. Groenwold and Kegel made certain approximations in their calculation, and one that seems particularly important here is that the number of particles per cluster $N \gg 1$. At volume fractions below $\phi = 0.07$, the clusters have a radius of less than 3 particles, so it seems reasonable to suggest that this approximation will not hold at low volume fractions $\phi \lesssim 0.07$ (note that this particular choice of the cut of is somewhat arbitrary, but below this value the experimental data is consistently lower than the theory would predict). To test this hypothesis, the graph is re-plotted excluding all points below $\phi = 0.07$, figure 8.16. It can be seen that by excluding these points, where the theory will no longer be valid due to the low aggregation number N, a straight line fit through the data passes through the origin.

The relationship between the critical radius $R_\star$ and the volume fraction predicted by Groenwold and Kegel [33] is given by equation 8.10, where k is a geometrical constant dependent on the size of the clusters, γ is a surface tension in units of k_BT per surface area and v is the particle volume. The typical distance between charges is given by b, l_B is the Bjerrum length, and $\Delta\epsilon = l_B/b$ is the dissociation energy. The charge density is σ and s is the surface area of the particle, so σs is the number of dissociation sites per particle.

$$R^3 = k^3 \left(\frac{\gamma v b^3 e^{\Delta\epsilon}}{l_B \sigma s} \right) \phi \tag{8.10}$$

The constant of proportionality between $R_\star^3$ and ϕ for PMMA colloids in CHB can be calculated using the following parameters. The geometric constant k for disk-like clusters is given as $k = 2.23$ [33]. The number of dissociation sites per particle is σs, and following the estimate of the charge per article in chapter 7.3.1 I take this to be 700 electronic charges. The surface tension γ is taken to be $U_{dep}(k_BT)$/surface area. The potential U_dep is calculated to be $U_{dep} = 4.8k_BT$ (for Maple code used to do this calculation see Appendix D), so $\gamma v = \frac{U_{dep}}{a^2} a^3 \sim 9 \times 10^{-7}$ m.

The Bjerrum length is given by $l_B = e^2/4\pi\epsilon_0\epsilon_r k_BT$. The dielectric constant of CHB is $\epsilon^{chb} = 5.3$, and that of decalin is $\epsilon^{decalin} = 2.15$. In the solvent used here they were mixed together at a ratio of $4:1$, and the dielectric constant of the solvent mixture was calculated in chapter 7.3.1 to be $\epsilon = 4.1$. Therefore the Bjerrum length can be calculated, and at room temperature in a solvent of dielectric constant $\epsilon_r = 4.1$, $l_B = 13.7$ nm.

The distance between opposite charges b is not known with certainty [33] and appears in the exponential. Therefore, using the above values for all the other parameters, the theory is fitted to the experimental data to obtain an estimate of b. The experimentally determined value for this constant of proportionality (given by the gradient of figure 8.16) is 7.3×10^{-16}, and fitting to this value gives an estimated distance of charge separation $b = 0.465$ nm. Given that b is the separation of charges, a reasonable estimate would be to take the radius of a bromine ion as a suitable length, since they are likely to be the counter-ions in the system (see discussion in chapter 7.3.4). The radius of a bromine is 0.2 nm, so the separation of two charges would be ~ 0.4 nm, and the value of $b = 0.465$ nm obtained from fitting the theory to the experimental data this way is not unreasonable.

Finally, by minimising the free energy of a range of different shaped clusters, Groenwold and Kegel predict that the preferred shape of the clusters is a disk rather than a sphere. Figure 8.17 shows a reconstructed image of a cluster using real particle coordinates from sample $\phi = 0.086$

MCT and CMCT Predictions

The sharp onset of aggregation (in this case leading to the stable cluster phase) occurs in the same region of the phase diagram as the onset of aggregation in the 'standard model' system. Furthermore, the initial stages of samples just above the first aggregation boundary look very alike in the two systems, figure 8.18.

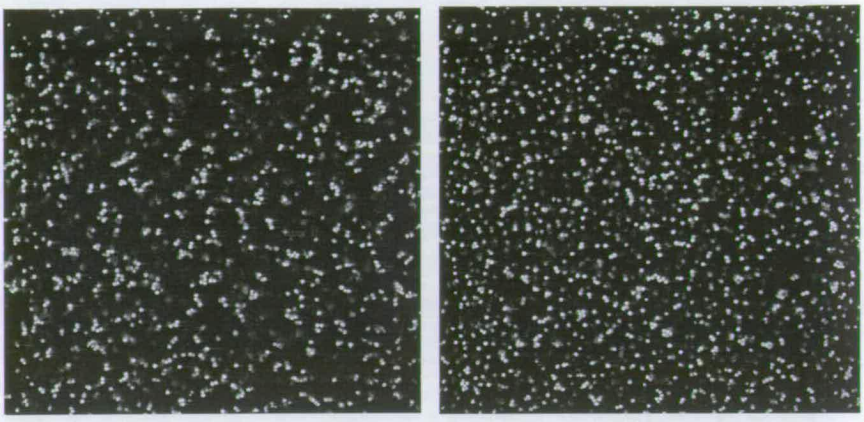

(a) (b)

Figure 8.18: First images, taken initially after sample preparation, of samples (a) $\phi = 0.029$ and $c_p = 7$mg/ml from the standard model system and (b) $\phi = 0.06$ and $c_p = 9.6$mg/ml from the charged phase diagram. Sample (a) evolves into large CMCT-predicted clusters and eventually turns non-ergodic whereas sample (b) evolves into the stable cluster phase which coexists with monomers. However, the initial stages of aggregation look very similar in the two different systems.

How does this fit with our earlier interpretation in terms of MCT and CMCT? We suggest that above the MCT non-ergodicity line the particles begin to aggregate, in the same way as for the standard model system. However, in the charged case there is a repulsion which prevents the clusters from growing further once they have reached a critical radius R^* as discussed in section 8.3.3. In this way the charge on the particles provides a mechanism for selecting the *size* to which the clusters can grow. The initial aggregation of the particles, however, is due to the sample become locally non-ergodic above the MCT transition line.

But what now of the non-ergodic behaviour observed at the highest polymer concentrations? It would be reasonable to suggest that an electrostatic repulsion would shift the CMCT transition line to higher polymer concentrations [48]. Therefore it is speculated that the samples become non-ergodic when they cross the CMCT line, that is, where the aggregating clusters become a repulsive glass.

and $c_p = 3$mg/ml, in which the cluster can be seen to be non-spherical (code provided by P. Smith [94]). Given this combined evidence, the observations are interpreted as follows. As the clusters grow the charge per aggregate increases. Once the clusters have reached a critical size given by $R_\star$ their electrostatic self energy prevents any further growth, and a long-lived and stable cluster phase is observed. If the charge is screened by adding salt (as in the first experimental system discussed) this mechanism of preventing cluster growth disappears, and aggregation continues.

Figure 8.17: Computer generated image, using particle co-ordinates of a typical cluster in sample $\phi = 0.086$ and $c_p = 3$mg/ml.

One striking difference between the 'cluster phase' and the non-ergodic samples is the coexistence of the clusters with a sea of monomers. In the Kegel model, the monomers are prevented from joining the clusters by electrostatic repulsion due to the *total* charge on the clusters. Implicit in this model is that the Debye screening length must be at least as large as the cluster, so that the net charge of a cluster can be felt by a neighbouring monomer. The initial fast aggregation of the particles slows down as the total charge on the cluster increases. This allows for rearrangement as aggregation proceeds, and the aggregates compactify into small but dense clusters coexisting with monomers.

However, as the polymer concentration increases, the rearrangement slows down and the clusters remain ramified for longer. Simultaneously, the increase in the surface tension γ means that the critical radius R_* increases, so the clusters can grow larger. Together these effects allow the cluster radius to exceed the Debye screening length. A neighbouring monomer will no longer feel repulsion from the net charge of the cluster, since some of the charge will be screened. This allows for the continued growth of the aggregates until a large, ramified non-ergodic structure is formed.

8.4 System 3

Uncharged Colloids in Gravity

8.4.1 Phase Diagram

In this section the phase behaviour of PMMA colloids suspended in *cis*-decalin on the addition of polymer is presented. This system differs from that presented in the first section (the 'standard model') because the particles and solvent have a different density, so sedimentation due to gravity will be more pronounced. The same fluorescently labelled PMMA colloids are used, and their radius in this solvent was measured to be 527nm. Polystyrene of molecular weight 212,400 daltons has a radius of gyration in *cis*-decalin $R_g = 13.7$ nm at $25°C$ [10], giving a size ratio of $\xi = 0.026$.

At low polymer concentrations samples remained in an ergodic, homogeneous, single fluid phase (○, figure 8.19). At high volume fractions $\phi \gtrsim 0.05$, on increasing the polymer concentration (◇, figure 8.19) the colloids aggregated into large non-ergodic structures reminiscent of the non-ergodic samples observed in the density matched system (section 8.2). However, on increasing the polymer concentration at lower volume fractions $\phi \lesssim 0.05$ (⋆, figure 8.19) the colloids aggregated into clusters which sedimented, the resulting phase being a dense population of aggregated colloids in the lower section of the sample, with a colloid-sparse region above it.

8.4.2 Detailed Observations

The phase observed at low ϕ and at moderate to higher c_p, (⋆, 8.19), will now be described in more detail. Figure 8.20 shows confocal micrographs of sample $\phi = 0.038$ and $c_p = 3.8$ mg/ml, taken ten minutes after preparation at a range of depths into the sample. All depths are measured from the bottom on the sample upward into the bulk. The build up of a dense (but not random close packed) sediment at the bottom of the sample is evident, while above $\sim 20\mu$m the colloids are formed into small clusters which are not part of the sediment.

A time series of images taken at $30\mu m$ above the cover slip of this sample is shown in figure 8.21. The first image was taken straight away, and shows the initial formation of clusters before sedimentation, and the following images were taken at ten minute intervals. The clusters remain mobile but are falling rapidly. As they fall an amorphous sediment forms at the bottom

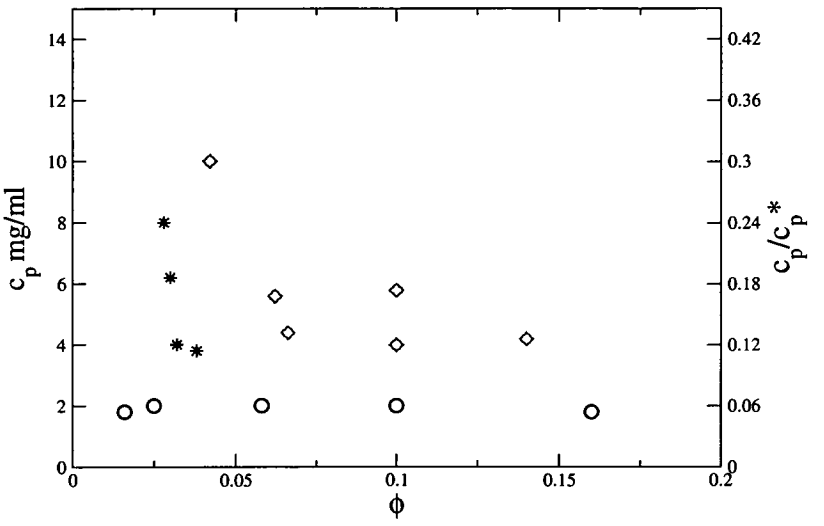

Figure 8.19: Experimental phase diagram PMMA-ps in cis-decalin, showing regions of fluid (○), large non-ergodic aggregates (◇) and sedimenting-clusters (⋆).

of the sample. The final state of such a sample is a dense (but not randomly close packed) sediment above which is an extended area of colloid-free solvent. The system never forms a sample-spanning structure since the clusters sediment too fast, and a colloid-sparse area inevitably builds up above the amorphous sediment forming at the bottom of the sample cell. There is a small region of individual clusters, a few particles deep, at the boundary between the sediment and the colloid-sparse phase above.

A series of micrographs illustrating the non-ergodic structure formed in sample $\phi = 0.066$, $c_p = 4.4$ mg/ml, taken at 30μm into the sample, is shown in figure 8.22. Each micrograph is separated by a time interval of 30 seconds, and the first image was taken ten minutes after the sample was placed on the microscope for observation. Although most colloids in the sample appear non-ergodic, sedimentation of some particles is clearly visible since the density of the gel increases with time. This suggests that either some particles break away from the surrounding structure and sediment, or that some particles are not incorporated into the structure fast enough and therefore sediment.

Consider for a moment the phase behaviour of the 'standard model' system presented in section 8.2. It was discussed it took a finite time for the samples to become non-ergodic. This timescale was experimentally found to be $5 - 15$ minutes for samples with volume fraction $\phi \gtrsim 0.05$, but

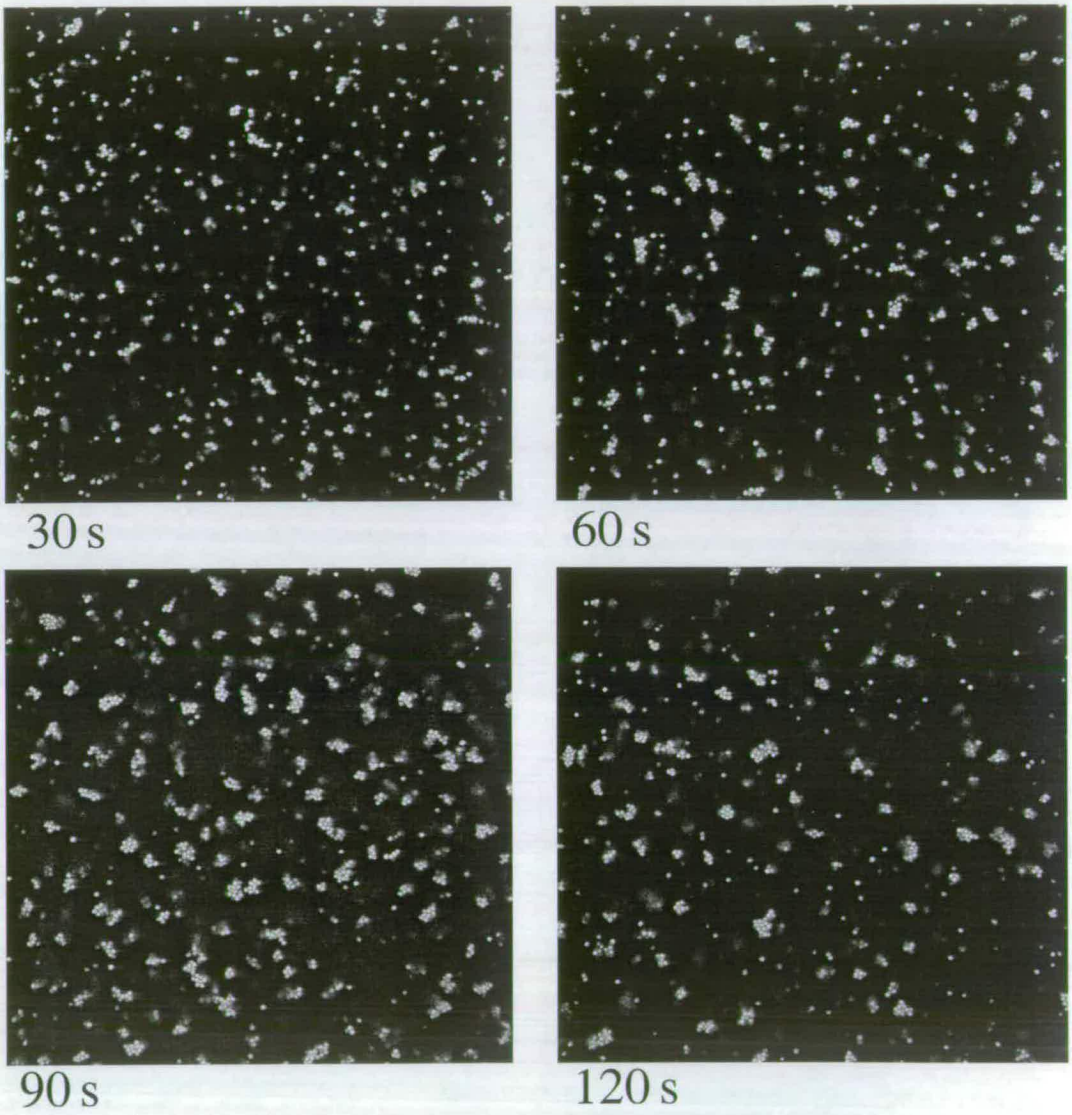

Figure 8.21: Sequence of images of sample $\phi = 0.038$, $c_p = 3.8$ mg/ml, taken ten minutes after initial sample preparation, at 30μm above the bottom cover slip. Each image is separated by 30 seconds.

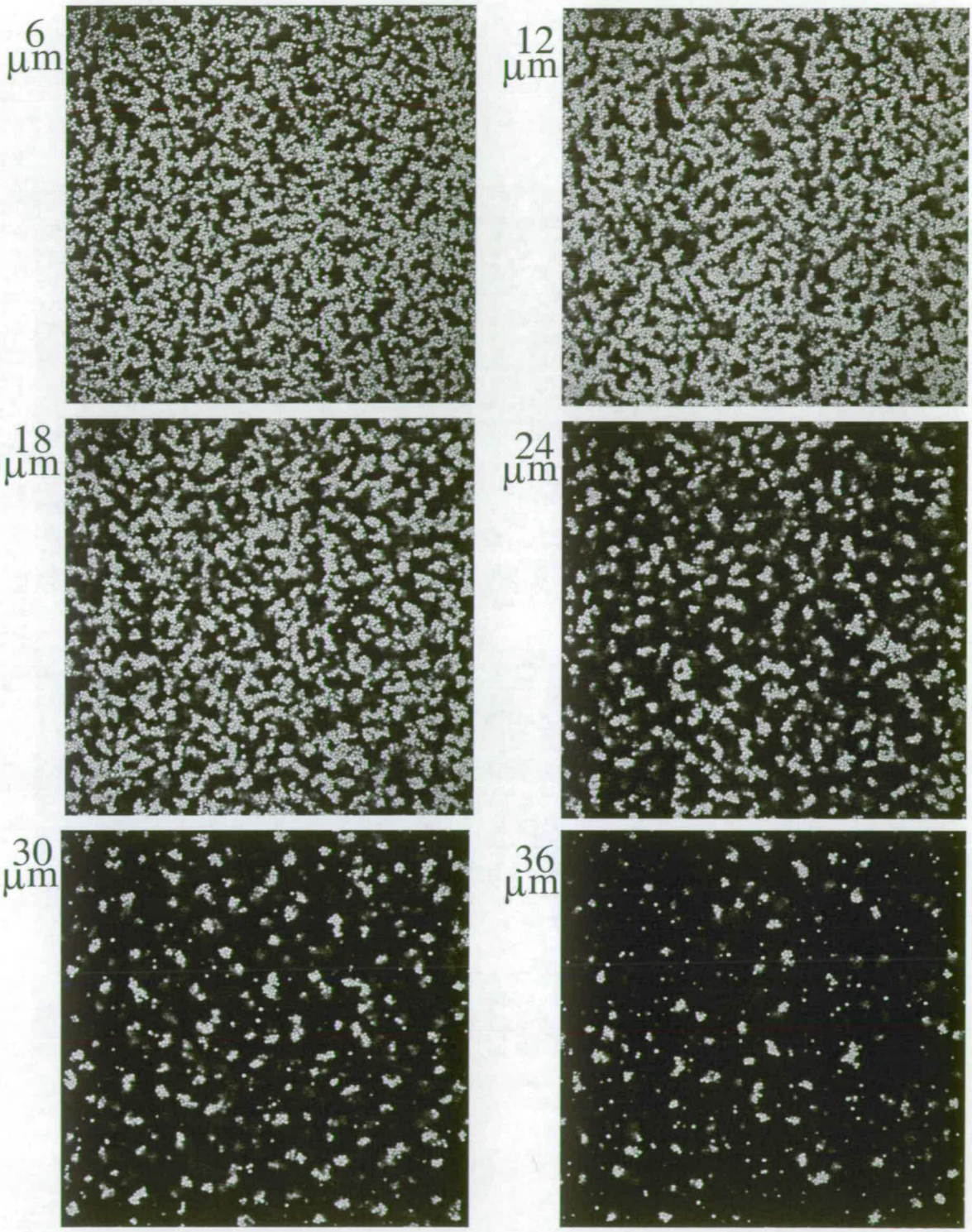

Figure 8.20: Series of images taken at different depths into sample $\phi = 0.038 c_p = 3.8 mg/ml$, taken at 6μm, 12μm, 18μm, 24μm, 30μm and 36μm into the sample. Images were taken ten minutes after initial sample preparation. The variation from a dense sediment to a sparse cluster phase as the height increases is clearly visible.

at lower ϕ it could take as long as an hour before samples appeared non-ergodic. An estimate of the sedimentation velocity of a single particle using equation 8.8 gives $v_s = 12\mu$m/min, and the gravitational Peclet number of a cluster of radius $\sim$ 10 particles is $Pe \sim 3$ (see chapter 3.6.5), so it is unsurprising that in the non-density matched system low ϕ samples sediment before they can become non-ergodic.

To summarise, there appear to be two competing timescales, the time it takes for the growing clusters to become non-ergodic, and the time in which they sediment. At low ϕ, the clusters sediment and a dense (but not random close packed), amorphous sediment forms at the bottom of the sample, leaving a colloid-sparse phase above. At higher ϕ the clusters grow large enough to become non-ergodic.

8.4.3 Interpretation

MCT and CMCT Predictions

The sharp onset of aggregation again occurs in the same region of the phase diagram as the onset of aggregation in the 'standard model' system, and the initial stages of samples look very alike in all three systems discussed so far. Thus it seems a reasonable interpretation to suggest again that above the MCT non-ergodicity transition line particles begin to aggregate. The same uncertainty as to whether the CMCT line is observed is still present, as discussed for the standard model.

If scenario 1 is assumed, then the samples which exhibited sedimenting-cluster behaviour are interpreted in the same way as the large-cluster samples in the standard model. It is clear that gravity has shifted the CMCT boundary to higher polymer concentrations compared to the standard model system, consistent with the expected effect of gravity on the CMCT line [48].

However, an alternative interpretation of the results would be that the CMCT line is higher than any of the samples observed, as in scenario 2. In a zero-gravity systems all samples would be an ergodic fluid of large clusters. It was discussed in section 8.2.3 that the small amount of gravity present in the density matched system causes the particles to sediment enough to form a gel in all but the uppermost region of the sample. The gravity present in this system may have the same effect. Initial sedimentation will increase the volume fraction of the majority of the sample at the expense of a colloid-sparse region above. If this effective volume fraction increases sufficiently, the clusters will become non-ergodic. The difference between the behaviour in this system compared to the density matched system is that at low volume fractions

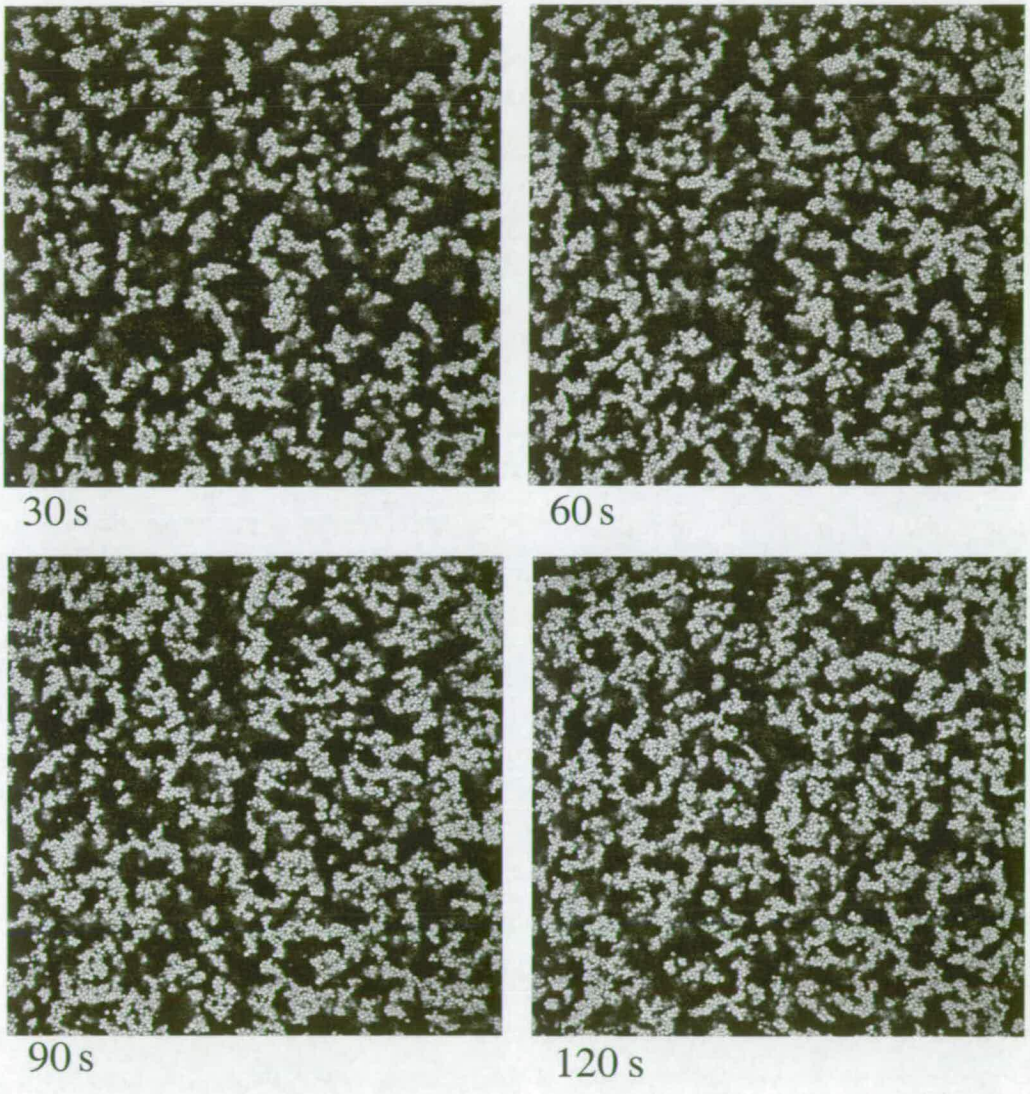

Figure 8.22: Sequence of images of sample $\phi = 0.066$, $c_p = 4.4$ mg/ml, taken ten minutes after initial sample preparation at 30μm above the bottom cover slip. The sequence of images shows the time evolution of a non-ergodic sample over the space of two minutes. Each image is thirty seconds apart.

sedimentation prevents non-ergodicity all together, resulting in the 'sedimenting cluster' phase observed.

Gravitational Effects

The effect of sedimentation on gelation has been considered by Poon [72] and Allain [2], and was discussed in chapter 3.6.5. It is suggested that due to the effects of gravity there is a threshold volume fraction $\phi^\star$ below which gelation does not occur. Below this threshold volume fraction the clusters cannot diffuse fast enough to form a sample-spanning network, but instead the clusters would sediment. The threshold volume fraction is given by:

$$\phi^\star \sim \left(\frac{9k_BT}{2\pi\Delta\rho g a^4}\right)^{\frac{d_f-3}{d_f+1}}, \tag{8.11}$$

where $\Delta\rho$ is the difference in the density between the particles and the suspending solvent, g is the gravitational acceleration constant, a is the radius of the particles, and d_f is the fractal dimension of the clusters, and for DLCA aggregates $d_f = 1.8$ (see chapter 3.6.5 for a full discussion). The threshold volume fraction can be estimated for the experimental system studied here, where the density difference is taken to be $\Delta\rho \sim 0.897 - 1.19$ g.cm^{-3} $= 293$kg.m^{-3}, giving:

$$\phi^\star \sim 0.24. \tag{8.12}$$

This is considerably higher than expected from the experimental data. Why is the predicted volume fraction so much higher than the experimental observations in this system? Equation 8.11 is valid in the limit of very dilute suspensions. Allain *et.al* [2] showed equation 8.11 to be consistent with experimental results over a volume fraction range of $10^{-4} < \phi < 10^{-2}$, but cluster-cluster interactions are neglected so equation 8.11 might not be expected to hold for more concentrated suspensions.

Summary of Interpretation

If scenario 1 is correct, then the onset of aggregation is due to the sample crossing the MCT line. The non-ergodic samples are above the CMCT line so are a non-ergodic 'cluster-glass'.

The CMCT line has been shifted upward relative to the standard model due to the effects of gravity, and the clusters within the 'cluster phase' are seen to sediment.

However, if scenario 2 is correct then all samples are above the MCT line but below the CMCT line, so are an ergodic fluid of large clusters. However, as discussed in section 8.2.3, sedimentation increases the effective volume fraction of the samples. In the samples which became non-ergodic the sedimentation increased the volume fraction just enough to form a 'cluster-glass' and the sample appeared non-ergodic, as in the standard model. However, in the sedimenting-cluster samples sedimentation was too fast for the 'cluster-glass' to form. Instead, the clusters fall to the bottom of the sample cell and form an amorphous sediment.

8.5 System 4

Charged Colloids in Gravity

8.5.1 Phase Diagram

The final system studied was that of PMMA colloids in a mixture of *cis*-decalin and CHB at a ratio of approximately 2:1. The effects of gravity are present in this system (although diminished) and the colloids are charged.

Three types of behaviour were observed in this system. At low polymer concentrations, as in all the systems studied, samples remained in a single homogeneous fluid phase (○, figure 8.23). On increasing the polymer concentration (∗, figure 8.23) the colloids aggregated into long-lived clusters which remain mobile of timescales of hours and coexist with a sea of monomers, figure 8.24(a). At the highest polymer concentrations observed the colloidal aggregates appeared non-ergodic, reminiscent of the non-ergodic samples in the previous three systems (◇ figure 8.23, figure 8.24(b)).

8.5.2 Detailed Observations

The topology of the phase diagram is similar to the charged and density matched suspension (system 2). However, detailed observation shows that the effects of gravity are more pronounced. The cluster phase is not homogeneous throughout the sample. An amorphous sediment builds up at the bottom of the sample, above which a cluster phase is observed. Above

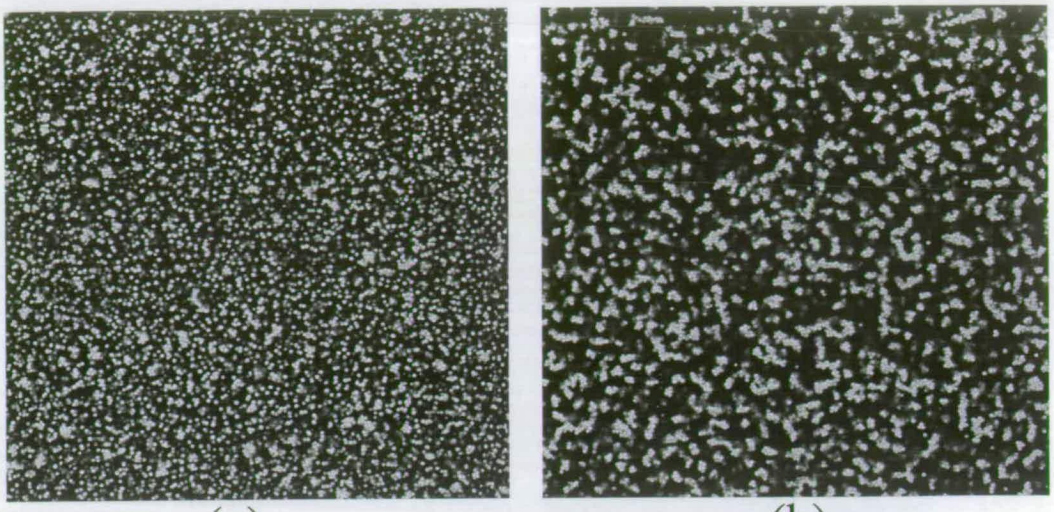

Figure 8.24: Example of a cluster phase and non-ergodic state at high colloid volume fraction, samples(a) $\phi = 0.097$, $c_p = 3.7$ mg/ml and (b) $\phi = 0.12$, $c_p = 7$ mg/ml respectively.

phase homogeneous fluid was observed and at higher polymer concentrations above a sharp boundary the colloids aggregated into large clusters which became non-ergodic after some time. A possible interpretation of these results using mode coupling theory and a renormalised variant are suggested.

The effect of charge on the phase behaviour of colloids in a close-to-zero gravity system was studied. Three phases were observed in this system. At low polymer concentrations a single phase homogeneous fluid was again observed, and above a sharp boundary the colloids aggregated. At the highest polymer concentrations the aggregates became non-ergodic as before. However, at intermediate polymer concentrations the colloids aggregated into small stable clusters, which coexisted with a sea of monomers and did not aggregate further. It is suggested that the charge per clusters increases as the clusters grow, until the electrostatic repulsion between the cluster and a neighbouring particle is sufficient to prevent further aggregation.

The effect of gravity on the phase behaviour was studied using uncharged colloids in *cis*-decalin. At low polymer concentration a single homogeneous fluid phase was again observed, and above a sharp boundary aggregation took place. At high polymer concentrations and at high ϕ the colloids again appeared non-ergodic. However, at low ϕ the aggregates sedimented, leading to a dense (but not randomly close packed) amorphous sediment at the bottom of the sample cell and a colloid-sparse region above.

In all three cases, there is a sharp transition above which the colloids aggregate, and the early

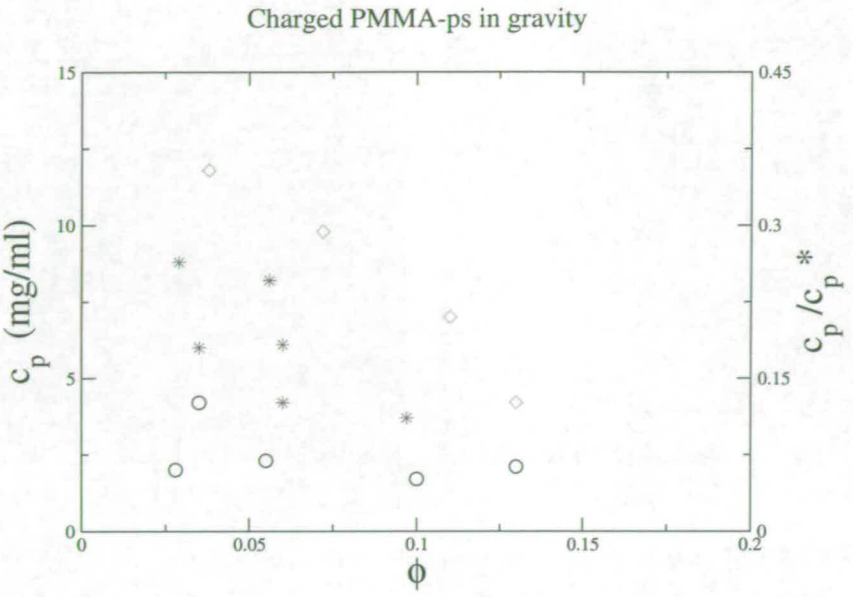

Figure 8.23: Phase diagram of charged PMMA in (reduced) gravity on the addition of ps, size ratio 0.026, showing regions of fluid(∘), clusters(⋆), and large non-ergodic aggregates(◊).

the cluster phase exists a colloid-sparse region from which all particles have sedimented. After several hours all the particles and clusters are incorporated into the amorphous sediment.

8.5.3 Interpretation

This final system behaves in a similar fashion to the charged and density matched system (system 2). This is unsurprising since the colloids are charged in both system. The effects of gravity are more pronounced than in the density matched system as would be expected, and the system displays sedimentation similar to the uncharged and *not* density matched system (system 3). Thus behaviour due to both charge and gravity is present, and the discussions about the preceding two systems would both be valid.

8.6 Summary

The first experimental system studied was that of uncharged colloids in a density matched solvent. In this 'standard model' the phase behaviour was studied without the complicating effects of either gravity or charge. Two phases were observed; at low polymer concentration a single

stages of aggregation look alike. It is suggested that the onset of aggregation can be associated with the MCT non-ergodicity transition. After initial aggregation, the CMCT transition from an ergodic fluid of clusters to a non-ergodic 'glass' of clusters was discussed. Finally, the subsequent behaviour of the samples was shown to depend on the charge per particle and on the effects of gravity in the system.

Chapter 9

Experimental System 2: *Protein Solutions*

9.1 Introduction

In this chapter the experimental system of the protein lysozyme on the addition of NaCl is described. Lysozyme is a globular protein with an average radius of 1.6 nm and a molecular weight $M_w = 14320$ daltons.

Firstly the charge on the protein is described, and it is discussed how the pH of the protein solutions can be maintained at a constant known value using a buffer. The effect of adding salt to lysozyme solutions is discussed. Then the preparation of the stock solutions, the final sample preparation, and the errors involved are described.

9.2 Controlling the Charge

Lysozyme is charged, the magnitude of the charge depending on the pH of the solution as discussed in chapter 5. The pH used in these experiments is pH= 4.5. The charge on the protein is maintained at a constant known value by the use of a buffer. For a full discussion on the working nature of buffers, see chapter 5. To maintain a constant pH of 4.5 a sodium acetate (NaAc) buffer was used, titrated by hydrochloric acid (HCl) to a pH of 4.5. Equations 9.1 and 9.2 show the processes that take place when the NaAc powder is dissolved in water:

$$NaAc + H_20 \rightarrow Na^+ + Ac^- + H_20 \tag{9.1}$$

$$Ac^- + H_20 \rightleftharpoons HAc + OH^- \tag{9.2}$$

The NaAc dissociates to produce acetate (Ac^-), which reacts with the water to form acetic acid (HAc). Titration with hydrochloric acid then has the effect of changing the ratio of [HAc] to [Ac^-]. It increases the concentration of [HAc] and decreases that of [Ac^-], thus lowering the pH. This reaction is shown in equation 9.3.

$$Na^+ + Ac^- + H^+ + Cl^- \leftrightharpoons Na^+ + Cl^- + HAc. \tag{9.3}$$

The NaAc powder was dissolved in water at a concentration of 50μM, and mixed by tumbling for $\sim$ 1 hour. The pH of the buffer solution was measured using a pH meter. The solution was titrated with hydrochloric acid by pipetting in a drop of HCl at a time, stirring to mix, and then re-measuring the pH. This process was repeated until a pH of 4.5 was reached. The buffer

solution is then kept refrigerated, and the pH checked before use. A fresh buffer solution was made every $2-3$ weeks to avoid bacterial growth.

The buffer itself has an ionic strength, which must be taken into account when calculating the total ionic strength of the solution, given by:

$$I_{total} = \frac{1}{2}\sum_i (c_i z^2), \tag{9.4}$$

where z is the valence of the cationic species, c is the concentration in mol/l, and the sum is taken over all species of counter-ions i. Since the buffer is monovalent, and the total concentration of the buffer in stock solution is 50mM then the ionic strength of the buffer is 50mM.

9.3 Effect of NaCl

The effect of the addition of NaCl to a lysozyme solution is to screen the charge on the molecules, as discussed in chapter 5. As the charge is screened an effective attractive interaction is introduced between the proteins. The degree of screening depends on the concentration of the NaCl added. The Debye screening length κ^{-1} of NaCl in water can be calculated, following the approach outlined in chapter 5.5, using equation 9.5:

$$\frac{1}{\kappa} = \left(\frac{\epsilon\epsilon_0 k_B T}{e^2 \sum_i (z_i^2 n_i)}\right)^{\frac{1}{2}}, \tag{9.5}$$

where n_i is the number of ionisable groups per unit area in the bulk solution, k_B is Boltzmann's constant, T is the temperature, z is the valence of the cationic species, and the sum is taken over the electrolyte ions i.

For the case of charged particles in an aqueous solution at room temperature, where $\epsilon = 81$ and the counter-ions added are monovalent (e.g. NaCl), the Debye screening length κ^{-1} is given in terms of the salt concentrations by:

$$\kappa = (0.327 \times 10^{10} m^{-1}) \times \sqrt{(c_s/M)}. \tag{9.6}$$

The Debye screening length can be modified for the case of protein in buffer, by taking into account the ionic strength of the buffer solution as well a that of the added NaCl. The ionic strength was defined in equation 9.4 in terms of the concentration c of ionic species in mol/l.

The number of ionisable groups per unit area n_i can be converted into a concentration c in mol/l via equation 9.7, so that the Debye screening length can be rewritten in terms of the total ionic strength, equation 9.8:

$$n_i = c_i \times N_A \times 10^3 \tag{9.7}$$

$$\frac{1}{\kappa} = \left(\frac{\epsilon\epsilon_0 k_B T}{2e^2 N_A 10^3 I} \right)^{\frac{1}{2}}. \tag{9.8}$$

Therefore the Debye screening length, taking into account the ionic strength of the buffer and added salt, is given by equation 9.9, where I is the total ionic strength (in Molar) of the solution.

$$\kappa = (0.327 \times 10^{10} m^{-1}) \times \sqrt{(I/M)}, \tag{9.9}$$

9.4 Protein Stock Preparation

Six times crystallised chicken egg white lysozyme (Seikagaku America) was used without further purification. Protein was dissolved in buffer at 150 mg/ml and samples were centrifuged at 10^4 rpm for 10 minutes to remove dust and any undissolved material.

The required volume of buffer was transferred using a precision pipette into an Eppendorf tube (plastic tube with lid). The required mass of protein was then weighed out and added on top of the buffer. This was mixed by initial rapid shaking by hand for $\sim$ 5 minutes, followed by slow tumbling for 3 – 4 days.

The volume fraction of the protein stock solution was calculated in the following way:

$$\phi = \frac{cVN_A}{M_w}, \tag{9.10}$$

where V is the volume of a protein molecule, N_A is Avogadro's constant, $M_w = 14320$ g/mol is the molecular weight of the protein and c the concentration of the protein (in g.m^{-3}). The volume was calculated assuming a sphere of radius of 1.7 nm, giving a protein volume in agreement with the published dimensions of lysozyme (see, for example, [18, 22, 79, 12, 71]). For a stock solution of 150 mg/ml the volume fraction is $\phi = 0.132$.

Higher concentrations (up to concentrations of $\sim$ 230 mg/ml were reached using a Vivaspin 6 ultra-filtration device. Exact concentrations were determined by UV absorption spectroscopy. Using a quartz glass cuevette of known path length (0.3 cm), the UV absorbance was measured using a UV spectrophotometer. The measured absorption is related to the concentration via Beer's law:

$$A = \epsilon bc, \tag{9.11}$$

where ϵ is the absorption coefficient, b is the path length and A is absorbance, given by $A = \log_{10} P_0/P$, where P_0 and P are the powers of the incident and transmitted radiation. For lysozyme, the absorption coefficient at a wavelength of 280 nm is 2.64 ml/mg.cm. UV spectroscopy provides optimal results for absorbance values less than 1, so to achieve this solutions were diluted 1000$\times$ in buffer, in steps of 10$\times$ dilution. The absorbance of the buffer alone was also determined, and subtracted from the results for each sample. Using equation 9.11, the concentration c of the solution was found from the measured absorbance, and then the volume fraction calculated. For a stock solution of protein concentration 200 mg/ml the volume fraction works out to be $\phi = 0.176$.

9.5 NaCl Stock Preparation

The NaCl stock solutions were prepared by dissolving the required mass of NaCl into deionised water at a concentration of 3 Molar. The required mass of salt for a 3 Molar stock solution is $3 \times M_w$ g/l, where $M_w = 58.44$ is the molecular weight of NaCl. Salt was dissolved in solution by repeated tumbling. Stock solutions were then stored in the fridge at $\sim 4°$ in sealed glass containers.

9.6 Sample Composition

The required amounts of salt solution followed by deionised water were added to the protein in buffer to give 200 μl samples in glass Durham tubes, which were then sealed. The sample was then mixed by manual shaking for $\sim$ 5 minutes. The final sample composition is stated in terms of the protein volume fraction ϕ and the salt concentration c_s(Molar), which are calculated from equations 9.12 and 9.13.

$$\phi = \frac{V_p}{V_t}\phi_{stock}, \tag{9.12}$$

$$c_s = \frac{V_s}{V_t}c_{s,stock}. \tag{9.13}$$

9.6.1 Errors

Uncertainties in the final sample composition (ϕ, c_s) and pH arise from (1) uncertainties in the concentration of protein, salt, and buffer stock solutions, (2) preparation errors, for example weighing and pipetting of solutions and the effect of additional salt on the pH, and (3) solvent evaporation from the sample once it has been placed in the sample cell.

Protein Stock Solution Composition

In calculating the volume fraction of the protein solution, the required mass of protein was weighed out, introducing weighing errors, and the required volume of buffer solution was measured using a precision pipette.

It is estimated that all masses on the balance are accurate to ± 0.001 g. Typical protein weights were 0.15 g. This leads to an uncertainty in the mass of the dry protein of $\pm 0.7\%$.

It is estimated that the pipette used to measure the required volume of buffer solution is accurate to volumes of ± 0.001 ml, and since the volumes used were of order 1 ml, the relative error is estimated at 0.1%.

Salt Stock Solution Composition

Uncertainties in the composition of the salt stock solution can arise from errors in weighing the dry NaCl. Making the salt stock requires the weighing of the required amount of salt ($\sim$ 3 g). It is estimated that all masses on the balance are accurate to ± 0.001 g. This leads to an uncertainty in the mass of the dry salt of $\pm 3 \times 10^{-4}\%$, which can be neglected.

Buffer Stock Composition

The errors in the composition of the buffer stock are limited to the errors in the pH meter, since it was with this that the final pH of the solution were determined. The accuracy of the pH meter is ± 0.01 giving a relative error of $\pm 0.2\%$.

The pH of the final sample may be different to that of the buffer stock solution, because the addition of salt to the solution can change the pH. The effect of the ionic strength of added salt solution on the pH of lysozyme solutions was studied by Kuehner *et.al.* [50] and discussed in chapter 5.3.1. The change in the average charge on the protein at pH= 4.5 was determined to be less than 0.5 electronic charges for ionic strengths ranging from $0.1 - 2$ Molar, so the effect was assumed negligible for my solutions.

Final Sample Preparation

Weighing errors in the preparation of samples must be considered. Samples were prepared with volumes of $\sim$ 0.1 ml of the stock solutions. Volumes measured by the pipette are accurate to 0.1μl leading to a percentage error in the final protein volume fraction and salt concentration of $\pm 0.1\%$.

Errors introduced during observation

Samples were placed in rectangular capillaries and sealed with Araldite glue for observation. Evaporation of the solvent during observation was monitored by weighing a sample for three hours, and no change in the weight of the sample beyond the uncertainty associated with the balance $\pm 0.001g$ was observed over this timescale. Therefore evaporation had a negligible effect on the sample composition.

In order to ensure that the bulk properties of the system are being observed, and that edge effects are negligible, samples of total thickness 0.1mm were viewed at 50μm into the sample.

Chapter 10

Results 2:
Protein Solutions

10.1 Introduction

Aqueous solutions of globular proteins exhibit some of the phase behaviour associated with nearly hard sphere colloidal suspensions. The addition of salt to the solution induces an effective attractive interaction between protein molecules by screening the inter-molecular electrostatic repulsion [63]. At low attractions a single phase homogeneous fluid is observed. On increasing the strength of the effective attraction (i.e. by the addition of increasing concentrations of salt) crystals nucleate [71], although the specific form and morphology of the crystals is itself a complex field of research [58]. In some specific globular protein solutions, most commonly lysozyme [12, 106, 63, 44, 70], a coexistence curve between two fluids of different concentrations has been reported in analogy to the gas-liquid phase separation observed in colloid-polymer mixtures. Thus the phase behaviour of these proteins may, to some extent, be comparable to that of colloid-polymer mixtures.

However, the detailed non-equilibrium phase behaviour of globular proteins is not understood. Reports of gelation [63, 51] and other non-equilibrium aggregates and structures [104, 52, 63], highlight the rich variety of phase behaviour exhibited by such systems. The research presented in the following chapter describes the different phenomena observed in one particular protein system, and a scheme is proposed by which the complex variety of behaviour reported throughout the literature can be explained.

In this chapter, the results obtained from the study of the globular protein lysozyme on the addition of NaCl at pH4.5 are presented. This system was first studied at room temperature ($22°C$) by optical microscopy and nuclear magnetic resonance spectroscopy. The phase behaviour at five different temperatures ranging from $-2°C$ up to $50°C$ is then discussed. These results are interpreted in terms of the interaction between gas-liquid phase separation and gelation, the precise nature of which is highly sensitive to the system parameters.

10.2 Phase Behaviour

To determine the phase diagram of the lysozyme-NaCl system at room temperature ($22°C$), a series of samples were prepared in glass Durham tubes at protein volume fraction ϕ and salt concentration c_s. Immediately after preparation, the samples were drawn into 0.1mm thick rectangular capillaries and sealed with Araldite glue for observation with a Zeiss optical microscope, and the remaining sample was sealed in the Durham tube using parafilm for direct

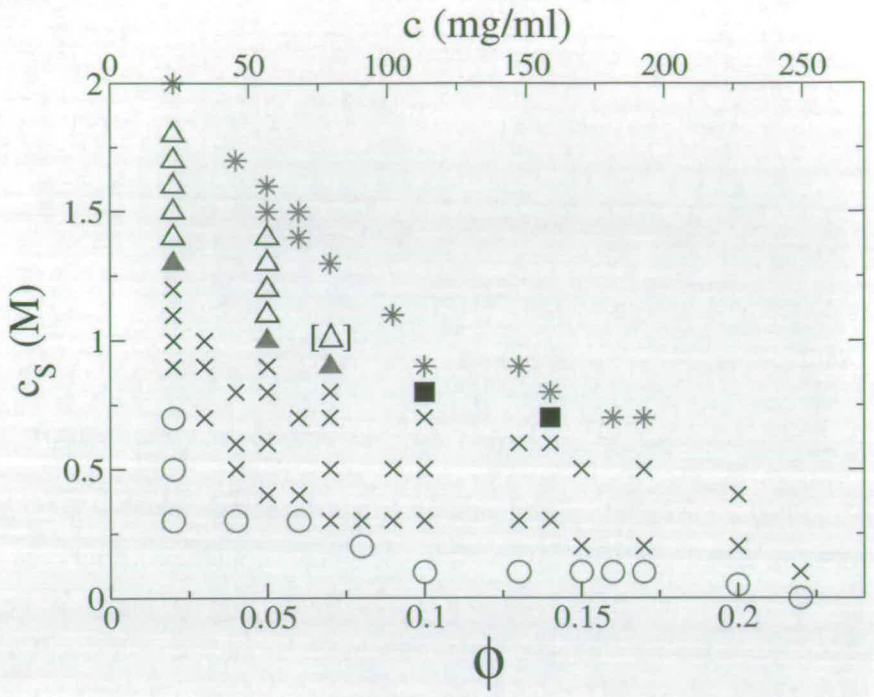

Figure 10.2: Experimental phase diagram, showing regions of single phase fluid ∘, crystals ×, bicontinuous texture ■, non-coalescing 'beads' ▲ and aggregates △, and transient gelation ⋆.

nucleated exclusively in one of the bicontinuous regions. Figure 10.6 shows a sequence of images of such a sample at $\phi = 0.1$ and $c_s = 0.8$, taken between 1 to 80 minutes after initial sample preparation. The formation and coarsening of the bicontinuous region and the subsequent nucleation of crystals can be seen. Figure 10.7 shows a similar sequence of images for sample $\phi = 0.14$ and $c_s = 0.7$.

Samples just across the non-equilibrium boundary but with $\phi < 0.1$ showed freely moving, non-coalescing spherical 'beads', a few micrometres in diameter, or small aggregates of these beads, figure 10.3 (b). Finally, at higher c_s (△, figure 10.2) progressively larger aggregates were observed. Within each aggregate structures on the scale of the previously mentioned beads could be discerned figure 10.3 (c). The beads and aggregates would slowly dissolve once crystallisation started within about an hour.

The sequence of images in figure 10.8 shows the increasing size of these aggregates with increasing salt concentration. The images are taken at a protein volume fraction of $\phi = 0.02$ and salt concentrations of $c_s = 1.4$ M, 1.5 M, 1.6 M, and 1.7 M.

The evolutions of samples in which beads and aggregates of beads were observed is very sim-

observation. The figure below illustrates the experimental setup for observation of samples in the microscope.

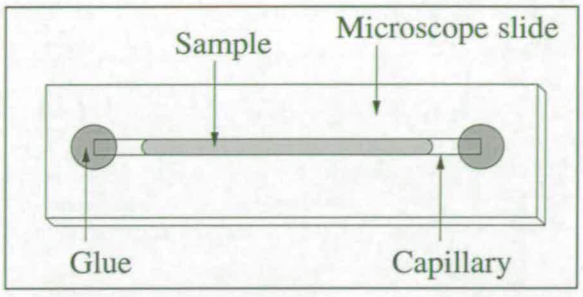

Figure 10.1: Schematic illustration of sample cell used for microscopic observations.

The observed phase diagram is presented in figure 10.2, and a micrograph of each type of behaviour observed is shown in figure 10.3. At increasing salt concentration c_s samples remained homogeneous ($\circ$, figure 10.2) until crystals ($\times$, figure 10.2, figure 10.3 (f)) nucleated beyond a crystallisation boundary. At higher c_s, beyond a non-equilibrium boundary all samples turned turbid after mixing. In the microscope, four regimes can be distinguished ($\blacksquare$, $\blacktriangle$, $\triangle$, $\star$,figure 10.2).

Microscopically, samples with the highest c_s turned white after mixing (*, figure 10.2). A plot of the height of the white portion of the sample vs time shows an inverse sigmoidal shape, figure 10.4, as rapid sedimentation would start after a latency period of $\sim 15 - 30$ minutes. A series of video images were taken, from which the sedimentation profile was measured, and these are reproduced in figure 10.4 (inset). Such delayed sedimentation is characteristic of transient gels. Note that the lysozyme gels appear to be inhomogeneous on the 10μm ($\sim 10^3$ particle) scale, figure 10.3 (e).

The evolution of the transient gels was observed by optical microscopy. The gel forms immediately within ~ 1 minute, the time taken to mix the samples. The gel persists for $\sim 30 - 60$ minutes. As the gel begins to collapse, illustrated by the sedimentation profile, crystals can be seen growing from the gel phase. The sequence of images in figure 10.5 shows the evolution of the gel over $5 - 100$ minutes, for a sample at $\phi = 0.05$ and $c_s = 1.6$M.

Non-gelling samples above the non-equilibrium boundary turned cloudy after mixing, and gave rise to turbid sediments without delay times. To the naked eye there is little to distinguish between samples in this region, but microscopy revealed three distinct regimes.

Just across the non-equilibrium boundary and at $\phi \geq 0.1$ ($\blacksquare$, figure 10.2), bicontinuous textures reminiscent of spinodal decomposition were observed, figure 10.3 (a). Crystals subsequently

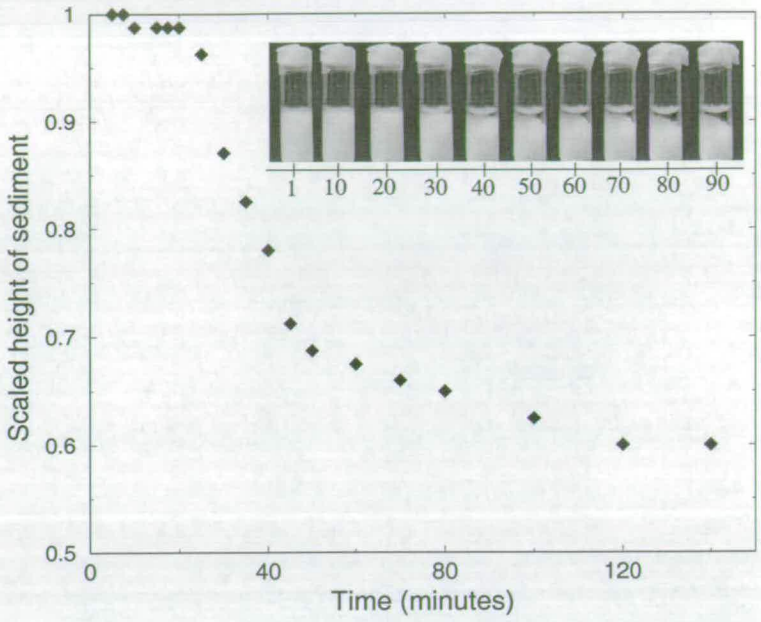

Figure 10.4: Sedimentation profile of a gelled sample at $\phi = 0.07$ and $c_s = 1.4$ M.

ilar. In both cases the beads (or aggregates of beads) from within $\sim$ 1 minute and persist for $\sim$ 1 hour, after which time crystals nucleate, usually from the fluid phase rather than from the beads themselves. Figure 10.9 shows time series of sample $\phi = 0.07$ and $c_s = 0.9$M, taken between 1 to 80 minutes after sample preparation. Figure 10.10 shows a similar time series for sample in which large aggregates of beads were observed, sample $\phi = 0.02$ and $c_s = 1.7$M. The sequence of images was taken between 10 to 90 minutes after sample preparation.

Finally, although the tetragonal crystals as imaged in figure 10.3(f) are the most common form of crystals observed, another crystal morphology was also observed in some samples. Samples of volume fraction $\phi = 0.02$ and salt concentration $c_s = 1.1$ and 1.2 grew 'sea urchin' type crystals, shown in figure 10.11. These types of crystal were also often observed in the final state of samples which initially gelled or formed beads.

10.3 Interpretation

The interaction between lysozyme molecules at high c_s can be modelled by an isotropic short ranged attraction, so the observation of gels ($*$, figure 10.2) is therefore unsurprising. 'Delayed sedimentation' is ubiquitous in synthetic colloids with short ranged attraction, where the non-permanent inter-particle bonds give rise to ageing and ultimately collapse of the gel structure

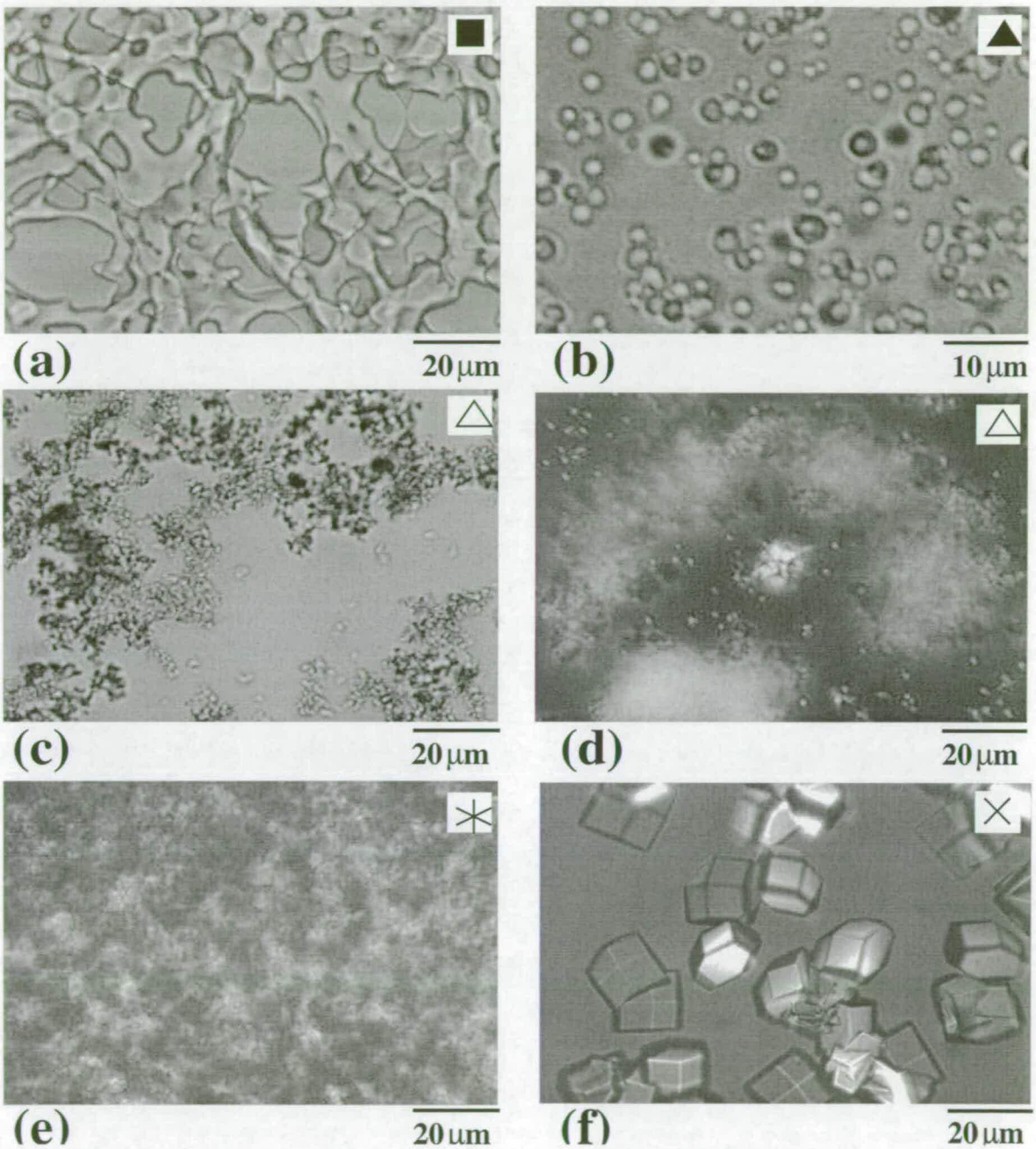

Figure 10.3: Optical micrographs showing (a) bicontinuous texture at $\phi = 0.14$, $c_s = 0.7$ M, (b) spherical beads (note higher magnification) at $\phi = 0.07, c_s = 0.9$ M (c) large aggregates $\phi = 0.02$, $c_s = 1.5$ M, (d) large aggregates and a crystal viewed through crossed polars $\phi = 0.05$, $c_s = 1.1$ M (e) transient gel $\phi = 0.1$, $c_s = 0.9$M with inhomogeneities on the $\sim 10\mu$m scale and (f) tetragonal crystals observed after 30 minutes at $\phi = 0.05$, $c_s = 0.6$ M.

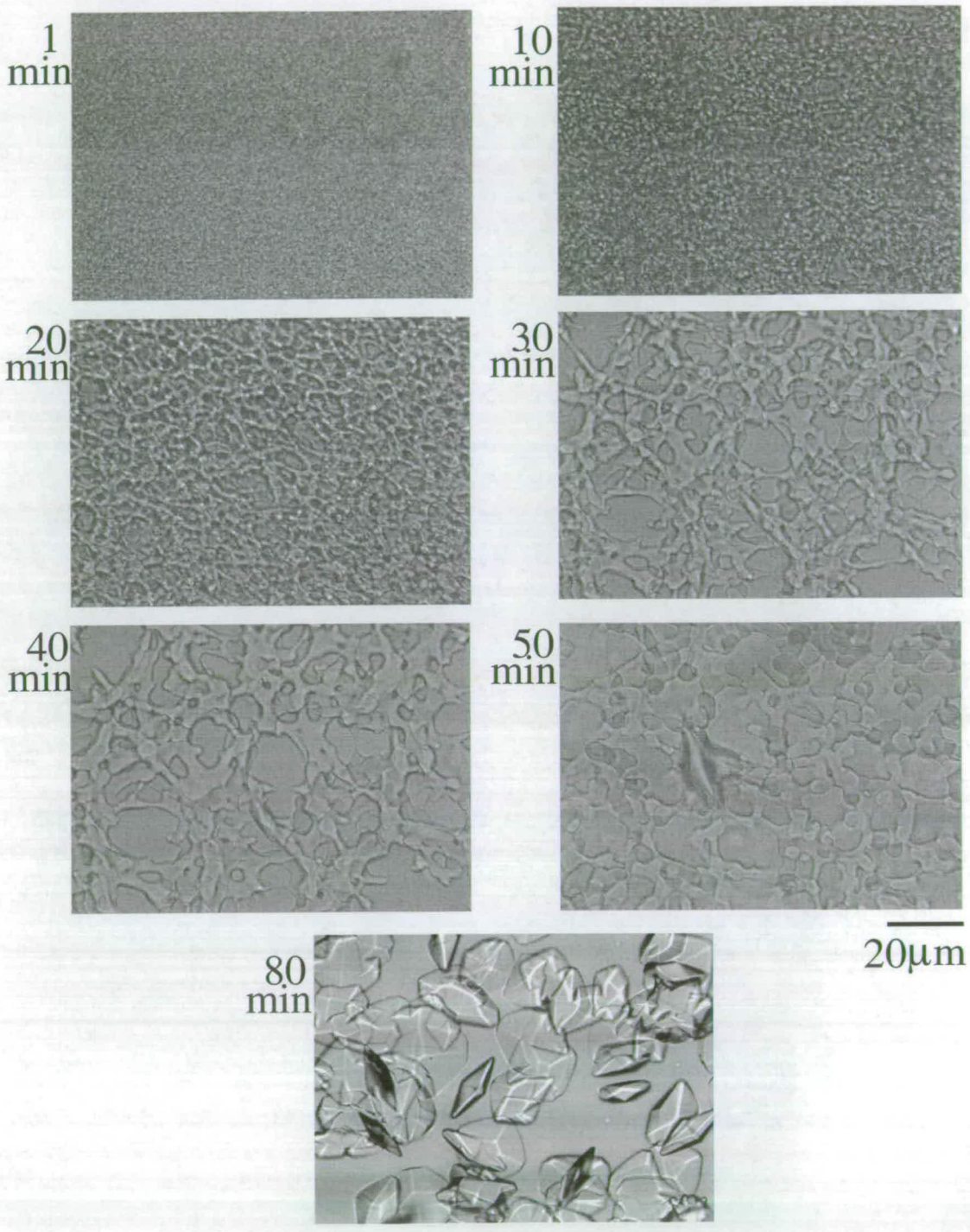

Figure 10.6: Time series of sample $\phi = 0.1$ and $c_s = 0.8$ M, showing the evolution of the coarsening bicontinuous texture reminiscent of spinodal decomposition. The bar indicates the scale on all the images.

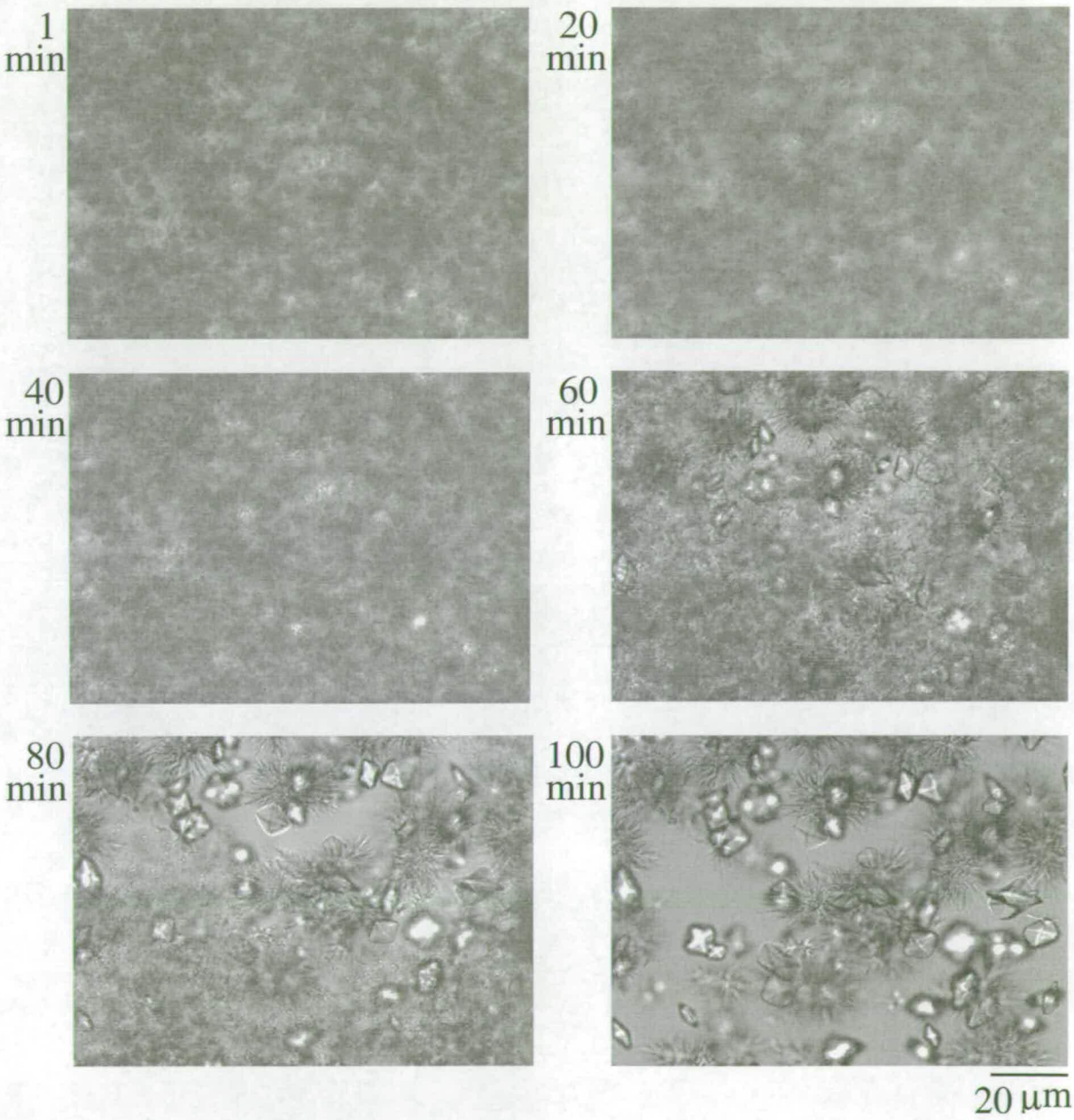

Figure 10.5: Series of images of sample $\phi = 0.05$ and $c_s = 1.6$ M, taken between 1 minute and 100 minutes after sample preparation, showing the evolution of a gelled sample.

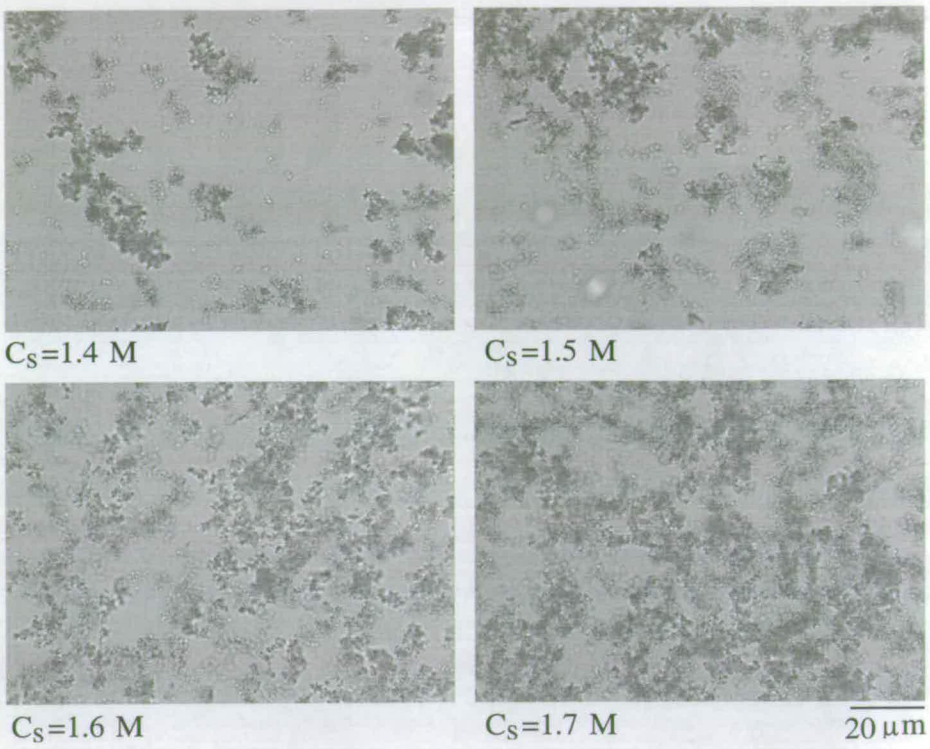

Figure 10.8: Increasing size of aggregates as the salt concentration increases, for sample at $\phi = 0.02$ and salt concentration from $1.4 - 1.7$ M.

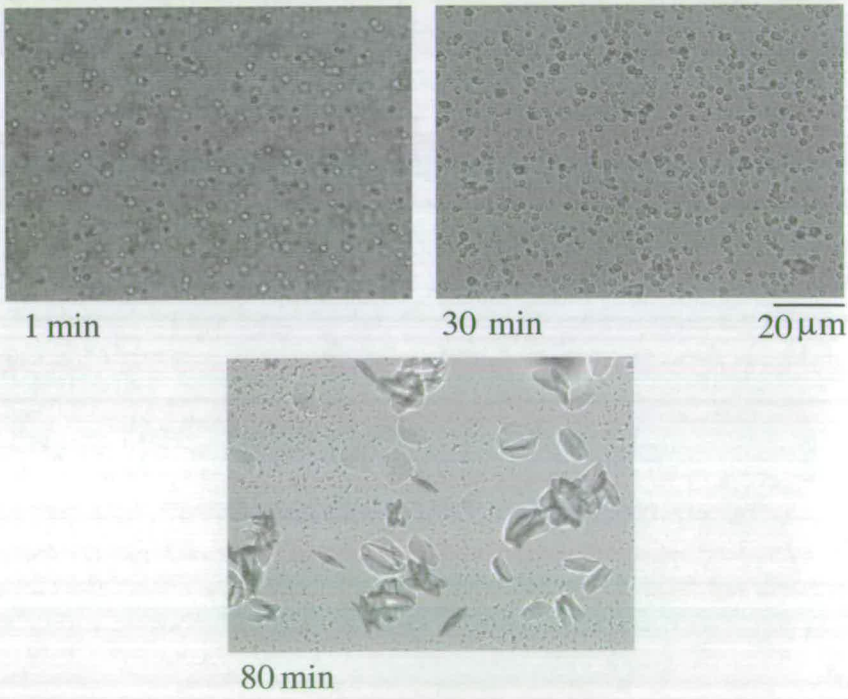

Figure 10.9: Series of images taken between 1 minute and 80 minutes of a sample at $\phi = 0.07$ and $c_s = 0.9$ M, showing the evolution of a sample in which spherical and non-coalescing beads were observed.

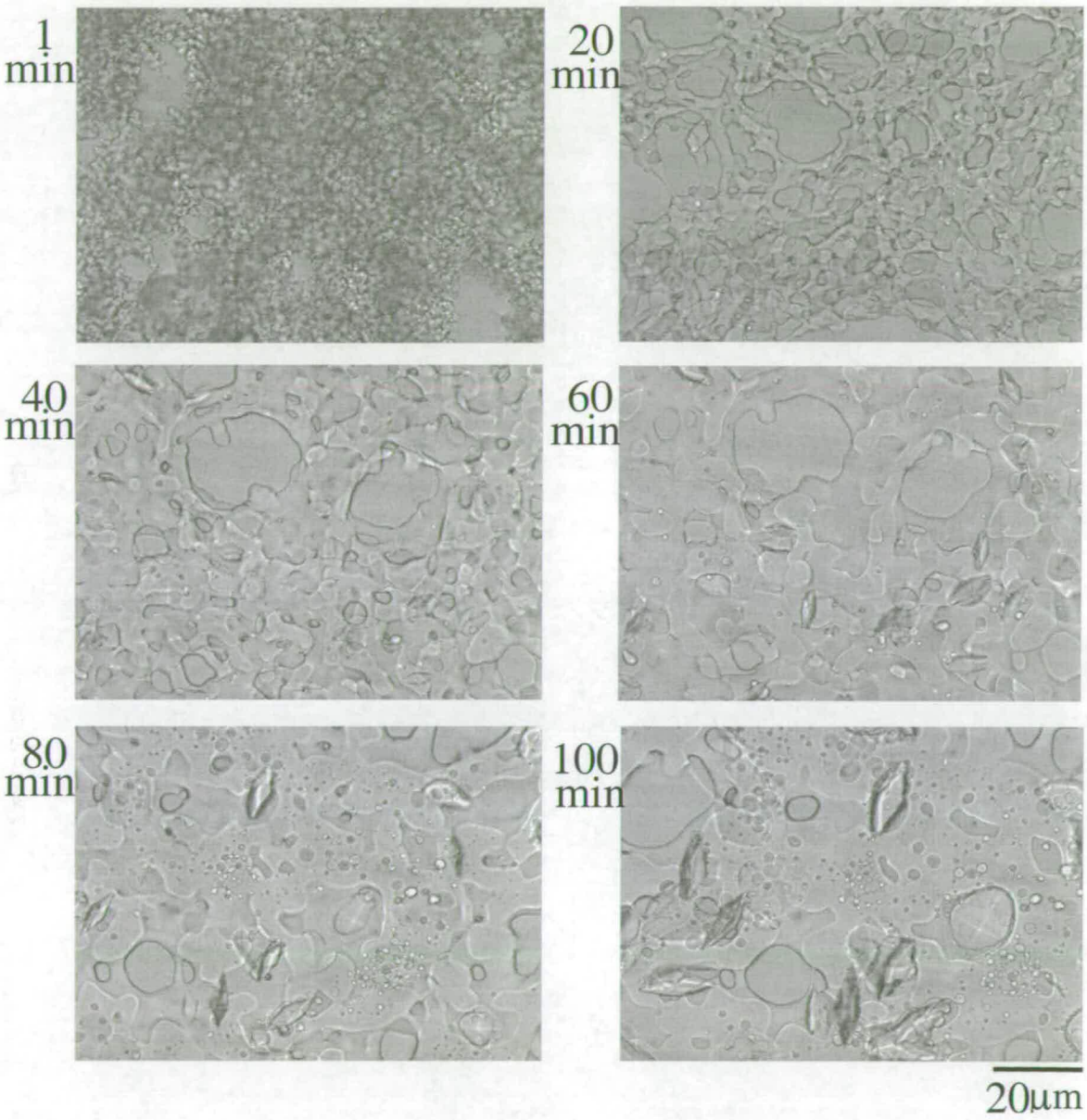

Figure 10.7: Time series of sample $\phi = 0.14$ and $c_s = 0.7$ M, showing the evolution of a sample which displayed a bicontinuous texture reminiscent of spinodal decomposition. the bar indicates the scale of all the images.

and rapid sedimentation after a latency period. After the lysozyme gels collapsed, crystals nucleated. The transient gelation is therefore a metastable state en route to thermodynamic equilibrium.

The bicontinuous spinodal type textures (■, figure 10.2) are also unsurprising. There is a metastable fluid-fluid binodal buried within the equilibrium fluid-crystal coexistence boundary of sticky particle systems including the lysozyme-salt system [63, 51].

The beads and large aggregates are more intriguing. The beads were *never* seen to coalesce, and preliminary x-ray diffraction measurements gave no powder rings. Under crossed polars the beads and aggregates appeared birefringent, although less so then neighbouring crystals (figure 10.3(d)). These results suggest that the beads consist of lysozyme in an amorphous solid state. It is suggested that the formation of 'beads' and large aggregates is due to the interaction between kinetic arrest and gas-liquid (fluid-fluid) phase separation. The proposal is summarised in figure 10.12. Here CB is the equilibrium crystallisation boundary and GL is the gas-liquid binodal. An ergodic to non-ergodic transition (kinetic arrest) occurs at NErg i.e. this is where gelation would occur in the absence of GL. The nature of this transition is debated, but here the precise identity of NErg does not affect what follows.

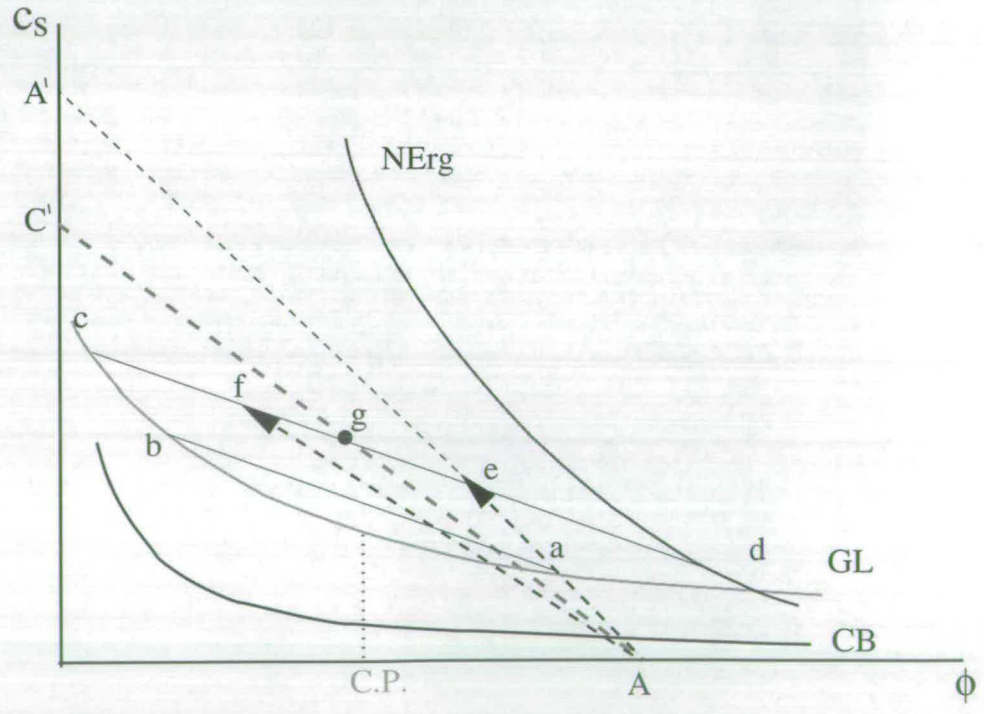

Figure 10.12: Schematic diagram illustrating the interpretation of the observed phase behaviour. CB is the crystallisation boundary, GL is the gas-liquid binodal and NErg the non-ergodicity transition line.

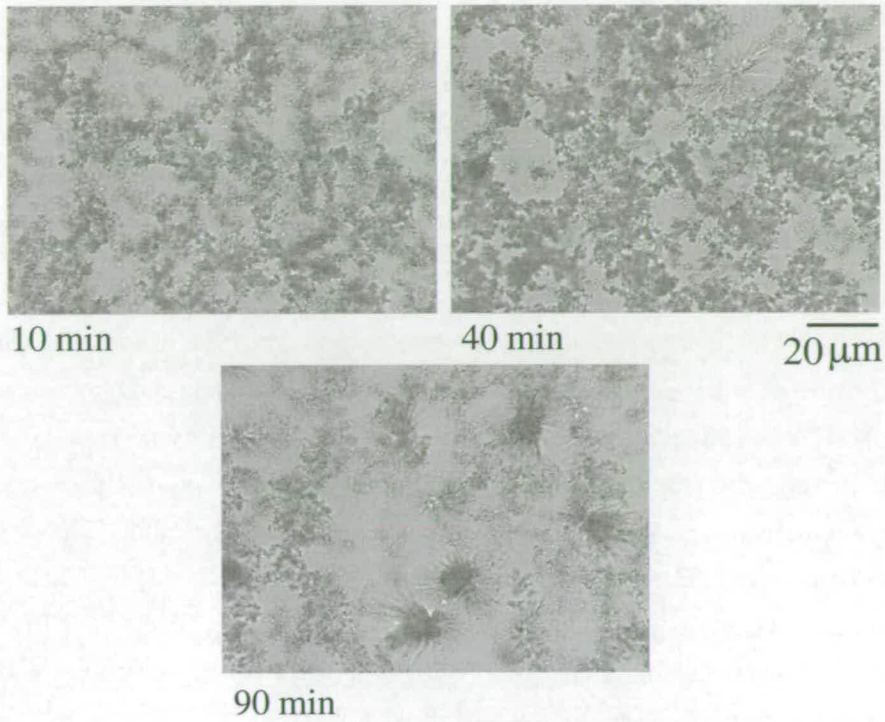

Figure 10.10: Series of images taken between 10 minutes and 90 minutes of a sample at $\phi = 0.02$ and $c_s = 1.7$ M, showing the evolution of a sample in which large aggregates of spherical beads were observed.

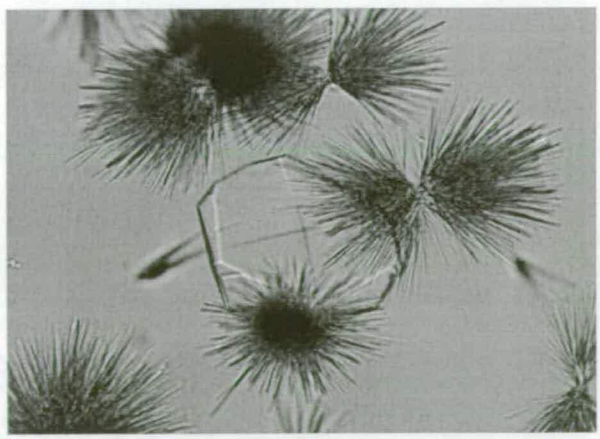

Figure 10.11: Image of sample $\phi = 0.02$ and $c_s = 1.1$ M in which sea urchin crystals were observed.

Recall that a sample with average composition e would have been prepared by mixing a protein solution of composition A with a salt solution of composition A'. It is suggested that in this process the protein solution is quenched along AA'. When the quench path crosses GL at a, phase separation into protein-rich and protein-sparse solutions with composition given by the ends of the tie line ab begins. If the quench is sufficiently slow compared to the rate of phase separation, there will be time for macroscopic domains to develop and densify following the binodal along ad and bc. In other words, a slow quench allows the assumption that the sample is always in local thermodynamic equilibrium. If the average composition is somewhere on ae, a continuously coarsening bicontinuous texture results, until one of the phases crystallises (, figure 10.2).

If the average composition is e then bicontinuous texture coarsens until the compositions of the phase separated regions reach c and d. Here the protein-rich continuous phase will become non-ergodic because d is on NErg. A gel will form with spacial inhomogeneities governed by the length scale of the bicontinuous texture at the point of gelation ($*$ figure 10.2 and figure 10.3(e)).

Along the tie line dc there exists a dynamic percolation threshold [38], point g, to the left of which the phase separated texture is no longer bicontinuous. When the protein rich portions of this *locally* bicontinuous texture become non-ergodic, large aggregates result ($\triangle$, figure 10.2). Paths further to the left of AgC' give more disconnected phase separated domains and therefore smaller non-ergodic aggregates. Thus, quenching along a path from A toward f should give more or less isolated domains: protein-rich 'droplets'. When the composition of these droplets reaches d they turn non-ergodic to give 'beads' ($\blacktriangle$, figure 10.2) whose mean size is determined by the interplay between the quench speed and the phase transition kinetics.

Thus, our prediction is that for all samples prepared by diluting protein solution A with salt solution A', and at protein concentration below d, $dg - gC'$ is the gelation boundary, and GL is the non-equilibrium phase boundary. Experimentally our gel boundary is consistent with this prediction: it is plausibly piece-wise straight. The observed non-equilibrium boundary (upper boundary of $\times$, figure 10.2) indeed has the shape of the gas-liquid binodal. Samples beneath the gel boundary but within the non-equilibrium region of the phase diagram should form increasingly disconnected domains the further away they are from the gel boundary.

All samples with volume fraction $\phi < 0.1$ were prepared by diluting a protein solution of $\phi = 0.132$ with salt solution. Consistent with this interpretation, the steeper part of the gel boundary extrapolates to $\phi \sim 0.13$. Again, consistent with our interpretation, the shallower part of the gel boundary is a tie line of the gas-liquid binodal. Assuming this interpretation for

the experimental gel boundary two deductions follow. Using the lever rule it can be estimated that a sample of $\phi = 0.14$ and $c_s = 0.7$ should have $\sim 2/3$ high protein concentration domains, consistent with figure 10.3(a). Secondly, the critical point of the gas-liquid binodal can be estimated at $\phi_{crit} \sim 0.12 - 0.13$, consistent with reports of $\phi_{crit} \sim 0.15$ under similar (but not identical) conditions [63].

Quench path dependence is a crucial part of the explanatory scheme. The gel boundary should change if the starting protein concentration (and hence quench path) were altered. A sample that gave large aggregates ([$\triangle$] figure 10.2), gelled when prepared using a protein solution of $\phi = 0.176$.

Finally, a possible interpretation of the unusual, sea-urchin crystal morphology can be made. At the left hand corner of the gas-liquid coexistence curve, there is a region of samples whose quench path would never pass through a region of phase-separation below the critical tie line. In this case, a high concentration liquid phase would never have the chance to coarsen and produce the large beads and aggregates observed. Instead, local density fluctuations would become non-ergodic producing small clusters of particles. It is speculated that these may form a nucleus from which the spiky, sea-urchin like crystals grow.

In summary, the predicted phase behaviour following this interpretation is as follows. Samples just above the gas-liquid binodal, below the tie line that intersects the non-ergodicity transition line, will undergo gas-liquid phase separation, until crystals nucleate out of the dense liquid phase. Samples above this tie line but to the left of the quench path which passes through the percolation point will form non-ergodic beads, or aggregates of these. Samples above the critical tie line to the right of the quench path which crosses the percolation point will become non-ergodic in the high concentration, percolating liquid phase and transient gelation will be observed. Measurements of lysozyme mobility which support this interpretation will now be presented.

10.4 NMR Measurements of Mobility

10.4.1 Lysozyme Spectra

It was discussed in section 10.2 that the interaction between the gas-liquid binodal and a non-ergodicity transition can cause nucleated drops of a high concentration liquid phase to become non-ergodic. If this is the case, then the non-ergodic 'beads' should coexist with a low concen-

tration 'gas' phase. To test this hypothesis nuclear magnetic resonance was used to measure the mobility of lysozyme in samples in which beads were observed.

Figure 10.13 shows the spectrum of 75 mg/ml ($\phi = 0.06$) lysozyme with no added salt, in a 50mM NaAc buffer in D_2O, titrated with HCl to a pH of 4.5. The sharp peak to the left of the centre is produced by the HCl buffer.

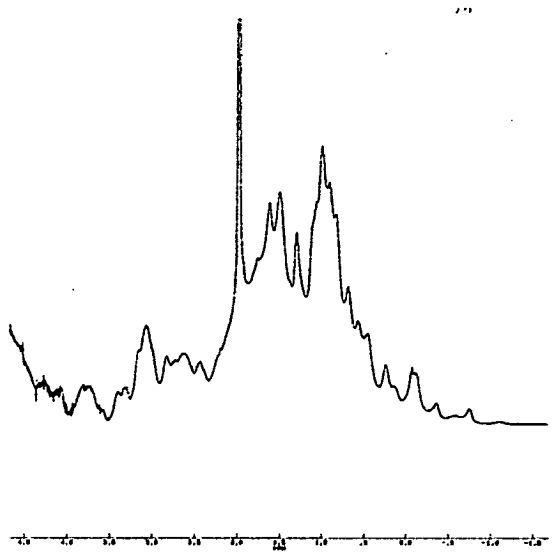

Figure 10.13: NMR spectrum of lysozyme at a volume fraction of $\phi = 0.06$ with no added salt.

Figure 10.14 shows the spectrum of lysozyme at volume fraction $\phi = 0.02$. The upper spectrum is from a sample of fluid phase lysozyme with no added salt. The lower spectrum shows a solution with 1.4M NaCl, in which microscopy revealed spherical and non-coalescing beads. The spectrum was taken 10 minutes after sample preparation, and showed no change after half an hour. Samples in which non-coalescing 'beads' were observed have a spectrum similar to that of fluid phase lysozyme but of lower intensity.

There are two possible reasons for a reduction in the intensity of an NMR spectrum. Firstly, if all the molecules in the sample were in a solid state, then a low and broad spectrum would be expected. This does not appear to be the case. Secondly, the intensity of the spectrum would be decreased if fewer molecules contributed to the signal. In other words, if some of the lysozyme is in a solid state then a very broad spectrum will be produced that is unrecognisable as a lysozyme spectrum. If the remaining lysozyme remains in a fluid phase, it will give rise to a lysozyme spectrum of lower intensity, because less molecules are contributing to the signal.

This implies that in samples where 'beads' were observed, part of the lysozyme is solid, and

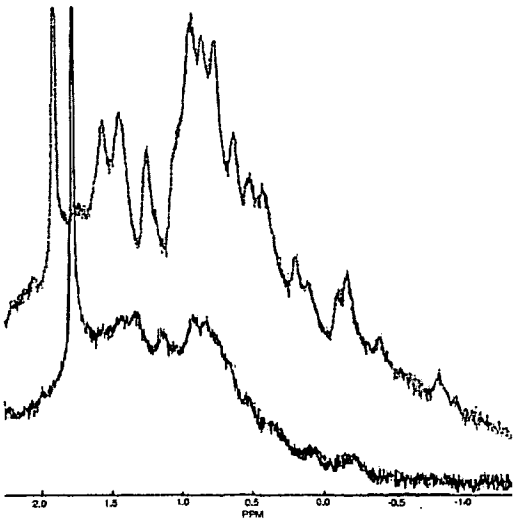

Figure 10.14: NMR spectra of lysozyme with volume fraction $\phi = 0.02$. The upper spectrum had no added salt, and the lower spectrum had $c_s = 1.4$M NaCl.

therefore only produces a broad spectrum, and part of the lysozyme remains in a fluid phase and produces a lysozyme spectrum of reduced intensity. If this is the case then the relaxation time of the spectra produced by fluid phase lysozyme should be the same in both the fluid and 'bead' samples.

10.4.2 Relaxation Time Measurements

To determine the relaxation time of the lysozyme in its different states, the T_1 (longitudinal) relaxation times were measured. T_1 is experimentally determined by inversion recovery, described in detail in chapter 6.2.3. A series of pulses are applied, of the form $180° - \tau - 90°$, where τ is a small time which is varied from one pulse sequence to the next. The first, 180° pulse inverts M_z, which then decays exponentially toward its original value. After time τ the magnetisation will have relaxed to a value M which can be measured by applying a 90° pulse which tips it into the (x, y) plane so it can be detected. A series of FIDs corresponding to different values of τ are accumulated and transformed. In the resulting set of partially relaxed spectra, the size of each individual peak is a function of its own T_1 value. The magnetisation M is determined from the height of the peak for each value of τ. The longitudinal relaxation time is given by equation 10.1:

$$ln(1 - \frac{M}{M_0}) = ln2 - \frac{\tau}{T_1}, \tag{10.1}$$

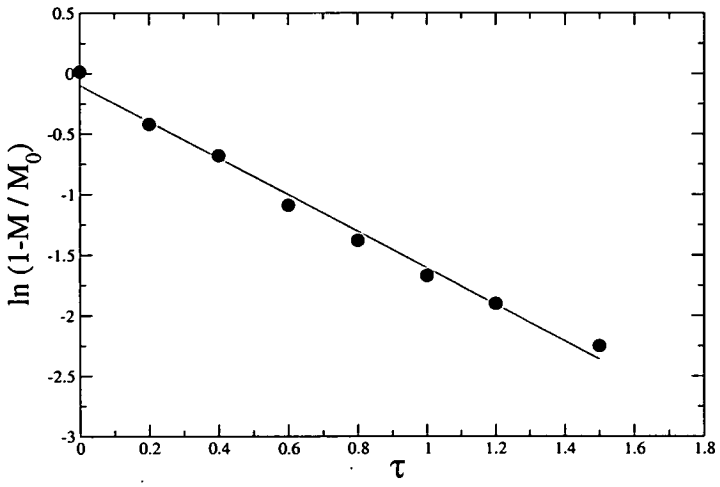

Figure 10.15: Plot of $ln(1 - \frac{M}{M_0})$ vs $\tau(ms)$ for sample $\phi = 0.02$ with no added salt.

where M_0 is the fully relaxed magnetisation. In a plot of $ln(1 - \frac{M}{M_0})$ vs $\tau(ms)$, the gradient of the best fit straight line will be $\frac{1}{T_1}$. Figure 10.15 shows the graph and fitted line for the fluid-phase lysozyme sample. The gradient of the straight line gave a relaxation time of $T_1 = 649$ms. Figure 10.16 shows the same graph for the measurements of a lysozyme sample in which 'beads' were observed, and in this case the relaxation time was found to be $T_1 = 663$ms.

The similar relaxation times imply that the spectrum obtained from the sample in which beads were observed is produced by mobile, fluid phase lysozyme. This is in agreement with the interpretation of the spectra. Therefore, some of the lysozyme is incorporated into the beads in a solid state, and is not contributing to the observed spectrum, while some of the lysozyme remains in a fluid state. A measurement of how much the intensity is reduced will give an estimate of how much lysozyme is incorporated into the beads, and how much remains in the fluid phase. The relative heights of the peaks in the fluid sample and the 'beads' sample were measured and a 58% reduction is observed, implying that 58% of the lysozyme molecules are incorporated into beads in a solid state.

To summarise, the spectra observed for a sample in a single phase fluid and a sample in which beads were observed are both produced by fluid-phase lysozyme of comparable mobility. The spectrum from the sample in which beads were observed has an intensity reduced to 42% of the single phase sample. This leads to the suggestion that 58% of the lysozyme is incorporated into the beads and exists in a solid state, while 42% of the lysozyme remains in a fluid phase.

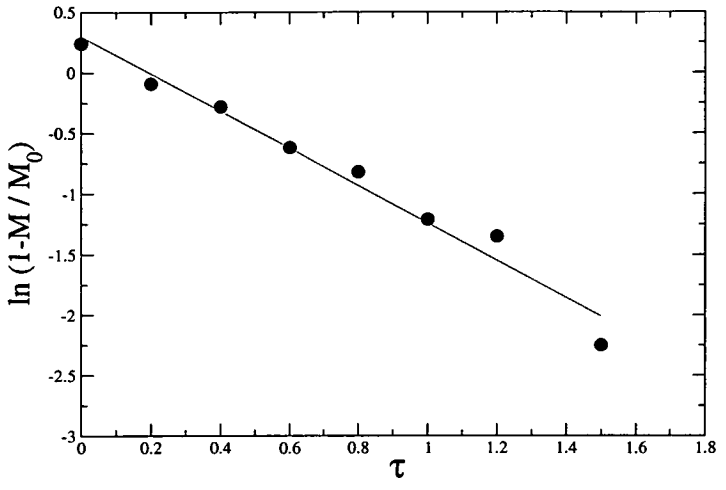

Figure 10.16: Plot of $ln(1 - \frac{M}{M_0})$ vs $\tau(ms)$ for sample $\phi = 0.02$ and $c_s = 1.4$Molar.

10.5 Temperature Dependence

The phase behaviour of lysozyme on the addition of NaCl was studied at five different temperatures, ranging from $-2°$ C to 50°C. These phase diagrams are shown in figure 10.17, where samples which crystallised are marked with $\times$, samples which displayed transient gelation are $\star$ and all other types of non-equilibrium behaviour are ■. The details of the non-equilibrium behaviour are discussed in detail in section 10.2 for the phase diagram at room temperature. Here the relative movement of the experimental phase boundaries is discussed.

At the lower temperatures, $-2°$ and 10°C, only two states were observed, those of fluid and transient gelation. However, at room temperature a variety of non-equilibrium aggregation was observed at salt concentrations below those required for gelation (as detailed in section 10.2), and the size of this region of non-equilibrium behaviour increases as the temperature increases. This is illustrated in figure 10.18, which shows a plot of salt concentration against temperature at which the experimental non-equilibrium and gelation boundaries were observed for constant volume fractions of $\phi = 0.1$.

As discussed in detail in section 10.2, it is suggested that gelation occurs when a phase separating sample becomes non-ergodic in the *percolating* high concentration phase. The non-equilibrium samples which do not gel are given by phase separation which either (a) was below the tie line which intersects the non-ergodicity transition, so the high concentration phase

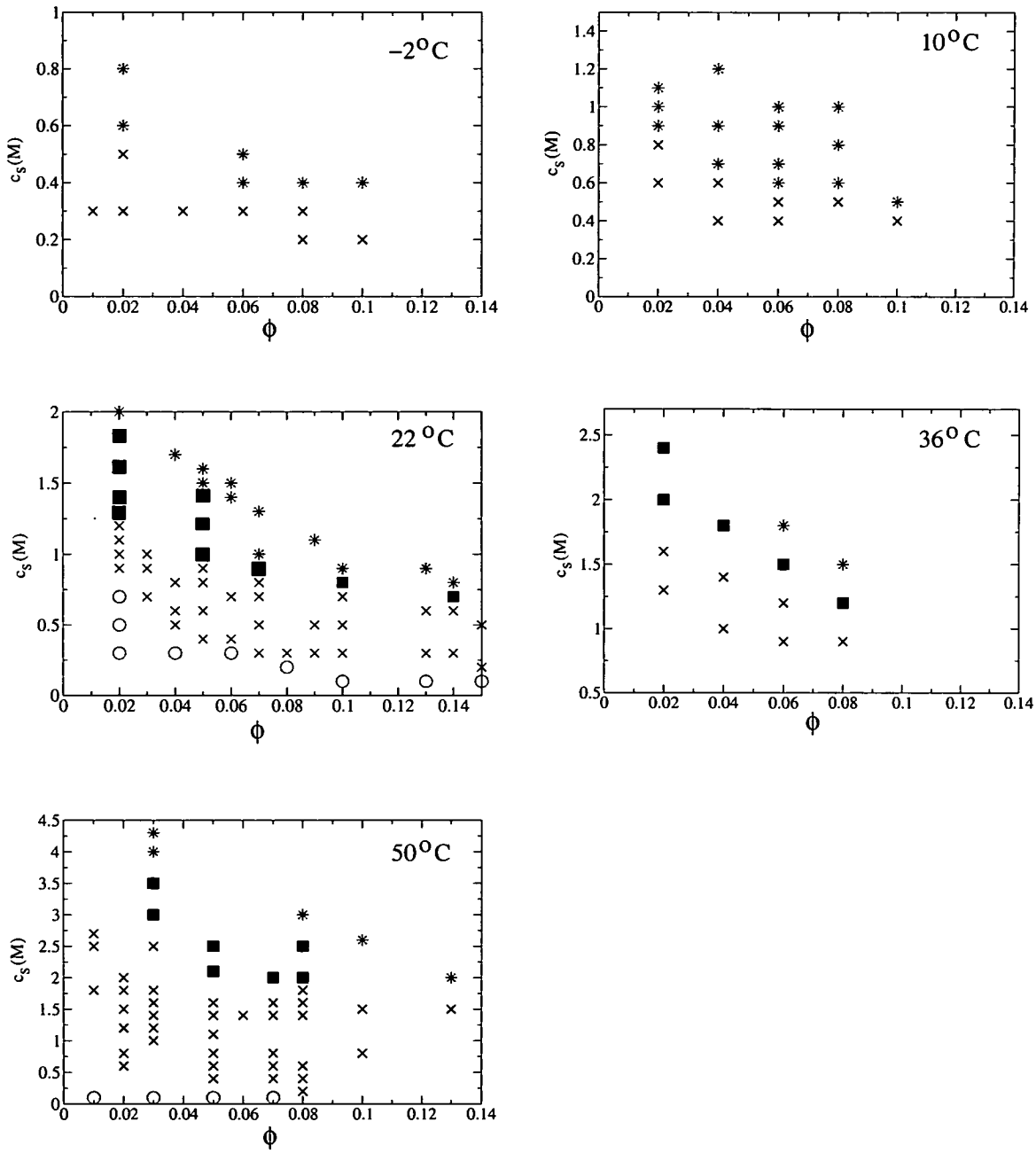

Figure 10.17: Phase diagrams at -2, 10, 22, 36 and $50°c$ (from top to bottom), the vertical axis is the NaCl concentration in Molar, c_s, and the horizontal axis is the protein volume fraction ϕ. Symbols denote the following, × =crystal, ■ =non-equilibrium behaviour and ⋆ =transient gelation. Phase diagrams at $-2°$ and 10°C were obtained by A.Salonen and the phase diagram at 50° was obtained by G.S.Roberts.

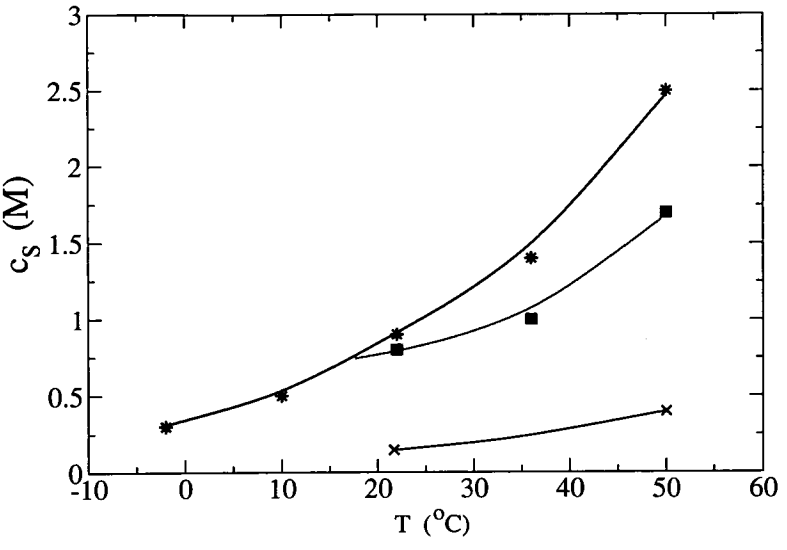

Figure 10.18: Plot of NaCl concentration against temperature at $\phi = 0.08$. Solubility data is included for completeness, taken from [63, 12].

never became non-ergodic, or (b) the high concentration phase became non-ergodic but was not percolating.

There are two ways in which the observed gelation boundary could be shifted to higher salt concentrations relative to the gas-liquid binodal with increasing temperature. Firstly, the quench path could be steeper at high temperatures. This would require using a lysozyme bulk solution of *lower* volume fraction than at room temperature, which was not the case since bulk volume fractions of $\phi = 0.132$ were used throughout. Secondly, if the non-ergodicity transition line intersects the gas-liquid binodal at higher volume fractions with increasing temperature, the region of non-equilibrium aggregation would increase.

Therefore, we speculate that the non-ergodicity line moves relative to the gas-liquid binodal as the temperature is varied. At low temperatures it lies below the binodal, and as the temperature is increased it moves to higher attractions relative to the binodal. This is sketched schematically in figure 10.19. The non-ergodicity transition moves down through the phase diagram with decreasing temperature, so that at low temperatures gelation is the first type of behaviour observed above the single phase fluid.

In the past DLVO theory has been used to model the interaction potential of lysozyme on the addition of salt at a constant temperature with some success [71], as discussed in chapter 5.8.

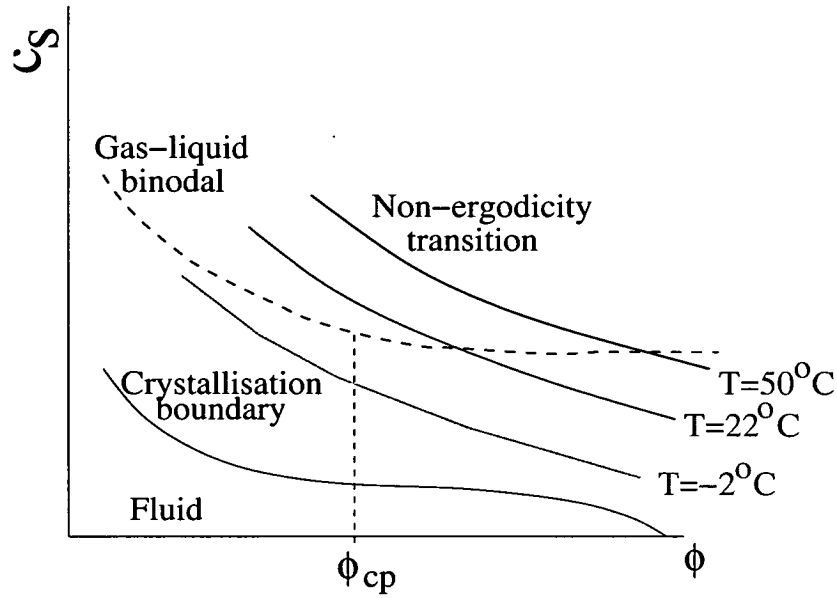

Figure 10.19: Schematic phase diagram showing the relative movement of the phase boundaries with decreasing temperature.

However, the movement of the gelation boundary observed here implies there must be a strong temperature dependence in the protein interaction, which does not appear in the simple DLVO potential. Recently mode coupling theory has been thought relevant to the gelation transition in colloidal systems, predicting a non-ergodicity transition at low volume fractions, as discussed in detail in chapter 9. The position of this non-ergodicity line is very sensitive to the range of the inter-particle attraction, and is dominated by the shortest ranged component of the potential. It is speculated that the temperature dependence of the system could be incorporated into the potential by the addition of a short ranged attraction, that is weak at high temperatures but gets progressively stronger with decreasing temperatures.

A recent publication by Huang and Chandler [40] has demonstrated that the temperature dependence of hydrophobic interactions changes significantly for surface sizes around $\sim$ 1nm. That is, the hydrophobic interaction has a strong and nonmonatonic temperature dependence around the length scale of proteins. Although the hydrophobic interactions are far from being completely understood, their temperature dependence at the right length scale for hydrophobic patches on protein molecules suggests that they may be responsible for the temperature dependence of the lysozyme phase behaviour observed here. Figure 10.20 shows their predictions for the excess chemical potential per solute volume as a function of temperature [40].

In summary, at room temperature the lysozyme-NaCl system exhibits a wide variety of non-

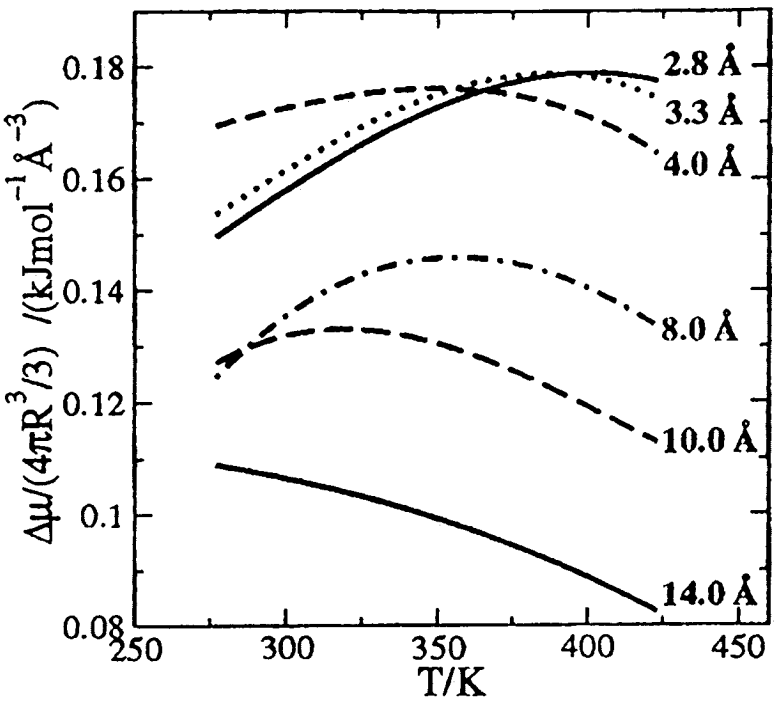

Figure 10.20: Temperature dependence of the hydrophobic interaction for different surface sizes. Taken from [40].

equilibrium behaviour, explained in terms of the interaction between the gas-liquid binodal and the MCT non-ergodicity transition. In a small region, below a tie line that intersects the non-ergodicity line, the system can gas-liquid phase separate and spinodal decomposition is observed. Above the tie line which intersects the non-ergodicity boundary, phase separating samples with volume fraction above the percolation point become non-ergodic in the high concentration liquid phase, and a gel is observed. The experimental gel line is associated with the tie line that intersects the non-ergodicity transition line followed by the quench path through the percolation point. Samples at low volume fractions do not percolate, but nucleated drops of the high concentration liquid phase become non-ergodic, and beads or aggregates of beads are observed.

A study of the phase behaviour of lysozyme on the addition of NaCl was carried out at a range of different temperatures. The topology of the phase diagram was shown to change, predom-

inantly due to the movement of the experimental gel line with temperature. A short ranged component in the protein interaction potential that is not included in the simple DLVO model, the strength of which increases with decreasing temperature, was suggested. The hydrophobic interaction has been suggested as a possible attraction between protein molecules with a strong temperature dependence.

10.6 Discussion

In this section the experimental results and interpretations that have been presented are compared to a variety of reports in the literature. The ideas discussed in this chapter are then applied to the previous system studied in this thesis, that of PMMA colloids on the addition of polymer. Finally other results from the colloid-polymer literature are discussed in terms of the ideas outlined in this chapter.

10.6.1 Literature Review

The phase behaviour of the lysozyme-NaCl system has been studied by a number of authors. In this section a review of the reported observations is given, and discussed in terms of the interpretation outlined in this chapter. The precise details of the interaction between phase separation and the non-ergodicity transition are sensitive to the system parameters such as temperature, pH, sample preparation and route and speed of mixing. The behaviour observed is therefore expected to be dependent not only on the solution conditions but also on the exact sample preparation, so considerable variation between the different reports is expected.

Gas-liquid phase separation in lysozyme solutions on the addition of NaCl was first reported by Ishimoto and Tanaka [44]. Their approach was to prepare solutions of lysozyme at varying concentrations, mixed with a 0.5M aqueous NaCl solution at pH= 5.4 at room temperature. The temperature was then decreased until rapid turbidity of the samples was observed, at the cloud point temperature. The cloud point curve was associated with the gas-liquid binodal (although two coexisting liquid phases are not explicitly reported), and the critical point of this curve was found at a temperature of $\sim$ 12°C. Their results are reproduced in figure 10.21.

How do these results relate to those presented in this thesis? The observation of a critical point is certainly indicative of gas-liquid phase separation. At $\sim$ 12°C it is not unreasonable to suggest that the gas-liquid binodal would indeed be the first phase boundary encountered

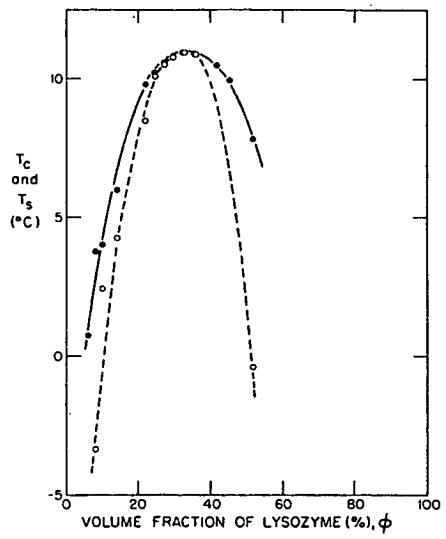

Figure 10.21: Phase diagram of lysozyme with 0.5M NaCl, taken from [44]. The lines are drawn as a guide to the eye, where the bold line represents the binodal and the dashed line the spinodal.

on decreasing the temperature. Since the further evolution of the samples was not studied, no further comparison can be made, but it is possible that the samples may have exhibited non-equilibrium behaviour similar to that observed in my system.

Following this work, Taratuta *et.al.* [106] measured cloud point curves for lysozyme as a function of temperature in a 0.6M sodium phosphate buffer. The cloud point curves they report have a critical point at around 0°C, with a considerable number of data points on both the high and low concentration branches of the curve, figure 10.22. The cloud point curve reported here looks convincingly like the gas-liquid binodal, despite being at a temperature where our interpretation predicts gelation to be the first transition encountered. However, there are significant differences between this system and my own. The pH is higher than in my system (pH= 6.0 is the lowest reported), and the ionic strength is provided by a sodium phosphate buffer rather than NaCl.

Perhaps the most thorough study of gas-liquid phase separation in lysozyme solutions to date was carried out by Muschol and Rosenberger [63], who studied the phase behaviour as a function of temperature at pH= 4.5 in solutions of NaCl at a range of ionic strengths. This study is therefore the most directly comparable to my own. They report cloud point curves consistent with my experimentally determined gas-liquid binodal at low volume fractions, and note that solutions left in the two phase region did not form two coexisting liquid phases but rather

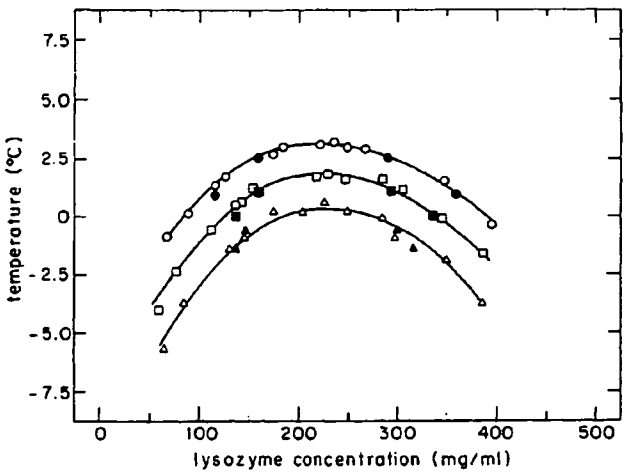

Figure 10.22: Phase diagram of lysozyme as a function of temperature in a 0.6M sodium phosphate buffer, showing the cloud point curve. The data are from three different pH solutions; pH 7.0 (circles), pH 6.5 (squares) and pH 6.0 (triangles). Solid lines are drawn as a guide to the eye. Taken from [106].

formed 'white precipitates', again consistent with my interpretations. The observations are reproduced in figure 10.23(a). To the right of the critical point the authors say that cloud point data was difficult to obtain, and that 'extensive gelation occurred', where these gels 'appeared translucent or milky'. The observations reported here are all in accord with my interpretation of the phase behaviour of this system. Furthermore, Muschol and Rosenberger [63] speculate that a 'gelation curve' may intersect with the gas-liquid coexistence curve. Their schematic interpretation of this situation is reproduced in figure 10.23(b).

More recently, Kulkarni *et.al* [51] studied the phase behaviour of lysozyme at pH= 7 in a sodium phosphate buffer of 0.6M ionic strength. This system is the same as that reported by Taratuta *et.al.* [106]. The phase behaviour was studied as a function of temperature. Interestingly gelation was reported as well as gas-liquid phase separation, and indeed at temperatures $\sim$ 10°C the gas-liquid coexistence curve is *inside* the gelation region. However, cloud point measurements of the gas-liquid coexistence curve can still be made because gels are reported to take $\sim$ 24 hours to form. This is strikingly different to the gels observed in my system, and those of Muschol and Rosenberger, which formed within $\sim$ 1 minute. I attribute this difference to the different system parameters, including the sodium phosphate buffer. Furthermore it can clarify the discrepancy between my work and that of Taratuta *et.al.* [106]. Their cloud-point measurements do show the gas-liquid coexistence curve, but as predicted here it *is* inside the gelation region, as demonstrated by Kulkarni *et.al.*. Phase separation can be observed because

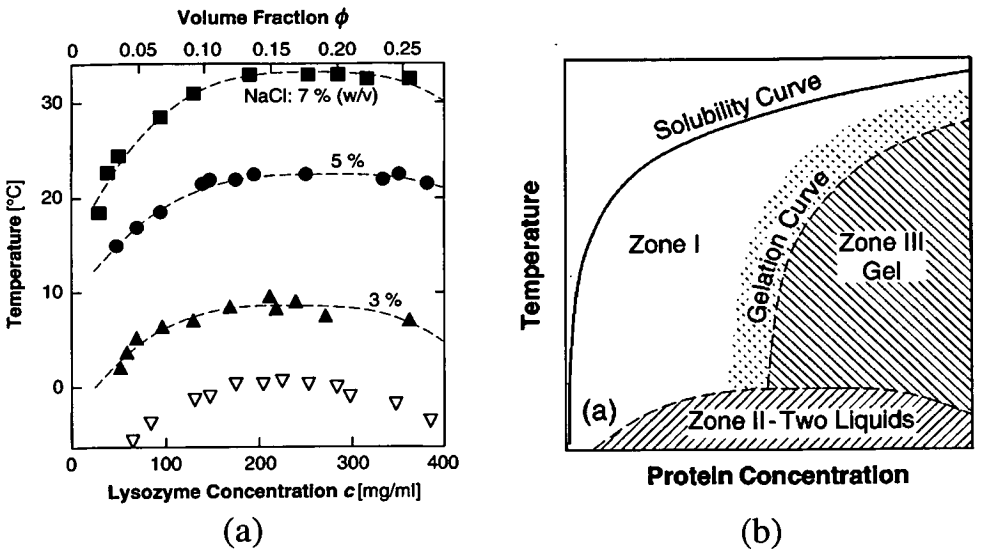

Figure 10.23: Phase diagram of lysozyme as a function of temperature in NaCl solution at a range of ionic strengths, showing the cloud point curve. Taken from [63].

of the long timescales of gel formation in this particular system compared to that of lysozyme on the addition of NaCl.

In figure 10.24 the phase diagram of Kulkarni *et.al.* is reproduced [51], together with the phase diagram of the system studied here at 10°C. Since the attraction was varied by temperature in one case and ionic strength in the other, both are shown in the (B_2/B_2^{HS}, ϕ) plane for direct comparison, where B_2 is the second virial coefficient of the osmotic pressure as defined in chapter 5.5. The salt concentration was transformed into a value of B_2 using a DLVO potential, as follows. B_2 can be calculated once the form of the potential is known using equation 10.2, where $U(r)$ is the interaction potential and r the inter-particle separation:

$$B_2 = 2\pi \int_0^\infty r^2 \left(1 - e^{-U(r)/k_B T}\right) dr. \tag{10.2}$$

The hard sphere part of this potential (an infinite repulsion that prevents the colloids from overlapping) can be factored out to give the reduced second virial coefficient as in equation 10.3, where $u(r)$ is the potential without the hard sphere repulsion term. For maple code used to transform the salt concentration into a B_2 value see appendix A.

$$B_2^* = \frac{B_2}{B_2^{HS}} = 1 + \frac{3}{8R^3}\int_{2R}^{\infty}\left(1 - e^{-u(r)/k_BT}\right) r^2 dr. \tag{10.3}$$

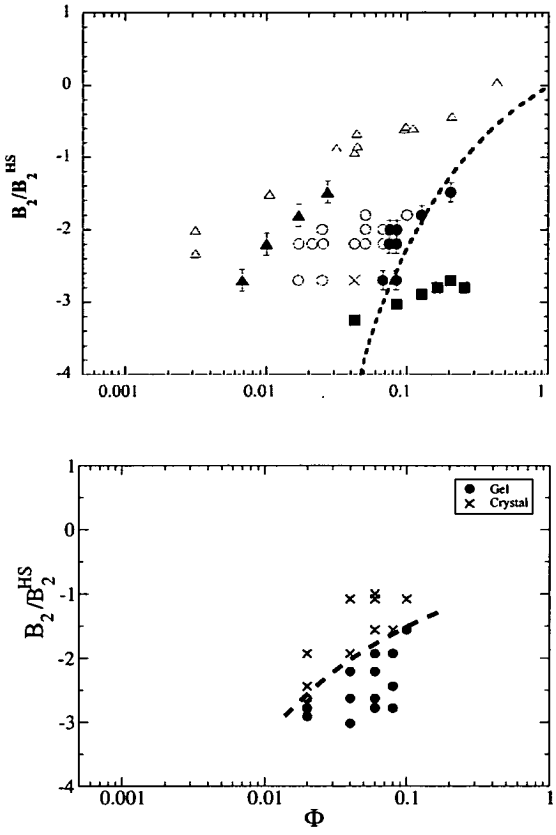

Figure 10.24: Phase diagram of lysozyme in the $(B2, \phi)$ plane. Top phase diagram determined by Kulkarni *et.al.* [51], where filled squares represent the gas-liquid binodal, filled circles represent the gelation boundary, and filled triangles represent the solubility boundary. Open circles are fluid samples which later crystallised, and the dashed line is the MCT bond formation line. Lower phase diagram determined here for the lysozyme-NaCl system at 10°C, where the line is drawn as a guide to the eye to represent the gelation boundary.

Tanaka and Ataka [104] reported the observation of 'droplets' in lysozyme solutions akin to the spherical beads reported here, and 'a sponge-like structure' which coarsened with time, reminiscent of spinodal decomposition. These observation are consistent with my own. Furthermore, Kuznetsov *et.al.* [52] report the observation of liquid phase droplets in solutions of immunoglobulins, where 'crystals are seen to nucleate on the surface of the liquid phase droplets... and they always grow outward into the exterior (low concentration) protein medium and not inward into the (high concentration) protein rich phase'. The similarity of the behaviour

of these droplets to the beads observed in my system suggest that the interpretations are applicable to other protein systems, and indeed such droplets have been reported in a variety of protein solutions [52].

Finally, this review is concluded by highlighting again the sensitivity of the system to solution parameters. Since studies are conducted at different pH, using different buffers and salts, and undoubtedly different preparation methods, it is unsurprising that a range of behaviour is reported. However, my interpretation can be applied to all systems in the literature without contradiction, and may also be relevant to solutions of other proteins.

10.6.2 Gas-Liquid Phase Separation in the Colloid-Polymer System

In this chapter the effect of the interaction between gas-liquid phase separation and a non-ergodicity transition on the phase behaviour of the lysozyme-NaCl system has been discussed. Consider now how these ideas can be applied to colloid-polymer mixtures.

As has been discussed, gelation is not necessarily caused by a non-ergodicity transition itself, but can occur in gas-liquid phase separating samples where the high concentration phase crosses a non-ergodicity line. With this in mind, reconsider the results presented in chapter 8 for the PMMA-PS colloid-polymer mixture.

Miller and Frenkel [60] accurately determined the gas-liquid critical point for adhesive hard spheres using Monte Carlo simulation techniques. They plot the gas-liquid coexistence curve in terms of an inverse stickiness parameter τ vs a density $\rho\sigma^3$, where σ is the particle diameter such that the volume of a particle will be $\pi\sigma^3/6$, and the volume fraction of the sample will be given by $\phi = \rho\sigma^3\pi/6$ [60].

In order to compare the predictions of different models to experimental data, a measure of the strength of interaction that is meaningful for all models is needed. For example, predictions using the Adhesive Hard Sphere (AHS) model of the gas-liquid coexistence curve are given in terms of an inverse stickiness parameter, and we now want to compare this parameter to the strength of the depletion attraction at varying polymer concentrations. This is best achieved by comparing the second virial coefficients B_2. The stickiness parameter is related to the second virial coefficient in the following way:

$$1 - \frac{1}{4\tau} = B_2^*, \tag{10.4}$$

where $B_2^* = B_2/B_2^{HS}$ is the reduced second virial coefficient and B_2^{HS} is the second virial coefficient of hard spheres. Using this expression the position of the gas-liquid coexistence boundary in the $(\tau, \rho\sigma^3)$ plane can be converted into the (B_2^*, ϕ) plane for comparison to my data.

The data points themselves must also be converted into the (B_2^*, ϕ) plane, which is done in the following way. As discussed above, B_2 can be calculated once the form of the potential is known using the equation:

$$B_2 = 2\pi \int_0^\infty r^2 \left(1 - e^{-U(r)/k_BT}\right) dr, \tag{10.5}$$

where $U(r)$ is the interaction potential and r the inter-particle separation. In our case, the interaction potential is the depletion potential, which was discussed in detail in chapter 3.2, and is given in equation 10.6:

$$U_{dep}(r) = \begin{cases} +\infty & : \quad r \leq \sigma \\ -\Pi_p V_{overlap} & : \quad \sigma < r \leq \sigma + 2R_g, \\ 0 & : \quad r > \sigma + 2R_g \end{cases} \tag{10.6}$$

where σ is the particle diameter. The hard sphere part of this potential (an infinite repulsion that prevents the colloids from overlapping) can be factored out to give the reduced second virial coefficient as:

$$B_2^* = \frac{B_2}{B_2^{HS}} = 1 + \frac{3}{8R^3} \int_{2R}^\infty \left(1 - e^{-u(r)/k_BT}\right) r^2 dr, \tag{10.7}$$

where $u(r)$ is the depletion potential without the hard sphere repulsion term. The original data points, each at a specific ϕ and c_p were first used to calculate the corrected values of the radius of gyration and size ratio as described in section 7.3.2. The corrected values for each data point were then used to calculate the strength of the attraction due to the depletion potential at each point. The maple code used to calculate B_2 values for each data point is shown in Appendix D, and the individual values are listed in table 1 in Appendix B. The data was then re-plotted in the (B_2, ϕ) plane and compared to the simulations of Miller *et.al.* [60]. The predictions of the non-ergodicity line from mode coupling theory were converted into the (B_2, ϕ) plane in the same way as the data points, and the experimental phase diagram and both predictions are shown in figure 10.25.

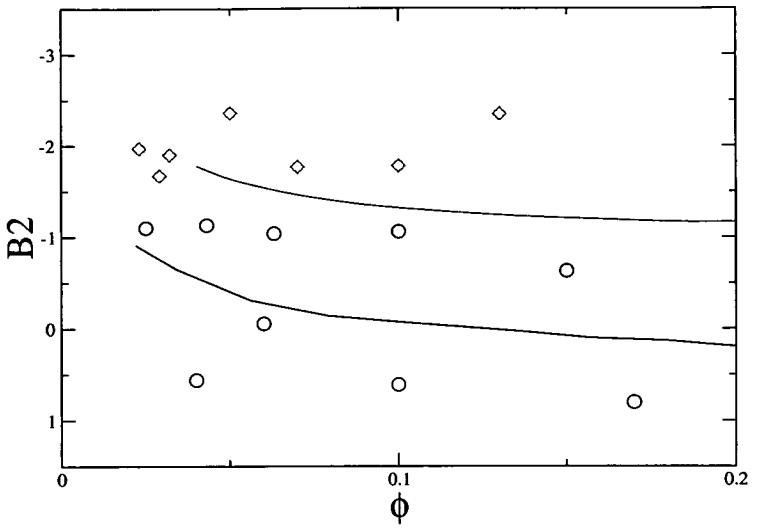

Figure 10.25: Phase diagram in the $(B2, \phi)$ plane, calculated as described above. The data points are those presented in chapter 8.2 for uncharged colloids in a density matched solvent, the upper line is the predicted position of the spinodal from Miller and Frenkel [60], and the lower line the MCT prediction of the non-ergodicity line including the polymer R_g and size ratio correction.

From the results outlined in this chapter it is clear that the *interaction* between gas-liquid phase separation and a non-ergodicity transition determines the phase behaviour that is observed. Compare this interpretation to the colloid-polymer system. The gas-liquid binodal simulated by Miller and Frenkel [60] fits the data very well. However, if there were no gel transition in this system then one would expect to see gas-liquid phase separation above the coexistence curve. Instead aggregation is observed.

The bare MCT non-ergodicity line is too low to fit the data, but it is possible that the MCT non-ergodicity line may lie higher in the phase diagram than predicted. A renormalised variant of the MCT non-ergodicity line, the CMCT line, may also be relevant as discussed in chapter 8. One possible interpretation is that the CMCT line cuts the gas-liquid coexistence curve, so that phase-separation is interrupted by the formation of a gel in the high concentration liquid phase. This interpretation would be similar to that for the protein system. However, the non-equilibrium behaviour expected, for example the formation of clusters or aggregates, are *never* observed in the colloid-polymer mixture. The alternative interpretation, that the system becomes non-ergodic above the MCT or the CMCT line and the gas-liquid binodal is *within* the gelation region, appears to be more likely for this system. Observations in the literature that

show the interaction between phase separation and kinetic arrest in colloid-polymer mixtures will now be discussed.

10.6.3 Literature Review

Reports of gelation are ubiquitous in the colloid-polymer mixture literature [73, 76, 108, 91] as well as in other related systems [51, 63, 90]. Furthermore, the importance of the interaction between gelation and gas-liquid phase separation has been reported [108]. Given the wealth of experimental evidence available, the interpretation outlined in this chapter can be tested against results from the literature. In this section experimental results where an extensive study of the phase behaviour has been conducted will be discussed[73, 76], and interpreted using the ideas presented above.

Consider the experimental system described in chapter 3.6.1. The experimental phase diagram determined for this system is reproduced in figure 10.26 [73].

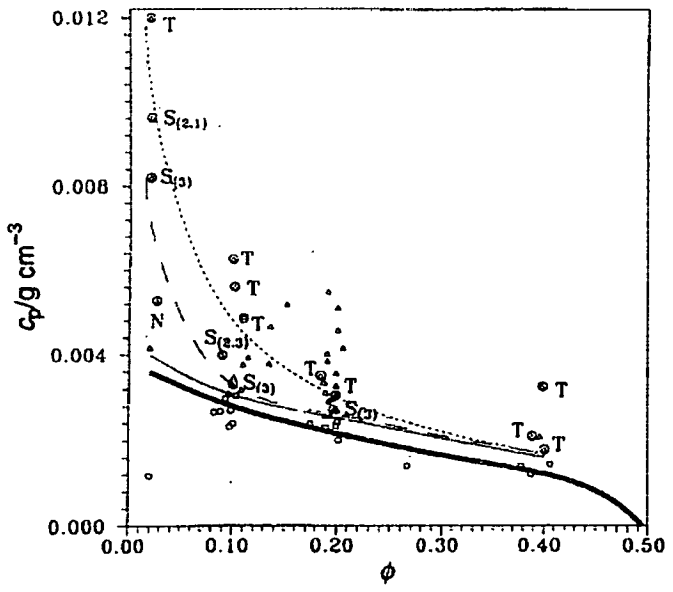

Figure 10.26: Experimental phase diagram of PMMA colloids on the addition of polystyrene at a size ratio $\xi = 0.1$. Regions of fluid ∘, fluid-crystal coexistence □ and non-equilibrium behaviour △ were observed. Lines are drawn to a guide to the eye, and show regions of nucleation-like behaviour labelled N, spinodal-like behaviour S and transient gelation T [73].

Consider first the 'Spinodal-like' behaviour (labelled 'S' in the phase diagram). As described in the paper [73], these samples gave small angle scattering rings that brightened and collapsed

continuously to leave peaked forward scattering over a matter of minutes, behaviour reminiscent of spinodal decomposition. However, no two coexisting liquid phases were observed, but rather the particles settled under gravity at rates much larger than those of the single phase colloidal fluid. My interpretation of this behaviour would be that the samples are above the gas-liquid phase separation curve. However, the high concentration liquid phase has crossed the non-ergodicity line and has begun to gel. Because gravity is present in this system, small gelled aggregates sediment before a sample-spanning gel is formed. The end result would be an amorphous sediment at the bottom of the tube and a clear supernatant above, with no latency time observed since the sample-spanning gel did not have time to form. This is indeed what is observed.

Consider now the samples which were labelled as 'Transient Gels' (T). The initial behaviour is the same as the Spinodal-like samples, but after the first few minutes the small angle ring appeared frozen. This lasted for a fixed period of time (the latency time of the gel) after which the gel collapsed, leaving an amorphous sediment below a clear supernatant. My interpretation of this data is that spinodal decomposition begins in the same way as for the spinodal-like samples. Again, the high concentration liquid phase gels. However, unlike the previous samples, the gel forms faster due to the high ϕ or c_p of the sample (as reported in chapter 8). A sample-spanning gel is formed, and after a latency time the gel collapses.

In this interpretation the difference between the spinodal-like and transient gel samples is due to sedimentation. If the individual clusters undergo significant sedimentation before the clusters meet and span space, a sample-spanning gel is not formed, but the aggregates sediment under gravity. Conversely, if the clusters grow large enough to touch before undergoing sedimentation, as would be the case at higher ϕ, a gel will form. The experimentally determined gelation boundary is the cross over between these two situations.

Finally, consider the nucleation-like samples (N). The initial behaviour of these samples is reminiscent of gas-liquid phase separation by nucleation, and microscopic observation of these samples showed disconnected droplets. However, no two separate liquid phases were observed, instead the particles are reported to sediment under gravity much faster than the single phase fluid. My interpretation of this behaviour is that the samples are above the binodal so phase-separation by nucleation begins. The high concentration liquid phase (in this case the droplets) crosses the non-ergodicity line and begins to aggregate. The aggregated droplets then sediment under gravity, leaving a final phase of a dense amorphous sediment at the bottom of the sample and a clear supernatant above, as was observed.

In summary, the non-equilibrium boundary is associated with the gas-liquid binodal. The spin-

odal separates the 'N' and 'S' types of behaviour. Finally the experimental gelation boundary is the line above which clusters can touch and gel before they undergo significant sedimentation.

When interpreting phase behaviour the following points must be considered. If a non-ergodicity line crosses the gas-liquid coexistence curve at a point $\phi^{cross}, c_p^{cross}$ then a tie line that first crosses this intersection point can be drawn. Samples with final composition within the gas-liquid coexistence region but above this critical tie line will become non-ergodic in the high concentration liquid phase. The nature of the high concentration phase depends on whether the liquid phase is percolating at the time of gelation. To the left of the percolation point, individual aggregates will be formed. To the right of the percolation point, a gel can be formed.

Thus far the interpretation is identical to that of the protein system. However, the effects of gravity must now be considered. If the gel takes a long time to form, as is the case at low volume fractions as illustrated by the results presented in chapter 8, then the growing aggregates will sediment before they meet and form a gel. This is where the description differs from that for the protein system. The experimental gel line is no-longer given by the quench path at low ϕ but rather is dependent on the rate of sedimentation in the system.

10.6.4 A Return to Gravity

Consider again the results of Poon *et.al* [73]. Small angle scattering of laser light by the samples was observed. The time dependent peak position, $Q_m(t)$ for samples above the non-equilibrium boundary is shown in figure 10.27. $Q_m(t)$ was found to scale approximately as $t^{-0.25}$ at early times for all samples of increasing polymer concentrations. For samples at lower polymer concentrations this scaling crossed over to an approximate t^{-1} scaling at long times. However, for samples with a higher polymer concentration the collapse of the small angle scattering peak is incomplete. These samples were labelled as transient gels. Notice that the initial behaviour of both types of samples is alike; both exhibit approximate $t^{-0.25}$ scaling at early times. The crossover to the subsequent two types of behaviour occurs at the same point. It is suggested that if the aggregates meet each other fast enough at this point the high concentration phase becomes fully non-ergodic and a transient gel is observed. However, if the individual aggregates undergo significant sedimentation before they meet, gelation will not occur.

These ideas were discussed for the colloid-polymer mixture studied in this thesis in chapter 8. The gelling mechanism is different in the two systems. In that studied by Poon *et.al.*, system (a), the sample gels because the high concentration phase of a phase separating sample becomes

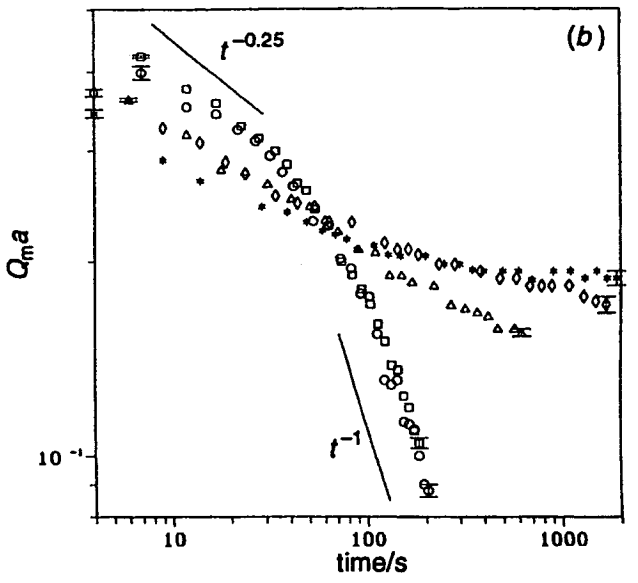

Figure 10.27: Small angle light scattering results showing the time dependent peak position $Q_m(t)$ of samples which exhibited non-equilibrium behaviour. The sequence of samples have increasing polymer concentration in the order ○, □, △, ◇, ⋆, and are the circled set of data points at $\phi \sim 0.1$ in figure 10.26. Taken from [73].

non-ergodic. In the system studied here, system (b), a non-ergodicity transition has itself been traversed. However, the same discussion should apply to both system. The formation of a non-ergodic structure by either mechanism takes time. Small aggregates form which grow, and will become non-ergodic if (a) they grow large enough to touch or (b) they grow large enough that their renormalised volume fraction is large enough to form a repulsive glass. In both cases, if the sedimentation velocity is faster than the growth of the aggregates, the sample will sediment and not become non-ergodic.

The effect of sedimentation on gelation has been considered by Poon [72] and Allain [2]. It is suggested that due to the effects of gravity there is a threshold volume fraction $\phi^\star$ below which gelation does not occur, equation 10.8:

$$\phi^\star \sim \left(\frac{9k_BT}{2\pi\Delta\rho g a^4}\right)^{\frac{d_f-3}{d_f+1}}, \tag{10.8}$$

where $\Delta\rho$ is the difference in the density between the particles and the suspending solvent, g is the gravitational acceleration constant, a is the radius of the particles, and d_f is the fractal dimension of the clusters, which for DLCA aggregates $d_f = 1.8$. The threshold volume fraction

System	Radius (nm)	Solvent	Predicted $\phi^\star$	Experimental $\phi^\star$
Sedgwick	527	*cis*-decalin	0.24	0.02
Poon *et.al.* [73]	238	*cis*-decalin	0.06	0.01
Poon *et.al.* [76]	301	*cis*-decalin	0.09	0.04

Table 10.1: Predicted threshold volume fraction and experimentally determined threshold volume fraction for four experimental systems.

can be calculated for the experimental system studied here and for two experimental systems in the literature, those of Poon *et.al.* [73, 76]. The predicted threshold volume fractions are summarised in table 10.1. However, as discussed in chapter 8.3, the predicted scaling does not hold in the system studied here. This is not entirely surprising since equation 10.8 is only valid in the limit of low ϕ, as discussed in chapter 8.3.

The results reported by Poon *et.al.* [73] are qualitatively consistent with both the experimental systems studied here. Firstly, their model colloid-polymer mixture exhibits the interaction between gas-liquid phase separation and kinetic arrest that was observed in the protein system. Secondly, gravity can be seen to interrupt aggregation in the same way as was observed for the colloid-polymer mixture studied here.

10.7 Summary

The phase behaviour of the lysozyme-NaCl system has been studied in detail, and the wide range of non-equilibrium behaviour observed was interpreted in terms of the interaction between gas-liquid phase separation and a non-ergodicity transition. The temperature is shown to change the relative positions of these two lines in the phase diagram, and so alter the topology of the phase diagram observed. The interpretations discussed are shown to be consistent with a range of reports on the lysozyme system in the literature.

The interpretation of the non-equilibrium behaviour in terms of the interaction between gas-liquid phase separation and a non-ergodicity transition was applied to colloid-polymer mixtures via reports in the literature, and shown to be consistent. For large particles (i.e. on the colloidal length scale of $\gtrsim$ 100nm as opposed to the protein length scale of $\lesssim$ 10nm) it was shown that gravity also plays an important role in determining the phase behaviour of the system, consistent with the results presented in chapter 8 for the model colloid-polymer mixture studied here.

Chapter 11

Future Work

11.1 Introduction

The work presented in this thesis has demonstrated the wide variety of behaviour that can arise in systems interacting with a short ranged attraction and a screened coulomb repulsion. The onset of aggregation and its relationship to theoretically predicted non-ergodicity transitions has been discussed, and the observations in the different colloid-polymer mixtures have raised many questions. The interaction between metastable phase separation and a non-ergodicity transition was highlighted in the protein system, and the range of behaviour that may result from the interaction between these two types of behaviour under different conditions is diverse. It is hoped that the work presented in this thesis will provide a basis for further study and understanding, and in this chapter some ideas for future research are highlighted.

11.2 Gelation and Aggregation

It follows on from the results presented in chapters 8 and 10 that two different types of gels can be formed. Firstly, the sample can cross a non-ergodicity transition line at low volume fractions. The non-ergodicity that arises, associated with gelation, is not dependent on phase separation. Secondly, it is possible for gels to form in the high concentration liquid phase of a phase separating sample. This appears to be the most common type of gel reported in the colloid-polymer physics literature. At size ratios of $\xi \sim 0.06$ and above, the spinodal line always lies below the gelation line, which means that in these systems it will always be the latter type of gel which is observed, and it seems associated with transient gelation.

The nature of the primary gel, that is not dependent on phase separation, may be hard to pin down. As discussed earlier, mode coupling theory predicts a non-ergodicity transition at low volume fractions which may be responsible for the onset of aggregation, but a renormalised variant may be relevant to the gelation transition observed in colloid-polymer mixtures. The interpretation of the results presented in this thesis in terms of these ideas is suggestive. It is hoped that further investigation of the experimental system studied here could advance our understanding, and distinguish between these two predictions with more certainty.

At size ratios $\xi > 0.06$ it may be possible to discern two fundamentally different gelled states, one due to kinetic arrest in the high concentration phase of a phase separating sample, and another where the non-ergodicity transition line has been crossed. Figure 11.1 shows two pictures taken by P. Smith [95], for a colloid-polymer mixture of size ratio $\xi = 0.15$. It can be

11.3 Charged Colloids

The charged colloidal system studied in this work, that of PMMA in a solvent mixture of CHB and *cis*-decalin, provides enormous potential for the study of charge effects in colloid-polymer mixtures and related systems. By varying the concentration of salt the repulsive interaction can be controlled and the phase behaviour that arises can be studied in a well characterised and density matched model system. Combined with the addition of polymer to induce attraction of controllable range and strength between the particles, the interaction potential of the colloids can be varied from attractive to repulsive, and from short to longer ranges.

The effect of charge on the aggregation of a colloid-polymer mixture has been investigated here, and the effect of charge on other types of phase behaviour can also be studied in the same system, from phase separation to glassy dynamics. The investigation need not be limited to colloid-polymer mixtures, the potential for studying more complex systems such as mixtures of charged colloids with charged polymer and surfactants is extensive.

Finally, the application of AC electric fields across charged colloidal suspensions gives rise to a range of fascinating behaviour [43, 53, 116], and preliminary results suggest that the motion and behaviour of the charged PMMA particles under an applied electric field could be studied in detail using confocal microscopy.

seen that the gel at the lower polymer concentration, figure 11.1(a), is very inhomogeneous, and almost reminiscent of the bicontinuous texture observed in spinodal decomposition. However, the gel at higher polymer concentration, figure 11.1(b), is more homogeneous. A possible interpretation is that the inhomogeneous gel is formed when the high concentration phase in a phase-separating sample becomes non-ergodic, but the homogeneous gel observed at higher attractions may be above the non-ergodicity transition line itself. This is speculation, but further investigation of these two gelled states could advance our understanding of transient gelation in colloid-polymer mixtures. Furthermore, the interaction between these two processes of kinetic arrest and phase separation could be studied as the interaction range varies with increasing size ratios.

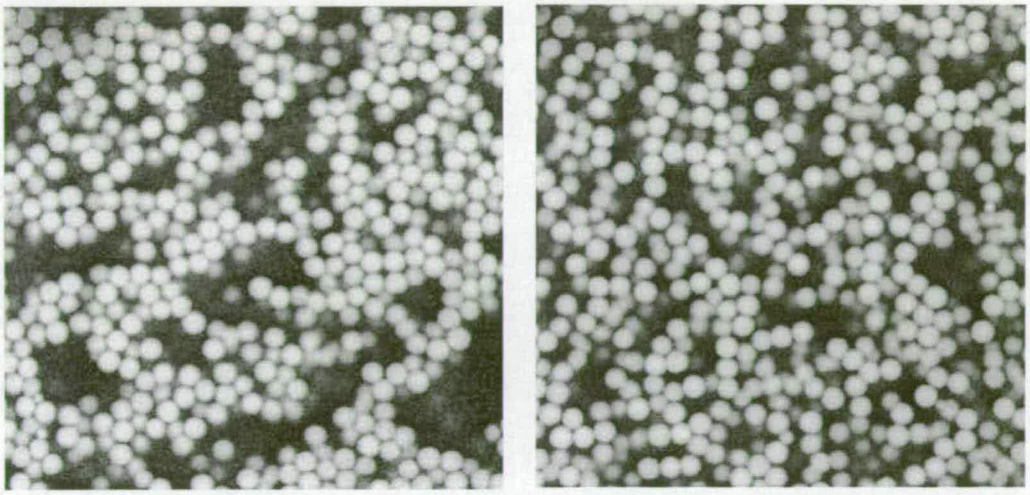

Figure 11.1: Confocal images of a colloid-polymer mixture of PMMA colloids on the addition of polystyrene. The colloid volume fraction and polymer concentration of the samples were (a)$\phi = 0.4, c_p = 0.0017 g/cm^3$ and (b) $\phi = 0.4, c_p = 0.0035 g/cm^3$. Experiments were performed by P. Smith at the University of Edinburgh [95].

The results presented in this thesis were all in systems with a very low colloid volume fraction. It has been discussed how the MCT non-ergodicity transition line may need to be renormalised at low volume fractions to describe weak gels, but has been shown to be relevant to the glass transition in colloid-polymer mixtures at high volume fractions. How do these two pictures, one of glassy behaviour and one of weak gelation, coincide at intermediate volume fractions? Further study in this area could enhance our understanding of the relationship between of the non-ergodicity transitions predicted and observed in experimental systems.

Chapter 12

Conclusion

The aggregation and gelation of colloidal systems has been studied for a model colloid-polymer mixture and a globular protein solution.

A model colloid-polymer mixture in a density matched solvent, with short-ranged attractions and polymer to colloid size ratio $\xi < 0.03$, was studied at low volume fractions $\phi < 0.2$. At low polymer concentration c_p an ergodic, single fluid phase was observed. On increasing c_p the colloids were observed to aggregate above a sharp boundary. The colloidal aggregates grew into large clusters. The centre of mass and orientation of these clusters was seen to fluctuate without any net long ranged motion. At $\phi > 0.05$ these fluctuations disappeared after ~ 10 minutes and the sample appeared frozen to the naked eye, but at lower ϕ the clusters fluctuated for $\sim 1 - 2$ hours. The *onset* of aggregation of the colloids is associated with the ergodic to non-ergodic transition line predicted by mode coupling theory (MCT) [9]. The relevance of the cluster mode coupling theory (CMCT) has also been discussed. Starting from this 'standard model' the effects of charge and gravity on the aggregation of colloidal systems have been explored.

When the colloids in this aggregating system were charged, a single phase ergodic fluid was observed at low c_p, and on increasing c_p the colloids again aggregated above a sharp boundary. However, the aggregation did not continue as for the standard model system. Instead, stable and long-lived mobile clusters were observed to coexist with a sea of monomers. At sufficiently high inter-particle attractions and volume fractions the samples became non-ergodic. The onset of aggregation is again associated with the MCT non-ergodicity transition, but the size to which the clusters can grow is limited by the charge on the particles. The electrostatic repulsion was found to stabilise the clusters against further growth, and the radius of the clusters was shown to be proportional to $\phi^{1/3}$ as predicted in a recent publication [33].

When gravity is introduced to the system of neutral particles sedimentation may prevent the sample from becoming non-ergodic. As before, a single phase ergodic fluid was observed at low c_p, and on increasing c_p the colloids aggregated above a sharp boundary. At high c_p the sample appeared non-ergodic, but at intermediate polymer concentrations the aggregates were observed to sediment. The onset of aggregation is again associated with the MCT non-ergodicity transition line. However, if the growing clusters undergo significant sedimentation before they can meet the sample does not become non-ergodic. The experimental non-ergodicity boundary was therefore observed at higher inter-particle attractions due to the presence of gravity.

The cluster mode coupling theory, a renormalised variant of MCT, is thought to be relevant to the non-ergodicity transition in colloid-polymer mixtures at low volume fractions [49]. An

ergodic fluid of clusters is predicted above the MCT transition. A second non-ergodicity transition then predicts where the clusters will become non-ergodic. An interpretation of my results using these ideas has been presented. In this scheme, above the MCT line colloids aggregate into clusters. The size to which these clusters can grow may be limited by either charge or gravity. Above a second non-ergodicity transition the sample becomes non-ergodic.

The phase behaviour of protein solutions has been studied. The addition of salt to a protein solution causes an effective attractive interaction between the proteins, and similarly to colloid-polymer mixtures non-equilibrium behaviour is observed at sufficiently high attractions. Optical microscopy revealed four regimes of non-equilibrium behaviour: gas-liquid phase separation, non-coalescing 'beads', large aggregates and transient gelation. The interaction between the gas-liquid binodal and the ergodic to non-ergodic transition line is found to be essential in understanding the non-equilibrium phase behaviour. Gas-liquid phase separation can be interrupted by the formation of a gel in the high concentration liquid phase. If the liquid phase is percolating the sample will form a transient gel.

Reports of phase separation and gelation throughout the protein and colloid-polymer literature were found to be consistent with this interpretation. These phenomena lead to the prediction of multiple gelled states in sticky-hard-sphere systems.

Appendix A

Maple Code

Calculation of the DLVO Potential

```
> restart;
```

Definitions of all the parameters of the system:

```
> T:=273.15 +22;
> k:=1.38e-23;
> A:=8.3*k*T;
> R:=1.7e-9;
> e:=1.6e-19;
> ep0:=8.854e-12;
> ep:=80;
> kappa:=c->0.327e10*sqrt(c);
> delta:=1.437e-10;
```

UvdW is the van der Waals component of the potential, given by:

```
> UvdW:=(r)->-(A/(12*k*T))*
> ((4*R^2/(r^2-4*R^2))+4*R^2/r^2+2*ln(1-4*R^2/r^2));
```

Uel is the Coulomb component of the potential, given by:

```
> Uel:=(r,q,c)->((q*e)^2*exp(-kappa(c)*(r-2*R)))/
> (4*k*T*Pi*ep0*ep*r*(1+kappa(c)*R)^2);
```

The total DLVO potential (excluding the infinite hard sphere repulsion) is U, given by:

```
> U:=(r,q,c)->UvdW(r)+Uel(r,q,c);
```

The full potential or its components can then be plotted for different parameters:

```
> plot([U(r,10,0.25)],r=2*R+delta..5*R,y=-0.2..0.2);
```

```
> plot([UvdW(r,10,0.25)],r=2*R+delta..5*R,y=-0.2..0.2);}
> plot([Uel(r,10,0.25)],r=2*R+delta..5*R,y=-0.2..0.2);
```

If required, the second virial coefficient of the osmotic pressure b2 as a function of the charge and the salt concentration can be calculated. This is the reduced second virial coefficient in which the hard sphere component has been factored out, i.e. b2= B_2/B_2^{HS}.

```
> b2:=(qq,c)->1+(3/(8*(R+delta/2)^3))*Int((r/(R+delta/2))^2*
> (1-exp(-U(r,sqrt(qq),c))),r=delta+2*R..50*R,10,_Dexp);
```

Appendix B

High Concentration Correction to R_g and ξ

In this appendix the corrections to the polymer radius of gyration R_g and the polymer to colloid size ratio ξ are described in detail.

Firstly, this correction is applied to the experimental data points, and table 12.1 lists all the original and corrected values. Secondly, the prediction of the MCT non-ergodicity line is discussed. The same corrections are applied to the predicted position of the line in the (ϕ, c_p) plane, and the corrected values are listed in table 12.2.

Finally, the corrected values of the second virial coefficient B_2 are listed for the data points (in table 12.1) and the MCT non-ergodicity line (table 12.2).

Correction to Experimental Data

As discussed in chapter 7, Wiltzius [113] performed a study showing that solutions of linear and flexible polymers can be characterised by a *concentration dependent* length. Using this approach corrections to the radius of gyration as the polymer solution becomes more concentrated can be made. A reduced concentration X is defined following the work of Ohta and Oono [66]. X is proportional to c/c^* and to a first order approximation is given by:

$$X\left[\frac{9}{16} - \frac{ln(M_w/M_n)}{8}\right] = B_2 \times c, \tag{12.1}$$

where c is the concentration of the polymer solution, and B_2 is the second virial coefficient of the osmotic pressure. If the second virial coefficient B_2 is known, then the reduced concentration X can be calculated using equation 12.1. Table 12.1 shows the calculated values of the reduced length X and the corresponding corrections.

In all that follows the radius of gyration of a single coil is taken to be $R_g = 13.7nm$ as calculated following the approach of Berry [10], giving an uncorrected size ratio of $\xi = 0.026$.

The second virial coefficient was measured by Berry [10] for *cis*-decalin. A value $A_2\sqrt{M_w}$ is plotted against the Fixman parameter z. Since $z = 0.149$ is known for the molecular weight of polystyrene used in this work, a value of $A_2\sqrt{M_w} = 0.032$ can be from this graph. A_2 differs from the second virial coefficient by a factor of the molecular weight of the polymer $B_2 = A_2 \times M_w$, therefore I find $B_2 = 0.032\sqrt{212400} = 14.75cm^3g^{-1}$.

Wiltzius [113] measured a reduced length Δ/R_g (where R_g is the radius of gyration of a single polymer coil in solution) as a function of X. By comparison to this data (figure 3 in reference [113]), an estimate of the reduced length can be made for a particular concentration of polystyrene, which is shown in table 12.1. The reduced length can then be converted into an effective radius of gyration using an approximate scaling (multiplication by a factor of $\sqrt{3}$).

Table 12.1 lists all the data point from the 'standard model' system which was studied (i.e. uncharged colloids in a density matched solvent), and shows the reduced length and final corrected value of the radius of gyration and the size ratio.

Furthermore, the second virial coefficient of the osmotic pressure can be calculated assuming an attraction of the depletion potential form. The maple code used to calculate the values of B_2 is shown in Appendix D. Table 12.1 also summarises the final (corrected) values of B_2 which were determined for each of the data points.

ϕ	c_p (mg/ml)	c_p^{free} (mg/ml)	X	Δ/R_g	Δ	$R_g^{corrected}$ (nm)	ξ	$B2$
0.04	1.9	1.99	0.052	0.58	7.946	13.76	0.0257	0.56
0.043	4	4.19	0.110	0.50	6.85	11.86	0.0222	−1.53
0.06	2.4	2.57	0.067	0.58	7.946	13.76	0.0257	−0.055
0.063	3.8	3.93	0.103	0.505	6.919	11.98	0.0224	−1.04
0.1	1.7	1.91	0.050	0.58	7.946	13.76	0.0257	0.61
0.1	4.3	4.83	0.127	0.47	6.439	11.15	0.0208	−1.06
0.17	1.2	1.47	0.039	0.58	7.946	13.76	0.0257	0.8
0.15	4.2	5.02	0.132	0.45	6.165	10.68	0.0200	−0.63
0.025	4.7	4.83	0.127	0.47	6.439	11.15	0.0208	−1.1
0.032	6.0	6.22	0.163	0.43	5.891	10.20	0.0191	−1.9
0.05	8.0	8.46	0.22	0.38	5.206	9.017	0.0168	−2.36
0.07	5.9	6.39	0.167	0.425	5.822	10.08	0.0188	−1.77
0.1	6.2	6.96	0.182	0.41	5.617	9.729	0.0181	−1.78
0.13	6.5	7.30	0.191	0.40	5.48	9.492	0.0177	−2.35
0.029	7.0	7.25	0.190	0.40	5.48	9.492	0.0177	−1.67
0.023	5.5	5.63	0.148	0.45	6.165	10.68	0.0200	−1.97

Table 12.1: Corrections to R_g and ξ for experimental data

Correction to MCT Predictions

It is possible, following the approach of Bergenholtz *et.al.* [9], to predict the position of the MCT non-ergodicity line in the (ϕ, c_p) plane. The polymer volume fraction in the free volume $\eta_p^{(R)}$ at which the non-ergodicity transition is predicted can be calculated in the limit of low ϕ and low ξ using the expression:

$$3.02 \sim \frac{K_c^2 \phi_c}{b_c} = \frac{\xi^2 \phi_c}{3\eta_{p,c}^{(R)}(1+\xi)} \exp[3\eta_{p,c}^{(R)}(1+\xi)/\xi] \tag{12.2}$$

MCT is consistently wrong in its prediction of the volume fraction of the hard sphere glass transition, and is therefore scaled to account for this as described by Bergonholtz *et.al.* [9]. The value obtained of η is converted into a value of c_p for direct comparison to experimental results using the equation:

$$c_p = \frac{3[\alpha\eta_p^{(R)}]M_w}{4\pi R_g^3 N_A}, \tag{12.3}$$

where α is the free volume fraction as defined in chapter 3.2, in which the uncorrected value of ϕ is used. In this way the scaling is applied only at the very end of the calculation.

On closer consideration it is clear that where the MCT line lies in the (ϕ, c_p) plane is dependent on both the radius of gyration and the size ratio in a non-trivial way. Thus, the correction to these values discussed above must also been included in this calculation. In this case, a starting value of $\xi = 0.026$ and $R_g = 13.7$nm were used, and the predicted values of c_p were found. Then, these values of c_p were put through the same correction process as the data points, described above. This gives a *corrected* value of both ξ and $R_g^{corrected}$.

These corrected parameters were then used to redo the same calculation, but this time corrected for concentration effects. Table 12.2 lists both the starting values and corrected values, and the final value of c_p which is where the predicted MCT non-ergodicity line will lie in a phase diagram.

It is clear that this is an iterative process, and could be refined further by repeated calculations always using the most recent corrected values for the parameters. However, after the calculation had been performed twice the value could not be refined further within the uncertainties in the original data of Wiltzius [113].

ϕ	c_p	c_p^{free}	X	Δ/R_g	Δ	$R_g^{corrected}$	ξ	c_p^{final}
0.022	2.989	3.062	0.080	0.51	6.987	12.10	0.0226	3.847
0.034	2.841	2.949	0.077	0.52	7.124	12.34	0.023	3.497
0.056	2.633	2.802	0.073	0.53	7.261	12.58	0.0235	3.057
0.079	2.475	2.706	0.071	0.537	7.261	12.74	0.0238	2.787
0.101	2.349	2.738	0.071	0.537	7.261	12.74	0.0238	2.537
0.135	2.186	2.559	0.067	0.58	7.946	13.76	0.0257	2.114
0.157	2.091	2.431	0.064	0.58	7.946	13.76	0.0257	2.017
0.180	2.005	2.489	0.065	0.58	7.946	13.76	0.0257	1.922
0.202	1.922	2.458	0.064	0.58	7.946	13.76	0.0257	1.837

Table 12.2: Corrections to R_g and ξ for MCT predictions

Finally, the MCT line can also be converted into values of B_2 for comparison to other work, in the same way as the experimental data reported here. The maple code used to perform the calculation of the MCT non-ergodicity transition, and to calculate the values of the second virial coefficient of the osmotic pressure B_2, is shown in Appendix C.

Appendix C

Maple Code

Calculation of the MCT Non-Ergodicity Transition

```
> restart;
```

First define all the constant parameters of the system:

```
> Mw:=212400;
> Na:=6.02*10^(23);
> R:=535*10^(-9);
> e:=1.6*10^(-19);
> E0:=8.8541878*10^(-12);
> pi:=3.1415927;Kb:=1.38*10^(-23);
> T:=295;
```

Define Vol as the volume of the overlapping deletion regions between two particles at separation r:

```
> Vol:=(r,xi)->(1-(3*r/(4*R*(1+xi)))+1/2*(r/(2*R*(1+xi)))^3)*
> pi/6*(2*R)^3*(1+xi)^3;
```

The polymer concentration in the free volume, cpfree, is given by:

```
> cpfree:=(cp,phi,xi)-> cp/alpha(phi,xi);
> alpha:=(phi,xi)->(1-phi)*
> exp(-A(xi)*G(phi)-B(xi)*G(phi)^2-C(xi)*G(phi)^3);
> A:=(xi)->3*xi+3*xi^2+xi^3;
> B:=(xi)->(9*xi^2/2)+3*xi^3;
> C:=(xi)->3*xi^3;
> G:=(phi)->phi/(1-phi);
> np:=(cp,phi,xi)->Na/Mw*cpfree(cp,phi,xi);
```

Osmotic is the expression for the osmotic pressure of the polymer solution:

```
> Osmotic:=(cp,phi,xi)->np(cp,phi,xi)*Kb*T;
```

Finally, the total depletion potential (not including the hard sphere repulsion) U is given by:

```
> U:=(cp,phi,r,xi)->(-1*Osmotic(cp,phi,xi)*Vol(r,xi))/(Kb*T);
```

The reduced second virial coefficient of the osmotic pressure b2 (where b2=B_2/B_2^{HS}) is given by the expression:

```
> b2:=(cp,phi,xi)->1+(3/(8*R^3))*Int
> (((1-(exp(-1*U(cp,phi,r,xi))))*r^2),r=2*R..2*(R+xi*R),10,_Dexp);
```

Now calculate the predicted position of the MCT non-ergodicity transition, using parameters xi1 and phi1, which are the values of the size ratio and volume fraction respectively. Note that the parameters can be corrected for the decrease in the radius of gyration of the polymer as the concentration increases, as discussed in appendix B. These corrected parameters can be used if required.

```
> xi1:=0.0238;
> phi1:=0.079;
> solve({(xi1^2*phi1*exp(3*eta*(1+xi1)/xi1))/(3*eta*(1+xi1))=3.02},
> {eta});
```

Eta is the volume fraction of polymer in the free volume. The solution to this equation gives the value of eta (at the colloid volume fraction phi1) at which the MCT non-ergodicity transition is predicted. This can then be converted into the value of the polymer concentration in the total sample volume, cp1:

```
> evalf(alpha(0.079, 0.0238));
> cp1:=3*0.915*0.0748*Mw/(4*pi*(12.74*10^(-9))^3*Na);
```

This is the value of the polymer concentration cp1 at which the MCT non-ergodicity line is predicted. Finally the b2 value at this particular polymer concentration, volume fraction and size ratio can be evaluated:

```
> evalf(b2(2787,0.079,0.0238));
```

Appendix D

Maple Code

Calculation of the Second Virial Coefficient B_2

Firstly define all the parameters of the system:

```
> restart;
> R:=535*10^(-9);Mw:=212400;
> e:=1.6*10^(-19);
> Q:=100*e;
> E0:=8.8541878*10^(-12);
> pi:=3.1415927;
> E:=5;
> Kb:=1.38*10^(-23);
> T:=295;
> Na:=6.02*10^(23);
```

Now define Vol as the volume of the overlapping deletion regions between two particles at separation r:

```
> Vol:=(r,xi)->(1-(3*r/(4*R*(1+xi)))+1/2*(r/(2*R*(1+xi)))^3)*
> pi/6*(2*R)^3*(1+xi)^3;
```

The polymer concentration in the free volume, cpfree, is given by:

```
> cpfree:=(cp,phi,xi)-> cp/alpha(phi,xi);
> alpha:=(phi,xi)->(1-phi)*
> exp(-A(xi)*G(phi)-B(xi)*G(phi)^2-C(xi)*G(phi)^3);
> A:=(xi)->3*xi+3*xi^2+xi^3;
> B:=(xi)->(9*xi^2/2)+3*xi^3;
> C:=(xi)->3*xi^3;
> G:=(phi)->phi/(1-phi);
> np:=(cp,phi,xi)->Na/Mw * cpfree(cp,phi,xi);
```

Next write down the expression for the osmotic pressure of the polymer solution, Osmotic:

```
> Osmotic:=(cp,phi,xi)->np(cp,phi,xi)*Kb*T;
```

Finally, the total depletion potential U (excluding the hard sphere repulsion) is given by:

```
> U:=(cp,phi,r,xi)->(-1*Osmotic(cp,phi,xi)*Vol(r,xi))/(Kb*T);
```

The reduced second virial coefficient of the osmotic pressure b2, where b2= B_2/B_2^{HS}, is given by the expression:

```
> b2:=(cp,phi,xi)->1+(3/(8*R^3))*Int
> (((1-(exp((-1*U(cp,phi,r,xi))))))*r^2),r=2*R..2*(R+xi*R),10,_Dexp);
```

The value of the reduced second virial coefficient b2 can then be calculated for each sample polymer concentration (cp), volume fraction (phi) and size ratio (xi). Note that the values of these parameters can be corrected for the change in the polymer radius of gyration as the concentration increases, as described in appendix B. The corrected values can then be used to calculate b2.

```
> evalf(b2(1900,0.04,0.0257));
```

List of Tables

7.1 Radius of gyration for polystyrene in *cis*-decalin 97

7.2 Phase behaviour of Charged PMMA Colloids 100

7.3 Values of the solvent density of the different solvents used. 106

7.4 Full characterisation of the four experimental systems studied. 107

8.1 Table showing the time taken for clusters to appear non-ergodic (τ) for a range of volume fractions. 126

10.1 Predicted threshold volume fraction and experimentally determined threshold volume fraction for four experimental systems. 195

12.1 Corrections to R_g and ξ for experimental data 209

12.2 Corrections to R_g and ξ for MCT predictions 211

List of Figures

2.1 The hard sphere phase diagram. Below a freezing volume fraction ϕ_F the stable phase is a fluid, and above a melting volume fraction ϕ_M the system is fully crystalline. At intermediate volume fractions the system phase separates into coexisting fluid and crystal phases. 7

2.2 Competition between configurational and free volume entropy 8

2.3 Schematic illustration of charge and sterically stabilised colloids 10

2.4 Schematic illustration of the repulsive interaction potential for ideal hard spheres, sterically stabilised 'nearly hard sphere' colloids and charge stabilised 'soft sphere' colloids [97]. 11

3.1 Schematic illustration of the overlapping depletion zones (dotted lines) around two colloidal particles in a colloid-polymer mixture. 15

3.2 Approximations to the free volume fraction α. First approximation (a) is the total volume less the volume occupied by colloids alone, and the second approximation (b) is the total volume less the volume occupied by the colloids and their depletion zones $\phi(1+\xi)^3$. The free volume V_{free} is represented by the shaded area. 16

3.3 Generic form of the depletion potential $U_{dep}(r)$ induced by the addition of non-adsorbing polymer to hard sphere colloids. In (b), the different curves illustrate the effect of increasing the number density of polymer molecules in the sample n_p, at fixed colloidal volume fraction ϕ. The depth of the potential increases as the amount of polymer increases. Graph (c) illustrates the effect of the polymer-colloid size ratio ξ on U_{dep}. The different curves correspond to different values of ξ, at fixed n_p and ϕ. As the size ratio ξ is increased both the range and the well depth of the depletion potential increase. 17

3.4 Schematic illustration of phase diagrams in (a) the temperature-density (T, ρ) representation, (b) the polymer effective volume fraction - colloid volume fraction representation $(\eta_p^{(R)}, \phi)$ and (c) the polymer concentration-colloid volume fraction (c_p, ϕ) representation, for size ratios ξ larger than ~ 0.25. 19

3.5 Schematic phase diagrams, Illet *et.al.*, [42], for size ratios of (a)$\xi = 0.08$, (b) $\xi = 0.25$ and (c) $\xi = 0.57$, the vertical axis plots the effective volume fraction of the polymer coils in the free volume of the sample $\eta_p^{(R)}$. 20

3.6 Experimental phase diagrams, Illet *et.al.* [42], for size ratios $\xi = 0.08$, 0.25 and 0.57. The vertical axis plots the polymer concentration in g/cm^4. Lines are drawn as guides to the eye. The symbols denote the following: $\circ$, fluid; $\Diamond$, gas plus liquid; $\times$, gas plus liquid plus crystal; $+$, liquid plus crystal; $\Box$, gas plus crystals; $\triangle$, gel ($\xi = 0.08$) or no visible crystallites ($\xi = 0.24$ and 0.57); $*$, glass. 20

3.7 Schematic phase diagram for a colloid polymer mixture of size ratio less than 0.25. The variables are the colloid volume fraction ϕ and the polymer chemical potential μ_p. The gas-liquid binodal is hidden within the fluid-crystal coexistence region. 21

3.8 Free energy landscape showing fluid and crystal branches 22

3.9 Schematic illustration of the free energy landscapes of the fluid branch for a colloid-polymer mixture on increasing polymer concentration [57]. 22

3.10 Free energy landscape for a colloid polymer mixture at high chemical potential. 23

3.11 Schematic illustration of a phase diagram showing the binodal and associated spinodal. 24

3.12 Schematic illustration of the free energy curves which lead to (a) stable and (b) unstable behaviour. 24

3.13 Schematic illustration of a free energy landscape leading to binodal and spinodal phase boundaries. 25

3.14 Experimental phase diagram of PMMA colloids on the addition of polystyrene at a size ratio $\xi = 0.1$. Regions of fluid $\circ$, fluid-crystal coexistence $\Box$ and non-equilibrium behaviour $\triangle$ were observed. Lines are drawn to a guide to the eye, and show regions of Nucleation-like behaviour labelled N, spinodal-like behaviour S and transient gelation T [73]. 26

3.15 Schematic illustration of delayed sedimentation 27

3.16 Schematic diagram showing the growth of a fractal cluster. As the cluster grows its average density decreases, and its structure becomes more tenuous [72]. . . 28

3.17 $2D$ reversible DLCA simulation of particle aggregation with varying bond strength. (a) $U_{dep} \gg k_BT$, (b) $U_{dep} \sim 3k_BT$, (c)$U_{dep} \simeq k_BT$, [35]. 29

3.18 Schematic illustration showing (a) a floppy piece of network with four distinct rigid clusters and (b) the placement of an additional link that can lock the previous four clusters into a single rigid cluster [47] 31

3.19 Schematic illustration showing predicted non-ergodicity transition and particle configurations for a colloid-polymer mixture of size ratio $\xi \sim 0.08$ which is (a) a repulsive glass, having crossed the non-ergodicity transition line, (b) a fluid at the same volume fraction as the glass but with a stronger attraction and (c) an attractive glass. Above the non-ergodicity line at high inter-particle attraction and lower volume fraction a gel might be expected (d). 32

3.20 Predictions of the gel line from percolation and MCT compared to experimental results [82]. Solid symbols are the experimental points delimiting the stable fluid regions for different size ratios. At size ratios of $\xi = 0.026$ (squares) the samples gelled, at $\xi = 0.115$ (circles) fluid-crystal coexistence was observed, and at $\xi = 0.377$ (diamonds) the liquid-liquid coexistence curve was the phase boundary crossed. The solid curves are the MCT gel line, the long-short dashed curves are the MCT gel lines taking into account a polymer free volume correction (for details see [82]), and the short dashed curves are the static percolation lines. The corrected MCT line at size ratio of 0.337 lies well below the data points for that size ratio (diamonds) and was not shown for clarity. 33

4.1 Schematic illustration of the electrical double layer of a charged colloid in solution. 39

4.2 Phase diagram for charged polystyrene spheres on the addition of HCl. Symbols denote the following: ■ = *bcc* crystal, △ = *fcc* crystal, □ = *fcc* + *bcc* coexistence, • = *glass*, ○ = *fluid*. The bold lines are drawn as guide to the eye phase boundaries. The dashed line is the liquid-fcc phase boundary as predicted by computer simulation using a Yukawa potential [85]. To give an estimate of the range of the potential, note that the radius was 46nm, and the Debye screening length varied from 40nm (at zero salt concentration and volume fraction $\phi = 0.1$) to 9nm (at 500μ M salt concentration and $\phi = 0.3$), [93]. 40

4.3 Schematic illustration of the DLVO potential and of the van der Waals and Coulomb components. 41

4.4 Predictions of the Van der Waals component using values of $R = 660$nm and $T = 295.15$, and plotting for values of the Hamaker constant of $50 \times 10^{-20}, 10 \times 10^{-20}$ and 1×10^{-20}J, as labelled. For calculations, written in Maple, see Appendix A. 43

4.5 Predictions of the Coulomb component of the DLVO potential for different values of the charge on the particle. These plots are for the case of aqueous solutions of small charged colloids. Values used were $T = 295.15$, $R = 100nm$, $\epsilon = 80$, $c = 0.1mM$, and plotting for charges of $q = 100$ and $Q = 500$. The Hard sphere component of the potential is not shown for clarity, but provides an infinite repulsion at the point of contact $r = 2R$. 44

4.6 Predictions of the DLVO potential and the Coulomb component, using values of $T = 295.15$, $R = 100$nm, $\epsilon = 80$, $A = 1.3 \times 10^{-20}$ [89], $Q = 200$ electronic charges and varying the concentration of salt. The three salt concentrations plotted are (a) the low screening case $c = 0.05$ mM, (b) intermediate screening $c = 0.2$ mM and (c) the high screening case $c = 5$mM. For details of the calculation performed in Maple see Appendix A. 45

4.7 Experimental phase diagram of charged polystyrene spheres, where kT/U_a is a dimensionless temperature and λ is the Debye screening length multiplied by the average interparticle spacing. Symbols denote the following, ○, fluid phase, ▲, BCC crystal, •, FCC crystal. Solid lines are MD simulation results using the DLVO potential from Robbins *et.al* [85]. Phase diagram taken from [61]. . 46

4.8 Morphology of phase-separating latex particles on the addition of HEC, taken from [99]. 48

4.9 Comparison of experimental data [99] and predictions [29] of the phase behaviour of polystyrene latex on the addition of HEC. The fluid solid transition, indicated by the solid line, is predicted for $a/r_g > 3$ while the fluid-fluid transition, indicated by the dashed line, emerges for $a/r_g < 3$. Taken from [89]. . 49

4.10 Schematic illustration of the resulting effective attraction of a negatively charged colloid to other like-charged colloids despite the electrostatically repulsive pair potential [111]. 52

4.11 Schematic illustration of the stable cluster phase predicted for charged colloidal suspensions. Effect of the charge is to stabilise clusters of radius R_* against further aggregation. 54

5.1 Experimental titration curve for the globular protein lysozyme, from Kuehner *et. al.* [50], Tanford *et. al.* [105] and Haynes *et. al.* [37]. Taken from [50]. . . 60

5.2 Experimental titration curves for the globular protein lysozyme in potassium chloride solutions of ionic strength ranging frome $0.1 - 2$ Molar. Taken from [50]. 61

5.3 Schematic titration curve, showing the buffering region around the pK_a value, taken from [5]. 64

5.4 Predictions of DLVO theory showing the Coulomb component of the potential U_C, the van der Waals component U_{VdW} and the resultant DLVO potential U_{DLVO}, for a pH of 4.5 and typical experimental NaCl concentrations of (a) 0.15 M, (b) 0.25 M and (c) 0.5 M. 67

5.5 Schematic illustration of the Hofmeister series, taken from [14] 69

5.6 Phase diagram of lysozyme on the addition of NaCl at pH= 4.5, pH= 5.9 and pH= 7.8, in the scaled (c_s/Q^2, ϕ) plane, taken from [71]. 71

6.1 Magnification by a converging lens of focal length f. 74

6.2 Magnification by an infinite tube length compound microscope. 75

6.3 Illustration of the numerical aperture of an objective lens [84]. 77

6.4 Diagram of the intensity across the Airy disk pattern of two points separated by a distance d just satisfying the Rayleigh criterion and hence just resolved. I_1 represents the intensity of each central maximum and I_2 the intensity of the resultant central trough. 78

6.5 Kohler illumination. The illuminating and images forming rays are shown separately. 79

6.6 The fluorescent microscope. 81

6.7 Illustration of the development of the confocal scanning microscope from the conventional microscope, (a) shows the optical system of a conventional microscope, (b) a form of the conventional scanning microscope, (c) Another form of conventional scanning microscope, and (d) The confocal optical system. Taken from [112]. 82

6.8 The optical sectioning property of the confocal microscope [112]. 84

6.9 The confocal microscope. 85

6.10 Illustration of (a) Precessing spin viewed in the laboratory (stationary) frame of reference, and (b) Precessing spin viewed in the rotating frame of reference so it appears stationary. The application of a rotating magnetic field B_1, which appears stationary in the rotating frame of reference, induced transitions between the two allowed states, (c). Taken from [83]. 86

6.11 Population of spins:top, disordered in the absence of a magnetic field; middle, aligned and precessing in an applied field; bottom, brought to a common origin. Taken from [83] 87

6.12 Magnetisation M_{xy} produced by phase coherence between spins after an applied radio frequency pulse. Taken from [83] 88

6.13 The five parameters of a high resolution NMR spectrum, taken from [83]. . . . 91

7.1 Schematic plot of a sterically stabilised PMMA colloid 95

7.2 Phase behaviour of PMMA colloids of radius $535nm$ (top) and $660nm$(bottom). In each case the symbols denote the following: $\circ$ =fluid, $\times$ =fluid-crystal coexistence, $\blacksquare$ =crystal and $\Diamond$ =glass. ϕ_F, ϕ_M and ϕ_G are the freezing, melting and glass transition volume fraction for hard spheres. 100

7.3 Predictions of DLVO theory, using values of $T = 295.15$, $A = 0.105x10^{-20}$J, $R = 660nm$ and $\epsilon = 4.1$, as discussed in section 4.3.1. Figures (a) to (c) show the high screening case where a salt concentration of 40μM has been used. The full DLVO potential (a), the Coulomb repulsion (b) and the van der Waals attraction (c) are shown separately for clarity. The van der Waals attraction dominates the DLVO potential in this high screening case. Figures (d) to (f) show the case of low screening, using an ion concentration of 5×10^{-7}M. This value is an estimate of the ion concentration when no salt is added, for colloidal particles with a charge of 700 electronic charges per particle. The full DLVO potential (d), the Coulomb repulsion (e) and the van der Waals attraction (f) are shown separately. For the Maple code used in calculating these potentials see Appendix A. 105

7.4 Plot showing the percentage decrease in the weight of a sample over two hours. 111

8.1 Experimental set up for sample observation in the confocal microscope. 115

8.2 Phase diagram of uncharged PMMA-PS in a density matched solvent mixture of CHB and *cis*-decalin, showing phases of fluid (○) and large non-ergodic aggregates (◇). 116

8.3 Confocal micrographs showing a samples (a) in the homogeneous fluid phase $\phi = 0.06$ and $c_p = 2.4$ mg/ml, (b) large non-ergodic aggregates at low volume fraction $\phi = 0.029$, $c_p = 7$ mg/ml and (c) large non-ergodic aggregates at higher volume fraction $\phi = 0.1$, $c_p = 6.2$ mg/ml. All images taken 1 hour after initial sample preparation. 118

8.4 A time series of sample $\phi = 0.029$ and $c_p = 7$ mg/ml taken from 1 to 80 minutes after sample preparation, illustrating the formation of large aggregates at low volume fractions. 120

8.5 Phase diagram showing the experimental data presented in section 8.2 and the calculated non-ergodicity lines predicted using Mode Coupling Theory. The upper line includes the correction for the decrease in R_g and ξ at increasing polymer concentrations. 122

8.6 Schematic parameter flows (arrows) in the CMCT scheme. Flow (a) within the lower coordinate plane ($\epsilon^{-1} = 0$) gives percolation of ICA clusters on passing through a non-equilibrium percolation line. Trajectories starting from finite ϵ^{-1} flow upward to smaller ϵ, larger ϕ and smaller δ. Those that arrive on the dark surface result in a semi-ergodic cluster phase. The marginal gel trajectory (b) ends at the intersection line of the repulsive (light surface) and attractive (dark surface) branches of the MCT transition. Taken from [49]. 124

8.7 Phase diagram in the (ϕ, c_p) plane. The data points are those presented in chapter 8.2, the upper line is the predicted position of the CMCT non-ergodicity line, and the lower lines are the MCT predictions of the non-ergodicity line with and without the correction to the polymer R_g and size ratio ξ. Samples which took timescales of hours to form are bracketed (◇). 125

8.8 Phase diagram of charged and density matched PMMA on the addition of polystyrene, size ratio $\xi = 0.021$, showing regions of fluid(○), small clusters(⋆), and large non-ergodic aggregates(◇). 128

8.9 Phase diagram of charged and density matched PMMA on the addition of polystyrene, size ratio $\xi = 0.026$, showing regions of fluid(○), clusters(⋆), and gel(◇). 129

8.10 Confocal images of samples (a) $\phi = 0.01$, $c_p = 0.5$ mg/ml, (b) $\phi = 0.086$, $c_p = 3$ mg/ml and (c) $\phi = 0.082$, $c_p = 6.3$ mg/ml taken 1 hour after sample preparation. 130

8.11 A time series of sample $\phi = 0.086$, $c_p = 3$ mg/ml showing a short time behaviour of a cluster sample. Images were taken 1 hour after sample preparation, and each image is separated by 10 seconds. 132

8.12 A time series of sample $\phi = 0.082$, $c_p = 6.3$ mg/ml, showing the short time behaviour of a non-ergodic sample. The images were taken 1 hour after sample preparation and each image is separated by 10 seconds. 133

8.13 A series of images of sample $\phi = 0.15$, $c_p = 1.9$ mg/ml showing the behaviour of a cluster sample over time, and $\phi = 0.15$, $c_p = 4$ mg/ml showing the behaviour of a non-ergodic sample over time. Both samples had high volume fractions. Images were taken 1 minute, 30 minutes and 1 hour after sample preparation. The images have been enlarged for clarity. 134

8.14 Sequence of images of sample $\phi = 0.06$, $c_p = 9.6$ mg/ml showing the behaviour of a cluster sample with time, and $\phi = 0.05$, $c_p = 13.5$ mg/ml showing the behaviour of a non-ergodic sample with time. Both samples have low volume fractions. Images taken 1 minute, 30 minutes and 1 hour after initial sample preparation. The images have been enlarged for clarity. 135

8.15 Plot showing the variation of cluster radius with volume fraction. 136

8.16 Plot showing the variation of cluster radius with volume fraction, for volume fractions $\phi \gtrsim 0.07$. 137

8.17 Computer generated image, using particle co-ordinates of a typical cluster in sample $\phi = 0.086$ and $c_p = 3$mg/ml. 139

8.18 First images, taken initially after sample preparation, of samples (a) $\phi = 0.029$ and $c_p = 7$mg/ml from the standard model system and (b) $\phi = 0.06$ and $c_p = 9.6$mg/ml from the charged phase diagram. Sample (a) evolves into large CMCT-predicted clusters and eventually turns non-ergodic whereas sample (b) evolves into the stable cluster phase which coexists with monomers. However, the initial stages of aggregation look very similar in the two different systems. 140

8.19 Experimental phase diagram PMMA-ps in cis-decalin, showing regions of fluid (○), large non-ergodic aggregates (◇) and sedimenting-clusters (⋆). 142

8.20 Series of images taken at different depths into sample $\phi = 0.038 c_p = 3.8 mg/ml$, taken at 6μm, 12μm, 18μm, 24μm, 30μm and 36μm into the sample. Images were taken ten minutes after initial sample preparation. The variation from a dense sediment to a sparse cluster phase as the height increases is clearly visible. 143

8.21 Sequence of images of sample $\phi = 0.038$, $c_p = 3.8$ mg/ml, taken ten minutes after initial sample preparation, at 30μm above the bottom cover slip. Each image is separated by 30 seconds. 144

8.22 Sequence of images of sample $\phi = 0.066$, $c_p = 4.4$ mg/ml, taken ten minutes after initial sample preparation at 30μm above the bottom cover slip. The sequence of images shows the time evolution of a non-ergodic sample over the space of two minutes. Each image is thirty seconds apart. 145

8.23 Phase diagram of charged PMMA in (reduced) gravity on the addition of ps, size ratio 0.026, showing regions of fluid(○), clusters(⋆), and large non-ergodic aggregates(◇). 149

8.24 Example of a cluster phase and non-ergodic state at high colloid volume fraction, samples(a) $\phi = 0.097$, $c_p = 3.7$ mg/ml and (b) $\phi = 0.12$, $c_p = 7$ mg/ml respectively. 150

10.1 Schematic illustration of sample cell used for microscopic observations. 163

10.2 Experimental phase diagram, showing regions of single phase fluid ○, crystals ×, bicontinuous texture ■, non-coalescing 'beads' ▲ and aggregates △, and transient gelation ⋆. 164

10.3 Optical micrographs showing (a) bicontinuous texture at $\phi = 0.14$, $c_s = 0.7$ M, (b) spherical beads (note higher magnification) at $\phi = 0.07, c_s = 0.9$ M (c) large aggregates $\phi = 0.02$, $c_s = 1.5$ M, (d) large aggregates and a crystal viewed through crossed polars $\phi = 0.05$, $c_s = 1.1$ M (e) transient gel $\phi = 0.1$, $c_s = 0.9$M with inhomogeneities on the $\sim 10\mu$m scale and (f) tetragonal crystals observed after 30 minutes at $\phi = 0.05$, $c_s = 0.6$ M. 165

10.4 Sedimentation profile of a gelled sample at $\phi = 0.07$ and $c_s = 1.4$ M. 166

10.5 Series of images of sample $\phi = 0.05$ and $c_s = 1.6$ M, taken between 1 minute and 100 minutes after sample preparation, showing the evolution of a gelled sample. 167

10.6 Time series of sample $\phi = 0.1$ and $c_s = 0.8$ M, showing the evolution of the coarsening bicontinuous texture reminiscent of spinodal decomposition. The bar indicates the scale on all the images. 168

10.7 Time series of sample $\phi = 0.14$ and $c_s = 0.7$ M, showing the evolution of a sample which displayed a bicontinuous texture reminiscent of spinodal decomposition. the bar indicates the scale of all the images. 169

10.8 Increasing size of aggregates as the salt concentration increases, for sample at $\phi = 0.02$ and salt concentration from $1.4 - 1.7$ M. 170

10.9 Series of images taken between 1 minute and 80 minutes of a sample at $\phi = 0.07$ and $c_s = 0.9$ M, showing the evolution of a sample in which spherical and non-coalescing beads were observed. 170

10.10 Series of images taken between 10 minutes and 90 minutes of a sample at $\phi = 0.02$ and $c_s = 1.7$ M, showing the evolution of a sample in which large aggregates of spherical beads were observed. 171

10.11 Image of sample $\phi = 0.02$ and $c_s = 1.1$ M in which sea urchin crystals were observed. 171

10.12 Schematic diagram illustrating the interpretation of the observed phase behaviour. CB is the crystallisation boundary, GL is the gas-liquid binodal and NErg the non-ergodicity transition line. 172

10.13 NMR spectrum of lysozyme at a volume fraction of $\phi = 0.06$ with no added salt. 175

10.14NMR spectra of lysozyme with volume fraction $\phi = 0.02$. The upper spectrum had no added salt, and the lower spectrum had $c_s = 1.4$M NaCl. 176

10.15Plot of $ln(1 - \frac{M}{M_0})$ vs $\tau(ms)$ for sample $\phi = 0.02$ with no added salt. 177

10.16Plot of $ln(1 - \frac{M}{M_0})$ vs $\tau(ms)$ for sample $\phi = 0.02$ and $c_s = 1.4$Molar. 178

10.17Phase diagrams at -2, 10, 22, 36 and $50°c$ (from top to bottom), the vertical axis is the NaCl concentration in Molar, c_s, and the horizontal axis is the protein volume fraction ϕ. Symbols denote the following, $\times$ =crystal, ■ =non-equilibrium behaviour and $\star$ =transient gelation. Phase diagrams at $-2°$ and 10°C were obtained by A.Salonen and the phase diagram at 50° was obtained by G.S.Roberts. 179

10.18Plot of NaCl concentration against temperature at $\phi = 0.08$. Solubility data is included for completeness, taken from [63, 12]. 180

10.19Schematic phase diagram showing the relative movement of the phase boundaries with decreasing temperature. 181

10.20Temperature dependence of the hydrophobic interaction for different surface sizes. Taken from [40]. 182

10.21Phase diagram of lysozyme with 0.5M NaCl, taken from [44]. The lines are drawn as a guide to the eye, where the bold line represents the binodal and the dashed line the spinodal. 184

10.22Phase diagram of lysozyme as a function of temperature in a 0.6M sodium phosphate buffer, showing the cloud point curve. The data are from three different pH solutions; pH 7.0 (circles), pH 6.5 (squares) and pH 6.0 (triangles). Solid lines are drawn as a guide to the eye. Taken from [106]. 185

10.23Phase diagram of lysozyme as a function of temperature in NaCl solution at a range of ionic strengths, showing the cloud point curve. Taken from [63]. . . . 186

10.24Phase diagram of lysozyme in the $(B2, \phi)$ plane. Top phase diagram determined by Kulkarni *et.al.* [51], where filled squares represent the gas-liquid binodal, filled circles represent the gelation boundary, and filled triangles represent the solubility boundary. Open circles are fluid samples which later crystallised, and the dashed line is the MCT bond formation line. Lower phase diagram determined here for the lysozyme-NaCl system at 10°C, where the line is drawn as a guide to the eye to represent the gelation boundary. 187

10.25Phase diagram in the $(B2, \phi)$ plane, calculated as described above. The data points are those presented in chapter 8.2 for uncharged colloids in a density matched solvent, the upper line is the predicted position of the spinodal from Miller and Frenkel [60], and the lower line the MCT prediction of the non-ergodicity line including the polymer R_g and size ratio correction. 190

10.26Experimental phase diagram of PMMA colloids on the addition of polystyrene at a size ratio $\xi = 0.1$. Regions of fluid $\circ$, fluid-crystal coexistence $\square$ and non-equilibrium behaviour $\triangle$ were observed. Lines are drawn to a guide to the eye, and show regions of nucleation-like behaviour labelled N, spinodal-like behaviour S and transient gelation T [73]. 191

10.27Small angle light scattering results showing the time dependent peak position $Q_m(t)$ of samples which exhibited non-equilibrium behaviour. The sequence of samples have increasing polymer concentration in the order $\circ$, $\square$, $\triangle$, $\Diamond$, $\star$, and are the circled set of data points at $\phi \sim 0.1$ in figure 10.26. Taken from [73]. 194

11.1 Confocal images of a colloid-polymer mixture of PMMA colloids on the addition of polystyrene. The colloid volume fraction and polymer concentration of the samples were (a)$\phi = 0.4, c_p = 0.0017 g/cm^3$ and (b) $\phi = 0.4, c_p = 0.0035 g/cm^3$. Experiments were performed by P. Smith at the University of Edinburgh [95]. 199

Index

Absorbance, 155
  Absorption Coefficient, 155

Acid, 60

Aggregation
  Experimental Examples, 26, 120
  Theoretical Descriptions, 27, 52, 122

Amino Acid, 62

Base, 60

Buffer, 63
  Ionic Strength, 64
  Preparation, 152
  Sodium Acetate, 152

B2, 213
  Depletion Potential,187, 213
  DLVO Potential, 184, 203
  Proteins, 67, 70, 184

Charged Colloids
  Experimental Determination, 100
  Experimental Results, 128
  Phase Behaviour, 39
  with Polymer,47

Cluster Phase, 128

Colloid Swelling, 99
  Cycloheptyl Bromide, 99

Confocal Microscope, 80
  Resolution, 82
  Optical Sectioning, 83

Common Tangent Construction, 20
  Fluid-Crystal, 20
  Gas-Liquid, 22

Coulomb Interaction, 43, 66
  See also DLVO Potential.

Critical Overlap Concentration, 98

Delayed Sedimentation, 26
  Experimental Results, 164

Density of Colloids, 99

Density of Solvents, 106

Depletion Potential, 14
  Calculation, 213

Dielectric Constant, 41, 101
  CHB:*cis*-decalin Mixture, 101

DLVO Potential, 40
  Calculation, 203
  Inadequacies, 50
  PMMA Colloids, 105
  Proteins, 66
  Real Systems, 67, 105

DLCA, 27

Debye Screening Length, 41, 66
  Cycloheptyl Bromide, 103
  Definition, 41
  NaCl in Water, 153

Entropy, 7, 14

Evaporation, 111
  Colloid Samples, 111
  Protein Samples, 157

Experimental Systems, 93, 151

Colloid-Polymer Mixtures, 94
Charged, 99
Uncharged, 94
Summary, 107
Protein Solutions, 152

Fixman Parameter, 96

Fluorescence Microscope, 81

Free Energy Landscapes, 20

Gas-Liquid Phase Separation, 22
Mechanisms, 23
Protein Solutions, 70, 160, 181

Gelation, 26
Charged Colloid-Polymer Mixtures, 52
Protein Solutions, 71
Structural Differences, 197

Gravitational Peclet Number, 34
Experimental Value, 146

Hamaker Constant, 42
Lysozyme, 67

Hofmeister Series, 69

Hydrophobic Interaction, 179
Temperature Dependence, 180

Infinite Tube Length Compound Microscope, 76

Ionic Strength, 67
Sodium Acetate Buffer, 152

Kohler Illumination, 78

Mode Coupling Theory, 31, 119
Calculation, 121, 211
Cluster Mode Coupling Theory, 122
Predictions, 122, 125

Nuclear Magnetic Resonance, 85
Experimental Results, 172
Inversion Recovery, 91, 173
Longitudinal Relaxation, 88
Spectrum, 91, 173
Transverse Relaxation, 89

Nucleation, 23
Experimental Results, 159
Crystals, 161
Gas-Liquid Phase Separation, 161, 168

Osmotic Pressure, 15

Optical Microscope, 74
Magnification of, 75
Resolution of, 75

Percolation, 29

pH, 59

Phase Diagrams
Charged Colloids, 40, 46, 49
Charged Colloid-Polymer Mixtures, 49
Colloid-Polymer Mixtures, 19, 21, 27, 33
Experimentally Determined, 113
Hard Spheres, 7
Proteins, 71
Representations, 18
Size Ratio Dependence, 20, 33
Topology, 20

Polarisation, 101
Solvent Mixture, 101

Polydispersity, 7
Colloid, 71
Polymer, 97

Proteins, 57
Sample Preparation, 151

Radius of Gyration, 95
in *Cis*-decalin, 97
Concentration Effects, 102
in Cycloheptyl Bromide,102
Temperature Dependence, 97

Salting-In, 68

Sample Cell, 115, 161

Sample Composition, 107
Colloids, 107
Proteins, 155

Sample Preparation, 93, 151
Colloids, 98, 104, 106
Proteins, 154

Scanning Microscope, 81

Sea Urchin Crystals, 169

Second Virial Coefficient, 67, 70, 184, 187, 203, 213
See also B2.

Sedimentation, 34
Delayed Sedimentation, 28
Experimentally Observed, 117, 126, 141, 147, 191

Sedimentation Velocity, 127
Experimental Values, 117, 127, 146

Size Ratio, 15
Correction, 102, 205
Experimental System, 107

Spinodal Decomposition, 23
Experimental Images, 166

Stabilisation, 8
Charge Stabilisation, 9
Steric Stabilisation, 10, 95, 105

Stoichiometric Point, 63

Tetrabutylammonium Chloride, 103
Screening Length, 104

Threshold Volume Fraction, 34
Experimental Values, 147
Literature Values, 192

Titration Curves, 64
pH Titration, 63
Protein Titration Curves, 60, 61,

Van der Waals Attractions, 40, 42, 8, 66

Volume Fraction, 107
Calculation, 108
Freezing, 7
Glass Transition, 7
Proteins, 156
Random Close Packing, 7
Sample Determination, 109

Washing, 95

Weight Fraction, 108

Bibliography

[1] B.J. Ackerson and P.N. Pusey. Shear-induced order in suspensions of hard spheres. *Physical Review Letters*, 61(8):1033–1036, 1988.

[2] C. Allain, M. Cloitre, and M. Wafra. Aggregation and sedimentation in colloidal suspensions. *Physical Review Letters*, 74(8):1478–1481, 1995.

[3] S. Asakura and F. Oosawa. *Journal of Polymer Science*, 22:1255, 1954.

[4] S. Asakura and F. Oosawa. Interaction between particles suspended in solutions of macromolecules. *Journal of Polymer Science*, 33(183), 1958.

[5] P.W. Atkins. *Physical Chemistry*. Oxford University Press, Oxford, 1992.

[6] J. Bergenholtz and M. Fuchs. Gel transitions in colloidal suspensions. *Journal of Physics:Condensed Matter*, 11:10171–10182, 1999.

[7] J. Bergenholtz and M. Fuchs. Nonergodicity transitions in colloidal suspensions with attractive interactions. *Physical Review E*, 59(5):5706–5715, 1999.

[8] J. Bergenholtz, M. Fuchs, and T. Voigtmann. Colloidal gelation and non-ergodicity transitions. *Journal of Physics:Condensed Matter*, 12:6575, 2000.

[9] J. Bergenholtz, W.C.K. Poon, and M. Fuchs. Gelation in model colloid-polymer mixtures. *Langmuir*, 19:4493–4503, 2003.

[10] G.C. Berry. Thermodynamic and conformational properties of polystyrene. 1. light scattering studies on dilute solutions of linear polystyrene. *Journal of Chemical Physics*, 44(12):4550–4564, 1966.

[11] Savile Bradbury. *An Introduction to the Optical Microscope*. Oxford University Press, Oxford, 1984.

[12] M.L. Broide, T.M. Tominc, and M.D. Zukowsky. Using phase transitions to investigate the effect of salts on protein interactions. *Physical Review E*, 53:6325–6335, 1996.

[13] M. Brostrom, D.R.M. Williams, and B.W. Ninham. Specific ion effects: Why dlvo fails for biology and colloidal systems. *Physical review Letters*, 87(16):168103, 2001.

[14] M.G. Cacace, E.M. Landau, and J.J. Ramsden. The hofmeister series: salt on solvent effects on interfacial phenomena. *Quarterly reviews of Biophysics*, 30(3):241–277, 1997.

[15] J.W. Cahn. *Trans. Metall. Soc. AIME*, 242:166, 1968.

[16] J.W. Cahn and J.E. Hillard. *Journal of Chemical physics*, 28:258, 1958.

[17] R. Chang. *Physical Chemistry with Applications to Biological Systems.* Macmillan ublishing Co.Inc., New York, 1981.

[18] G. Chirico, S. Beretta, and G. Baldini. Conformation of interacting lysozyme by polarized and depolarized light scattering. *Journal of Chemical Physics*, 110(4):2297–2304, 1999.

[19] K.D. Collins and M.W. Washabaugh. The hofmeister effect and the behaviour of water at interfaces. *Quarterly Reviews of Biophysics*, 18(4):323–422, 1985.

[20] P. Debye. *Polar Molecules*, chapter 1, page 12. Dover Publications, 1929.

[21] R. Ditteon. *Modern Geometrical Optics.* John Wiley and Sons, New York, 1997.

[22] S.B. Dubin, N.A. Clark, and G.B. Benedek. Measurement of the rotational diffusion coefficient of lysozyme by depolarized light scattering: Configuration of lysozyme in solution. *Journal of Chemical Physics*, 54(12):5158–5164, 1971.

[23] M.S. Elliot. *The Optical Microscopy of Colloidal Suspensions.* PhD thesis, The University of Ediburgh, 1999.

[24] W.H. Elliot and D.C. Elliot. *Biochemistry and Molecular Biology.* Oxford Universoty Press, Oxford, 1997.

[25] J.W. Essam. Percolation theory. *Reports on the Progress in Physics*, 43:833–912, 1980.

[26] D.J. Fairhurst. *Polydispersity in Colloidal Phase Transitions.* PhD thesis, The University of Edinburgh, 1999.

[27] W. Gall and N. McCrum. Internal friction in stereoregular poly-(methyl methacrylate). *Journal of Polymer Science*, 50:489, 1961.

[28] L.A. Galloway. *Phase Behaviour of Colloid-Micelle Mixtures.* PhD thesis, The University of Edinburgh, 2001.

[29] A.P. Gast, C.K. Hall, and W.B. Russel. Polymer induced phase separations in nonaqueous colloidal suspensions. *Journal of Colloid and Interface Science*, 96(1):251–267, 1983.

[30] A.P. Gast, W.B. Russel, and C.K. Hall. An experimental and theoretical study of phase transitions in the polystyrene latex and hydroxyethylcellulose system. *Journal of Colloid and Interface Science*, 109:161–171, 1986.

[31] A. George and W.W. Wilson. Predicting protein crystallization from a dilute solution property. *Acta Crystallographica*, D50:361–365, 1994.

[32] M.C. Grant and W.B. Russel. Volume-fraction dependence of elastic moduli and transition temperatures for colloidal silica gels. *Physical Review E*, 47:2606–2614, 1993.

[33] J. Groenwold and W.K. Kegel. Anomalously large equilibrium clusters of colloids. *J. Phys. Chem B*, 105:11702–11709, 2001.

[34] J.D. Gunton, M. San Miguel, and P.S. Sahni. *Phase Transitions and Critical Phenomena.* Academic Press, New York, 1983.

[35] M.D. Haw. *Computer Simulation of Aggregation and Gelation in Colloidal Suspensions.* PhD thesis, The University of Edinburgh, 1996.

[36] M.D. Haw, M. Sievwright, W.C.K. Poon, and P.N. Pusey. Cluster-cluster gelation with finite bond energy. *Advances in Colloid and Interface Science*, 62:1–16, 1995.

[37] C.A. Haynes, E. Sliwinsky, and W. Norde. Structural and electrostatic properties of globular proteins at a polystyrene water interface. *Journal of Colloid and Interface Science*, 164(2):394–409, 1994.

[38] S. Hayward, D.W. Heermann, and K. Binder. Dynamic percolation transition induced by phase separation: A monte carlo analysis. *Journal of Statistical Physics*, 49(5/6):1053–1081, 1987.

[39] W.G. Hoover and F.H. Ree. Melting transition and communal entropy for hard spheres. *Journal of Chemical Physics*, 49(8):3609–3617, 1968.

[40] D.M. Huang and D. Chandler. Temperature and length scale dependence of hydrophobic effects and their possible implications for protein folding. *Proceedings of the National Academy of Science*, 97(15):8324–8327, 2000.

[41] R.J. Hunter. *Foundations of Colloid Science*, volume 1. Oxford University Press, 1986.

[42] S.M. Illet, A. Orrock, W.C.K. Poon, and P.N. Pusey. Phase behavior of a model colloid-polymer mixture. *Phys. Rev E*, 1995.

[43] H. Isambert, A. Ajdari, J.L. Viovy, and J. Prost. Electrohydrodynamic patterns in charged colloidal solutions. *Physical Review Letters*, 78(5):971–974, 1997.

[44] C. Ishimoto and T. Tanaka. Critical behavior of a binary mixture of protein and salt water. *Physical Review Letters*, 39:474–477, 1977.

[45] J. Israelachvili. *Intermolecular and Surface Forces.* Academic Press, London, 1991.

[46] K. Ito, H. Yoshida, and N. Ise. *Science*, 263:66, 1994.

[47] D.J. Jacobs and M.F. Thorpe. Generic rigidity percolation in two dimensions. *Physical Review E*, 53(4):3682–3693, 1996.

[48] K. Kroy. Private communication.

[49] K. Kroy. A cluster mode-coupling approach to weak gelation in attractive colloids. *Condensed Matter*, 0310566, 2003.

[50] D.E. Kuehner, J.Engmann, F. Fergg, M. Wernick, H.W. Blanch, and J.M. Prausnitz. Lysozyme net charge and ion binding in concentrated aqueous electrolyte solutions. *Journal of Physical Chemistry B*, 103:1368–1374, 1999.

[51] A.M. Kulkarni, N.M. Dixit, and C.F. Zukoski. Ergodic and non-ergodic phase transitions in globular protein suspensions. *Faraday Discussion*, 123:37–50, 2003.

[52] Y.G. Kuznetsov, A.J.Malkin, and A. McPherson. The liquid protein phase in crystallization: A case study - intact immunoglobulins. *Journal of Crystal Growth*, 232:30–39, 2001.

[53] B. Ladoux, H. Isambert, J.F. Leger, and J.L. Viovy. New rectifying electrohydrodynamic instability at the boundary of charged gels in alternating electric fields. *Physical Review Letters*, 81(17):3793–3796, 1998.

[54] J.S. Langer. *Solids Far From Equilibrium*, chapter 3. Cambridge University press, Cambridge, 1991.

[55] J.L. Lebowitz, E. Helfand, and E. Praestgaard. Scaled particle theory of fluid mixtures. *Journal of Chemical Physics*, 43(3):774–779, 1965.

[56] G.F. Lothian. *Optics and its Uses*. Van Nostrand Reinhold Company, London, 1975.

[57] V.C. Martelozzo. *Crystallisation and Phase Separation in Colloidal Systems*. PhD thesis, The university of Edinburgh, 2001.

[58] A. McPherson. *Crystallization of Biological Macromolecules*. CSHL Press, New York, 1999.

[59] S.P. Meeker. *Low shear rheology and Delayed Sedimentation of Colloidal Systems*. PhD thesis, The University of Edinburgh, 1997.

[60] M.A. Miller and D. Frenkel. Competition of percolation and phase separation in a fluid of adhesive hard spheres. *Physical rEview Letters*, 90(13):135702, 2003.

[61] Y. Monovoukas and A.P. Gast. The experimental phase diagram of charged colloidal suspensions. *Journal of colloid and interface science*, 128:533–548, 1989.

[62] P. Mouroulis and J. Macdonald. *Geometrical Optics and Optical Design*. Oxford University press, 1997.

[63] M. Muschol and F. Rosenberger. Liquid-liquid phase separation in supersaturated lysozyme solutions and associated precipitate formation/crystallization. *Journal of Chemical Physics*, 107(6):1953–1962, 1997.

[64] M.A. Nazareno, S.M. Palacios, and R.A. Rossi. Reactions of cycloalkyl chlorides and bromides with diphenylphosphide ions in liquid ammonia. *Journal of Physical Organic Chemistry*, 6(7):421–426, 1993.

[65] B.W. Ninham. On progress in forces since the dlvo potential. *Advances in colloids and Interface Science*, 83:1–17, 1999.

[66] T. Ohta and Y. Oono. Conformation space renormalization theory of semidilute polymer solutions. *Physics letters*, 89A(9):460–464, 1982.

[67] K. Pham. Dynamic light scattering measurements performed by K. Pham at Edinburgh University found the hydrodynamic radius of these colloids to be $527nm$.

[68] K.N. Pham, A.M. Puertas, J. Bergenholtz, S.U. Egelhaaf, A. Moussaid, P.N. Pusey, A.B. Schofield, M.E. Cates, M. Fuchs, and W.C.K. Poon. Multiple glassy states in a simple model system. *Science*, 296:104–106, 2002.

[69] Plato. *Timaeus*. ca. 360 BC.

[70] W.C.K. Poon. Crystallization of globular proteins. *Physical Review E*, 55(3):3762–3764, 1997.

[71] W.C.K. Poon, S.U. Egelhaaf, P.A. Beals, A. Salonen, and L. Sawyer. Protein crystallization: Scaling of charge and salt concentration in lysozyme solutions. *Journal of Physics: Condensed Matter*, 12:L569–L573, 2000.

[72] W.C.K. Poon and M.D. Haw. Mesoscopic structure formation in colloidal aggregation and gelation. *Advances in colloid and INterface Science*, 73:71–126, 1997.

[73] W.C.K. Poon, A.D. Pirie, and P.N. Pusey. Gelation in colloid-polymer mixtures. *Faraday Discuss*, 101:65–76, 1995.

[74] W.C.K. Poon, F. Renth, and R.M.L. Evans. Kinetics from free energy landscapes - how to turn phase diagrams into kinetic maps. *Journal of Physics:Condensed Matter*, 12:A269, 2000.

[75] W.C.K. Poon, F. Renth, R.M.L. Evans, D.J. Fairhurst, M.E. Cates, and P.N. Pusey. Colloid-polymer mixtures at tripple coexistence: Kinetic maos from freeenergy landscapes. *Physical Review Letters*, 83(6):1239, 1999.

[76] W.C.K. Poon, L. Starrs, S.P. Meeker, A. Moussaid, R.M.L. Evans, P.N. Pusey, and M.M. Robins. Delayed sedimentation of transient gels in colloi-polymer mixtures: Dark-field observation, rheology and dynamic light scattering studies. *Faraday Discuss*, 112:143–154, 1999.

[77] V. Prasad. *Weakly Interacting Colloid Polymer Mixtures*. PhD thesis, Harvard University, 2002.

[78] V. Prasad, V. Trappe, A.D. Dinsmore, P.N. Segre, and D.A. Weitz. Universal features of the fluid to solid transition for attractive colloidal particles. *Faraday Discussion*, 123:1–12, 2003.

[79] W.S. Price, F. Tsuchiya, and Y. Arata. Lysozyme aggregation and solution properties studied using pgse nmr diffusion measurements. *Journal of American Chemical Society*, 121:11503–11512, 1999.

[80] P.N. Pusey and W.van Megen. Phase behaviour of concentrated suspensions of nearly hard colloidal spheres. *Nature*, 320:340–342, 1986.

[81] M. Quesada-Perez, J. Callejas-Fernandez, and R. Hidalgo-Alvarez. Interaction potentials, structural ordering and effective charges in dispersions of charged colloidal particles. *Advances in Colloid and INterface Science*, 95:295–315, 2002.

[82] S. Ramakrishnan, M. Fuchs, K.S. Schweizer, and C.F. Zukoski. Entropy driven phase transitions in colloid-polymer suspensions: Tests of depletion theories. *Journal of Chemical Physics*, 116(5):2201–2212, 2002.

[83] H. Rattle. *An NMR Primer for Life Scientists*. Partnership press, 1995.

[84] D.J. Rawlins. *Light Microscopy*. BIOS Scientific Publishers, 1992.

[85] M.O. Robbins, K. Kremer, and G.S. Grest. Phase diagram and dynamics of yukawa systems. *Journal of Chemical Physics*, 88:3286–3312, 1988.

[86] G.C.K. Roberts, editor. *NMR of Macrmolecules: A Practical Approach*. Oxford University press, Oxford, 1993.

[87] R.van Roij and R. Evans. Phase equilibria in a modal of low-salt suspensions of charged colloids. *Journal of Physics:Condensed Matter*, 11:10047–10060, 1999.

[88] D. Rosenbaum, P.C. Zamora, and C.F. Zukoski. Phase behavior of small attractive colloidal particles. *Physical review Leters*, 76(1):150–153, 1996.

[89] W.B. Russel, D.A. Savile, and W.R. Schowalter. *Colloidal Dispersions*. Cambridge University press, Cambridge, 1989.

[90] H. Sedgwick, K. Kroy, A. Salonen, M.B. Robertson, S.U. Egelhaaf, and W.C.K. Poon. Non-equilibrium behaviour of lysozyme solutions: beads, clusters and gels. *Condensed Matter*, 0309616, 2003.

[91] P.N. Segre, V. Prasad, A.B.Schofield, and D.A. Weitz. Glasslike kinetic arrest at the colloidal-gelation transition. *Physical Review E*, 86:6042–6045, 2001.

[92] S.A. Shah, Y.L. Chen, K.S. Schweizer, and C.F.Zukoski. Phase behavior and concentration fluctuations in suspensions of hard spheres and nearly ideal polymers. *Journal of Chemical Physics*, 118(7):3350–3361, 2003.

[93] E.B. Sirota, H.D. Ou-Yang, S.K. Sinha, and P.M. Chaikin. Complete phase diagram of a charged colloidal system-a synchrotron x-ray scattering study. *Physical Review Letters*, 62:1524–1527, 1989.

[94] P. Smith. Code used for visual reconstruction of particle co-ordinates provided by P. Smith, University of Edinburgh.

[95] P. Smith. PhD thesis, University of Edinburgh, 2003.

[96] I. Sogami and N. Ise. *Journal of Chemical Physics*, 81:6320, 1984.

[97] A.K. Sood. Structural ordering in colloidal suspensions. *Solid State Physics*, 45:1, 1991.

[98] M. Sperl. Dynamics in colloidal liquids near a crossing of glass- and gel-transition lines. *Condensed Matter*, 0308425, 2003.

[99] P.R. Sperry. Morphology and mechanism in latex flocculated by volume restriction. *Journal of Colloid and Interface Science*, 99(1):97–108, 1983.

[100] P.R. Sperry, H.B. Hopfenberg, and N.L. Thomas. Flocculation of latex by water-soluble polymers: Experimental confirmation of a nonbridging, nonadsorptive, volume-restriction mechanism. *Journal of Colloid and Interface Science*, 82(1):62–76, 1980.

[101] L. Starrs. *Collapse of Transient Gels in Colloid-Polymer Mixtures*. PhD thesis, The University of Edinburgh, 1999.

[102] L. Starrs, W.C.K. Poon, D.J. Hibberd, and M.M. Robins. Collapse of transient gels in colloid-polymer mixtures. *Journal of Physics: Condensed Matter*, 14:2485–2505, 2002.

[103] D. Stauffer and A. Aharony. *Introduction to Percolation Theory, Rev. 2nd edition*. Taylor and Francis, London, 1994.

[104] S. Tanaka and M. Ataka. Pattern formation and coarsening during metastable phase separation in lysozyme solutions. *Physical review E*, 65:0518XX, 2001.

[105] C. Tanford and R. Roxby. Interpretation of protein titration curves. application to lysozyme. *Biochemistry*, 11(11):2192–2198, 1972.

[106] V.G. Taratuta, A. Holschbach, G.M. Thurston, D. Blankschtein, and G.B. Benedek. Liquid-liquid phase separation of aqueous lysozyme solutions: Effects of ph and salt identity. *Journal of Physical Chemistry*, 94:2140–2144, 1990.

[107] H. Verduin and J.K.G. Dhont. Phase diagram of a model adhesive hard-sphere dispersion. *Journal of Colloid and Interface Science*, 172:425–437, 1995.

[108] N.A.M. Verhaegh, D. Asnaghi, H.N.W. Lekkerker, M. Giglio, and L. Cipelletti. Transient gelation by spinodal decomposition in colloid-polymer mixtures. *Physics A*, 242:104–118, 1997.

[109] G.A. Vliegenthart, J.S.van Duijneveldt, and B. Vincent. Phase transitions and gelation of silica-polystyrene mixtures in benzene. *Faraday Discussion*, 123:65–74, 2003.

[110] A. Vrij. Polymer at interfaces and the interactions in colloidal dispersions. *Pure and Applied Chemistry*, 48:471–483, 1976.

[111] P.B. Warren. A theory of void formation in charge-stabilised colloidal suspensions at low ionic strength. *Journal of Chemical Physics*, 112(10):4683–4698, 2000.

[112] T. Wilson, editor. *Confocal Microscopy*. Academic Press, London, 1990.

[113] P. Wiltzius, H.R. Haller, and D.S. Cannell. Universality for static properties of polystyrene in good and marginal solvents. *Physical Review Letters*, 51(13):1183–1186, 1983.

[114] P.R.T. Wolde and D. Frenkel. Enhancement of protein crystal nucleation by critical density fluctuations. *Science*, 277:1975–1978, 1997.

[115] W.W. Wood and J.D. Jacobson. Preliminary results from a recalculation of the monte carlo equation of state of hard spheres. *Journal of Chemical Physics*, 27:1207, 1957.

[116] A. Yethiraj and A.van Blaaderen. A colloidal model system with an interaction tunable from hard sphere to soft and dipolar. *Nature*, 421:513–517, 2003.